The Characterization of Material Properties and Structural Dynamics of the Manduca Sexta Forewing for Application to Flapping Wing Micro Air Vehicle Design

DISSERTATION

Ryan P. O'Hara, Major, USAF

AFIT/DS/ENY/12-06

DEPARTMENT OF THE AIR FORCE
AIR UNIVERSITY

AIR FORCE INSTITUTE OF TECHNOLOGY

Wright-Patterson Air Force Base, Ohio

APPROVED FOR PUBLIC RELEASE; DISTRIBUTION UNLIMITED.

AFIT/DS/ENY/12-06

The Characterization of Material Properties and Structural Dynamics of the Manduca Sexta Forewing for Application to Flapping Wing Micro Air Vehicle Design

DISSERTATION

Presented to the Faculty
Graduate School of Engineering and Management
Air Force Institute of Technology
Air University
Air Education and Training Command
In Partial Fulfillment of the Requirements for the
Degree of Doctor of Philosophy

Ryan P. O'Hara, B.S.M.E., M.S.M.E.
Major, USAF

September 2012

APPROVED FOR PUBLIC RELEASE; DISTRIBUTION UNLIMITED.

AFIT/DS/ENY/12-06

The Characterization of Material Properties and Structural Dynamics of the Manduca Sexta Forewing for Application to Flapping Wing Micro Air Vehicle Design

Ryan P. O'Hara, B.S.M.E., M.S.M.E.
Major, USAF

Approved:

Dr. Anthony N. Palazotto (Chairman)	Date
Dr. Richard G. Cobb (Member)	Date
Dr. Peter J. Collins (Member)	Date

Accepted:

M. U. Thomas Dean, Graduate School of Engineering and Management	Date

AFIT/DS/ENY/12-06

Abstract

The *Manduca Sexta* species of moth serves as a source of biological inspiration for the future of micro air vehicle flapping flight. The ability of this species to hover in flapping flight has warranted investigation into the critical material, structural, and geometric properties of the forewing of this biological specimen. Using biomimicry we have studied the forewing of the *Manduca Sexta* to distill the principles and functions of this system that have developed through evolution, and applied this knowledge to develop an engineered wing that is able to produce comparable lift as its biological analog. A rigorous morphological study of the *Manduca Sexta* forewing was conducted to characterize the physical and material properties of the biological forewing for the purpose of developing an advanced parametric three dimensional finite element analysis (FEA) model. This FEA model was tuned to match the experimentally determined structural dynamics of the biological specimen and serves as the starting point for an engineered wing design. A derivative engineered wing model is produced by replacing the biological materials with advanced ultra high stiffness composite laminates and polymer based microfilms. The engineered model is then tuned to match the structural dynamics of the biological forewing and serves as the baseline engineered wing design. Through the use of Design of Experiments (DOE) and multiple single factor analyses the primary structural factors are determined. Manufacturing methods are developed and implemented to fabricate the baseline engineered wing design. Biological wings and engineered wings are experimentally tested to determine the aerodynamic lift production of each wing type under the same boundary conditions. Through this research, a structural dynamics based engineering methodology has been developed and applied to the design, development, and identification of biomimetic engineered wings that experimentally produce aerodynamic forces equivalent to their biological analog.

This dissertation is dedicated to my family. For those who came before me, I honor your dedication and hard work by capitalizing on the efforts that you have made to allow for me to succeed. For my wife, this is dedicated to you for allowing me to spread my wings and be both an intellectual man and the loving father that I always hoped I could be. Without your encouragement, daily support, and tireless efforts none of this would have been possible. For my children, I hope that you see that you can achieve whatever you set your mind to. I only hope that I can continue to be there to teach, guide, and encourage you on your path to fulfilling your dreams.

Acknowledgements

The road to the completion of this document has been both a difficult and arduous challenge. Luckily, at every obstacle there has been the opportunity to consult and receive help from a myriad of mentors along the way. Without the aid of these wonderful individuals the completion of this research could not have been completed.

First and foremost, I want to thank my advisor, Dr. Anthony Palazotto, for your dedication to seeing that I complete this journey with you. Your tremendous depth of knowledge and perseverance to share this with me has been a truly great experience. I would like to thank my committee members Dr. Richard Cobb and Dr. Peter Collins for their time, guidance, material, and laboratory support. I would also like to thank Mr. Jay Anderson and his devoted team of laboratory and support technicians. Mr. Anderson and his team are the unsung heroes within the AFIT/ENY Department and without their aid the extensive experimental testing of this research could not have been realized. I am deeply indebted to you for your efforts and truly appreciate the friendship we have developed during my time here. To Mr. Nelson Freeman, I have been truly impressed by your professionalism and dedication to learning. Your tireless efforts and steady hands made the accomplishments of this research possible. I am greatly indebted to Dr. Mark Willis and Jennifer Avondet from Case Western University, for the wealth of biological knowledge and understanding. Through their aid, the Manduca Sexta specimens for this study were obtained from their Manduca Sexta colony. Finally, I would like to thank Dr. Doug Smith of the Air Force Office of Scientific Research (AFOSR), and Dr. Richard Snyder of the Air Force Research Lab (AFRL) for financial support of this research.

Ryan P. O'Hara

Table of Contents

List of Figures

Figure Page

List of Tables

List of Abbreviations

Abbreviation		Page
FEA	Finite Element Analysis	iv
DOE	Design of Experiments	iv
FMWAV	Flapping Wing Micro Air Vehicle	1
DARPA	Defense Advanced Research Projects Agency	1
MAV	Micro Air Vehicle	1
FSI	Fluid Structural Interaction	3
CT	Computed Tomography	9
EI	Flexular Stiffness	14
E	Elastic Modulus	14
I	Area Moment of Inertia	14
LEV	Leading Edge Vortex	19
TEV	Trailing Edge Vortex	20
TiV	Tip Vortex	20
CFD	Computational Fluid Dynamics	25
AFIT	Air Force Institute of Technology	27
UV	Ultra Violet	28
DIC	Digital Image Correlation	34
PZT	Lead Zirconate Titanate - Piezo Electric Material	37
CAD	Computer Aided Design	60
IGES	Initial Graphics Exchange Specification	60
AFRL/RX	Air Force Research Laboratory Materials Directorate	84
PET	Polyethylene Terephthalate	99
MIMO	Multiple Input Multiple Output	107
SPE	Sorted Parameter Estimate	107
CAM	Computer Aided Machining	120
DXF	Drawing Exchange Format	120

THE CHARACTERIZATION OF MATERIAL PROPERTIES AND STRUCTURAL DYNAMICS OF THE MANDUCA SEXTA FOREWING FOR APPLICATION TO FLAPPING WING MICRO AIR VEHICLE DESIGN

I. Introduction

The *Manduca Sexta* species of moth serves as a source of biological inspiration for the future of micro air vehicle flapping flight. The ability of this species to hover in flapping flight warrants investigation into the critical material, structural, and geometric properties of the forewings of this biological specimen. Through the use of biomimicry we have studied the forewing of the *Manduca Sexta* to distill the principles and functions of this system that have developed through evolution, and applied this knowledge to produce a novel and exciting solution to some of the difficulties associated with the use of Flapping Wing Micro Air Vehicles (FMWAV) [77]. This biomimetic investigation warranted the use of advanced multidisciplinary analytical, numerical, and experimental research. It has been shown that the critical material properties, geometric properties, and structural dynamics of the forewing can be identified and reproduced in an engineered specimen with specific multi-functional characteristics for FWMAVs.

1.1 Motivation

The Defense Advanced Research Projects Agencies' (DARPA) current vision of the optimal Micro Air Vehicle (MAV) motivates this research. This MAV's dimensions are less than 15 cm, and has a range and speed of 1 km and 15 m/s [17]. The Air Force Research Laboratory has gone on to further define and expand upon the role that MAVs will fulfill in the future.

> *The urban battlefield calls for tools to increase the warfighter's situational awareness and capacity to engage rapidly, precisely, and with minimal collateral damage. Micro air vehicles will be integrated into future*

> *Air Force layered sensing systems. These systems may be air dropped or hand launched. The small size of micro vehicles allows them to be hidden in plain sight. Once in place the micro air vehicle can enter a low-power extended surveillance mode for missions lasting days or weeks. This may require the micro air vehicle to harvest energy from environmental sources such as sunlight or wind or from man-made sources such as power lines or vibrating machinery. It will blend in with its surroundings and operate undetected. Micro air vehicles will use micro sensors and microprocessor technology to navigate and track targets through complicated terrain; such as urban areas. Micro air vehicle operating in urban terrain will have more agility challenges than larger unmanned aerial vehicles. Obstructions can cause wind gusts, even on a calm day. One way to overcome this is to learn from examples in nature and use flapping wings to fly. Sensing an oncoming gust, feedback control directs the wings to flap asymmetrically compensating for the wind. Small size and agile flight will enable micro air vehicles to covertly enter locations inaccessible by traditional means of aerial surveillance. Micro air vehicles will use new forms of navigation such as a vision-based technique known as optic flow. This system remains robust when traditional methods such as GPS are unavailable. Multiple micro air vehicles each equipped with small sensors will work together to survey a large area. Information from the sensors will be combined providing the swarm of micro air vehicles with a big picture point of view. Data will be communicated amongst the micro air vehicles to enable real-time reliable decision-making and provide an overall surveillance picture for other surveillance platforms or operators. Each individual micro air vehicle may perform a very distinct mission from its fellow swarm members. While some micro air vehicles may be used purely for visual reconnaissance, others may be used for targeting or tagging of sensitive locations. Individual micro air vehicles may perform direct attack missions and could be equipped with incapacitating chemicals, combustible payloads or explosives for precision targeting capabilities. Micro air vehicles may carry sensors to detect chemical, biological, or nuclear radiation threats and relay this information to human operators or other unmanned platforms. Like their biological inspiration, micro air vehicles are not limited purely to fight. The agile, hovering, perching, and crawling micro air vehicle will fulfill the mission, popularly termed, "dull, dirty, and dangerous" like no current system can. Micro air vehicles will become a vital element in the ever-changing war fighting environment and will help ensure success on the battlefield of the future. Unobtrusive, Pervasive, Lethal. Micro air vehicles will enhance the capabilities of future war fighters. [43]*

These definitions are purposefully ambiguous and leave room for the use of a variety of platforms and concepts to meet the requirements of the future. For our purposes, the focus is on the development of a biomimetic wing that can be used in a future FWMAV platform.

1.2 Research Challenges for Flapping Wing Micro Air Vehicles

There are many significant hurdles that need to be overcome to fully understand the structural dynamics and aerodynamics associated with flapping flight. Specifically, the most challenging of these areas are the low Reynold's number unsteady aerodynamics associated with flapping flight. As a wing flaps during hover or slow forward flight, it must continually cross the wake that it just created in order to generate lift and stay aloft. Currently, there is much computational and experimental testing that is being undertaken to solve the complex equations associated with these types of analyses. These types of analysis require significant time and computational resources and are not ready to be used as design tools for the aspiring MAV developer. Assuming a valid aerodynamic model is available, it would be of great benefit to tie the unsteady aerodynamic prediction to a large deformation non-linear structural model in order to properly model the fluid structural interaction (FSI) of the wing as it crosses through the unsteady flow. As it currently stands, a high fidelity FSI model has not been produced and due to the aforementioned computational constraints this is also not a viable design tool at this time. Finally, the creation of a large deformation non-linear structural model for application of the structural dynamics of a MAV wing is entirely possible. Current computational architectures allow for the solution of such models with both high resolution and modest computational resources. Further, these methods have been validated against known solutions and could provide the MAV developer with a valuable resource in the understanding of the behavior of a flapping wing in vacuum. Since many of the regimes of the flight stroke are dominated by inertial forces, this insight could prove to have considerable design implications.

1.3 Problem Statement

The goal of this research is to increase the understanding of the structural dynamics of the wing structure of a FWMAV by making use of the forewing from the *Manduca Sexta* species of moths. There are already numerous biological specimens that can already perform the roles that are currently desired in an engineered micro air vehicle. These biological specimens have undergone millions of years of evolution and have evolved into highly specialized and efficient systems. If such a system were to exist, then the critical features of this evolution could be extracted it would be of great benefit to the advancement of micro air vehicle design. This is especially important when considering that many of the aforementioned aerodynamic and coupled structural analysis tools are not yet available to analyze and subsequently perform design optimization, or evolution like the biological specimen has already undergone.

Thesis Statement: By carefully characterizing the structural material and geometric properties of the forewing of the Manduca Sexta species it is possible to design, fabricate, and experimentally validate that the critical features of the biological wing can be produced in an engineered wing and flapping mechanism that produces comparable amounts of lift as the Manduca Sexta species.

II. Background and Previous Work

In order to properly understand the complexities involved in attempting to accomplish the thesis statement of Chapter 1, it is necessary to provide a detailed background investigation of the *Manduca Sexta* species. This investigation will discuss key aspects why this species was chosen for study. Areas to be discussed, will include, but will not be limited to, the species itself, wing morphology, wing kinematics, and the coupled relationship of the structural and material properties of the wing in relation to their aerodynamic effects. Priori research and development of biomimetic wings and flapping mechanisms will also be presented to show the current state of the art in the evaluation of the structural and aerodynamic performance of wings that are relevant to a FWMAV.

2.1 Manduca Sexta

Manduca Sexta, commonly referred to as the Tobacco Hawkmoth, is a moth of the family *Sphingidae* and is indigenous to North America. During their larval stage they are commonly referred to as hornworms. These hornworms primarily feed on tobacco and tomato plants, but will occasionally feed on potato and pepper crops and other plants in the *Solenaceae* family, hence their name *Manduca*, which is the Latin word for “glutton”. Adults are large moths with long forewings. They are strong fliers, that have highly flexible wings that reverse camber and allow them to hover, with a rapid wing beat and are sometimes mistaken for hummingbirds [19]. Adults are generalist nectar feeders. *Manduca Sexta* are readily studied because they are easily reared in a laboratory, have short life cycles, and their large size allows for many various scientific investigations on their various systems. Research topics include: Flight mechanisms, nicotine resistance, hormonal regulation, and hemolymph physiology [74]. The biological classification of the *Manduca Sexta* is found in Table 1.

Figure 1: *Manduca Sexta* Life Cycle [99]

Table 1: *Manduca Sexta* Classification [57]

Kingdom: *Animalia*
Phylum: *Arthropoda*
Class: *Insecta*
Order: *Lepidoptera*
Family: *Sphingidae*
Genus: *Manduca*
Species: *Manduca Sexta*

2.1.1 Wing Morphology. Insect wings are formed from a complex makeup of polymer based chains, Chitin, that form the Cuticle, which provides the strong exoskeleton, of the body, limbs, and wings and act as a barrier between the living tissues of the insect and the environment. The Cuticle can range from rigid and armor like (venation) to thin and flexible as in the membrane of the wing [28]. A fully developed wing consists of membranous regions of epidermal bilayers supported by venation. Extracellular cuticle layers expressed dorsally and ventrally from the epidermis determine the structural characteristics of the wing membrane [19]. Wing veins are typically hollow and are elliptical in cross section. The veins serve as not only structural members, but as conduits for nerves and hemolymph, as shown in Figure 2.

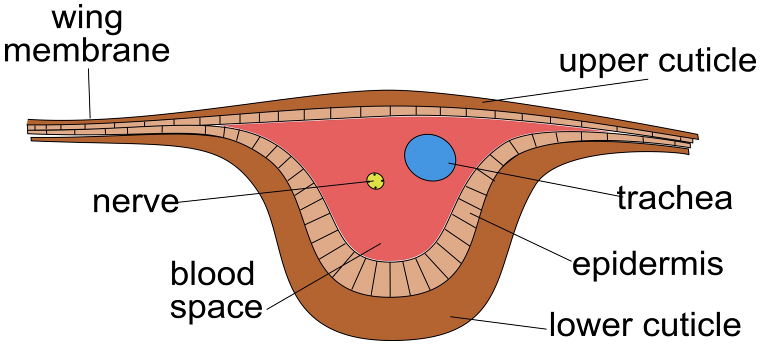

Figure 2: Venation Cross Section

A venation map of the *Manduca Sexta* forewing is presented in Figure 3. The naming convention and descriptions of the mapping found in Figure 3 are based off the Comstock-Needham System [54]. Additionally, this diagram indicates the Median Flexion Line, a radial groove or region of increased flexibility along which the wing can deform and yield variable camber [19]. The claval furrow, a similar line of flexion, where longitudinal bending occurs between the posterior anal veins and the posterior margin is also indicated. Wing mass is dominated by the mass contributions of the venation (80%), the membrane (10%), and flattened epidermal cells called scales (10%). The latter features are primariliy used for coloration, but may subtly influence flow patterns and boudnary layer structure over wings [19]. The full effects of the scales is not known, but considering the mass that they represent they assumably pose a valuable contribution to the insects overall ability to function.

The wing shape is described by a number of common features related to the geometry of the wing. The wing length is represented by R and is typically found to be roughly 40-50 millimeters in length. The wing area S is typically found to be

400-500 (mm^2). It is more useful to express the wing area in terms of the wing length, R, and aspect ratio, AR, which is equal to the span, $2R$, divided by the mean chord, $S/2R$, where $AR = 4R^2/S$ [97]. Aspect ratios of the forewing of *Manduca Sexta* have been experimentally found to fall in the 3.5-4.0 range. The area centroid is computed as the center of the area of the wing.

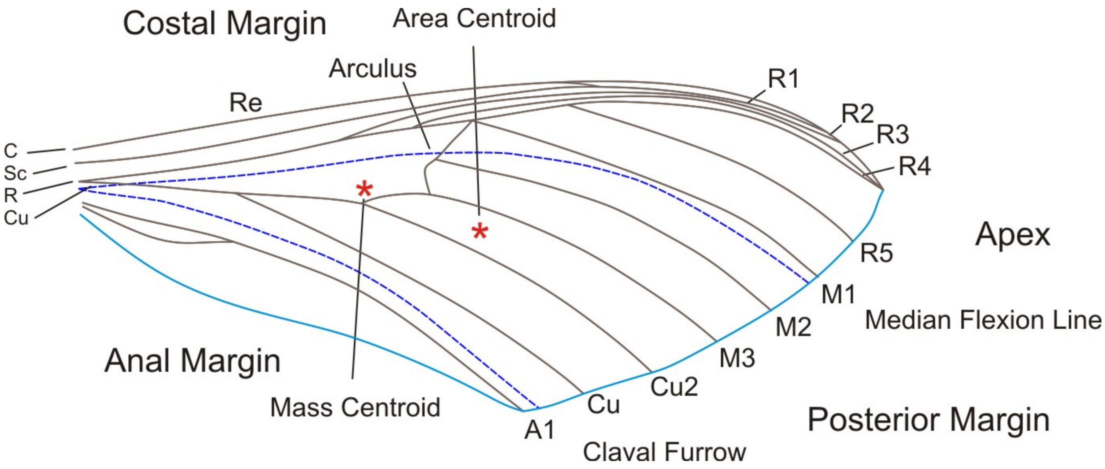

Figure 3: Venation Map of *Manduca Sexta* Forewing [54]

2.1.2 Wing Material Properties. Chitin, a long-chain polymer and a derivative of glucose, is the main component of the exoskeletons and wings of insects . Due to the ability of the biological specimen to vary the bonding chains, assemblage of nanofibers, and crystalline structure, the material properties of chitin can vary over a wide range. In terms of elastic modulus, this appears to vary from 1-10 gigaPascals (GPa), over a large variety of flying insect species [98].

Table 2: Cicada and Dragonfly Elastic Modulus [40, 84]

	Body	**Venation**	**Membrane**	
Cicada	n/a	1.9	3.7	GPa
Dragonfly	4.7	2.9	1.5	GPa

Detailed investigation has been performed to determine the material properties of the forewing of the cicada using traditional engineering mechanics approaches.

Through the isolation of the leading edge veins and measurement of the cross sectional area of these veins, an experimental tensile test of multiple samples showed that the elastic modulus of the vein was approximated to be 1.9 GPa, Figure 4. In a seperate test, through the application of nanoindentation [68] to the isolated membrane cells of the cicada wing the elastic modulus of the membrane was found to be 3.7 GPa [84]. A similar approach was applied to the *Ansioptera* species of dragonflies where by the elastic moduli of 4.7±0.6 GPa, 2.9±-0.8 GPa, 1.5±0.5 GPa for the dry body cuticle (abdominal tergite), dry wing veins and wing membrane respectively was found [40]. The application of these very common material property techniques shows the possibility of applying similar techniques to the *Manduca Sexta* forewing.

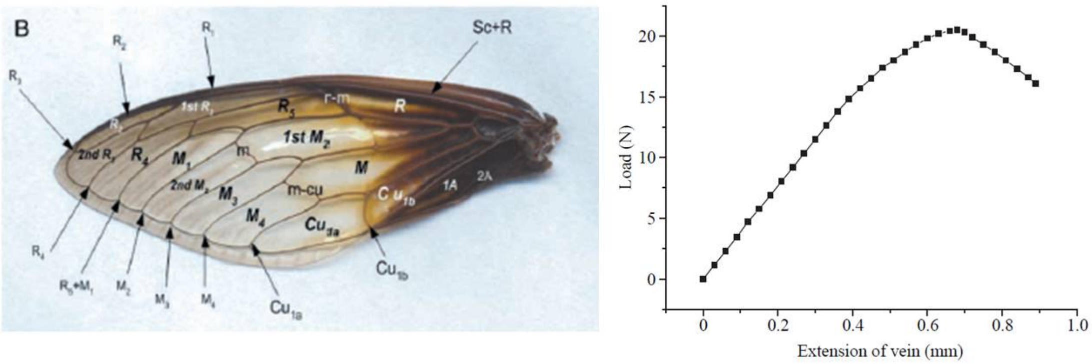

Figure 4: Cicada Vein Tensile Test [84]

Additionally, Computed Tomography (CT) investigation has been initiated on the forewing of *Manduca Sexta* and has revealed that the density of the veins and membrane appear to be relatively homogeneous [80]. This is important in that the material properties of the wings could be determined at one point and applied over the entire wing.

2.1.3 Flight Muscles. The *Manduca Sexta* species is able to actuate its wings through the contraction of intrinsic flight muscules to generate forces that are transmitted to the surrounding cuticle of the exoskeleton into the base of the insects wings. These primary flight muscles are located within the thorax of the moth [19].

Two different sets of thoracic muscles are primarily responsible for wing motion. A set of dorsal longitudinal muscles compress the thorax from front to back, causing the dorsal surface of the thorax (notum/tergal plate) to bow upward, making the wings flip down. A set of dorsal ventral muscles compress the thorax from top to bottom, causing the dorsal surface of the thorax (notum/tergal plate) to go down, making the wings flip upward. The rotational axis for wing depression and elevation is predominantly defined by dorsal ventral movement of the first axillary sclerite against the notum, and particularly against the anterior notal process, Figure 5. Action of the direct flight muscles, the basallar and subalar muscles, with that of the additional axillary muscles influences both stroke amplitude and wingtip paths [19]. These direct flight muscles, directly connect from the thoracic wall to individual sclerites located at the base of the wing, through ligament attachments [41].

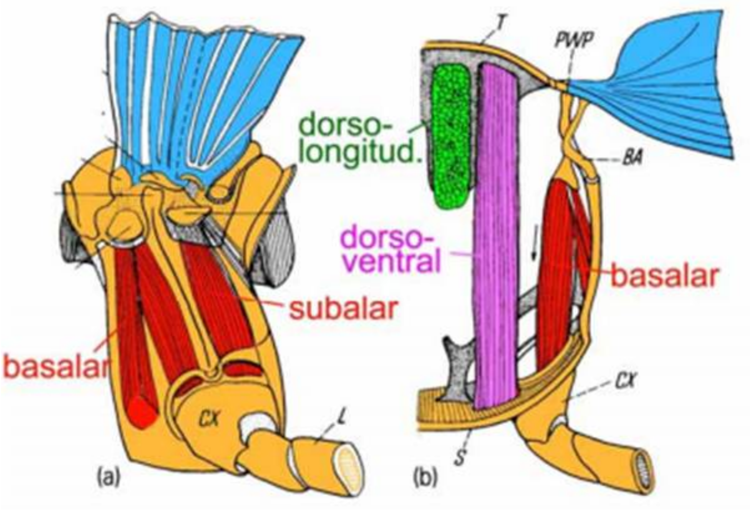

Figure 5: Flight Control Muscles [41]

2.1.4 Wing Kinematics. *Manduca Sexta* has the unique capability of being able to not only fly forward but also to hover in midair. This ability is based upon the kinematics and structural dynamics of the wings, flight muscles, and body of this species. A visual depiciton of a complete flapping cycle of the *Manduca Sexta* in hover is shown in Figure 6. During the down stroke, the wing has a slight camber and twist. At supination, the transition from downstroke to upstroke, the leading-edge comes to a halt and rotates to move backward and up. The wings display ventral flexion during supination, with the tip of the wing bending forward and down. The wings twist extensively, as a torsional wave passes from the wing tip to the base at supination. This bending and twisting is essential in order place the the wing into a beneficial orientation for the upstroke [11, 112]. During pronation, the transition from upstroke to downstroke, the wing rotates forward to the downstroke, and displays less bending and torsion than during supination [11]. This is a very simplified description of the wing kinematics for the *Manduca Sexta* species, more detailed explanations of the trajectories of the wings can be found, but are beyond the scope of this document [49, 104–106].

The *Manduca Sexta* species possesses both a forewing and a hindwing. Despite the relatively large size and mass, one would assume that the hindwing of the species would be critical to maintain both forward flight and hover. However, this this is not the case as this species possesses the ability to fly quite well, with only their forewings, with only a loss to extreme maneuvering, as does many other species of *Lepidoptera* [36, 103].

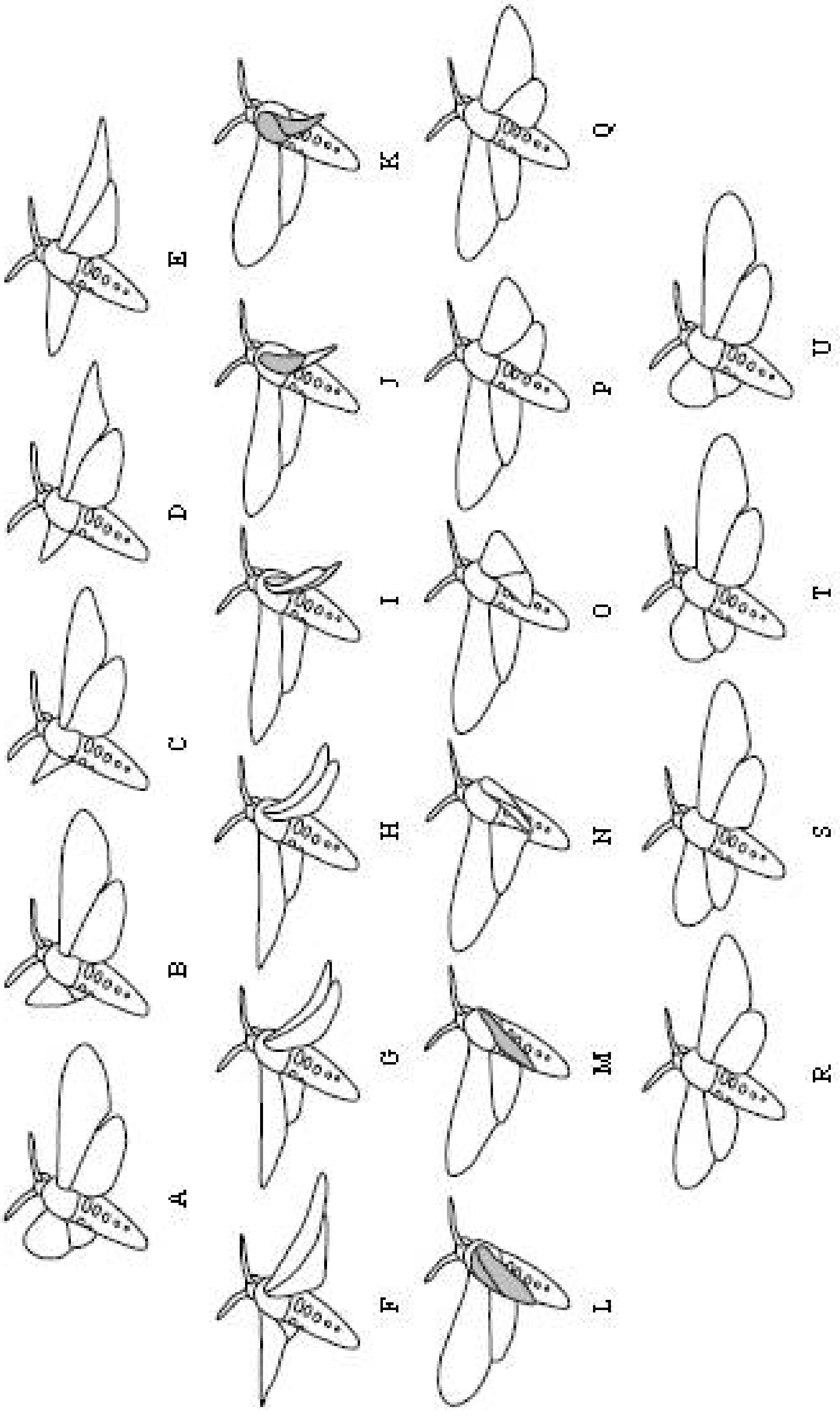

Figure 6: Hawkmoth Wing Kinematics [105]

2.1.5 Wing Forces. Wings are subjected to three primary types of forces while flapping: intrinsic forces applied by muscles to the wing base to drive wing motion, aerodynamic forces applied to the wings provide lift and thrust, and inertial forces due to accelerations during flapping that induce deformation, bending and torsion. They must act as levers (transmitting forces from muscles at the wing base to the air), oscillating airfoils (accelerating air to generate and transmit aerodynamic forces to the body), and cantilevered beams (accepting changing patterns of bending and twisting forces without failure) [11, 112]. Venation patterns correspondingly appear to reduce and control the extent of wing bending in both transverse and longitudinal planes [11, 19, 112]. Previous work has shown that both aerodynamic and inertial effects, fluid-structural interaction, dominate the response of the wings of the Hawkmoth as it flaps in air [62], despite previous beliefs to the contrary [14].

2.1.6 Wing Camber. Hovering is usually limited to insects with highly flexible wings that effectively reverse camber [19]. The camber of flexible wings can change significantly, 10-20% of chord length depending on location during the wing stroke [100]. At rest, the forewing of the *Manduca Sexta* has both a concave up and concave down shape, 5% in the chordwise direction and 4%in the spanwise direction, that is very slight. This camber seems to impose a relatively minor effect on flexural stiffness [12]. The effects of camber on torsional stiffness have not been studied, but are suspected to have a minor effect on this measure of structural performance.

The three-dimensional surface contour of insect wings has important aerodynamic consequences. Effective airfoils are often cambered structures, and increased camber enhances lift production. Imposition of aerodynamic and inertial forces alters camber results in conformational changes during the wing beat, most pronounced of which is camber reversal between down and upstrokes. Aerodynamic forces produced during the wing strokes will result in torsion and camber of the wing which should improve its aerodynamic efficiency [23]. These aerodynamic effects of camber contribute to the unsteady force production in translating flexible wings [11]. Radial flexion combined with camber changes can dynamically yield a great diversity of wing profiles and configurations. Modification of the wing curvature during the flapping stroke in reaction to inertial and aerodynamic forces indicates that wings may act as reactive airfoils that are morphologically responsive to variable dynamic circumstances [19].

2.1.7 Wing Stiffness.

Studies of the flexular stiffness of the forewing of *Manduca Sexta* have been carried out to characterize the stiffness of the wing in both the spanwise and chordwise directions [13]. These studies have focused on the characterization of the flexular stiffness (spanwise) and torsional stiffness (chordwise) directions in order to determine parameter estimates of these stiffnesses in order to determine their effect on the generation of lift for flexible wings.

2.1.7.1 Cantilever Point Load.

It has been suggested that overall wing stiffness is determined primarily by wing size as shown in Figure 7 [12]. Although both spanwise and chordwise flexural stiffness scale with wing length, the magnitude of flexural stiffness in these directions differs greatly; spanwise EI (Flexular Stiffness (EI) = Elastic Modulus (E) x Area Moment of Inertia (I)) is approximately 12 orders of magnitude higher than chordwise EI in all species tested. Modal analysis has shown that the dynamic stiffness of the chordwise stiffness (first bend) and spanwise stiffness (first torsion) of the *Manduca Sexta* forewing is on the order of 2x, differing greatly from the static measures of these parameters [62].

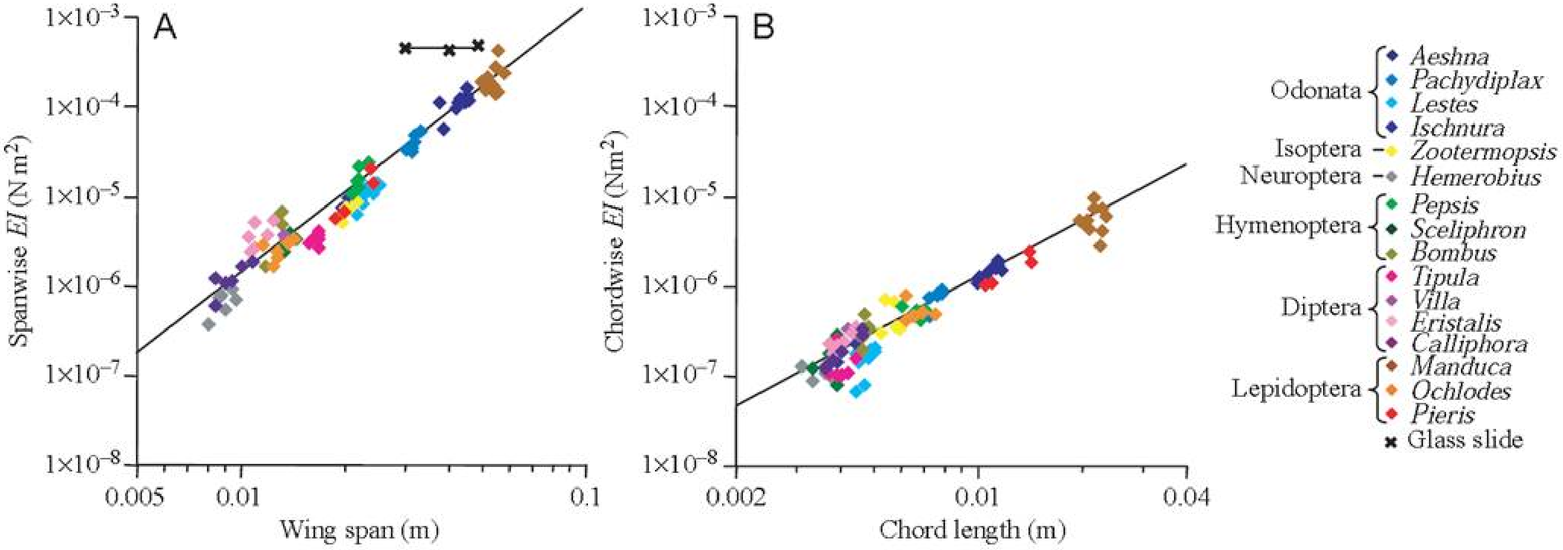

Figure 7: Flexular Wing Stiffness of Various Insect Species [12]

The measurement of the wing stiffness in the two critical directions is typically done under static test conditions where a point load is applied near the location of the center of pressure, which is typically calculated as 70% span and 30% chord [120]. The applied load is measured with a calibrated load cell and the prescribed deformation is measured with a simple length measuring device as shown in Figure 8. It has been shown that as the wing dessicates the stiffnes of the wing increases greatly and the mass decreases [53]. When conducting these experiments it is critical that these tests be completed as quickly as possible after liberating the wing from the specimen.

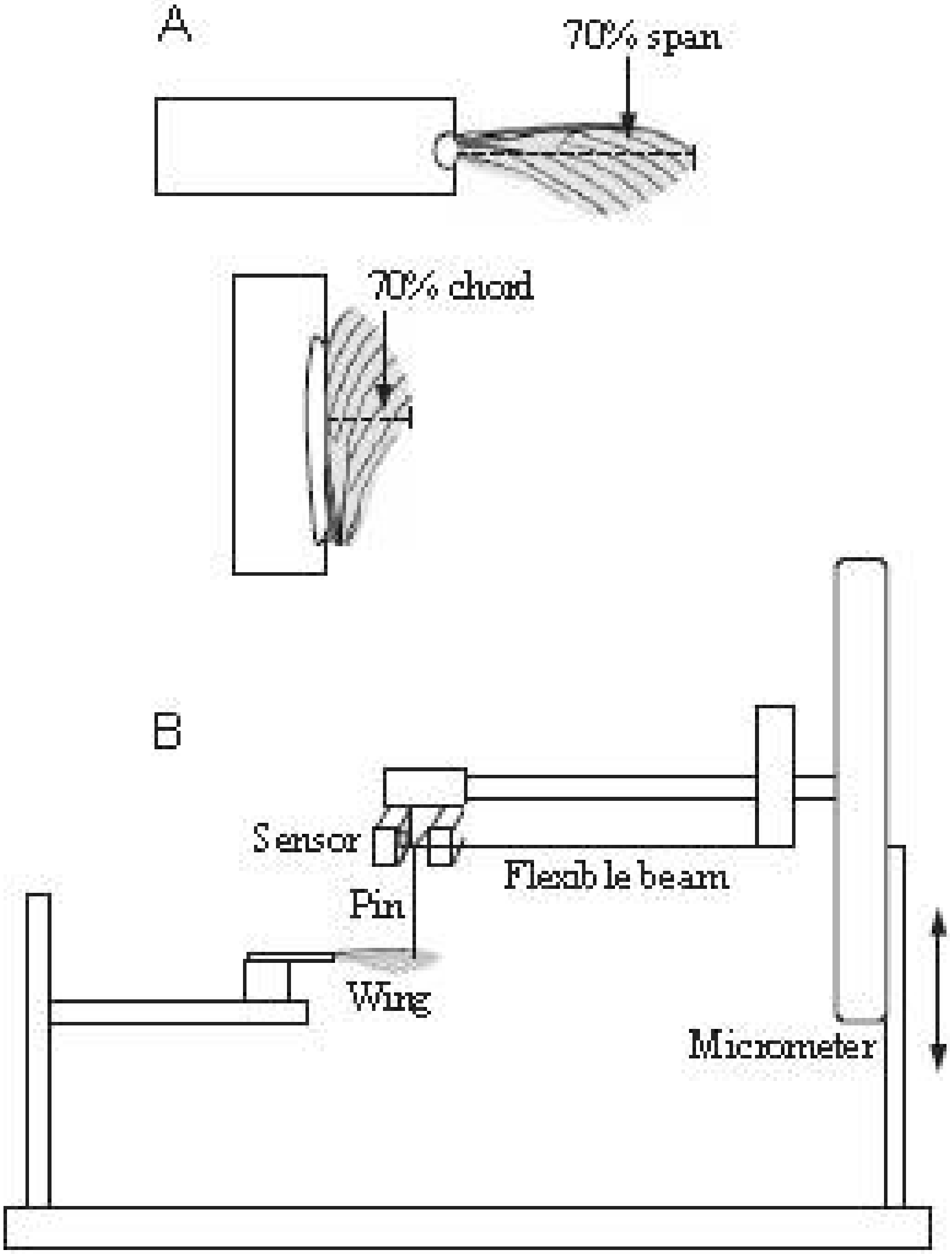

Figure 8: Stiffness Test Apparatus [12]

2.1.7.2 Modal Analysis. It has been shown that wings with stiff leading edges, hence high flexular stiffness values, that are relatively flexible in the chordwise directions are able to generate larger leading edges vortices [33, 120]. The coupling of these two stiffnesses is prescribed by the venation pattern of the wing. More specifically, these values are coupled by the arculus, a transverse or oblique vein, located midspan along the wing, that links the Radial (R) and Medial (M) veins as shown in Figure 2. In flight, aerodynamic pressure is centered within the area supported by the branches of R and M, and would tend to raise these veins, hinging them upward at the arculus. This in turn tends to pronate the wing's leading edge, although to a limited extent because it is rather rigid in torsion, and more effectively to lever down the trailing edge of the wing, cambering the wing and maintaining its aerodynamic effectiveness [117]. This passive pitching, due to torsional flexibility, has been shown to allow for a passive pitching motion due to inertial forces during wing rotation at stroke reversals . The ratio of the flapping frequency to the first natural frequency of the wing was important to determine the modes of passive pitching of the wing. If the flapping frequency was less than the wing, the wing experienced an advanced pitching motion, which led to lift enhancement by the intercepting the stronger wake generated during the previous stroke [23, 79].

Through the use of modal analysis to determine the resonant frequencies of the *Manduca Sexta* forewing held in a clamped boundary condition, the ratio of the first bending frequency (ω_1) to the first torsional frequency (ω_2) has been shown to be remarkably consistent. Despite variation in the wing size and shape from one specimen to the next, the ratio of these modes, Equation 1, empirically equates to 1.85, shown in Figure 9 [62].

$$Ratio\ of\ Modes = \frac{\omega_2}{\omega_1} \cong 1.85 \tag{1}$$

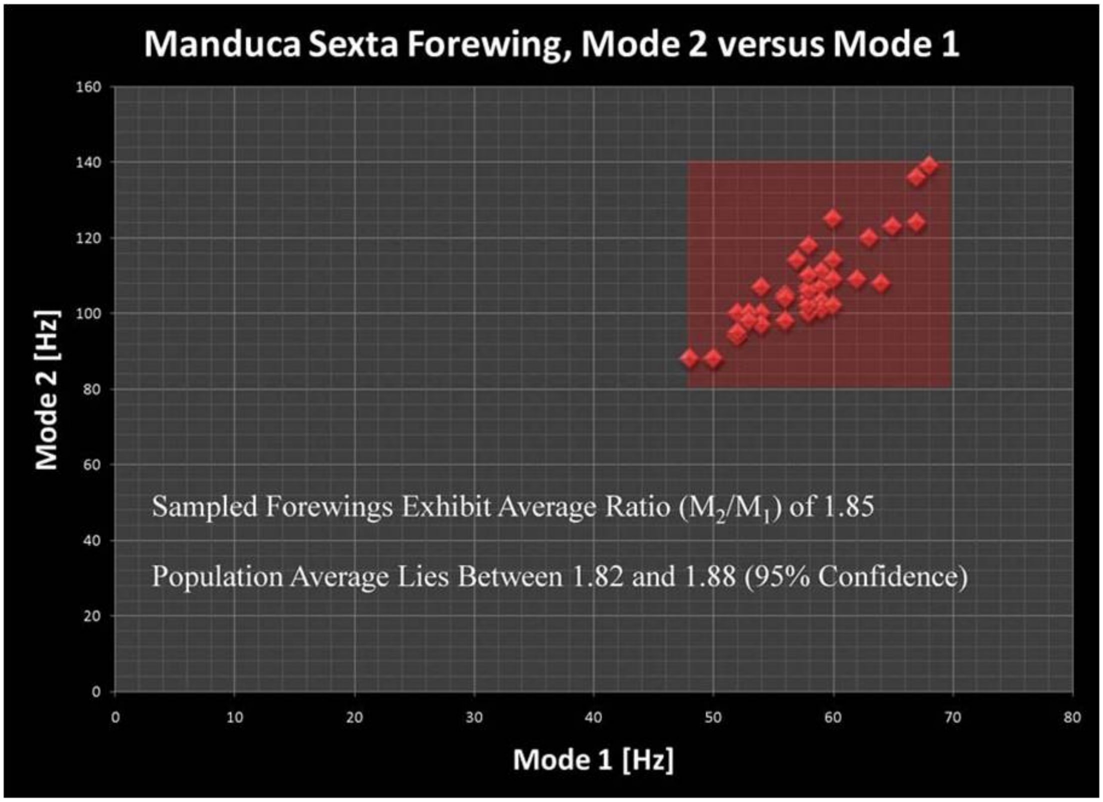

Figure 9: Ratio of Modes [62]

2.1.8 Wing Aerodynamics. The flow associated with the flapping flight of the *Manduca Sexta* is incompressible, laminar, unsteady and occurs at low Reynolds numbers, Re of O(10^4) [42, 79]. Compared to the predictions derived from conventional steady-state aerodynamic theory, these unsteady aerodynamic mechanisms may account for the majority of total lift produced by a flying insect [44]. The wings of *Manduca Sexta* generate forces much higher than their quasi-steady equivalents due to the presence of a number of unsteady aerodynamic effects [22]. The flow is comprised of two components: attached and separated flow [10]. The attached flow refers to the free stream flow on the airfoil as well as that due to its unsteady motion (sweeping, heaving and pitching). For insect-like flapping wings, flow separation is usually observed at both leading and trailing edges. The leading-edge vortex (LEV) is bound to the wing for most of the duration of each half-stroke, and the trailing edge wake, leaves smoothly off the trailing edge. Flow is more or less attached in the remaining regions of the wing [42]. When a flapping wing travels several chord lengths, the flow separates from the leading and trailing edges, as well as at the wingtip, and forms large organized vortices known as a leading edge vortex, a trailing edge vortex (TEV), and a tip vortex (TiV) [79]. The leading-edge vortex is believed to be predominantly responsible for the augmented forces observed [46]. The complex nature of these unsteady phenomenon can be seen in Figure 10. Flexible wings, in both the spanwise and chordwise directions, with camber generate larger amounts of lift, due to the larger generation of vortices that are produced throughout the wing stroke due to the dynamic nature of the wing shape that these characteristics produce [119, 120].

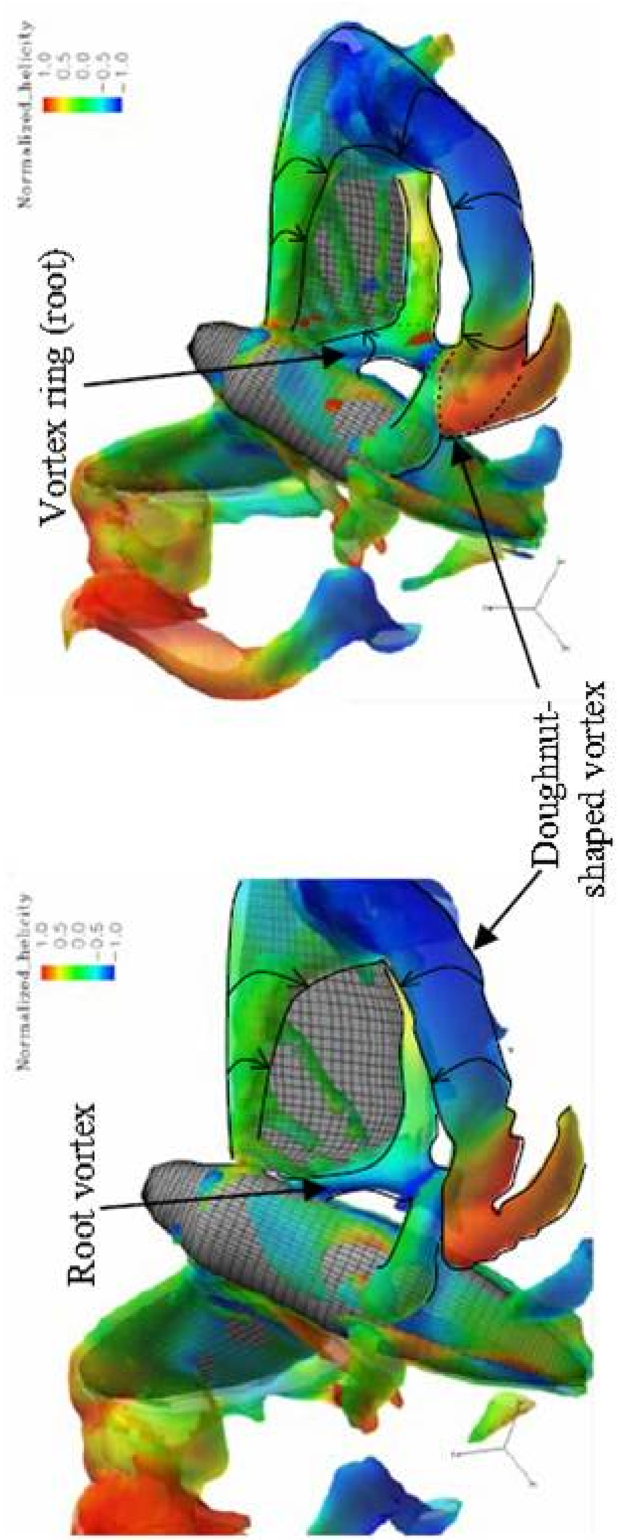

Figure 10: Hawkmoth Vortex Visualization [79]

2.1.9 Wing Passive Rotation. As the wing of the *Manduca Sexta* travels through it flapping cycle, it is necessary for the wing to reverse directions at the top of the upstroke and bottom of the downstroke. This is achieved through the pitch reversal of the wing, whereby the rapid change of angle of attack quickly changes near the up and downstroke transitions. The reciprocating kinematic motion of flapping requires that the insect quickly rotate the wing in order to keep the leading edge of the wing, leading the trailing edge of the wing, into the next stroke cycle [10]. Without this rotation it would not be possible for *Manduca Sexta* to be able to generate lift. Due to the structural makeup of the wing, the chordwise center of wing mass typically lies behind the rotational axis of the wing, and the wing deceleration at the end of halfstrokes swing the wing mass chordwise about the longitudinal axis. This inertially induced rotation will vary according to the local sectional mass along the span and that to the distance between the rotational and inertial axes [19]. The coupling of aerodynamic and inertial forces that cause this rotation are deemed to be passive, despite the fact that many insects possess basallar and subalar muscles, Figure 5, that can induce torsional forces through the base of the wing. The location of the center of wing mass behind the wing's rotational axis will promote both pronation (upstroke) and supination (downstroke). Detailed equations of motion have been derived and used with blade-element and quasi-steady calculations to supply aerodynamic force and moment estimates for the passive rotation of a variety of wings. Experiments confirm that the inertial effects of this passive rotation can be predicted and experimentally validated [10, 102]. The stiffness of the joint at the rotational axis has a direct effect on the flapping frequency, stroke reversal and lift generation capabilities of an insect wing. When a torsional spring of high stiffness versus one of low stiffness was compared, the more compliant spring was able to generate significantly higher amounts of lift [81, 93]. Through passive rotation, the pitching of the wing does not require additional power input from the muscles during the flapping cycle. Despite the fact that insects have the ability to pitch their wings actively during hovering flight, they are benefiting from a power and controls perspective, if the cyclic rotation of their wings is completely passive [20, 81, 102]. This additionally has a significant impact on the ability of this rotation to be created in a FWMAV if this is incorporated into the structural design of the flapping mechanism and wing itself.

2.1.10 Wing Structural Modeling. It has been shown that the morphological makeup of the forewing *Manduca Sexta* is extremely diverse. Linear dimensions range over three orders of magnitude and the shapes and relative size of the wing very greatly. Venation patterns ranges from extremely complex to very simple, while the arrangement of these veins varies significantly over the entire wing. The membrane varies considerably in terms of thickness and possibly material properties in a fashion similar to that of the veins. Despite this complexity it has been shown that given enough knowledge about the vein and membrane dimensions, cross-sectional geometry, and material properties, it is possible to generate high fidelity, three-dimensional, structural, numerical models that accurately represent them and can be used to predict the static and dynamic structural response of the wing of a variety of insect species. Such models have been generated using advanced computer aided three-dimensional design and finite element analysis software. The finite element method is a numerical technique for finding approximate solutions of complex partial differential equations.

The first application of finite element analysis was applied to the wings of insects in 1995 [116]. Since this initial application of FEA, there have been numerous examples of researchers applying this methodology to determine the structural response of dragonfly wings [15, 37, 51], locusts [113–115], hawkmoth [12, 80], and cicada [52, 53]. The models are comprised primarily of quadratic beam (venation) and shell (membrane) elements. A majority of these articles focus on the determination of the resonant frequencies of the wing structures where by the base of the wing/rotation joint is treated as a clamped boundary conditions.

FEA models of the hawkmoth progressed to include variable vein thicknesses [80] and dynamic bending of the wing through a representative flight stroke, without aerodynamic loads.

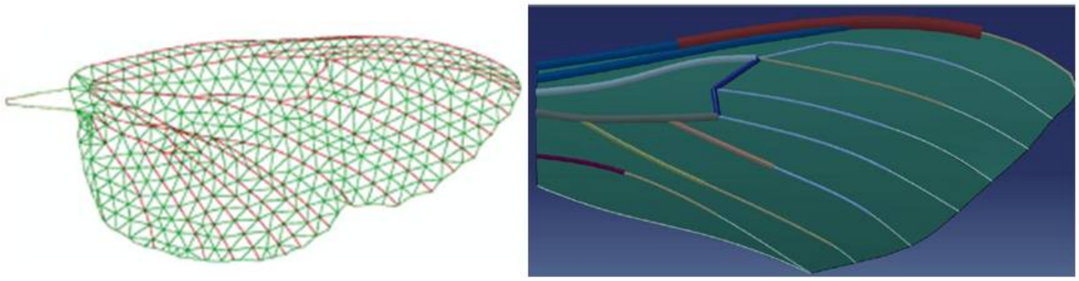

Figure 11: FEA Wings: Hawkmoth [12, 80]

The most comprehensive study of the structural response of the wing of an insect, by a single team of researchers, to include: geometric measurements, material property characterization, experimental stiffness measurements, and finite element modeling with modal analysis and point loading was first done to the hindwing of the locust [113–115]. A graphic illustration of the FEA model and point loading results are shown in Figure 12.

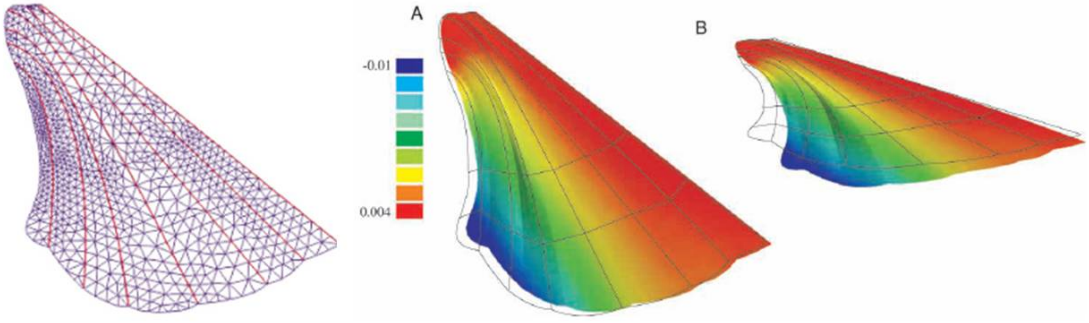

Figure 12: FEA Wings: Locust Hindwing [116]

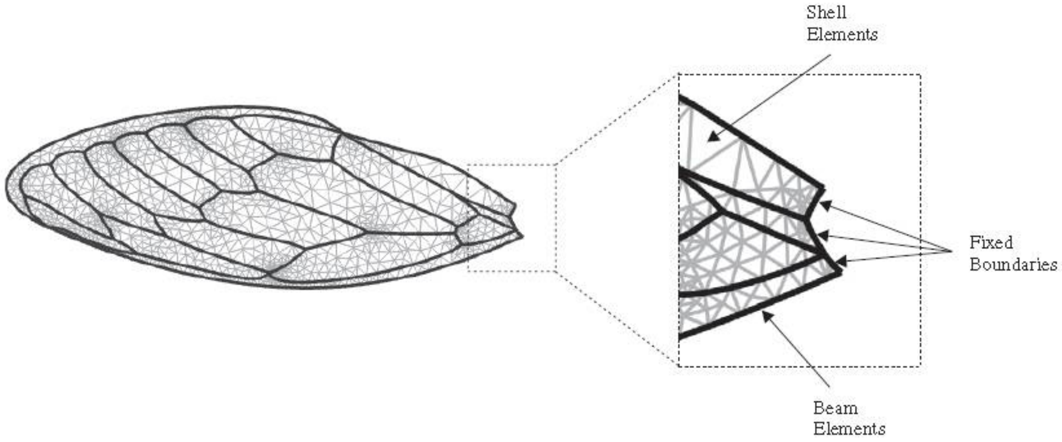

Figure 13: FEA Wings: Cicada Forewings [52]

Through a culmination of research by multiple institutions, a comprehensive insect wing model of the dragonfly was recently completed [37, 84]. This last model steps beyond previous models that focused on purely structural analysis and includes the mapping of quasi-steady blade element calculations of the aerodynamic forces due to flapping upon the FEA model as shown in Figure 14 [37]. Although not as rigorous as a computational fluid dynamics simulations (CFD), quasi-steady models continue to offer a tractable means of calculating instantaneous forces from measured kinematics. These models are readily applicable to the analysis of energy and power requirements and are more easily incorporated into dynamic control models of insect flight [50, 76].

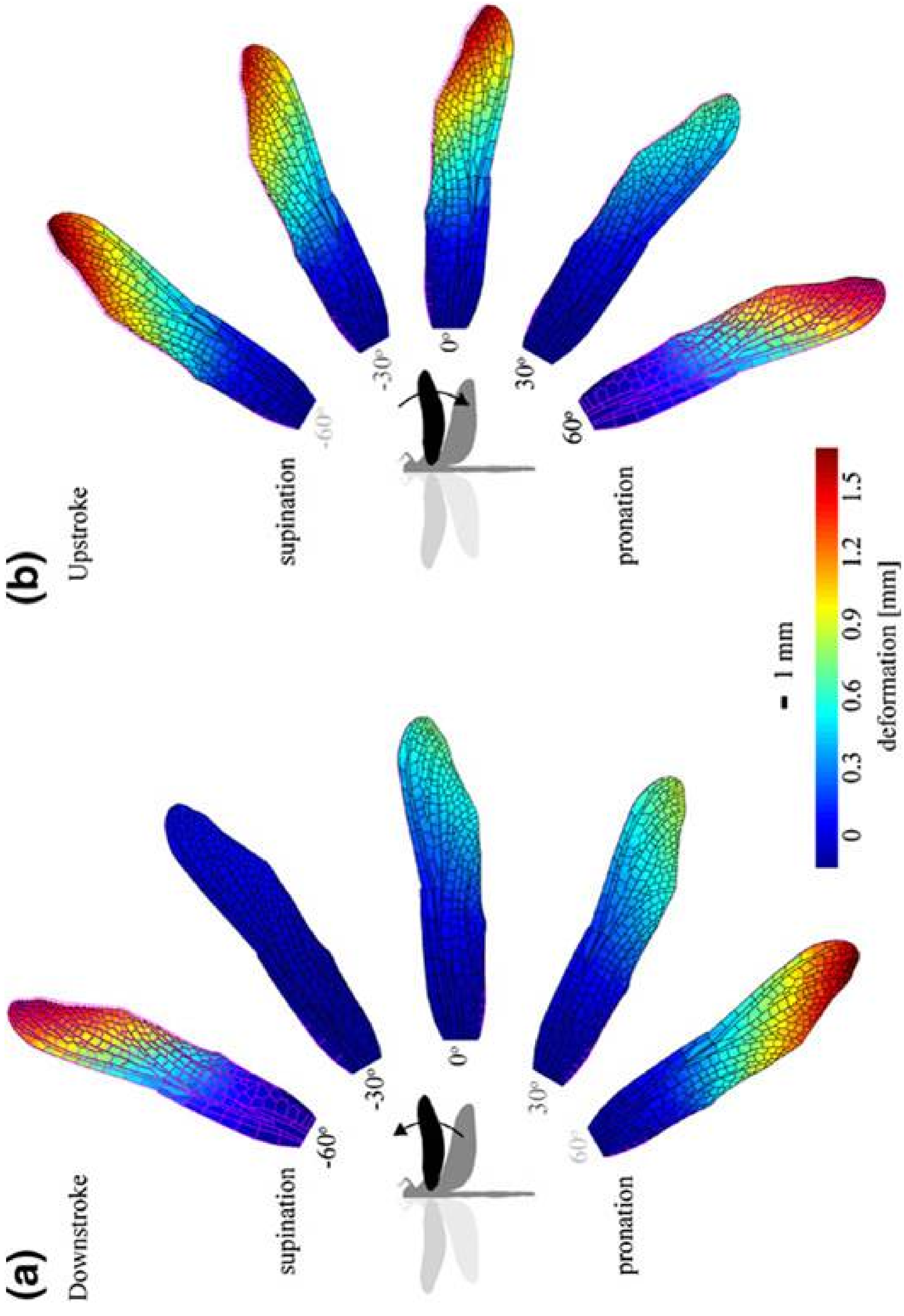

Figure 14: Coupled FEA and Blade Element Aero Analysis [37]

2.2 Fabrication Methods

The development of a flapping wing micro air vehicle requires that the wings be able to produce the most lift with the least amount of energy input required. This requires a wing to be multifunctional, of low mass, and easily controllable. Developing an engineered wing based off a biological analog holds great promise in terms of delivering upon aforementioned requirements. However, critical to achieving these goals is a requirement that the wings be able to be manufactured in a manner that is easily reproducible. Based on the technologies and materials that are readily available, the methodology to achieve these requirements has not been accomplished to date. A number of significant strides have been made to achieve these goals, however there is still work to be done in this area of research. Presented below are some of the most promising techniques that have been currently implemented.

2.2.1 MEMS based Chemical Etching. The use of Micro Electro-Mechanical Systems (MEMS) based manufacturing methods, where by a substrate is chemically etched through the use of a mask and a chemical solvent, as shown in Figure 15, can be used to fabricate wings for FWMAVs [33, 71]. The process involves the use of Titanium (6Al-4V) as the wing frame and poly-monochloro-para-xylylene (parylene-C) as the wing membrane. The technique was applied to both spanwise (bat) and chordwise (cicada) compliant wing structures. Wind tunnel test results show that nature-mimicked MEMS wings with complicated structure performed poorly when compared to the real wings. This is because the real wings were much lighter and more rigid. The real wings were also three dimensional structures versus the planar prototypes. Work recently performed at the Air Force Institute of Technology (AFIT) sought to mimic three-dimensional geometry through the use of cold forming and plastic deforming the titanium structure to increase stiffness [16]. Both approaches to this methodology were able to produce membranes with variable thickness. The application of parylene-C involves the deposition of material upon the substrate, while the kapton approach presented here, went through a final step where a plasma etching allowed for the removal of membrane material. Although novel, both approaches still produced very heavy wings. Ultimately, this method was unable to produce the desired results due to the high density of the Titanium ($\sim 4500 kg/m^3$) versus the density of chitin based structures ($\sim 1800 kg/m^3$) and is not recommended for FWMAVs.

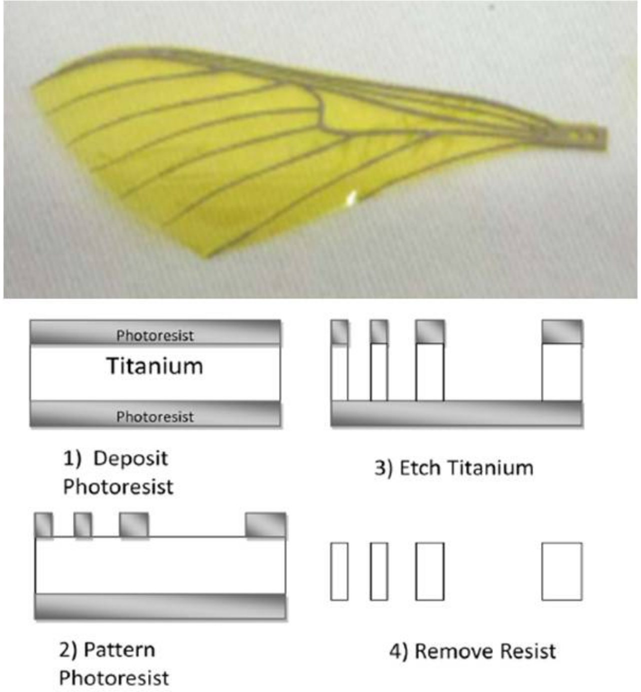

Figure 15: Etched Titanium Wing and Kapton Membrane [16]

2.2.2 Polymer Based Wings . Within the past decade there has been an explosion in the availability of three dimensional rapid prototyping machines that are able to use an inkjet layer deposition process to rapidly form Ultra Violet (UV) cured polymer based models. The ability of these machines to produce complex polymer based models in an extremely rapid fashion would leave one to believe that these devices would be perfect for the manufacturing of bioinspired wing designs. The use of these machines is often used for the individual components of the flapping mechanisms in many research projects, but has seen limited use in the fabrication of wings. The most successful use of this technology to produce a FWMAV was conducted at Cornell University [75]. As shown in Figure 16, a flying FWMAV was produced entirely of rapid prototyped UV cured polymer. The nature of fabrication lent itself to the fabrication and ability to test a significant number of wing designs.

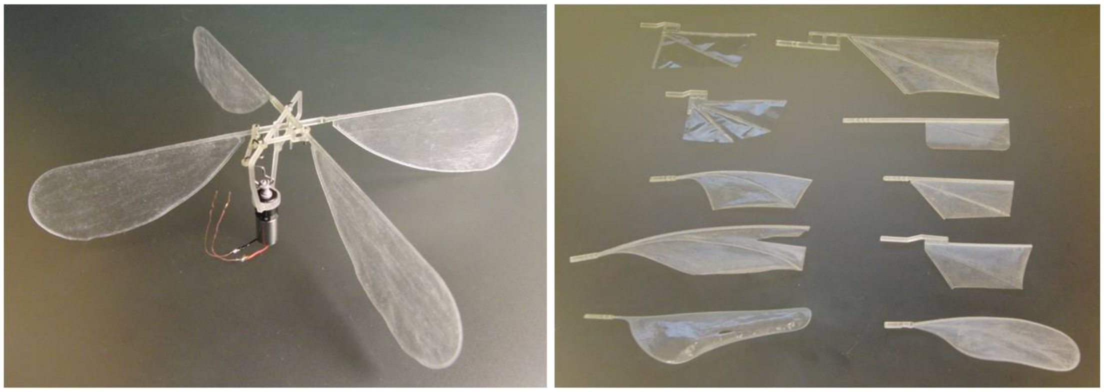

Figure 16: Flying UV Polymer Based FMWAV [75]

Recent work at AFIT intended to implement similar methods to produce hawkmoth inspired wing designs as shown in Figure 17 [17]. Despite the benefits of being able to mold a truly three dimensional wing with camber, the initial tests showed that the stiffness to weight ratios of the polymers were insufficient to handle the aerodynamic and inertial loads associated with the kinematics of the *Manduca Sexta*.

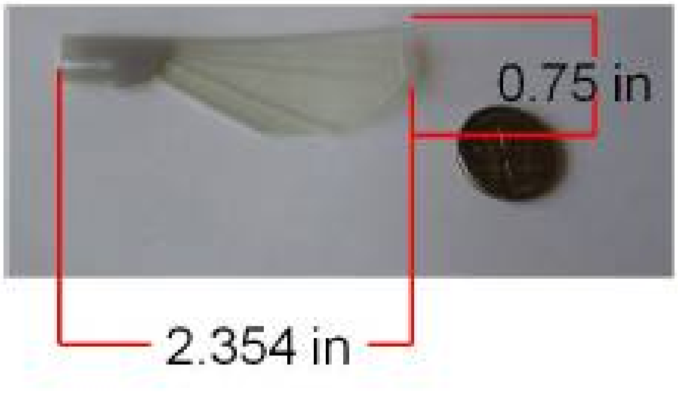

Figure 17: Rapid Prototype Simplified Wing [17]

Other work has been conducted on centimeter scaled wing using a three dimension micromolding technique through the use of a thermosetting polyurethane resin and a thin polydimethylsiloxane mold for fabricating 3D plastic frames integrated with a parylene-C film, Figure 18 [91]. This methodology was able to fabricate a wing with similar planform area, three dimensional camber and venation patterns as a real wing. Testing of a similar methodology was employed and tested recently and compared to a much stiffer carbon fiber spar with thin mylar membrane [93]. Due to the lack of stiffness from the polymer design and the ability of the wing to keep the leading edge vortices attached to the wing properly, lift generation was significantly less than the much stiffer carbon fiber sparred wing.

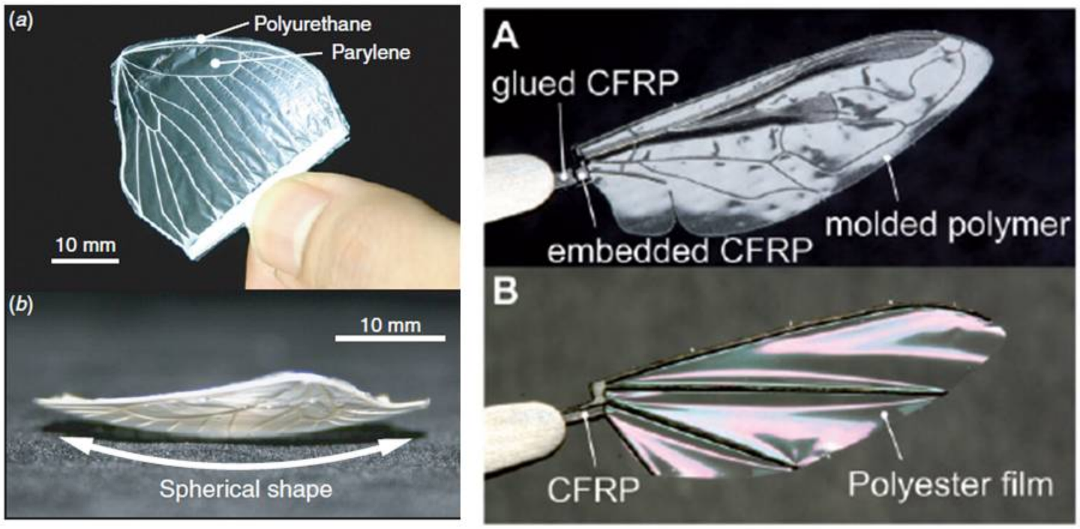

Figure 18: Micromolded Polymer Wings [91, 93]

2.2.3 Unidirectional Carbon Fibers and Micro Molding. It has been shown that biomimetic wings can be fabricated in a manner to closely match the biological analog in terms of both venation and membrane patterns. The best attempts at doing so have focused on the use of placing unidirectional fibers and aligning them by hand, through the use of a mold, or through laser micromachining, Figure 19. The processes and the resulting wings presented here attempt to match their biological parts in terms of mass, planform area and flexular stiffness. In order to construct these wing designs a number of simplifications were necessary when working with the unidirectional carbon fibers. These simplifications included making planar wings (without three-dimensional relief), extreme curvatures were reduced, complex structures ere removed, and all veins within a wing were created to uniform width [78].

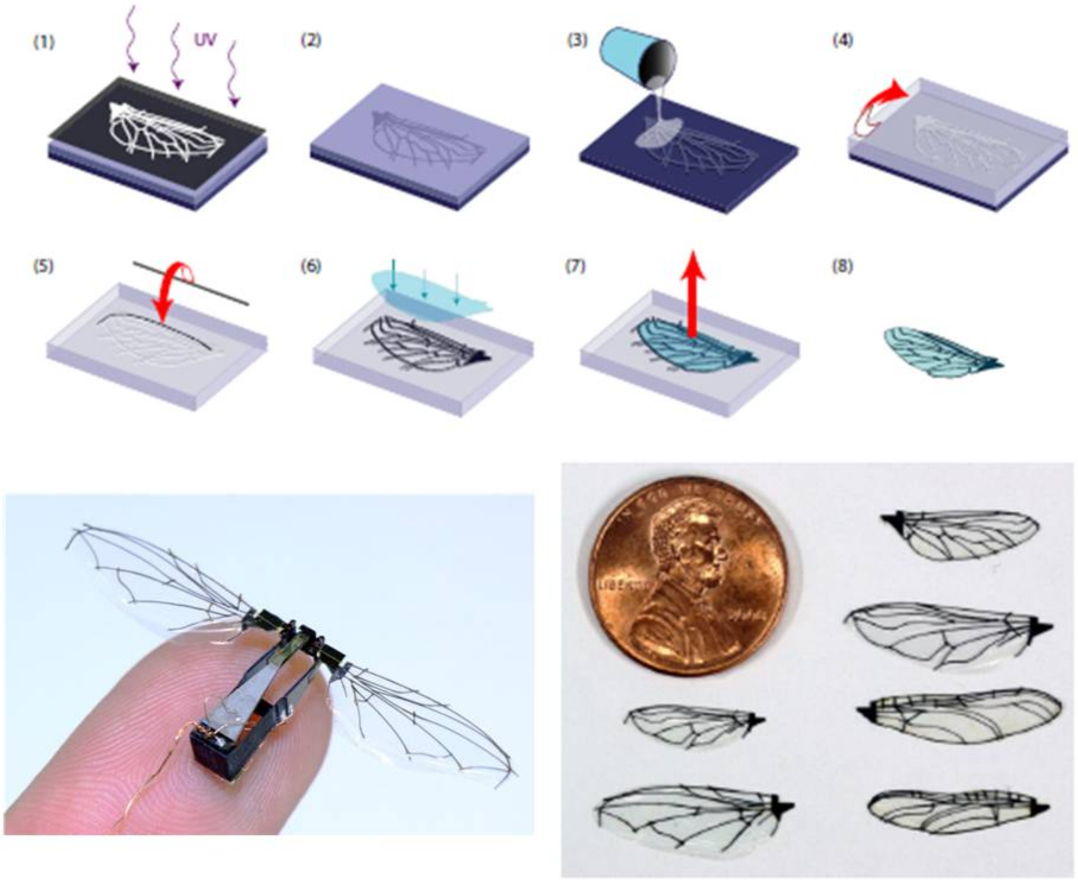

Figure 19: Biomimetic Composite Wings [78]

Despite the inherent simplicity of these designs when compared to their biological counterparts the use of carbon fiber allows for the ability to tailor the number of fibers and their patterns in a manner similar to the biological counterparts. Due to the high stiffness to weight ratio of the fibers significant improvements have been made to the structures in terms of mass and stiffness when compared to their polymer only based analogs, Figure 20 [118].

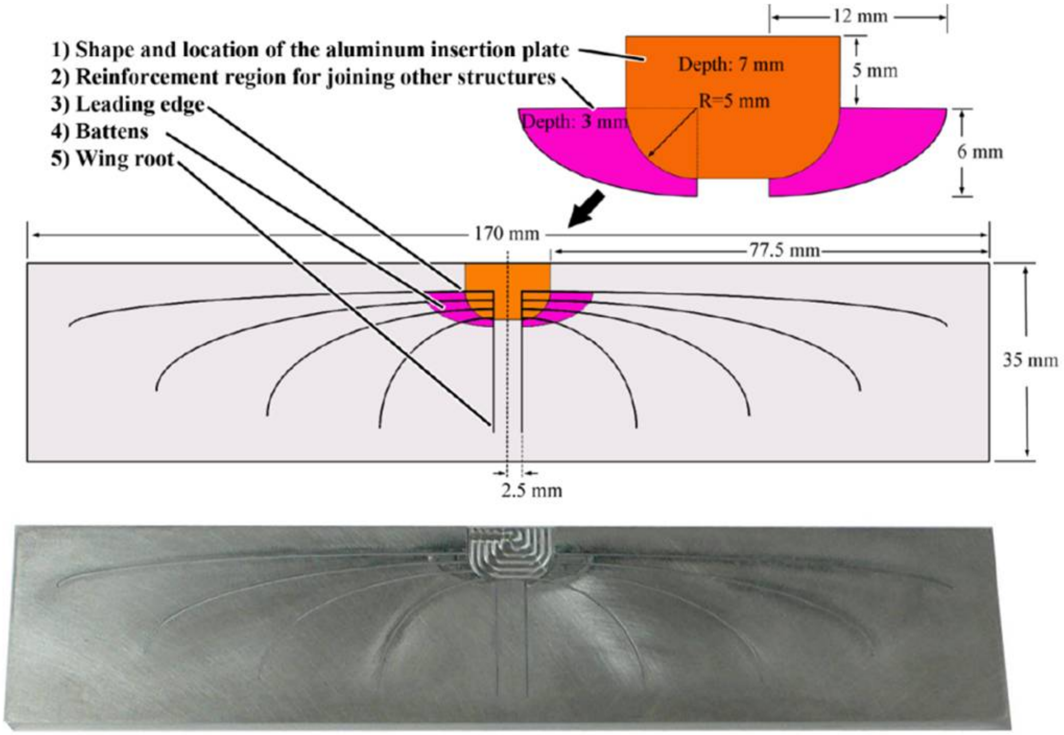

Figure 20: Unidirectional Carbon Fiber Wing and Mold [118]

These fabrication methods have allowed for wings to flap within a flapping mechanism at representative flapping frequencies and have generated significant amounts of forward velocity, when tethered to a horizontal wire, and lift of approximately 2 grams, using wings that are approximately 50 millimeters of span, Figure 21 [60].

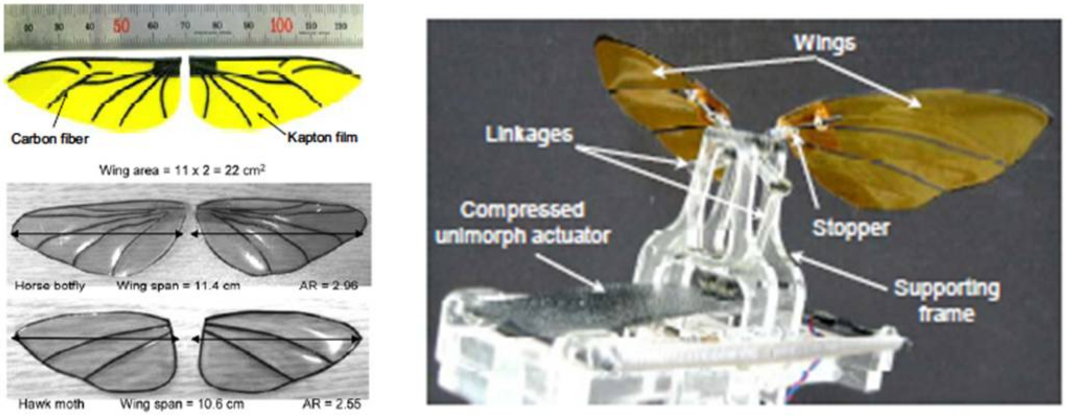

Figure 21: Hand Fabricated Uniaxial Carbon Fiber Wings [60, 61]

Wings have been produced in a hybrid method whereby the underlying vein structure has been intricately cut with a laser micromachining method and placed into a mold and the membrane applied using the previously discussed thermosetting polymer. This hybrid method appears to allow for the three dimensional molding capability to be applied to a set of unidirectional fibers. The trouble with this method is the inability to apply significant amount of pressure, to the carbon fibers without the use of an autoclave, to cure the carbon fibers. However, the methods presented thus far this is the most promising in the ability to deliver a truly representative biomimetic wing.

2.3 Flapping Mechanisms

In order to validate the design of a wing it is critical that a test platform be available that can prescribe the correct kinetics to the wing: amplitude, frequency, position, velocity, and acceleration. In addition, to correctly flapping the wing it is essential that other critical input and output measurements be available. Critical to these include the input power measurements, output force measures (Fx, Fy, Fz, Mx, My,Mz), and actual trajectory measurements of the wing itself. A culmination of prior research has shown that a number of methods are available to achieve all of these requirements. Of all of these though, the mechanism through which the kinetics and subsequent boundary conditions are applied is essential to successful evaluation of a wing design [18]. Further, it would be preferable if the mechanism could be scaled in a way that a flight vehicle could be produced from a comparable design.

2.3.1 Rotary Motor Based. For several decades now rotary based mechanisms have been extensively used to drive the wings of ornithopters and smaller insect size specimens. Figure 22, represents a classic design of such a electric motor based flapping mechanism. In this manner, an electric rotary motor is connected to a series of gears to reduce the speed of the motor, that are subsequently connected to a series of linkages to translate the rotary motion into the required kinetics necessary to flap the wings in a predetermined path. The mechanism in Figure 23, has shown that a test platform that is able to actuate wings, measure the aerodynamic and inertial forces associated with flapping in air and in vacuum, and that a three dimensional tracking technique, digital image correlation (DIC), can be implemented in a manner to properly evaluate the performance of a FWMAV wing design. Although a simple premise, the translation of rotary motion at the motor to angular motion at the wing root is actually quite complex. This complexity involves a significant amount of design and fabrication to achieve the required results. The design of MAVs demand high force, high displacement, low mass actuators [111]. This configuration is able to meet two of these three requirements. Unfortunately, the energy density of small rotary motors is not high, when compared to other alternatives, and therefore the high mass of the motor relative to the power it makes is therefore undesirable for a flight vehicle. In a laboratory situation an electric motor is a viable solution to flap wings. However, another short coming of this methodology is that due to the linkage design translation of the motion of the motor, the prescribed motion is only able to operate over a fixed amplitude stroke angle. Having the ability to vary the amplitude of flapping is a requirement that cannot be overlooked in both a laboratory flapping mechanism, but also more importantly in a flight vehicle.

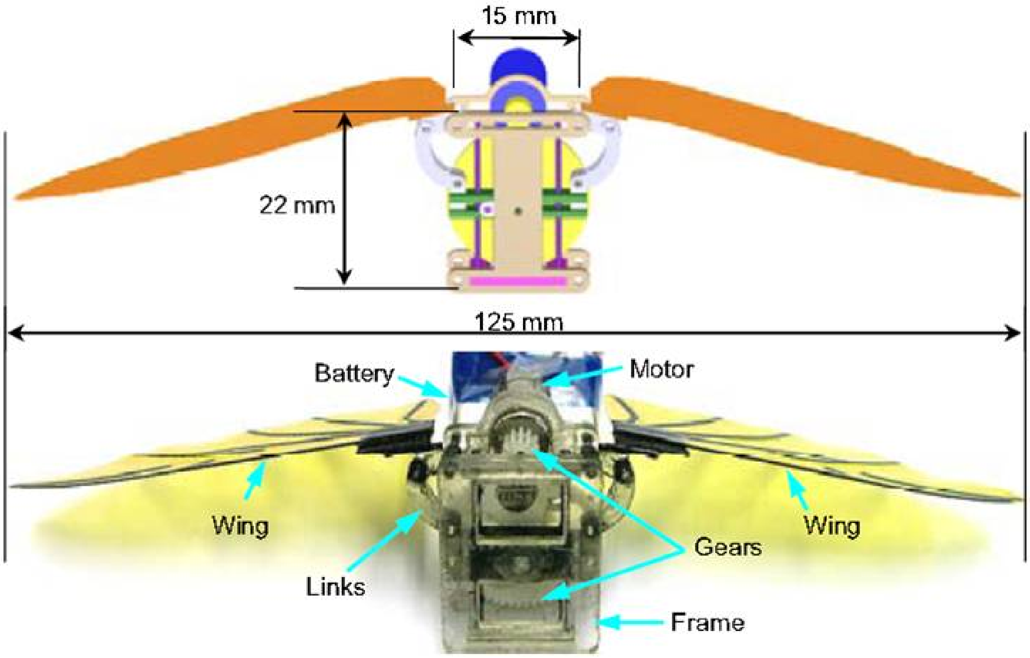

Figure 22: 3D CAD Model and Assembled Flapper [60]

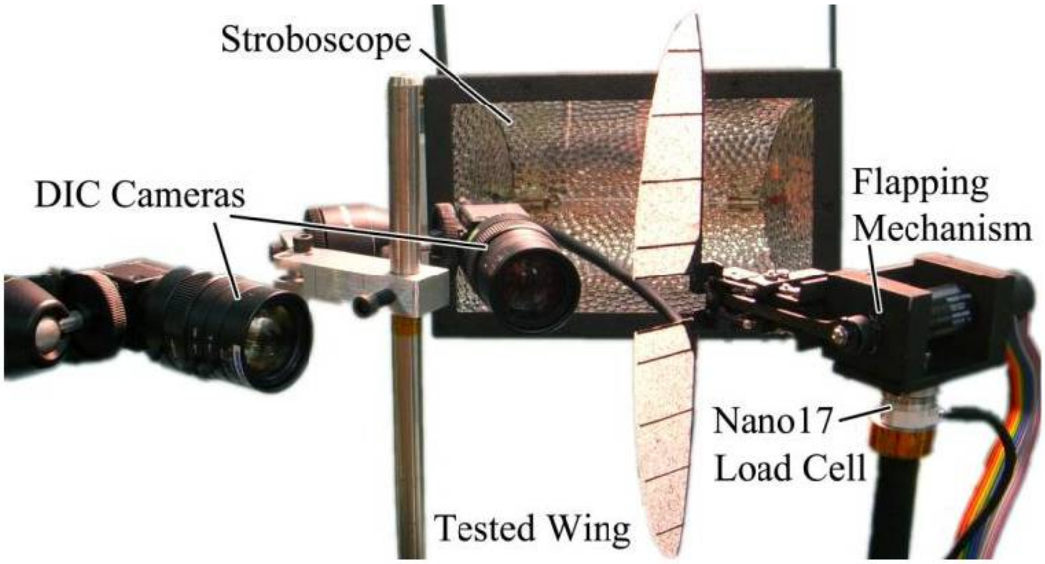

Figure 23: Rotary Motor Test Platform [118]

Despite the negatives of an electric motor based solution, it has been shown that through the storage of elastic energy, a rotary based flapping mechanism was able to produce small amounts of lift. Through the use of a simple rubber band and rotating mechanism the flapping of a swallow tail butterfly with biomimetic polymer wings was able to glide over a short distance [92]. An example of this mechanism is shown in Figure 24.

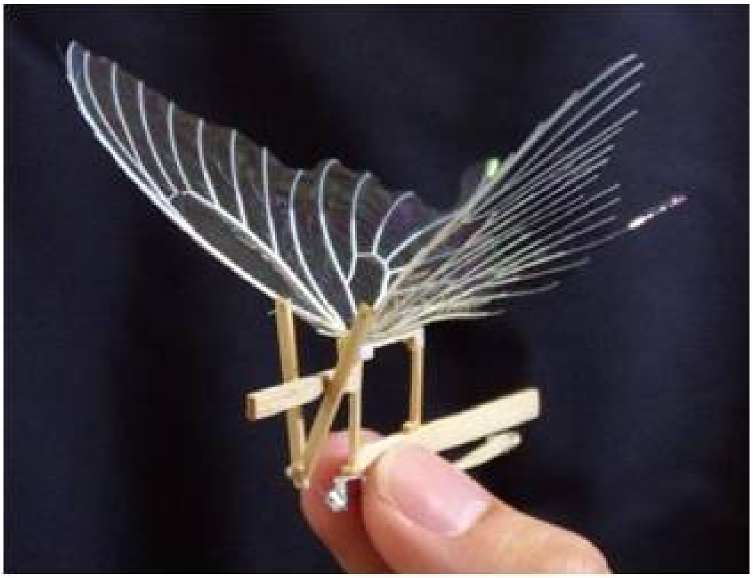

Figure 24: Tailless Ornithopter Mimicking a Swallowtail Butterfly [92]

2.3.2 Bimorph Piezo Based Actuators. Piezoelectric bending actuators are an attractive option for driving microrobots due to their light weight, scalability, ease of integration, and high bandwidth [86]. A set of clamped-free bending bimorph polycrystalline piezoelectric actuators act as a local minimum in complexity while meeting the key specifications for bandwidth, power density, and efficiency [39, 110]. Furthermore, using *Manduca Sexta* size wings, this type of actuator can outperform insect flight muscle by a factor of two or more [85]. Finally, the first flight of an insect sized based FWMAV has been achieved through the use of this actuator type. Figure 25 is a series of images that show several phases on this historic first flight [108]. The aforementioned capabilities make the use of this type of actuator a very attractive option.

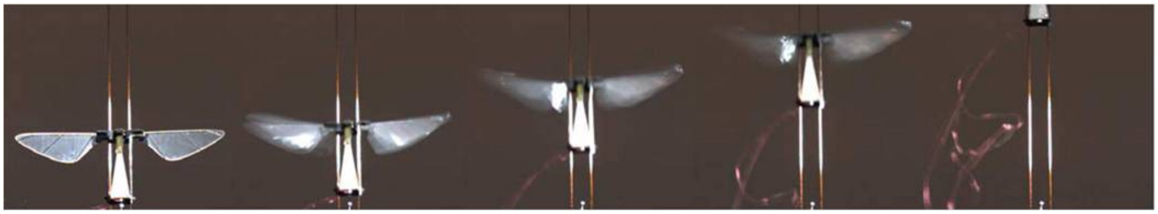

Figure 25: First Flight of an Insect Sized FWMAV [108]

The use of a piezo actuator involves the use of a slider-crank mechanism to translate the small displacement of the tip actuator into angular motion of the mechanism and can be seen in Figure 26. The ratio of this translation is deemed the transmission ratio and effectively determines both the motion and force applied to the root of the wing [107, 109]. The inherent makeup of a piezoelectric actuator PZT actuator requires that a high voltage analog waveform be used for control of the actuation of the device. This allows for the ability to control both the amplitude, and frequency of the actuator.

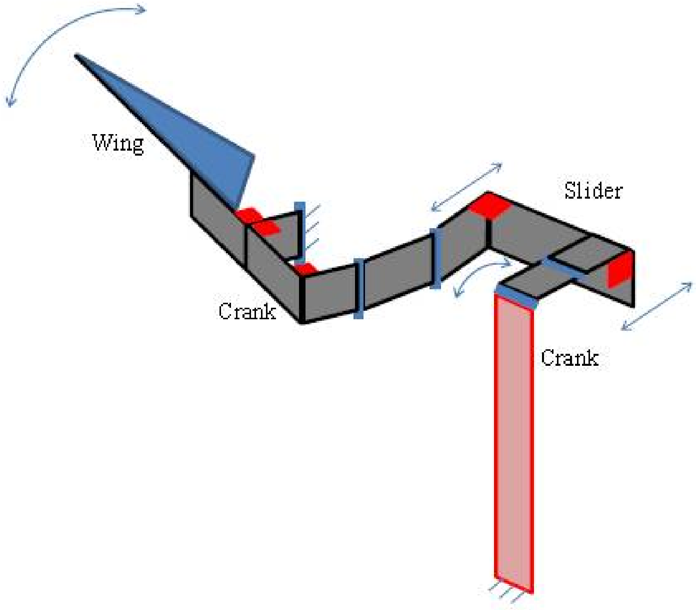

Figure 26: Hybrid PZT Flapping Mechanism [107]

Previous efforts have shown that a single PZT actuator can be used to effectively actuate and flap two wings of a FWMAV, Figures 27-28. However, to properly control such a vehicle, the use of 1 or more actuators is required to properly control the FWMAV. Mechanisms involving a single large actuator and one or more smaller actuators have shown that from two degrees of input, five degrees of freedom control can be achieved [2–5, 25–27].

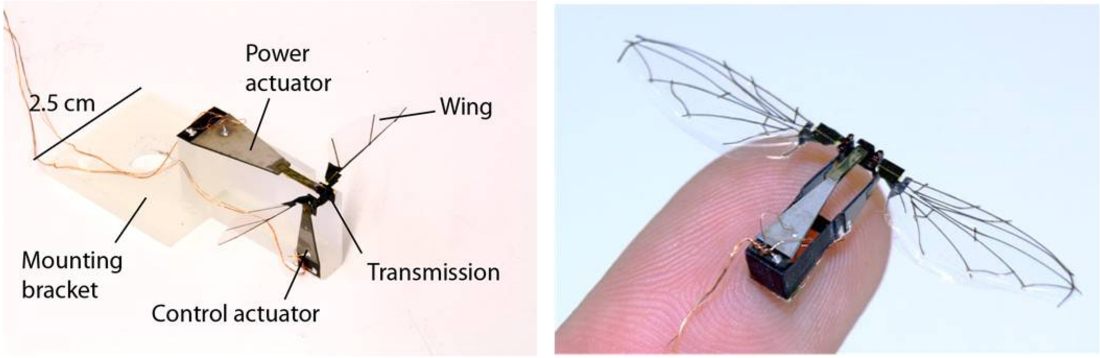

Figure 27: Three Actuator Controlled FWMAV [25–27, 78]

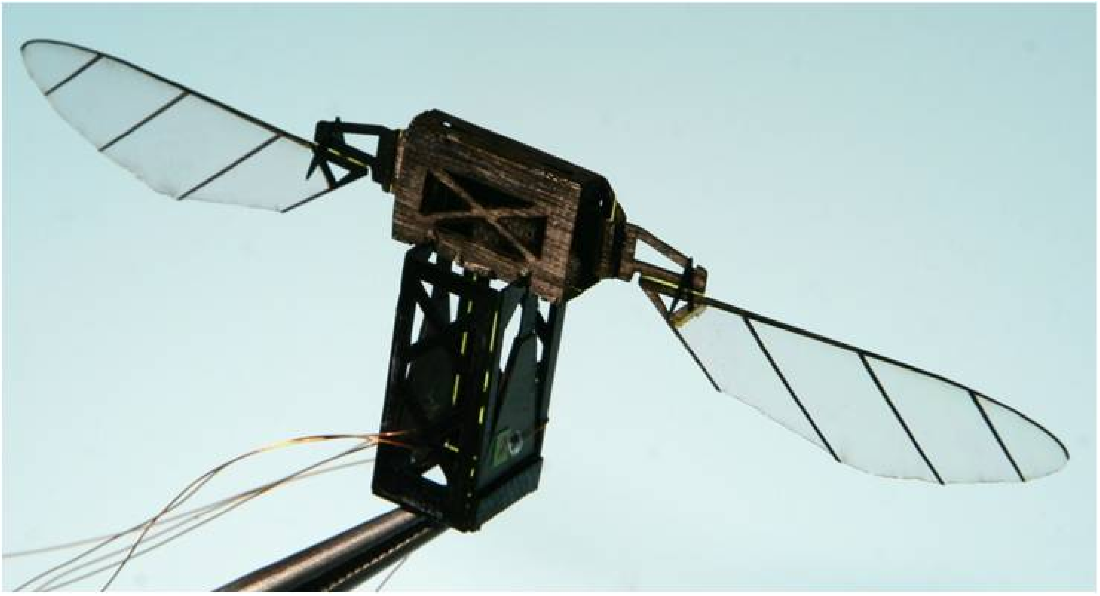

Figure 28: Two Actuator Based 5DOF Controlled FWMAV [2–5]

III. Morphological Study

To properly model the structural dynamics of the forewing of the *Manduca Sexta* species, it is critical that the material and structural properties of the biological specimen be understood. A morphological study has been conducted to identify the material and structural properties of a sample of male and female *Manduca Sexta* specimens. The average mass, area, shape, size, and camber of the wing were evaluated using novel measurement techniques. Further emphasis is placed on studying the critical substructures of the wing: venation and membrane. The venation cross section is measured using detailed pathological techniques over the entire venation of the wing. The elastic modulus of the leading edge veins is experimentally determined using advanced non-contact structural dynamic techniques. The membrane elastic modulus is randomly sampled over the entire wing to determine global material properties for the membrane using nanoindentation. The data gathered from this morphological study forms the basis for the replication of future finite element structural models and engineered biomimetic wings for use with Flapping Wing Micro Air Vehicles.

Figure 29: *Manduca Sexta* Specimen

To date a detailed study, with accompanying data, has not been conducted on the Manduca Species that is sufficient enough to generate a representative structural dynamics model of the *Manduca Sexta* forewing. To properly understand the structural dynamics of the forewing of the *Manduca Sexta*, it is important to properly understand the context of the structural properties of the system to which this wing belongs. In order to fill this gap, a detailed morphological study of key features of numerous *Manduca Sexta* specimens is presented here.

Male and female specimens are received as pupae and placed into an incubator [103]. After a period of several days, eclusion occurs, and the the adult specimen emerges from its pupal case. After a period of 2-3 days, to allow the moths wings to fully harden, the specimen is harvested for further study [62].

3.0.3 Mass and Area Measurement Techniques. When a moth is ready for study, the entire moth is weighed and a top down image of the specimen is taken, Figure 29. The specimen is then dissected into seven component pieces, Table 3.

Table 3: *Manduca Sexta* and Primary Subcomponents

1	Forewing - Left
2	Forewing - Right
3	Hindwing - Left
4	Hindwing - Right
5	Head
6	Thorax
7	Abdomen

Each of these pieces is then placed on a green colored background with a reference marker and photographed with a digital camera as shown in Figure 30. Using common image analysis techniques, the pixel by pixel area of each of the component pieces can be analyzed [72]. Using the image processing toolboxes available through

Matlab, the image background is removed, translated into grayscale, and thresholded to black and white. Small objects are removed, and the remaining boundaries of the moth subcomponents are traced. Using a reference marker of a known shape and size, the pixel information can be translated to physical measurement units. Depending on the sub-component, the length, width, area, and approximate volume can be determined. Each of the component pieces are then individually weighed with a very precise digital scale, Ohaus Voyager Pro (VP214CN), that is calibrated to measure repeatably to 0.1 milligrams. The total processing time of mass and area measurements is completed in less than ten minutes for each specimen.

3.0.4 Mass Properties. Mass properties for 30 different specimens are presented in summary in Table 4 and in detail in Table 24 - Appendix A. The table lists the measured values for the moth and each subcomponent. The mass of the subcomponents relative to the weight of the entire insect is shown as a percentage. This latter value could prove to be useful to FWMAV design engineers in determining the design space for their application. This testing revealed that the average weight of a single specimen is 1.55 ± .050 grams. The weight of the forewings averages to 34.6 milligrams grams and represents 2.23% of the total mass of the insect. The hindwings weigh, on average, 12 milligrams and make up 0.78% of the total mass. The head, which could be akin to the control system, weighs approximately 105.6 milligrams and represents 6.81% of the mass of the moth. The thorax, which is the primary drive mechanism for flight, weighs approximately 58.3 milligrams and represent 37.6% of the total mass. Finally, the abdomen, which performs power generation and energy storage in addition to carrying the primary payload of the moth (eggs), typically weighs 72.1 milligrams and represents approximately 46.47% of the mass of the moth. As a check, the sum of the component measurements is presented and indicates that there is a 3% loss of mass from the first measurement of the entire specimen. These small differences are attributed to handling of the specimen and possible loss of very small pieces of the specimen during the dissection process.

Table 4: *Manduca Sexta* Mass Properites

SAMPLE	**MOTH**	**FW LT**	**FW RT**	**HW LT**	**HW RT**	**HEAD**	**THO**	**ABD**	**Total**	**Diff**
	(grams)	**(grams)**	**(grams)**	**(grams)**	**(grams)**	**(grams)**	**(grams)**	**(grams)**	**(grams)**	**(grams)**
AVG	**1.55304**	**0.03466**	**0.03576**	**0.01217**	**0.01220**	**0.10574**	**0.58396**	**0.72167**	**1.50615**	**0.04689**
STD	**0.50759**	**0.00767**	**0.00747**	**0.00286**	**0.00311**	**0.01939**	**0.14861**	**0.32059**	**0.48336**	**0.04658**
MAX	**2.70160**	**0.05210**	**0.04940**	**0.01960**	**0.01760**	**0.13770**	**0.91790**	**1.59760**	**2.58220**	**0.14141**
MIN	**0.76870**	**0.01860**	**0.01990**	**0.00780**	**0.00700**	**0.05850**	**0.26830**	**0.29760**	**0.75400**	**-0.00100**
% Total		**2.23%**	**2.30%**	**0.78%**	**0.79%**	**6.81%**	**37.60%**	**46.47%**	**96.98%**	**3.02%**

Table 5: *Manduca Sexta* Scale Mass

Sample	**Wing w/Scales**	**Wing w/out Scales**	**Difference**	**Scale Percentage**
	(grams)	**(grams)**	**(grams)**	**-**
AVG	**0.0296**	**0.0233**	**0.0063**	**20.6%**
STD	**0.0064**	**0.0040**	**0.0030**	**5.4%**
MAX	**0.0401**	**0.0291**	**0.0118**	**31.2%**
MIN	**0.0197**	**0.0162**	**0.0035**	**13.5%**

An additional study was carried out to determine the mass contribution of the scales that are indicative to the wings of this species. This study was performed by liberating the forewings of the *Manduca Sexta* as previously described. This process was performed as gently as possible to prevent the removal of any of the scales during the liberation process. The wings were immediately weighed and their masses recorded. Following this, the scales were carefully removed, using a bristled brush, that had been slightly dampened with water to prevent the aerial dispersal of the scales. Upon removal of the wings scales, the wings were then weighed again. The time for this process was on the order of 3-5 minutes, eliminating the possible loss of mass to dessication. Due to the hydrophobic nature of the scales and the membrane, as evidenced by the beading of water on these surfaces, it is felt that there is no mass contribution to the use of water and a bristled brush to remove the scales. This was confirmed by rewetting the wing membrane after measurement, lightly drying the membrane with a paper cloth and remeasuring the wing. Differences in mass were less than 0.5 milligrams of the first membrane only measurement. The results of this study are presented in summary in Table 5 and in detail in Table 25 - Appendix B. This testing has revealed that for the forewing of the *Manduca Sexta* species, the scales of the forewing represent on average, 20.6% of the forewing mass. This is a significant amount of mass and is considerably larger than amounts previously reported in more general studies of a number of different species of insects [19].

Figure 30: *Manduca Sexta* Component Raw and Threshold Images

3.0.5 Forewing Area Properties. Using the methods described above, 24 individual forewings, both left and right, were measured to determine their basic shape. A summary of the results of this analysis are presented in Table 6 and in detail in Table 26 - Appendix C. The wing shape is described by a number of common features related to the geometry of the wing. The wing length is represented by R and is typically found to be roughly 45-55 millimeters in length. The wing area S is typically found to be 715 mm^2. It is more useful to express the wing area in terms of the wing length, R, and aspect ratio, AR, which is equal to the span, *2R*, divided by the mean chord, *S/2R*, where $AR = 4R^2/S$ [97]. Aspect ratios of the forewing of *Manduca Sexta* fall in the 14.0-15.0 range. The area centroid is computed and falls at roughly 37.3% of the wing length and at 59.5% of the maximum wing chord.

Table 6: *Manduca Sexta* Forewing Area Properties

	AR	**S**	**CentroidX**	**CentroidX**	**CentroidY**	**CentroidY**	**Length**	**Chord**
		(mm$\hat{2}$)	**(mm)**	**% Length**	**(mm)**	**% Chord**	**R (mm)**	**C (mm)**
AVG	**14.42**	**702.46**	**18.61**	**37.3%**	**14.046**	**59.5%**	**50.18**	**22.97**
STD	**0.44**	**99.20**	**7.65**	**15.5%**	**5.164**	**10.8%**	**3.53**	**5.31**
MAX	**15.46**	**896.06**	**29.89**	**56.9%**	**20.708**	**78.4%**	**57.85**	**32.83**
MIN	**13.82**	**514.00**	**8.61**	**18.2%**	**7.607**	**45.1%**	**42.59**	**16.64**

3.1 Venation

3.1.1 Optical Venation Pattern Detection. When initially viewed, the geometric structure of the Hawkmoth wing can be seen as being very detailed and complex. However, after a period of study it can be found that there are actually many repeatable features in the wings themselves. Identification of the location of the main veins can be easily accomplished through graphical picking of a two dimensional image. This image can be generated through any optical technique. All that is required is that the face of the imaging device be parallel to the surface of the wing to avoid any z-direction distortion. Scanning of the wing using an optical scanner is an excellent way to capture the required data. Removal of the scales from the wing is preferred to allow light to pass through the membrane to properly capture the location of the veins. The inclusion of a reference scale to allow for a known distance to pixel ratio calculation can also be helpful, but is not required.

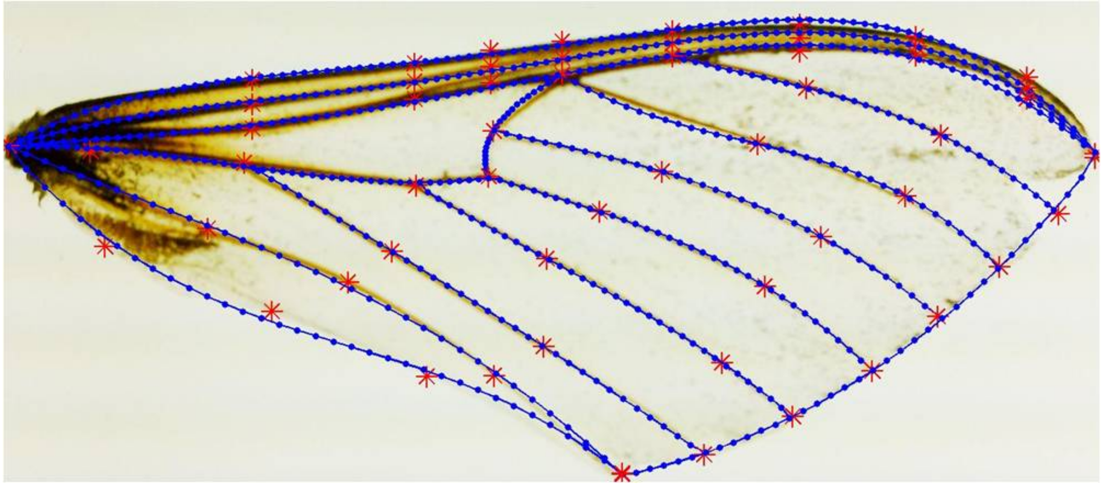

Figure 31: Splined Wing

Once the digital image of the wing is captured the leading edge vein can be identified by ten points at or near the root, 1/4 point, midpoint, 3/4 point, and tip. These points can be used with a 4th order polynomial curve fit to correctly identify the curvature of the leading edge vein. Remaining veins can also be described by four points at the root, midpoint, and tip of the veins with a third order polynomial curve fit. With these equations in hand, 50-100 points are interpolated along each of these paths. The results of this graphical picking can be seen in Figure 31. It can be clearly seen that all critical features and joint intersections have been properly located. This pattern detection will be used in section 3.1.2 to account for measurement error of the presented technique to determine the venation diameters of the wing.

3.1.2 Venation Cross Section. Previous research was performed using computed tomography to analyze the cross sectional area of the wing by looking at individual slices of CT data from the leading edge to the trailing edge of the wing [66]. Due to the small size of these veins, the CT imagery resolution of approximately 25 microns was not adequate to resolve the features along the length of the wing. A methodology for measuring the fine features of the venation using common pathological techniques was used to measure individual veins, with a resolution of less than 1 micron. The measurements from the presented techniques allow for a very accurate determination of the cross-sectional area of the vein than previous applied methods [84].

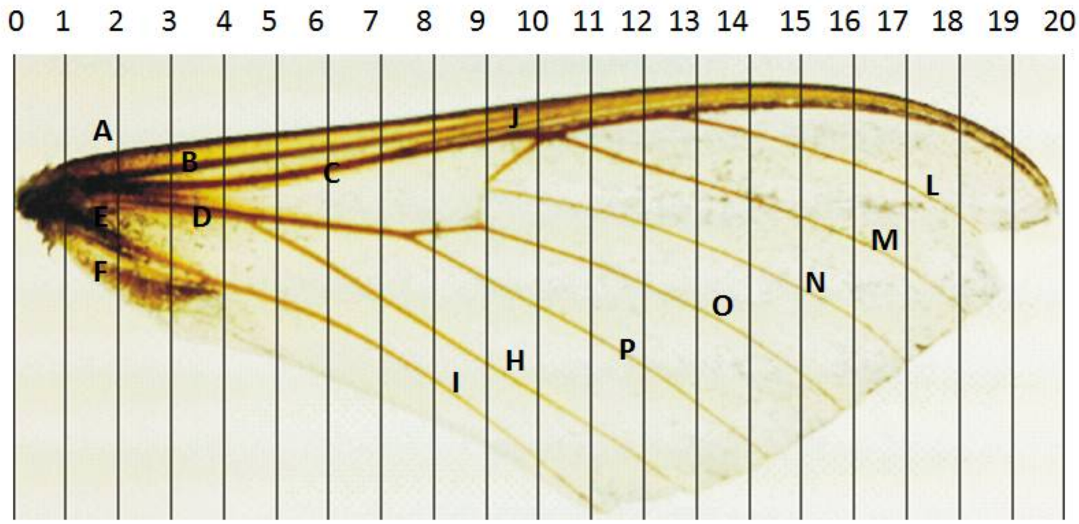

Figure 32: *Manduca Sexta* Forewing Vein Structure Characterization

A study was carried out on five individual wings to determine the inner and outer diameters of the veins of the forewing of the *Manduca Sexta* species. This was performed by placing the entire wing in a sectional mold of paraffin wax. As depicted in Figure 32, sectional cuts were made from the root to the tip of the forewing at 2.5 millimeter intervals. The sectional cuts were then allowed to cool and then sliced using a microtome. They were either directly measured or dyed to allow easy visualization of the structure and then measured [87]. Each of the sectional slices was then interrogated to determine two critical measurements of each of the veins in the sectional cut. Figure 33, depicts a sample result of the described process. Measurements of the outer and inner diameters of four veins, from a sectional cut at 40% of the wing length are shown. The first vein, Costal (C) is located to the left of the wing, along the leading edge. The remaining subcostal (Sc) and radial (R1,R2) veins follow from left to right. It can be clearly seen that the veins are not circular, but rather elliptical in shape with large asymmetric fillet transitions [13, 115]. Using the previously defined optical measurements of the venation curvature, a correction of the diameter measurements based upon the oblique sectional cuts can be calculated. The data reported here includes this corrected measurement for each wing. It is also of importance to note that the centroid of the veins is offset below the top surface of the membrane.

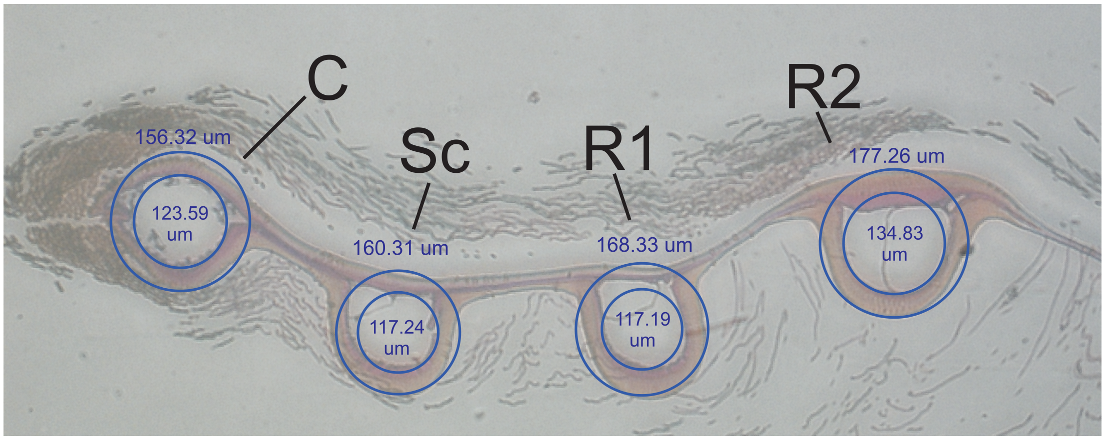

Figure 33: Vein Pathology Measurements: Wing 1 40% Wing Length (R)

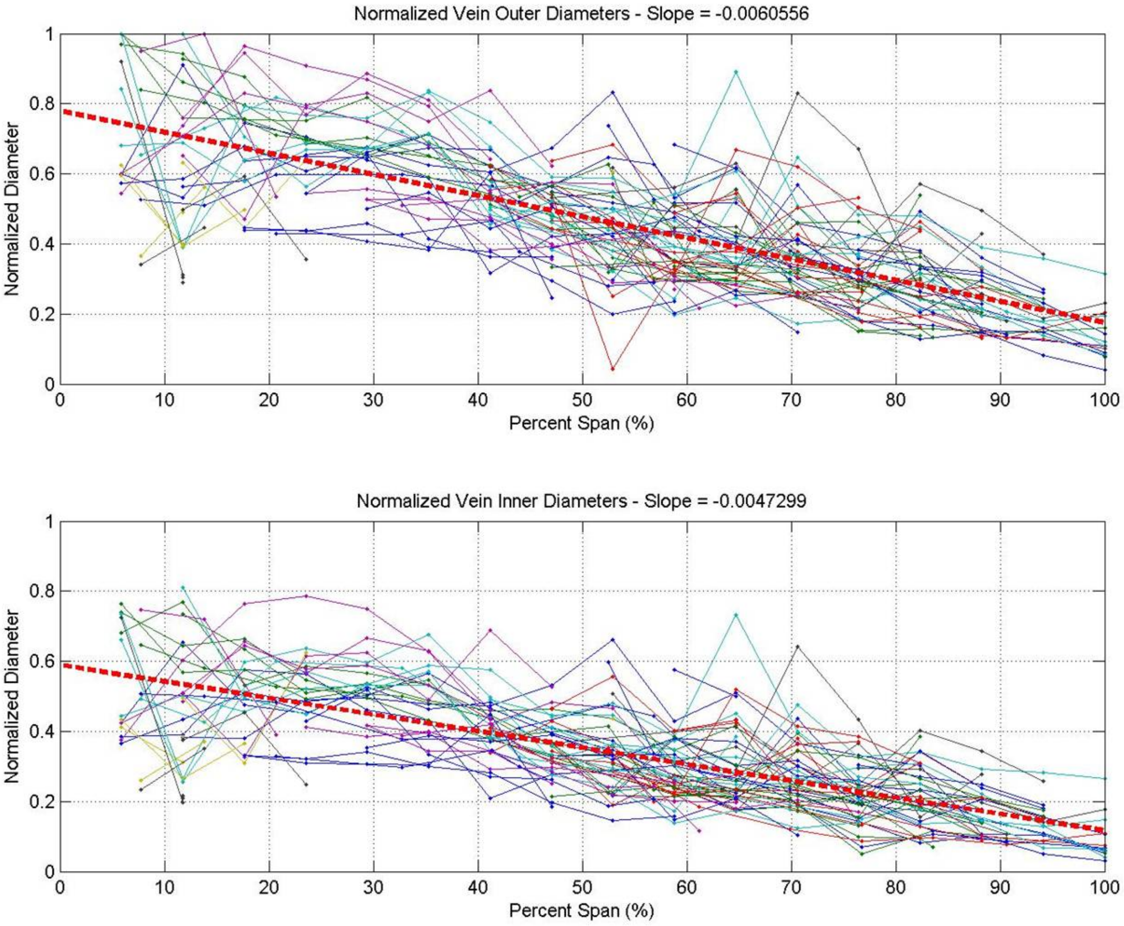

Figure 34: Normalized Wing Vein Outer and Inner Diameters

Figure 34, depicts the results of over 900 individual measurements of the outer and inner diameters of the five specimens. Each color in Figure 34 represents the venation measurements of a single vein from the study. Due to the varibility in the sizes of the wings samples, the measurement of the vein diameters were normalized by the diameter of the costal vein at the root of the wing. For all of the wing specimens, the outer and inner diameters of the veins linearly decline from root to tip as depicted by the dashed linear trend lines in Figure 34 and Equation 2. Y-values of Equation 2 equal the calculated vein diameter and X-Values refer to the percent of the wing length.

$$\begin{array}{cc} Mean\ Outer\ Diameter & Mean\ Inner\ Diameter \\ y(x) = p1 * x + p2 & y(x) = p1 * x + p2 \\ p1 = -0.006056 & p1 = -0.00473 \\ p2 = 0.7795 & p2 = 0.5896 \end{array} \tag{2}$$

A linear relationship between the inner and outer vein diameters was also determined, Equation 2. The inner diameter of the vein is on average within 73.2% of the vein outer diamter over the length of the wing. Maximum outer diameter measurements occur near the root of the wing along the leading edge, in the costal and radial veins. They typically range from 400-500 microns at these locations. Minimum outer vein measurements occur near the tip of the wing along the trailing edgein the anal veins. They typically range from 30-60 microns at these locations. It is far easier to measure the outer diameter of the veins using physical or optical measurement techniques. Through Equation 2, the calculation of the interior features of the veins can be accounted for without directly taking these interior measurements and will aid in the determination of venation material properties in subsequent specimens.

3.1.3 Venation Elastic Modulus. The dynamic forced response of five costal and radial veins of the *Manduca Sexta* are tested using simple cantilever beam conditions to predict the elastic modulus of the structure. The experimental forced response of the vein structure was tested using laser vibrometry and modal analysis. Through the use of previously discussed venation measurement technique, the outer diameter of the vein specimen can be physically measured and the subsequent volumetric structure of the wing can be analytically approximated using simple finite element analysis techniques. Using an unconstrained optimization technique, the unknown elastic modulus, E, of the vein structure can be easily approximated by tuning the analytical model to match the experimental results. This methodology has been used to successfully determine the material properties of composite plates and is applied here [35].

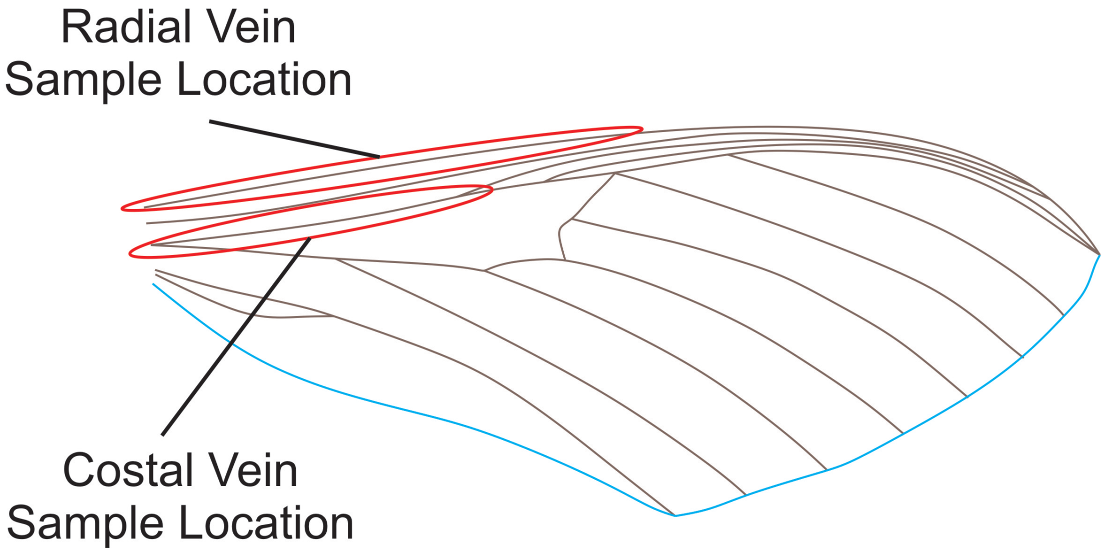

Figure 35: Radial and Costal Vein Harvest Locations

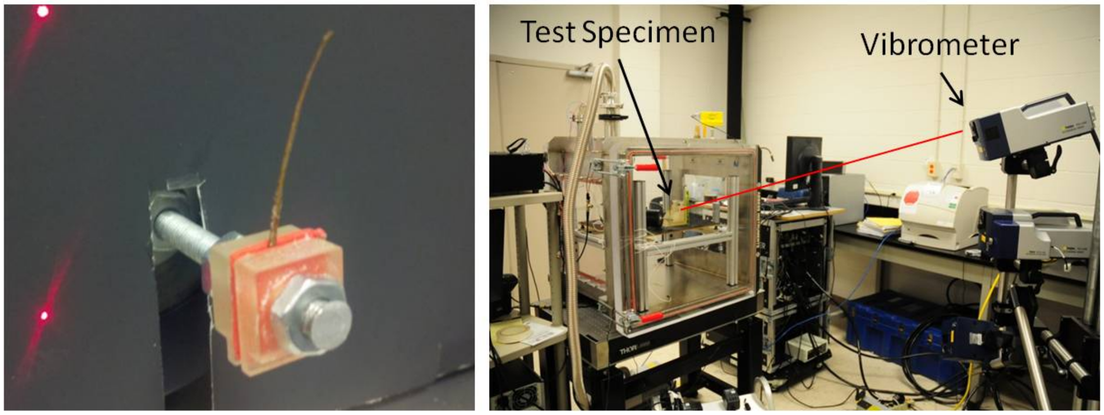

Figure 36: Experimental Modal Analysis: Radial Vein and Scanning Laser Vibrometer

The experimental sample is harvested from a wing in which the membrane scales have been removed. Then a section of the leading edge radial vein or the costal vein is harvested from the wing as shown in Figure 35. The membrane is closely trimmed to isolate the vein. The vein is then placed into a small clamping device that is lined with a medium density foam. This foam lined clamps allows the vein structure to be held, but not crushed. The vein and clamping structure are then placed to a piezo shaker that will provide the required base excitation required for modal analysis. In this case, the first eigenvalue of the vein structure is determined by experimentally determining the forced response of the vein, Figure 36, through the use of a laser vibrometer and a pseudo random excitation. The results of this experimentation are shown in Figure 37. The FEA model implements data from the venation cross sectional analysis to determine the inner diameter of the veins based on external measurements using both machinists calipers and optical measurements from a microscope. Volume is calculated during the FEA analysis and is coupled with a measurement of the mass of the vein to determine of the density of the venation material.

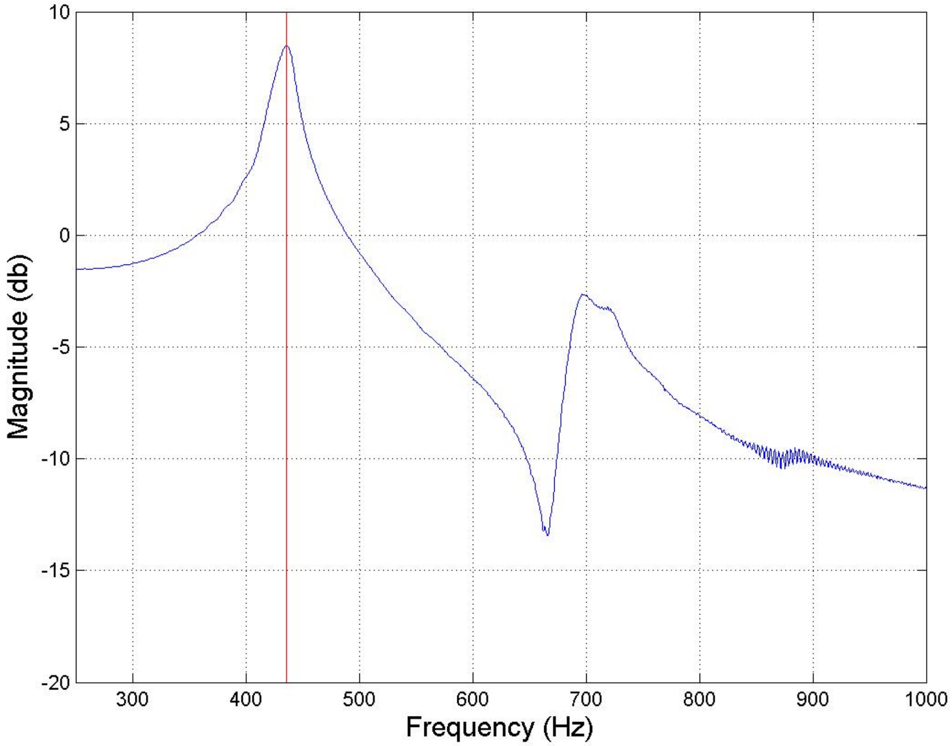

Figure 37: Experimental Frequency Response Function at the Vein Tip

With this data a one-hundred element tapered beam FEA model is generated to model the tested vein. Equation 3, depicts the simple cost function used to tune the fundamental frequency of the model to the experiment. By iterating on the elastic modulus variable of the FEA model, the minimization of J is realized as depicted in Figure 38.

$$J = \sum_{n=1}^{n_{modes}} \left[\left(\frac{\omega_{x,n}}{\omega_{f,n}}\right) - 1\right]^2 \cdots \begin{array}{l} \omega_{x,n} = EXP \\ \omega_{f,n} = FEA \end{array} \tag{3}$$

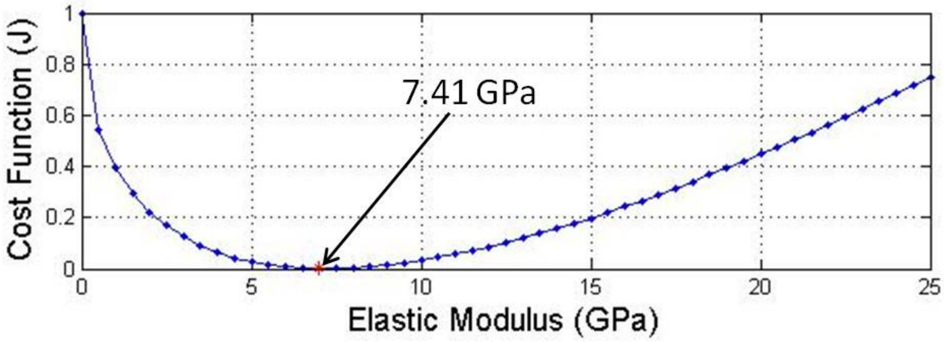

Figure 38: Cost Function Minimization

Table 7: Experimental FEA Input Variable and Venation Elastic Modulus Results

Vein Location	**Root OD**	**Tip OD**	**Length**	**Omega**	**Density**	**E**
	μm	**μm**	**μm**	**Hz**	**G/cm3**	**Gpa**
Radial	500	476	15724	518	2.6925	**6.23**
Costal	432	365	13240	558	1.5152	**7.82**
Radial	418	391	14472	470	2.3956	**8.20**
Radial	413	337	13385	469	2.8963	**7.63**
Costal	432	320	15153	436	2.6292	**7.17**
AVG	-	-	-	-	**2.4258**	**7.41**
STD	-	-	-	-	**.5394**	**0.75**

The results of this testing, as presented in Table 7, show the mean elastic modulus to be 7.41 GPa ± 0.75 GPa. This value lies within the range expected for similar flying species [84, 114].

3.2 Membrane

3.2.1 Membrane Material Properties. The method of measuring hardness and elastic modulus by instrumented indentation is a common practice for determining the mechanical properties of thin films and small structural features [68]. The application of nanoindentation has been performed to determine the mechanical properties of the membranes of cicadas [84] and the tergal plate of *Manduca Sexta* [34].

Nanoindentation was conducted using a MTS G200 Nanoindenter on a single wing using membrane sections that had been isolated from the forewing of the *Manduca Sexta*, Figure 40. These membrane samples were processed by removal of the membrane's scales and mounted to a glass slide through the application of a thin layer of cyanoacrylate adhesive. This glass slide had been previously mounted to an aluminum puck using a Crystal Bond adhesive and allowed for easy mounting into the specimen carriage of the nanoindenter. Nanoindentations were made on a 5 x 5 grid, with 25 micron spacing, at a depth of 500 nanometers into the membrane surface, at random locations of the wing specimen as shown in Figure 39. Approximately, 20 minutes was required to process nanoindentations at each site. The total testing time of approximately of 100 minutes is well within the 180 minute window in which the wing has been show to significantly dessicate [95]. Care was taken to ensure that all nanoindentaion samples were taken over a homogeneous area of the wing membrane and not over the follicle of a wing scale. The surface of these membranes is presented in Figure 41. The 25 indentation samples from each site location were then averaged to determine the local mean modulus over the particular measurement area. The local modulus values were then averaged to determine the global mean elastic modulus of the specimen which was found to 2.446 ± 1.37 GPa. Both the local site modulus and global membrane modulus are presented in Table 8. These results are consistent with other species and fall within the range of similar species of winged insects [19, 84].

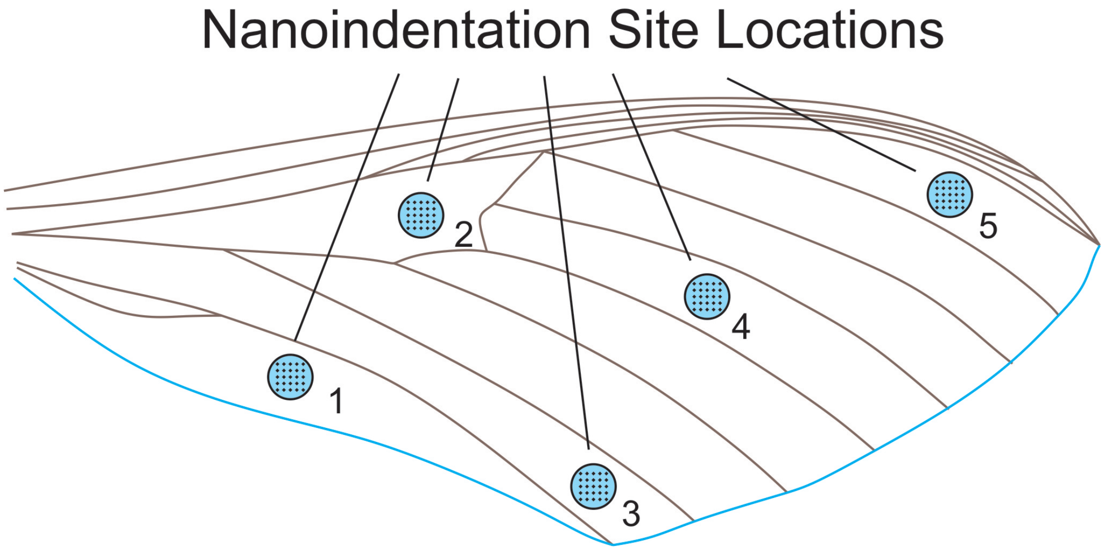

Figure 39: Nanoindentation Site Locations

Table 8: Nanoindentation Site Location Values

Site	**Site Mean**	**Site STD**
1	1.91	1.04
2	4.77	1.21
3	1.49	1.29
4	2.59	0.73
5	1.47	0.98
Global Mean	**2.45**	-
Global STD	**1.38**	-

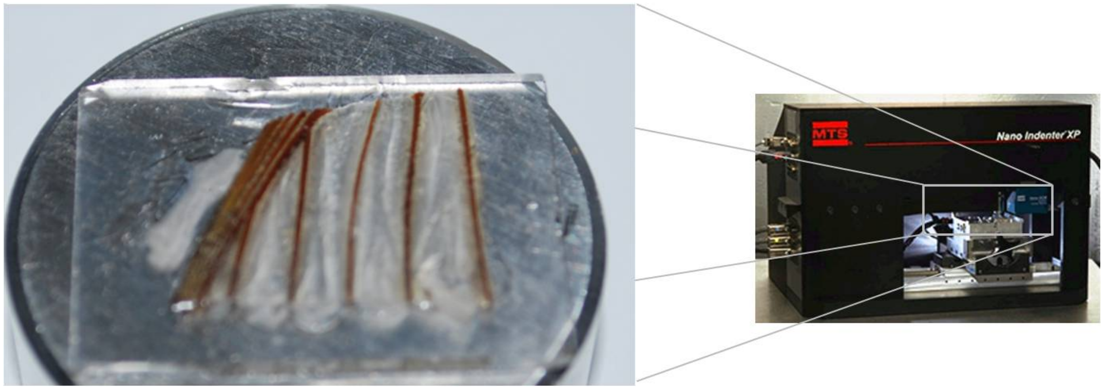

Figure 40: Membrane Specimen Mounted for Testing in MTS Nanoindenter

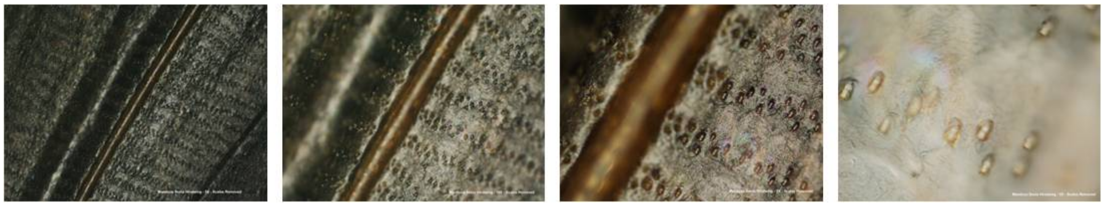

Figure 41: Membrane Surface without Scales: 5X,10X,20X,50X

3.3 Wing Camber

The forewing of the *Manduca Sexta* species is a complicated three dimensional structure. In addition to the planar properties of span, chord, planform area, and aspect ratio, it is important to quantify the shape of the wing. This three dimensional shape is quantified by the mean camber line of the wing. This camber is very important in determining the structural response and aerodynamic performance [19,80]. Since the wing of the *Manduca Sexta* species is so thin, the camber line represents its camber. Using a 3D coordinate measurement arm and laser line scanning system, it is possible to measure the camber of both engineered and biological wing profiles [47,65]. Due to the variability of the size, shape, and orientation of the forewings of the *Manduca Sexta*, a methodology to measure the camber of the wings is presented that closely preserves the shape of the wing while it is attached to the abdomen of the specimen. The measurements taken in this study are of freshly liberated forewings that are placed into a clamping jig with soft foam. When the wing is liberated from the host, a conscience effort to keep the axillary sclerites at the wing base intact is made. In doing so, the axillary sclerites serve as a mount to hold the wings within the soft foam lining of the clamp without distorting the camber of the wing as compared to when the wing is attached to the specimen. The scanning process is completed within 5 minutes after liberation. The jig, shown in Figure 42, was designed to have special alignment features to allow for easy postprocessing of the camber measurements in a known reference frame. The wings themselves were scanned with a Faro Platinum Laser Line Scanner, Figure 43, with ± 35 um accuracy and a scan rate of over 45,200 points per second. For this study, 5 pairs (left and right), for a total of 10 forewings were scannned. Due to the rapid acquisition of the laser scanning system, roughly 80,000 three dimensional points were captured for each wing.

Figure 42: Alignment Jig with Wing Unclamped and Wing Clamped

After the surface of each wing was captured, the wings were post processed to allow for proper orientation and comparison to the other wing scans. Using a polynomial least squares surface fitting technique, a third order cubic polynomial was fitted to the data in both the X-axis and Y-axis and is represented as Equation 4.

Figure 43: Faro Laser Line Scanner Actively Scanning Wing

$$\begin{gathered} z(x,y) = p00 + p10 * x + p01 * y + p20 * x^2 + p11 * x * y \\ + p02 * y^2 + p30 * x^3 + p21 * x^2 * y + p12 * x * y^2 + p03 * y^3 \end{gathered} \tag{4}$$

$$\begin{array}{cccc} p00 = 0.1976 & p10 = 0.07711 & p01 = 0.1724 & p11 = 0.01626 \\ p02 = -0.01184 & p30 = .00002401 & p12 = 0.0003256 & p20 = -0.003529 \\ & p21 = -0.0001687 & p03 = 0.00061 & \end{array} \tag{5}$$

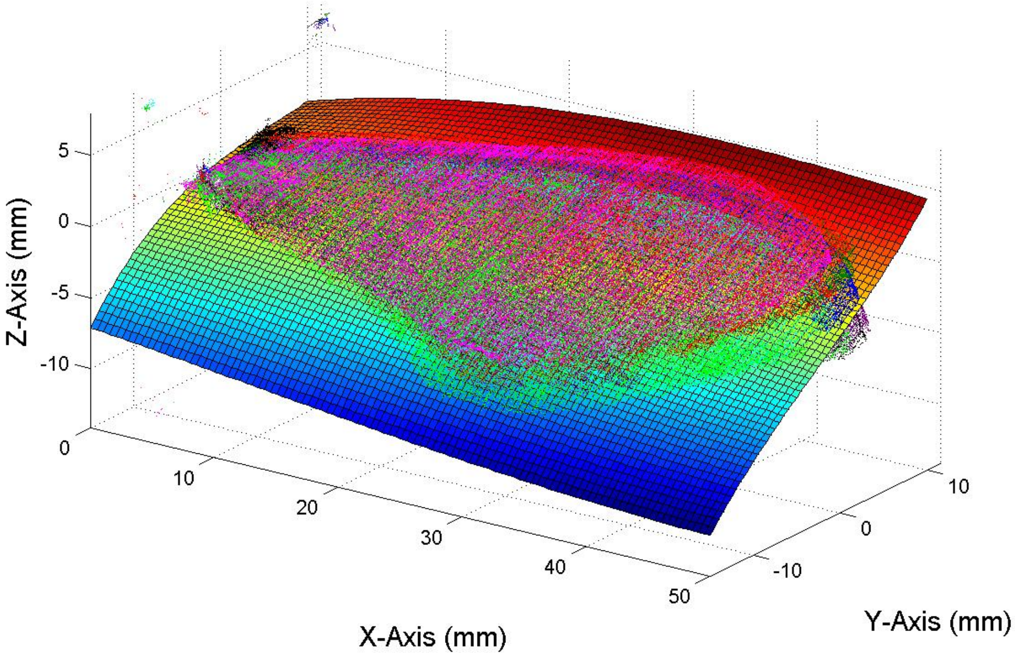

Figure 44: Point Cloud Data Fitted with Surface Model

Empirical testing found that this third order polynomial surface fit, was the best compromise in terms of goodness of fit and overall representation of the camber of each wing. Additionally, the mean surface was calculated for all of the wings and the polynomial coeffcients of this fit are presented in Equation 5. The result of this surface fit as compared to the point clouds of each wing is presented in Figure 44. With this three dimensional surface fit, the two dimensional data values of x and y can now be processed through the polynomial function in order to generate the z data required to properly model the camber for either an FEA structural model or for an equivalent engineered wing design. It is important to note that at the root of the wing the overall shape of the wing is concave up, and at the tip of the wing the shape is concave down. The transition between the two types of concavity occurs at 52%

of the wing length. These shapes are much more complex than previous studies have realized and reflect the complex nature of this species [19, 23].

3.4 Summary

Through this detailed morphological study of the forewing of the *Manduca Sexta* species, a better understanding of this species has been realized. A detailed study of the mass, area, and volume properties of the moth and its subcomponents allow biologists and engineers to have a better understanding of the mass and size associated with these systems. This allows for the identification of the design space of a FWMAV if this species of moth were to be used for the basis of a biomimetic design. Through the determination of the geometric properties of the venation and the surface of the wing, statistical models have been developed to determine these geometries along any percent of the span of a wing. These models will aid in the future design of structural models and engineered wings that correctly reflect the geometry of this species. The determination of the material properties of the venation and the membrane coupled with these geometry models will allow for the calculation of the true stiffness of the wing. This calculated stiffness can then be used for the identification of engineered materials and the subsequent geometries necessary to fabricate wings with similar structural dynamics and aerodynamic characteristics as its biological counterpart.

IV. *Manduca Sexta* Forewing Structural Dynamics

Through the application of experimental testing and finite element analysis the structural dynamics of the *Manduca Sexta* forewing can be characterized both experimentally and analytically. Laser vibrometry and laser scanning techniques are used to perform modal analysis and static displacement tests for baseline testing of the structure. This testing is then coupled with advanced computer vision processing techniques for the automated generation of finite element models of the forewing. These models include material properties, venation cross sections, and camber from Chapter III to represent a complete analytical model of the wing. Empirical refinement is used to tune the model to match the results of the experimental testing.

4.1 Wing Model Generation

4.1.1 Geometry Generation. Using the optical venation detection technique described in Chapter III - Section 3.1.1 the splined veins are simply represented as X and Y cartesian coordinates. The origin of the wing model lies at the base of the costal and radial veins. These coordinates are then translated into a format for automated generation of splines within the Solidworks 3D Computer Aided Design (CAD) modeling environment. When the series of points have all been splined, a skeletal framework of veins now exists. The skeletal framework is then saved in Initial Graphics Exchange Specification (IGES) format. This IGES file is then imported into the Abaqus FEA working environment. To properly model the *Manduca Sexta* forewing it is required that the membrane be present upon the venation framework. To accomplish this a series of surfaces are used to cover the venation patterns, from Solidworks, within Abaqus. The results of these efforts are depicted in Figure 45.

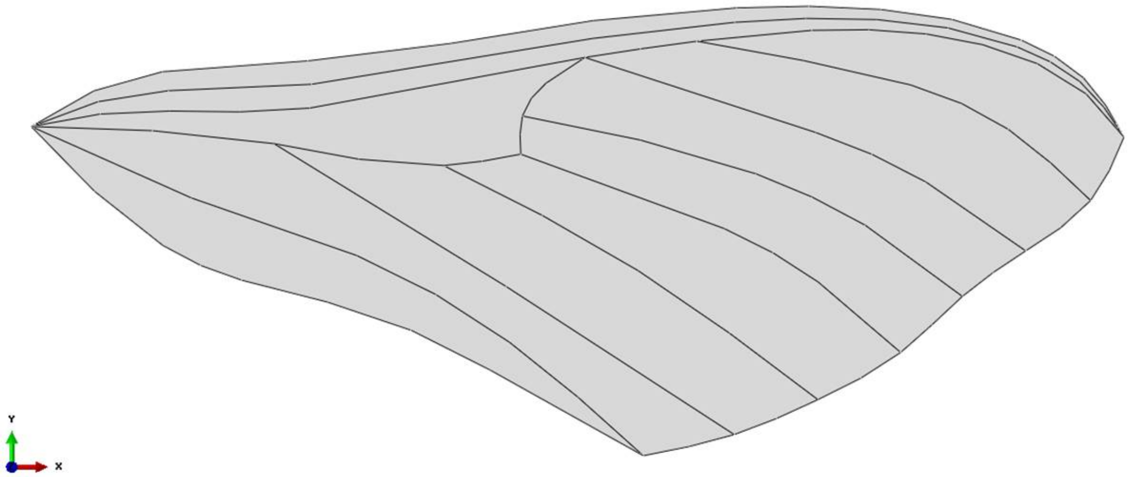

Figure 45: Venation Framework and Membrane Surfaces

4.1.2 FEA Venation and Membrane Elements and Material Properties. With the two dimensional geometry of the wing properly described, it is then necessary to focus on the generation of the mesh of the FEA model. The venation of the wing is modeled using, B32, Timoshenko Beam Elements. These elements allow for finite axial strain, shear flexible beams with quadratic interpolations [1]. 1039 beam elements were used to correctly model the forewing venation. The cross section of the veins are modeled using a tubular cross section, that tapers linearly from the root of the vein to the tip. The inner diameter of the vein is modeled as 73.2% of the outer diameter. The baseline dimensions of the venation cross sections is depicted in Table 9. The venation is modeled as an isotropic material with an elastic modulus of 7.41 GPa, Poisson's ratio of 0.3, and a density of 2452 kg/m^3. Both the venation cross section and material properties were gathered from an extensive morphological study of the *Manduca Sexta* forewing and are applied here for analytical evaluation [67].

Table 9: Venation Diameters

Vein	**Root Diameter**	**Tip Diameter**
	μm	μm
Costal	250	25
Subcostal	250	25
Radial	250	25
Cubitus	250	125
Arculus	125	75
Radial 5	125	25
Medial 1	125	25
Medial 2	125	25
Medial 3	125	25
Cubitus 1	150	25
Cubitus 2	150	25
Anal	150	25

Membrane elements are modeled using, S8R (8 noded 3D quadratic shell elements) and STRI65 (6 noded 3D triangular shell elements). 7,183 S8R elements and 175 STRI65 elements were used to properly model the membrane of the forewing. The thickness of the membrane is specified as being 5 microns thick and is based upon empirical measurement of the membrane over the entire wing surface [67]. The membrane is modeled as an isotropic material with an elastic modulus of 2.4 GPa, Poisson's ratio of 0.3, and a density of 1400 kg/m^3 [67]. The results of the application of FEA elements to the geometry can be seen in Figure 47.

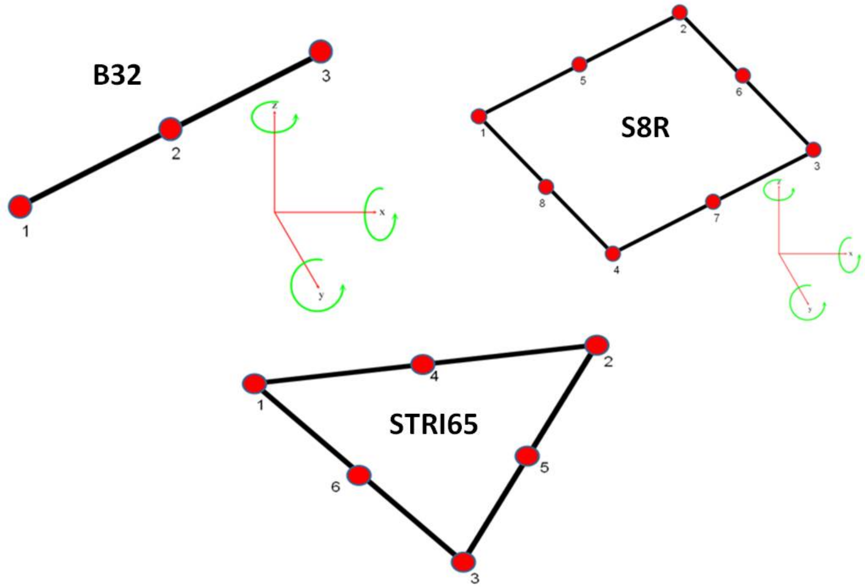

Figure 46: FEA Element Types

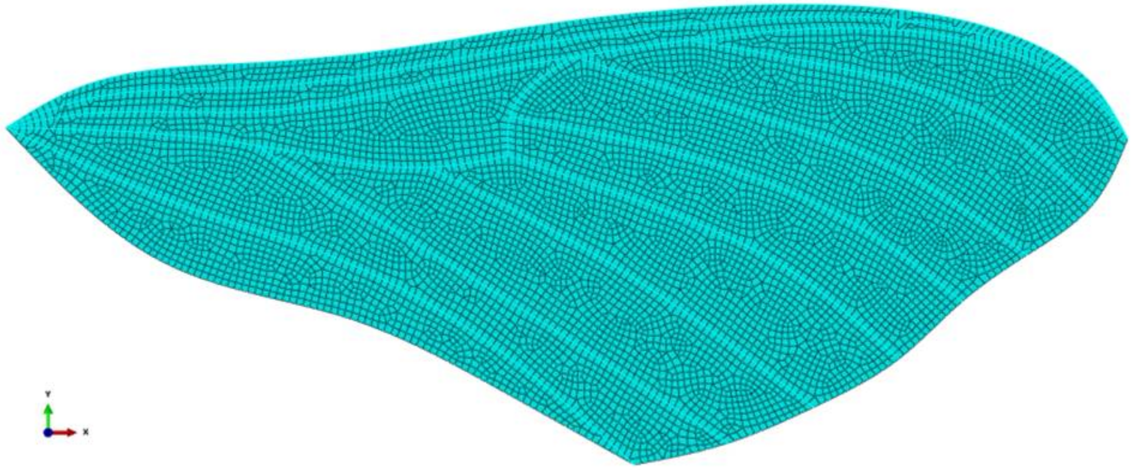

Figure 47: FEA Mesh: Venation and Membrane Elements

4.1.3 Camber. Three dimensional imaging technologies using Computed Tomography and Laser Line Scanners have been used to measure the camber of the forewing of the *Manduca Sexta* [66, 67]. These measurements have shown that the surface camber of the wings is a complex three dimensional shape. At the root of the wing the camber can be described as concave down and transitions to a concave up shape at the tip, with the transition from concave up to down occuring at 52% of the midspan of the wing. The maximum height of the curvature, at the root and tip of the wing, is approximately 1 mm, respectively. With this information the appropriate three dimensional camber can be applied to the FEA model of the wing. The inclusion of camber represents a leap forward in modeling capability that allows for the proper strucural dynamic characterization of the wing.

4.1.4 Boundary Conditions. The wing is placed in a clamped boundary condition at the root of the wing that provides for no x, y, z displacement or rotations to occur. This boundary condition is applied in all analytical and experimental tests. In modal analysis experiments this boundary condition is applied by placing the root of the wing in a two-piece plastic clamshell. The inner lining the clamshell is made with a high density foam that properly constrains the wing without crushing the biological structure of the wing.

4.1.5 Parametric FEA Model Implementation. After the initial model generation, the Abaqus interface is no longer used to interact with the defined model. Instead, the input file that is generated from the Abaqus user interface is used to iterate on the model and its associated features. This input file is a text file that sheds the previously defined geometry and instead has replaced this data with a series of nodes and elements that form the basis of the finite element method. Because the input file is in a text based format, it is possible to use Matlab to read this text file, manipulate the data, and rewrite this input file. A command line interface is then used to call Abaqus to solve the newly generated model. All post processing is then completed in Matlab to determine the subsequent results. In this manner all aspects of the model can be manipulated and adjusted such that the model is truly parametric. This includes the venation and membrane material properties, size, and three dimensional location. A detailed flowchart is presented in Figure 48 that provides a high level summary of the process involved to realize a parametric FEA model using this methodology.

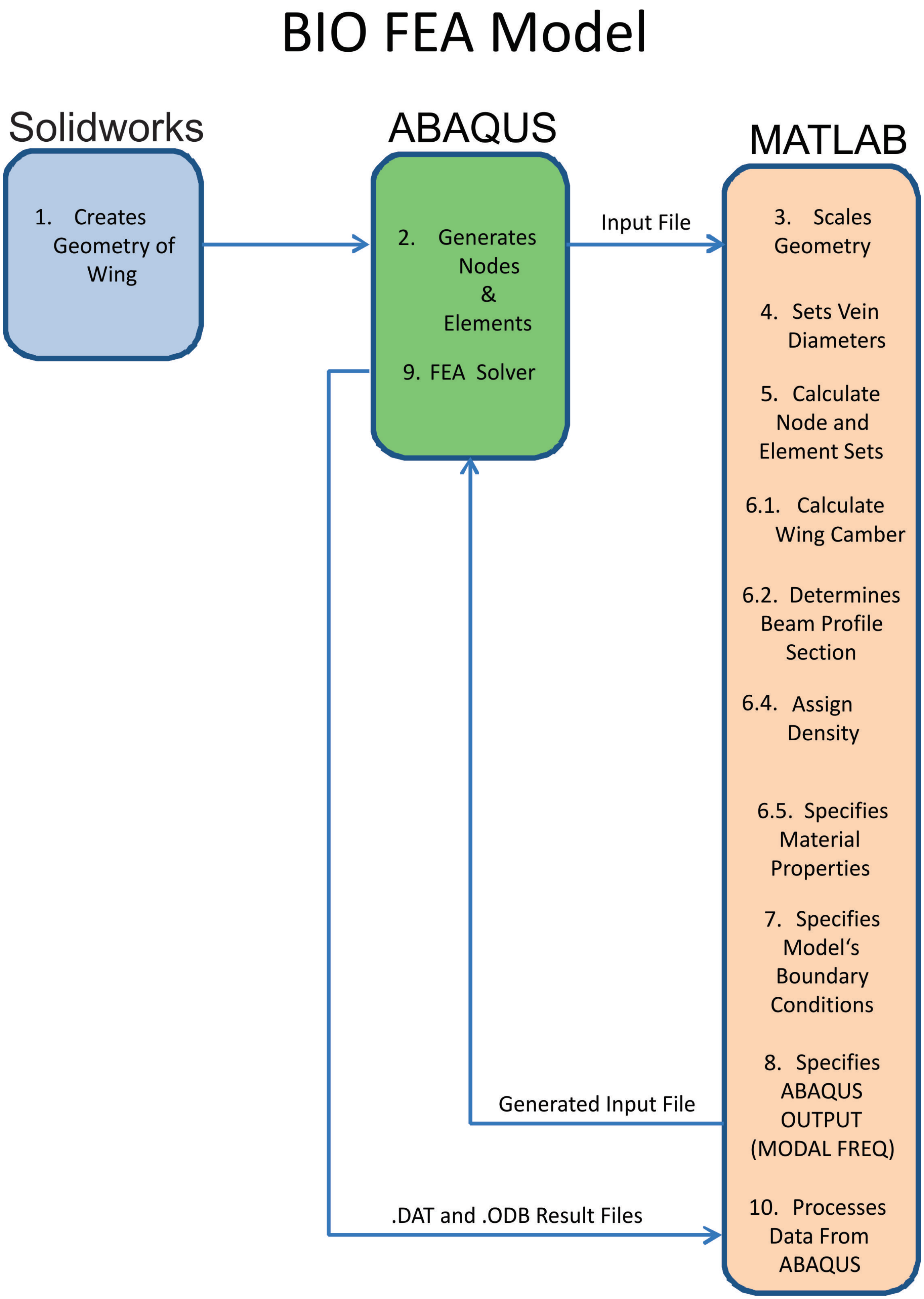

Figure 48: FEA Process Flowchart

4.2 Results

4.2.1 FEA Model Geometric Properties. The model presented in Figure 45, represents the most highly refined structural dynamics model presented to date. By modeling the wing venation and membrane geometry (cross section, thickness, and camber) and material properties, the dynamics of the wing structure can now be determined with a high degree of confidence, prior to experimental validation. In this manner, a whole host of structural properties can be identified for a biological specimen that are experimentally difficult to measure. By identifying the properties presented in Table 10 comparisons can be made for engineered FWMAV wings of similar shape and size. The physical location of the origin, area centroid, and mass centroids are visually depicted in Figure 3.

Table 10: Biological Wing Mass, Moment/Product of Inertia Properties

Mass		**Total**		
		2.86E-05		kg
Center of Area	**X**	**Y**	**Z**	
	22.1E-03	4.0E-03	0	m
Center of Mass	**X**	**Y**	**Z**	
	16.2E-03	0.5-03	0	m
Moment of Inertia at Origin	**Ixx**	**Iyy**	**Izz**	
	2.99 E-10	1.14E-08	1.16E-08	kg· m^2
Product of Inertia at Origin	**Ixy**	**Iyy**	**Izz**	
	-2.54E-10	1.01E-29	-5.92E-29	kg· m^2
Moment of Inertia at Center of Mass	**Ixx**	**Iyy**	**Izz**	
	2.91E-10	3.89E-09	4.18E-09	kg· m^2
Product of Inertia at Center of Mass	**Ixy**	**Iyy**	**Izz**	
	-1.64E-11	1.01E-29	-5.92E-29	kg· m^2

4.2.2 Experimental and Analytical Modal Analysis. Using a scanning laser vibrometer and clamping the wing at the root the eigenvalues and eigenvectors of the *Manduca Sexta* forewing were captured and identified for the forewing of the specimen being modeled, Figure 49 [17]. The first eigenvalue associated with the first bend mode occured at 65 Hz. The second eigenvalue associated with the first torsion mode occurred at 110 Hz. Using Abaqus, a modal analysis was performed to refine the FEA model input parameters shown in Table 9 to nearly exactly match previously performed experimental tests [17]. Due to differing boundary conditions from previous tests [62], a ratio of modes of 1.64 was measured during these tests.

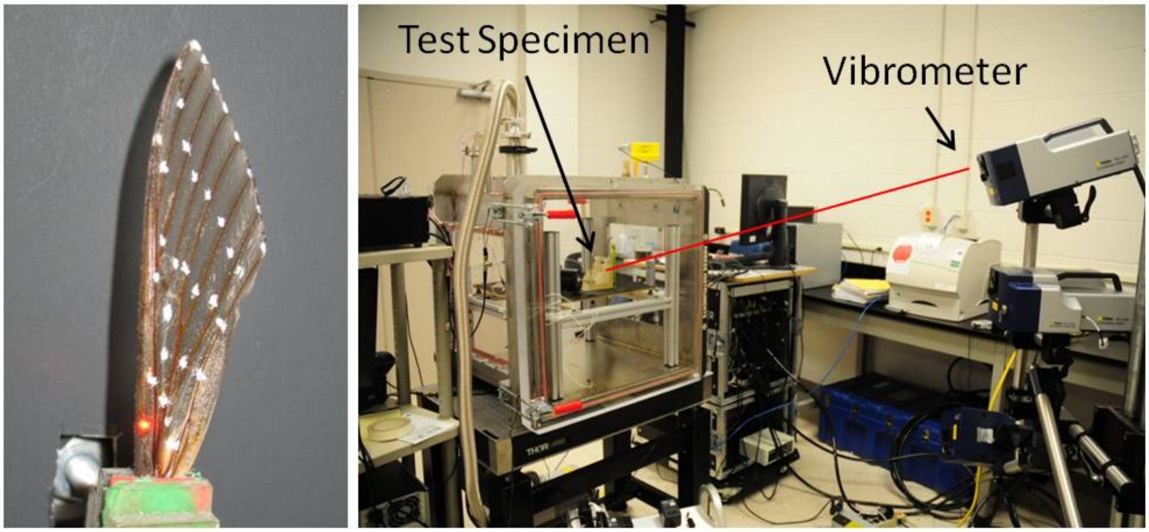

Figure 49: Experimental Modal Analysis of *Manduca Sexta* Forewing

Table 11: Experimental vs FEA Modal Analysis Results

	Biological (Hz)	**FEA**	**% Error**
Mode 1	65	65.2	0.31%
Mode 2	110	110.15	0.14%

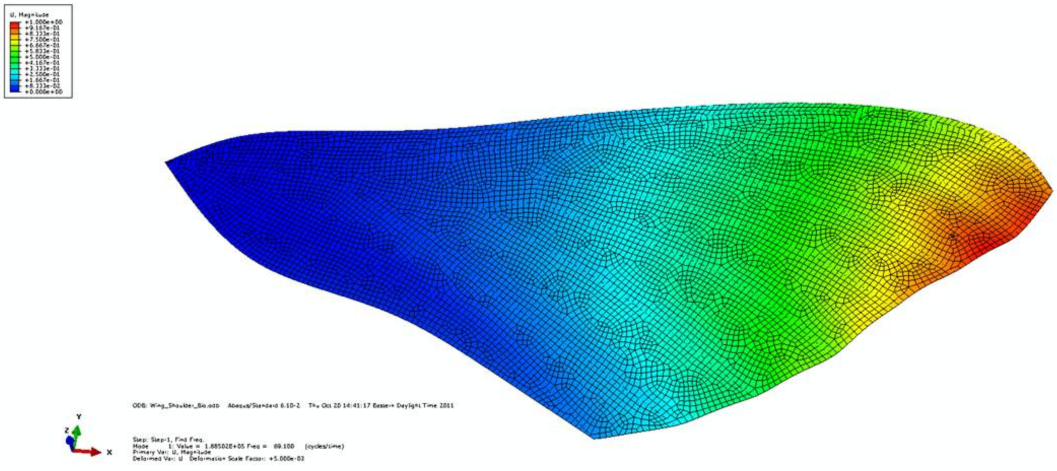

Mode 1 – First Bend – 65.20 Hz

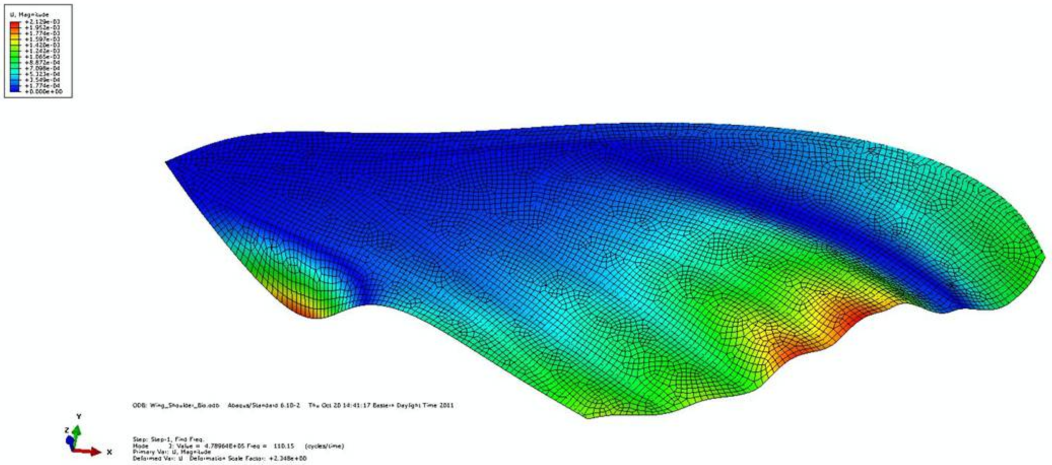

Mode 2 – First Torsion – 110.15 Hz

Figure 50: FEA Modal Analysis of *Manduca Sexta* Forewing

4.3 Summary

With the morphological study presented in Chapter III and applied to the FEA model of the forewing presented here the understanding of the structural dynamics of the biological forewing has been performed in a manner that has not been acheived prior to this data. Therefore, if an understanding of the biological system can be understood and predicted with reasonable confidence, it is fair to say that the ability to use this methodology with engineered materials can be performed to develop an engineered wing model with similar structural dynamics as its biological analog. The ability to develop and refine an engineered wing design independent of experimental testing poses a huge leap forward in capability. This capability allows for the study of candidate engineering materials and the ability to test and identify critical features inherent to this biomimetic wing design that drive the structural dynamics of the system.

V. Engineered Wing Material Selection

This chapter focuses on the considerations associated with the identification of a material that will allow for the analysis, design and fabrication of an engineered wing with similar structural properties and dynamic response as the forewing of the *Manduca Sexta* species. Aspects of all the areas that were investigated are presented, with a focus on implications of the materials ability to meet these requirements. Many factors are considered but the driving factor is the ability to match the structural response of the wing while flapping in air. The identification of a material that has a high stiffness to weight ratio and will allow for ease of manufacturing is identified.

5.1 Engineered Wing Vein Material

It has been shown that the material properties of the veins can be determined through modal analysis if the inertial properties: mass and geometry were known. Through the use of finite element analysis, the material properties could then be solved through the use of cost minimization. A similar approach is used here to determine the proper size and type of material that should be considered for the vein material. In this case, we will be using the combination of the material's elastic modulus (E) and the second moment of area (I) to calculate the flexular stiffness of the material to match the flexular stiffness of the *Manduca Sexta*'s veins, as shown in Equation 6. In doing so, the flexular stiffness of the engineered veins is ultimately determined by the material bending elastic modulus and the width of the veins.

$$E_{bio} I_{bio} = E_{eng} I_{eng} \tag{6}$$

5.1.1 Isotropic Metals. Isotropic metals were considered for their high elastic modulus values: Steel (304 Stainless - 193 Gpa) and Titanium (Ti6Al4V - 113 GPa) [71]. A chemical etching method was initially used to fabricate the 75 μm thick stainless steel specimens using Ferric Chloride (FeCL) at 55 $^{\circ}C$ in an agitated bubble tank. Both simple and more complex designs were modeled and fabricated using a precision UV Laser machining center. Several specimens were constructed to test the ease of fabrication and ability to match finite element analysis predictions for resonance and flapping. Through a simple modal analysis of the wing configured the cantilever boundary commission results show, as expected, that the isotropic properties of the stainless steel veins make for simple FEA models that match closely to experimental values.

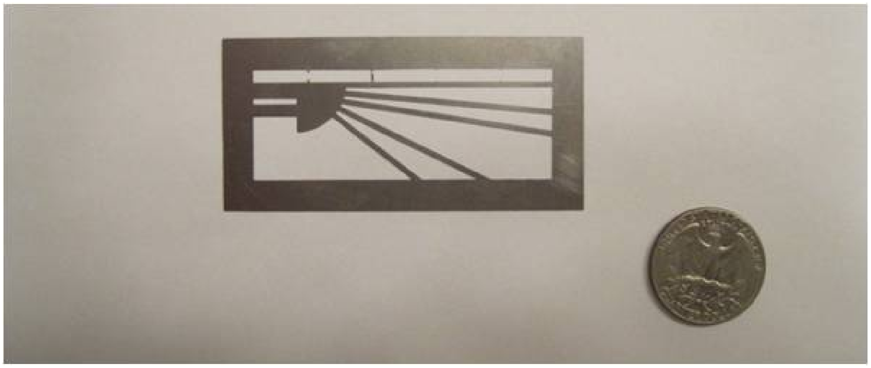

Figure 51: Etched Wing

Due to the isotropic material properties of both the Stainless Steel and Titanium specimens, the flexular stiffness and resonant frequencies of the design were easily predicted. Unfortunately, both materials possessed a low stiffness to density ratio, and in essence were very heavy when compared to their biological equivalents. A freshly liberated *Manduca Sexta* forewing has a mass on the order of 55 mg. These engineered wings, as depicted in Figure 52, were on the order of 150-300 mg respectively. Due to the large mass of these wings extremely large deformations resulted when the wing was flapped under conditions replicating the amplitude and frequency produced by the thorax of the *Manduca Sexta*.

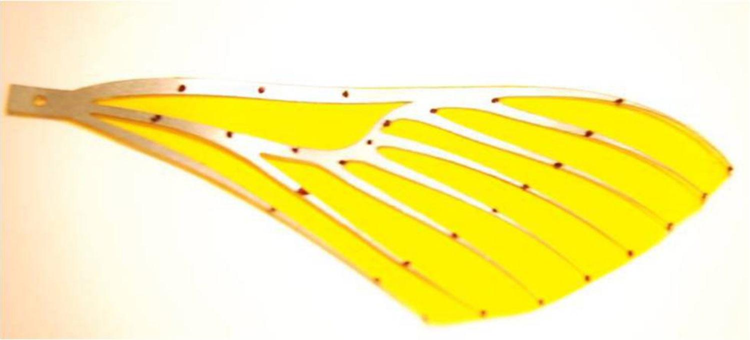

Figure 52: Laser Cut Stainless Steel Wing [17]

These tests emphasized the importance of not only matching the flexural stiffness properties of the biological specimen but also the inertial properties as well [20]. These large displacements are clearly seen Figure 53. For this reason isotropic metals are not well suited for our purposes as a material for use in fabrication of the wing despite their high stiffness values and ability to be easily machined.

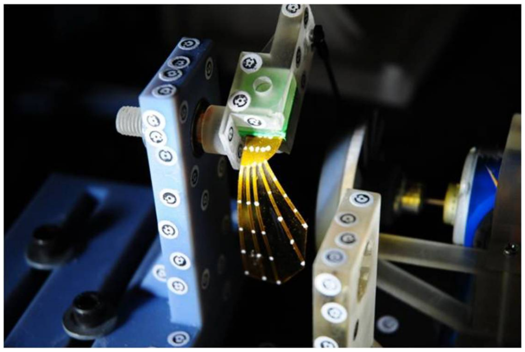

Figure 53: Stainless Steel Wing Flapping Conditions

5.1.2 Shape Memory Alloys. It has been found that the *Manduca Sexta* forewing does indeed have a measurable amount of camber that is inherent to the wings and it is therefore required that the final engineering material be able to incorporate similar features as the biological specimen. It is therefore required that the camber of the wing be imparted through the use of a three dimensional mold constructed in a fashion that accurately represents the intended shape of the final wing design. Mass and stiffness constraints require the use of very thin sheets of metal, additionally the intended camber is very slight and therefore, the metal cannot be plastically deformed into the desired shape. To manufacture the very small features (10-250 μm) a precision laser must be used to fabricate the shapes of the veins in the final material. This laser fabrication method requires that the material be flat at the time the part is manufactured. Therefore the actual camber must be imparted to the material after the veins have been cut. This can be accomplished with a variety of different materials, but for metal alloys the use of Nitinol shows the most promise. Initial investigation of this alloy was performed using NITI Shape Memory Alloy with the following properties: Thickness 75 μm, Width 100 mm, Length 400 mm, flat annealed surface, pickled AF, 45-90C [58].

The use of a Nitinol shape memory or super elastic element for a particular application generally requires the setting of a custom shape in a piece of Nitinol. The process required to set the shape is similar whether beginning with Nitinol in the form of wire, ribbon, strip, sheet, tubing, or bar. Shape setting is accomplished by constraining the Nitinol element on a mandrel or fixture of the desired shape and applying an appropriate heat treatment [58].

For this study, the Nitinol sheet was trimmed to fit the mold and placed in a temperature controlled oven at 400 $^{\circ}C$ for 90 minutes. A thermocouple was added to the cavity of the mold to ensure that the mold and Nitinol sheet reached the desired time and temperature required. The Nitinol sheet and mold were quenched in room temperature water, negligible amounts of steam were produced due to the small thermal mass of the aluminum mold and thin Nitinol sheet. The camber imparted to the sheet had minimal spring back, despite the complex curvature (concave up and concave down). The results of the methodology can be seen in Figure 54. Although, this method was employed on an unmachined Nitinol sheet, it shows that if material was removed through the laser cutting process that the veins could easily be manufactured to have the desired camber.

Figure 54: Machined Aluminum Mold with Sample Nitinol Sheet

Despite the ability of Nitinol to be formed in a manner that would allow for camber to be imparted to a wing, the additional stiffness that this camber would provide is likely not sufficient to overcome the inertial loads of the venation geometry that would be required of this material. Based on the stiffness to weight ratios of this material, it would be susceptible to the same high inertial loads as the isotropic metals of the previous section. Therefore, this material is not a viable material type and was not further pursued.

5.1.3 UV Cured Polymers. Upon initial investigation of the material properties of the veins of *Manduca Sexta*, it was determined that the elastic modulus for the vein and membrane were in the 2.4 to 7.41 GPa range. These material properties are characteristic of polymer related materials. It was immediately concluded that it would be quite feasible to fabricate both wings and membranes using common polymer fabrication methods. In fact, a class of polymer materials that can be rapidly prototyped are available for use here at the Air Force Institute of Technology. These rapid prototyping machines can print both single and dual materials. The latter could presumptively print one material for the veins and one for the membrane. The integration of such a method to the fabrication process greatly relieves the burden associated with the design and assembly of these fine and delicate pieces.

Figure 55: Eden 500V

The first machine utilized was the Eden 500V, Figure 55, from Objet Geometries Ltd. This machine is capable of building objects with dimensions of of up to 500 x 400 x 200mm. Each layer of the build object is fabricated and 16 μm thick layers one at time, this process is very similar to that of stereo lithography, however Objet's proprietary technology dispenses a liquid ultraviolet sensitive resin through an inkjet head and immediately cures the resin through the application of an ultraviolet light source. The machine can maintain accuracies of 42 μm in the X and Y directions and 16 μm in the Z direction. These tolerances are slightly larger than the smallest diameter of a single vein measured in the forewing of the *Manduca Sexta* [63].

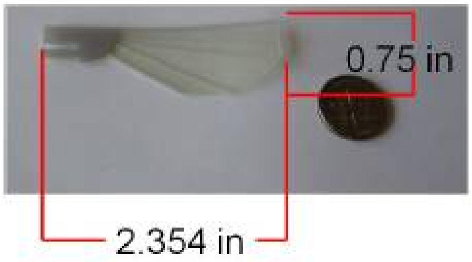

Figure 56: Rapid Prototype Simplified Wing

Several biomimetic designs, similar to Figure 56, were produced using two different material types: FullCure 720 Transparent (Membrane - 2.5 GPa elastic modulus) and the FullCure 840 Vero Blue (Vein - 2.5 GPa Elastic Modulus) [64]. Unfortunately, despite the ability to print different materials, the difference in the elastic modulus of the materials available is very slight, and therefore not conducive to produce a specimen with distinctly different stiffnesses from one feature to another. The only usefulness here would be for the production of materials with different colors.

Experimental testing of initial designs through the use of modal analysis and experimental flapping frequency and amplitudes similar to those of the hawkmoth produce results that were less than stellar. For a number of reasons, the measurement of the velocities of the scan points made to the use of the Polytec Scanning Laser Vibrometer were difficult to make due to the low reflectivity of the polymer surface. Additionally, due to the low stiffness of the material a specimen did not behave in a manner conducive to a strong signal return as the material tended to exhibit nonlinear material properties at the size and thickness used in this specimen. Under flapping conditions, large mass and low stiffness caused extremely high deformations from the tip to the chord of the wing. This induced large nonlinear plastic deformation at the base of the wing and through this low cycle fatigue the wing failed within several cycles. Based on this initial testing, this fabrication method has the potential for future use assuming that material properties and resolution of the features able to be fabricated can be improved. Once again, this material was not further pursued.

5.1.4 Composite High Modulus Thin Ply Laminates. Previous testing has shown that the initial intent to match flexular stiffness should not be the only consideration in terms of matching material properties of the *Manduca Sexta* forewing [12]. The use of metal alloys made it very clear that in addition to flexular stiffness, it is very important to match the inertial properties of the biological specimen. When flexular stiffness and mass are considered it is possible to not only match the geometric, and hence static deformations of the wing, but also the dynamic response of the wing under flapping conditions. To this end, it is therefore necessary to find a material with a high stiffness to weight ratio. When one takes into consideration these factors, one of the first material that comes to mind are those composed of carbon fiber and epoxy resin. In addition, to possessing high stiffness to weight ratios, these materials offer the ability to tailor the fiber orientation and number of plys to best suit the loading conditions being applied.

Previous work done at the Harvard Micro Robotics Research Laboratory pioneered the use of ultra high modulus unidirectional composite lamina plies for the use in their micro air vehicles [107]. This material is composed of a pitch based carbon fiber (XN-50A) embedded in a cyanate ester resin (RS-3C) produced by Tencate. Being a pitch based fiber, the tensile modulus of the fiber used in this laminate is extremely high when compared to other fiber types, Figure 57 [88]. Use of these fibers and resin systems is common in satellite structures that require high stiffness to weight ratio requirements for space-based structures [69]. These listed fibers are additionally well suited for applications of this size due to the extremely fine tow size in relation to the fabricated feature size.

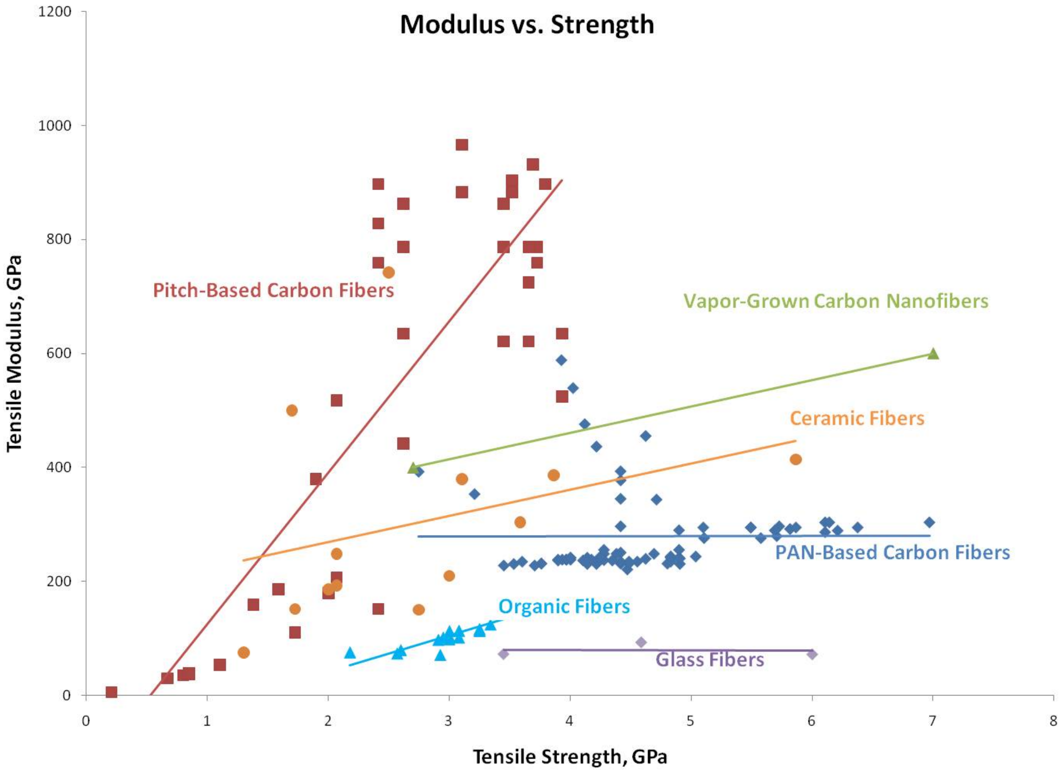

Figure 57: Composite Fiber Types [89]

Initial samples of this material type were obtained from the Harvard researchers and sampled to determine the feasibility for use as compatible engineering material to match flexular stiffness and inertial properties using a design akin to the design used to test the compatibility of the metal alloy [101]. Producing a three layer composite laminate composed of 0-90-0 lamina based upon the YSH-50A fiber type produced, showed a dramatic weight reduction, nearly 100 grams, and produced the first engineering sample that weighed less than that of the actual biological specimen. This promising outcome resulted in the identification of candidate materials that could be used to produce results similar to those found during this initial investigation. Inquiries to a number of manufacturers resulted in the identification that the initial sample type that was made available by the Harvard researchers was no longer available. However, an additional fiber type, YSH-70A is currently available and readily manufactured. The YSH-70A fibers that were used in this testing fall into the class of high modulus fibers. In addition, this fiber type has a higher tensile modulus and is produced with a yield size better suited to the larger scale designs that were produced when compared to the Harvard counterparts. Finally, if lead times and availability are less of a consideration, it would be advantageous to consider the use of the ultra high modulus fibers similar to YSH-95A. A direct comparison between the three fiber types can be found in Table 12.

Table 12: High Modulus Fiber Comparison

Fiber	Tensile Modulus	Tensile Strength	Density	Fiber Dia	Yield
YSH-50A	520 GPa	3.9 GPa	2.10 g/cm3	10 um	30 g/1000 m
YSH-70A	720 GPa	3.6 GPa	2.14 g/cm3	7 um	75 g/1000 m
YSH-95A	900 GPa	3.5 GPa	2.19 g/cm3	7 um	125 g/1000 m

5.1.4.1 Ply Number and Orientation. Due to dynamic forces associated with flapping flight, it is important to have the highest stiffness and lowest mass structure possible. In order to achieve this, it is necessary to determine the fewest number of unidirectional plys required to achieve a composite laminate that can meet these requirements. Through experimental testing and layup, it has been determined that the minimum number of plys required is three, with a fiber orientation of 0-90-0. This number of plys and orientation is required to meet the above specifications for several reasons. Firstly, due to the complex nature of the vein patterns, the vein structures must traverse a path that varies from 0 to 90 degrees. Additionally, the vein structures must support loads both in the axial and transverse directions, and therefore it is required that fibers run both in the axial and longitudinal directions. However, due to the dynamic loads of flapping majority of the loads are in the axial direction, therefore a laminate dominated by lamina in this direction is required. Testing has shown that by adding a single lamina with a 90 degree orientation satisfies these requirements. Additionally, such a specification also allows for the support of torsional loads that are encountered by the geometry of the wing due to aerodynamic and inertial loads.

With the composite laminate fiber orientation and layup predetermined, an extensive amount of testing and analytical study has been conducted to determine the laminate properties that have been specified by initial testing by a number of researchers. The results of this investigation are presented below.

5.1.4.2 Determination of Lamina and Laminate Material Properties - Tensile Testing. The ASTM D 3039 [7] and D 3518 [6] Standards were used to determine the 0° tension modulus (E_1), 90° tension modulus (E_2), and the 45° in-plane shear modulus (G_{12}) of the as manufactured YSH-70A/RS-3C prepreg unidirectional tape. This testing was done in coordination with the Air Force Research Laboratory Materials Directorate [89] and the University of Dayton Research Institute [94]. Twenty plys of the YSH-70A/RS-3C pre-preg lamina were laid up and oriented in a zero degree fiber orientation. These samples were then vacuum bagged and cured in an autoclave at the manufacturers suggested temperature and pressure profiles of 100 psi for two hours at 350 degrees Fahrenheit.

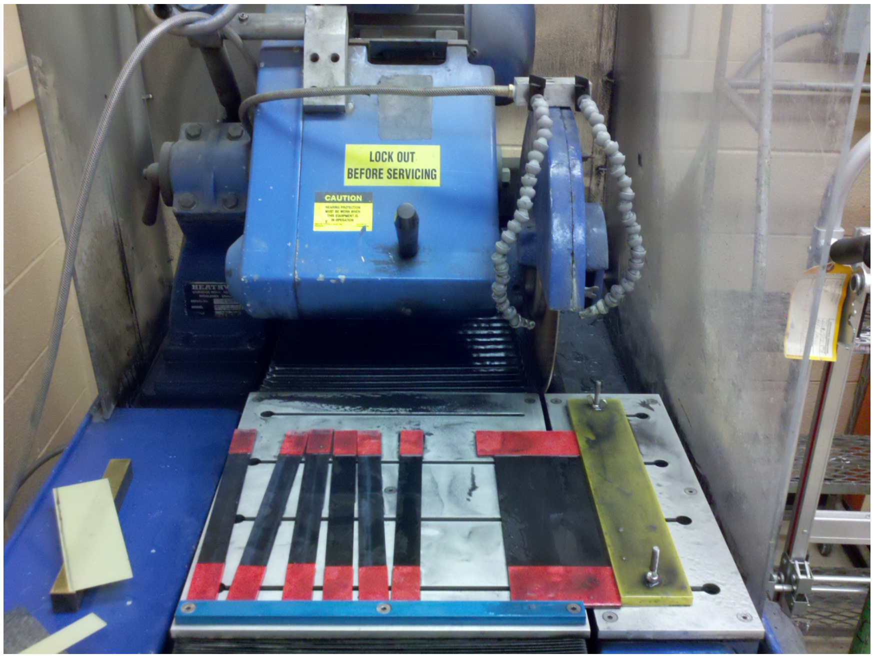

Figure 58: Coupons Being Cut In Diamond Saw

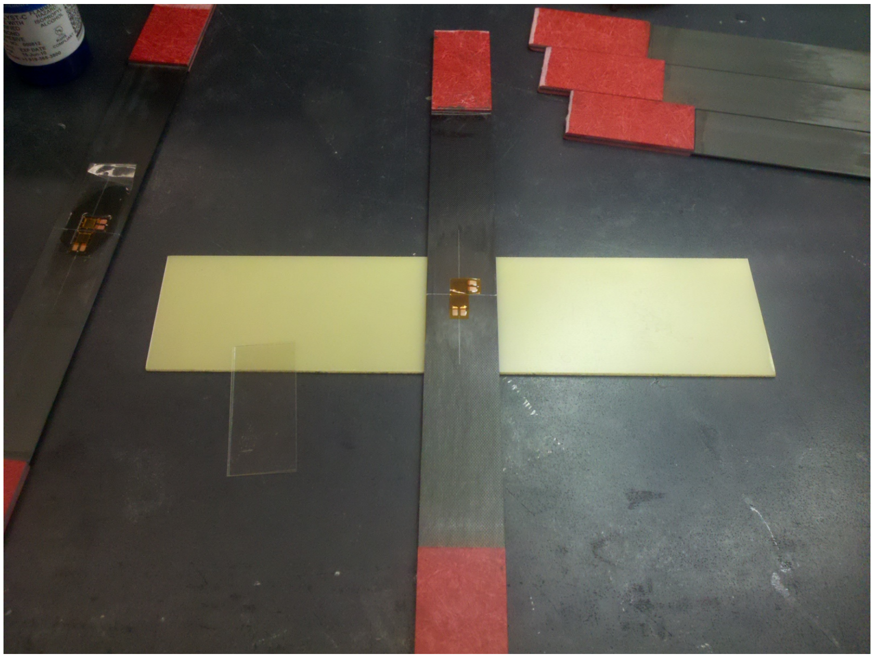

Figure 59: Coupons with Applied Strain Gages

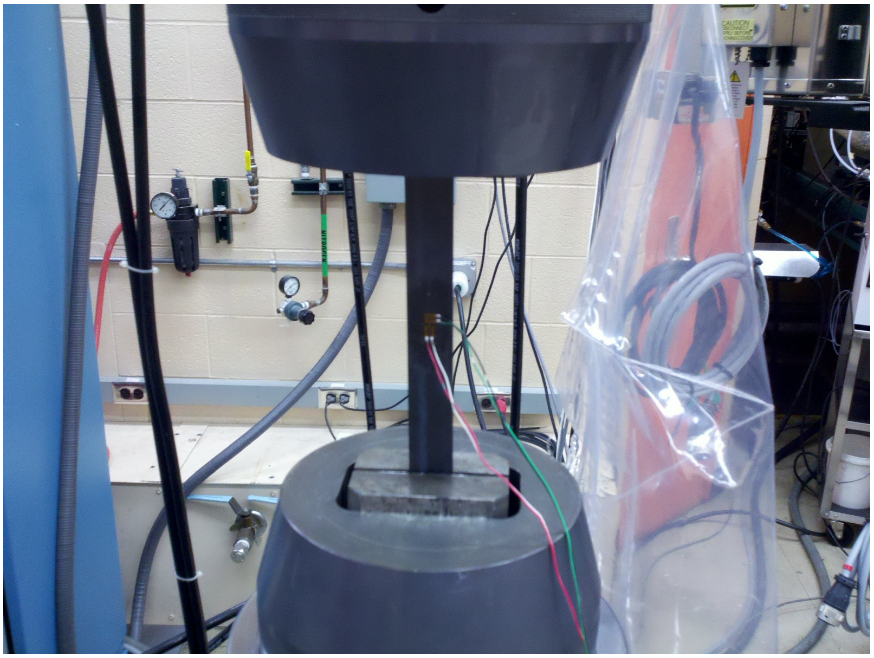

Figure 60: Coupons in 5 KIP MTS Tensile Test Machine

These panels were then processed into 25 mm x 200 mm specimens through the use of precision gages and a diamond saw, Figure 58. After being cut, the samples were tabbed with fiberglass tabs and a two part epoxy resin. After processing the samples had the appropriate strain gages applied, Figure 59, to the surface and prepared for final insertion into uniaxial tensile test machine, Figure 60. The results from this testing were compared to the manufacturer's specifications and are detailed in Table 13.

Table 13: Lamina and Laminate Material Properties

		Tensile 20 Ply	**Tensile 20 Ply**
		Manufacturer	As Tested
Ef	Pa	7.24E+11	6.55E+11
Em	Pa	2.96E+09	2.00E+09
Gf	Pa	1.74E+12	6.57E+09
Gm	Pa	3.32E+09	3.32E+09
vf		3.00E-01	3.00E-01
vm		3.00E-01	3.00E-01
df	kg/m$\hat{3}$	2.14E+03	2.14E+03
dm	kg/m$\hat{3}$	1.19E+03	1.19E+03
Vf		6.39E-01	6.39E-01
Vm	m	3.61E-01	3.61E-01
t	m	4.60E-05	4.60E-05
tf	m	7.00E-06	7.00E-06
h	m	9.20E-04	9.20E-04
E1	Pa	4.60E+11	4.15E+11
E2	Pa	8.15E+09	5.51E+09
v12		3.00E-01	3.00E-01
G12	Pa	9.15E+09	4.85E+09
Exb	Pa	4.60E+11	4.15E+11
Eyb	Pa	8.15E+09	5.51E+09
Gxyb	Pa	9.15E+09	4.85E+09
Ex	Pa	4.60E+11	4.15E+11
Ey	Pa	8.15E+09	5.51E+09
vxy		3.00E-01	3.00E-01
Gxy	Pa	9.15E+09	4.85E+09
Gxz	Pa	9.15E+09	4.85E+09
Gyz	Pa	5.30E+09	3.58E+09

Similar specimens were prepared for a 0/90/0 three ply laminate, that will be used as the base engineering material for future designs. For a number of reasons that will be outlined below, it was deemed necessary to measure the actual material of the properties of a cured 3 ply laminate under actual fabrication conditions and processes to determine the actual material properties of the laminate. This was deemed necessary to ensure that classic laminate theory would still apply despite the very thin nature of the 3 ply laminate (140 μm) as compared to the 20 ply laminates (1000 μm) thickness. Additionally, due to fabrication requirements, accessibility and availability, the 3 ply laminates are to be cured in a heated pressure plate system, located at AFIT, versus the autoclave system, located at the Air Force Research Laboratory Materials Directorate (AFRL/RX), for the 20 ply laminate. Due to the hand layup of the laminate, this testing allowed for the verification of material properties of the completed laminate, based on actual lamina orientations introduced by the variability of this alignment process. Finally, a laser system was employed to cut the 3 ply samples, just as they would be cut for use of an actual wing. In doing so, any laminate fiber alignment issues could also be tested.

From Figures 61-62, it can be seen that both the 20 ply and 3 ply laminates behaved as would be expected from an axial tensile test specimen. From these stress-strain curves it is clear that the elastic modulus of the laminate behaves in a linear fashion all the way to failure. Stress-strain curves were obtained for 0, 45, and 90 degree fiber laminate orientations in order to determine the material properties of each laminate.

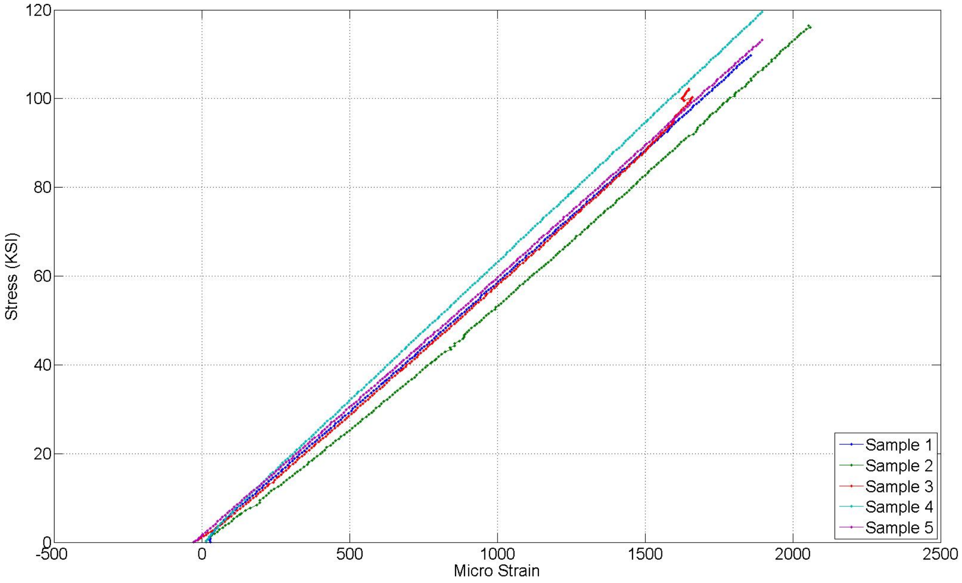

Figure 61: 20 Ply Laminate Stress Strain Curves

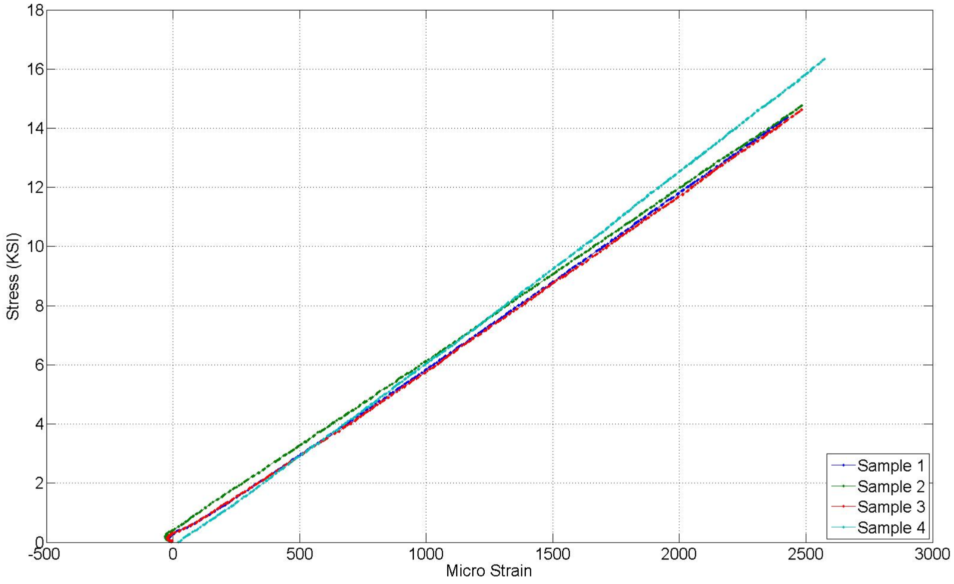

Figure 62: 3 Ply Laminate Stress Strain Curves

The calculations for the lamina and laminate material properties were determined through the use of the Rule of Mixtures, the Halpin-Tsai Equations [29], and Classical Laminate Theory [73] [48] [55].

Where the rule of mixtures defines the lamina properties based on the material properties of the individual fibers and the matrix resin [32]. E_1 is the lamina 0° tension modulus, E_f is the fiber elastic modulus, E_m is the matrix elastic modulus, , E_2 the 90° tension modulus, V_f is the fiber volume, v_f is the Poisson's ratio of the fiber, v_m is the Poisson's ratio of the matrix, G_{12} is the 45° in-plane shear modulus. Figure 63, serves to graphically define the lamina coordinate system (numbered) and the global laminate coordinate system (lettered).

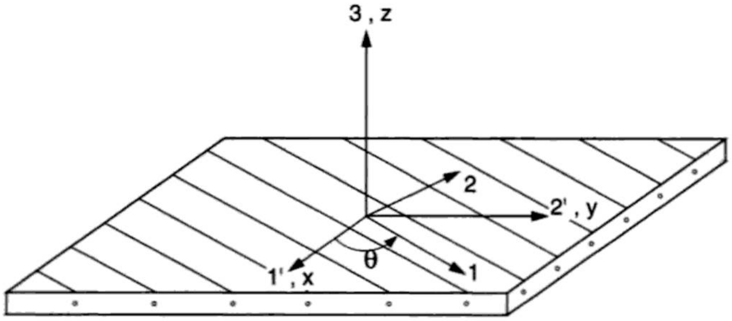

Figure 63: The Principal Directions (1,2,3) of a laminate layer, and The Reference System (1,2,3)=(x,y,z) of The Laminate [9, 59]

$$\begin{aligned}
E_1 &= (E_f - E_m)\, V_f + E_m \\
E_2 &= \frac{E_m}{V_f \left(\frac{E_m}{E_f} - 1 \right) + 1} \\
\nu_{12} &= V_f(\nu_f - \nu_m) + \nu_m \\
\nu_{21} &= \frac{E_2}{E_1} \nu_{12} \\
G_{12} &= \frac{1}{\frac{V_f}{G_f} + \frac{V_m}{G_m}} \\
G_{13} &= G_{12} \\
G_{23} &= \frac{1}{2} E_2 \left(1 + \nu_{12}\right)
\end{aligned} \tag{7}$$

Because the pieces being fabricated are very narrow and cut across individual fibers it is necessary to account for these short fibers through the use of the Halpin-Tsai Equations [29] [96]. Where the engineering constants E_f, E_m, G_f, G_m are directly employed for P_f and P_m in Equation 8.

$$\frac{\overline{P}}{P_m} = \frac{1 + \zeta\eta\phi}{1 - \zeta\eta\phi} \tag{8}$$

Where L is the length of the tape in the 1-direction, t is the thickness of the tape in the 3-direction, w is the width of the tape in the 2-direction (circular fibers w=t).

$$\begin{aligned}
\zeta_{E_{11}} &= 2(l/t) \\
\zeta_{E_{22}} &= 2(w/t) \\
\zeta_{G_{12}} &= 1
\end{aligned} \tag{9}$$

$$\eta = \frac{\frac{E_f}{E_m} - 1}{\frac{E_f}{E_m} + \zeta} \tag{10}$$

With the effective lamina properties determined, Classical Laminate Theory can be applied to determine the multi-layered laminate material properties based on fiber orientations, stacking sequence, and ply level properties.

In principal material coordinates of an orthotropic material, the plane stress constitutive equations can be simplified:

$$\begin{Bmatrix} \sigma_1 \\ \sigma_2 \\ \tau_{12} \end{Bmatrix} = \begin{bmatrix} Q_{11} & Q_{12} & 0 \\ Q_{12} & Q_{22} & 0 \\ 0 & 0 & Q_{66} \end{bmatrix} \begin{Bmatrix} \varepsilon_1 \\ \varepsilon_2 \\ \gamma_{12} \end{Bmatrix} \tag{11}$$

The stiffness matrix, Q_{ij}, can be written in terms of engineering constants:

$$\begin{aligned} Q_{11} &= \frac{E_1}{1-\nu_{12}\nu_{21}} \\ Q_{12} &= \frac{\nu_{12}E_2}{1-\nu_{12}\nu_{21}} \\ Q_{22} &= \frac{E_2}{1-\nu_{12}\nu_{21}} \\ Q_{66} &= G_{12} \end{aligned} \tag{12}$$

By applying the 3-D transformation equations for rotation we can calculate the equivalent stresses and strains:

$$\begin{Bmatrix} \sigma_1 \\ \sigma_2 \\ \tau_{12} \end{Bmatrix} = T \begin{Bmatrix} \sigma_x \\ \sigma_y \\ \tau_{xy} \end{Bmatrix} \tag{13}$$

$$\begin{Bmatrix} \varepsilon_1 \\ \varepsilon_2 \\ \gamma_{12} \end{Bmatrix} = T \begin{Bmatrix} \varepsilon_x \\ \varepsilon_y \\ \gamma_{xy} \end{Bmatrix} \tag{14}$$

The transformation matrix is defined as:

$$T = \begin{bmatrix} m^2 & n^2 & 2mn \\ n^2 & m^2 & -2mn \\ -mn & mn & m^2 - n^2 \end{bmatrix} \tag{15}$$

Where for plane stress problems:

$$\begin{gathered} m = cos(\theta) \\ n = sin(\theta) \end{gathered} \tag{16}$$

The plane stress transformed reduced stiffness matrix:

$$[\overline{Q}] = [T][Q][T]^{'} \tag{17}$$

The axial, coupling, and bending stiffness matrices:

$$\begin{aligned} [A] &= \textstyle\sum_{k=1}^{N} [\overline{Q}]^k (z_k - z_{k-1}) \\ [B] &= \tfrac{1}{2} \textstyle\sum_{k=1}^{N} [\overline{Q}]^k (z_k^2 - z_{k-1}^2) \\ [D] &= \tfrac{1}{3} \textstyle\sum_{k=1}^{N} [\overline{Q}]^k (z_k^3 - z_{k-1}^3) \end{aligned} \tag{18}$$

The constituitive equation can now be reassembled, where it is assumed that there are nonzero B_{ij} terms, and that there is coupling between the axial and bending matrices:

$$\begin{bmatrix} N_x \\ N_y \\ N_{xy} \\ M_x \\ M_y \\ M_{xy} \end{bmatrix} = \begin{bmatrix} A_{11} & A_{12} & A_{16} & B_{11} & B_{12} & B_{16} \\ A_{12} & A_{22} & A_{26} & B_{12} & B_{22} & B_{26} \\ A_{16} & A_{26} & A_{66} & B_{16} & B_{22} & B_{66} \\ B_{11} & B_{12} & B_{16} & D_{11} & D_{12} & D_{16} \\ B_{12} & B_{22} & B_{26} & D_{12} & D_{22} & D_{26} \\ B_{16} & B_{26} & B_{66} & D_{16} & D_{22} & D_{66} \end{bmatrix} \begin{bmatrix} \varepsilon_x^0 \\ \varepsilon_Y^0 \\ \gamma_{xy}^0 \\ \kappa_x \\ \kappa_y \\ \kappa_{xy} \end{bmatrix} \tag{19}$$

The Global Axial Laminate Engineering Constants are related by:

$$\begin{aligned} E_x &= \tfrac{\sigma_x}{\varepsilon_x^0} = \tfrac{N_x \cdot \frac{1}{h}}{\varepsilon_x^0} \\ E_y &= \tfrac{\sigma_y}{\varepsilon_y^0} = \tfrac{N_y \cdot \frac{1}{h}}{\varepsilon_y^0} \\ G_{xy} &= \tfrac{\tau_{xy}}{\gamma_{xy}^0} = \tfrac{N_{xy} \cdot \frac{1}{h}}{\gamma_{xy}^0} \\ \nu_{xy} &= -\tfrac{\varepsilon_y^0}{\varepsilon_x^0} \\ \nu_{yx} &= -\tfrac{\varepsilon_x^0}{\varepsilon_y^0} \end{aligned} \tag{20}$$

The Global Bending Laminate Engineering Constants are related by:

$$\begin{aligned} \tfrac{M_x}{E_{xb} I} &= \tfrac{\partial^2 w}{\partial x^2} = \kappa_x \\ \tfrac{M_y}{E_{yb} I} &= \tfrac{\partial^2 w}{\partial y^2} = \kappa_y \\ \tfrac{M_{xy}}{G_{xyb} I} &= 2\tfrac{\partial^2 w}{\partial xy} = \kappa_{xy} \end{aligned} \tag{21}$$

To find E_x, only the x-direction in-plane load is applied and the relation between N_x and ε_x^0 is sought. The constituitive equation now becomes [59]:

$$\begin{bmatrix} N_x \\ 0 \\ 0 \\ 0 \\ 0 \\ 0 \end{bmatrix} = \begin{bmatrix} A_{11} & A_{12} & A_{16} & B_{11} & B_{12} & B_{16} \\ A_{12} & A_{22} & A_{26} & B_{12} & B_{22} & B_{26} \\ A_{16} & A_{26} & A_{66} & B_{16} & B_{22} & B_{66} \\ B_{11} & B_{12} & B_{16} & D_{11} & D_{12} & D_{16} \\ B_{12} & B_{22} & B_{26} & D_{12} & D_{22} & D_{26} \\ B_{16} & B_{26} & B_{66} & D_{16} & D_{22} & D_{66} \end{bmatrix} \begin{bmatrix} \varepsilon_x^0 \\ \varepsilon_Y^0 \\ \gamma_{xy}^0 \\ \kappa_x \\ \kappa_y \\ \kappa_{xy} \end{bmatrix} \tag{22}$$

Using Cramer's Rule to solve for ε_x^0 [59]:

$$\varepsilon_x^0 = \frac{\begin{vmatrix} N_x & A_{12} & A_{16} & B_{11} & B_{12} & B_{16} \\ 0 & A_{22} & A_{26} & B_{12} & B_{22} & B_{26} \\ 0 & A_{26} & A_{66} & B_{16} & B_{22} & B_{66} \\ 0 & B_{12} & B_{16} & D_{11} & D_{12} & D_{16} \\ 0 & B_{22} & B_{26} & D_{12} & D_{22} & D_{26} \\ 0 & B_{26} & B_{66} & D_{16} & D_{22} & D_{66} \end{vmatrix}}{\begin{vmatrix} A_{11} & A_{12} & A_{16} & B_{11} & B_{12} & B_{16} \\ A_{12} & A_{22} & A_{26} & B_{12} & B_{22} & B_{26} \\ A_{16} & A_{26} & A_{66} & B_{16} & B_{22} & B_{66} \\ B_{11} & B_{12} & B_{16} & D_{11} & D_{12} & D_{16} \\ B_{12} & B_{22} & B_{26} & D_{12} & D_{22} & D_{26} \\ B_{16} & B_{26} & B_{66} & D_{16} & D_{22} & D_{66} \end{vmatrix}} \tag{23}$$

Through the use of cofactor expansion, the numerator can be simplified [59]:

$$\varepsilon_x^0 = \frac{N_x \begin{vmatrix} A_{12} & A_{16} & B_{11} & B_{12} & B_{16} \\ A_{22} & A_{26} & B_{12} & B_{22} & B_{26} \\ A_{26} & A_{66} & B_{16} & B_{22} & B_{66} \\ B_{12} & B_{16} & D_{11} & D_{12} & D_{16} \\ B_{22} & B_{26} & D_{12} & D_{22} & D_{26} \\ B_{26} & B_{66} & D_{16} & D_{22} & D_{66} \end{vmatrix}}{\begin{vmatrix} A_{11} & A_{12} & A_{16} & B_{11} & B_{12} & B_{16} \\ A_{12} & A_{22} & A_{26} & B_{12} & B_{22} & B_{26} \\ A_{16} & A_{26} & A_{66} & B_{16} & B_{22} & B_{66} \\ B_{11} & B_{12} & B_{16} & D_{11} & D_{12} & D_{16} \\ B_{12} & B_{22} & B_{26} & D_{12} & D_{22} & D_{26} \\ B_{16} & B_{26} & B_{66} & D_{16} & D_{22} & D_{66} \end{vmatrix}} \tag{24}$$

Using Equation 20a, E_x can be found by evaluating [59]:

$$\frac{N_x \cdot \frac{1}{h}}{\varepsilon_x^0} = E_x = \frac{\begin{vmatrix} A_{11} & A_{12} & A_{16} & B_{11} & B_{12} & B_{16} \\ A_{12} & A_{22} & A_{26} & B_{12} & B_{22} & B_{26} \\ A_{16} & A_{26} & A_{66} & B_{16} & B_{22} & B_{66} \\ B_{11} & B_{12} & B_{16} & D_{11} & D_{12} & D_{16} \\ B_{12} & B_{22} & B_{26} & D_{12} & D_{22} & D_{26} \\ B_{16} & B_{26} & B_{66} & D_{16} & D_{22} & D_{66} \end{vmatrix}}{\begin{vmatrix} A_{12} & A_{16} & B_{11} & B_{12} & B_{16} \\ A_{22} & A_{26} & B_{12} & B_{22} & B_{26} \\ A_{26} & A_{66} & B_{16} & B_{22} & B_{66} \\ B_{12} & B_{16} & D_{11} & D_{12} & D_{16} \\ B_{22} & B_{26} & D_{12} & D_{22} & D_{26} \\ B_{26} & B_{66} & D_{16} & D_{22} & D_{66} \end{vmatrix}} * \frac{1}{h} \tag{25}$$

The remaining five global laminate engineering constants can be solved in a similar manner, to that as shown for E_x, using Equations 18-25 [59].

5.1.4.3 Fiber Volume. The volume of fiber in a composite material laminate can be determined by digestion of the composite matrix through acid digestion. Whereby the composite matrix is dissolved and the fibers weighed and subtracted from the total composite laminate weight as seen in Figure 64. This chemical digestion process is guided by ASTM D3171 - 09 Standard Test Methods for Constituent Content of Composite Materials [8]. Tests were performed in accordance with this guidance for representative samples of both 20 ply unidirectional YSH-70 prepreg and for 3 ply 0-90-0 laminate. Results of this testing are presented in Table 14. These results show that fiber volume, resin volume, and void percentages are consistent between the different ply layups. This is especially important considering that each ply was cured under the same temperature and pressure profile, where the twenty ply laminate was cured in an autoclave under both vacuum and pressure and the three ply specimen was cured in a heated plate press.

Table 14: Fiber Volume Measurements

Number of Plys	20	3
% Fiber Volume	62.74	62.27
% Resin Volume	36.56	35.9
% Void	0.695	1.17

Figure 64: Recovered Composite Fibers

5.1.4.4 Determination of Lamina and Laminate Material Properties - Modal Analysis. Determination of material properties through tensile testing poses significant constraints on time and resources. This is due to the lengthy material processing requirements and availability of test equipment, not to mention the destructive nature of tensile testing. Further, the processed tensile specimens were significantly larger in both length (3X) and width (10X) then the features associated with the engineered vein structures. Therefore, a non-contact, non-destructive, and rapidly implementable testing method that could be performed on specimens of the same scale as the designed structures was sought. The method chosen was to very similar to the method applied to the determination of the material properties of the leading edge vein of the *Manduca Sexta* forewing.

Figure 65: 40 mm x 2.5 mm beam with airhorn excitation

The experimental setup is very simple and involves the simple clamping of a 40 mm x 2.5 mm beam in a fixture. Excitation is provided via an air horn that is placed in very close proximity to the tip of the beam as shown in Figure 65. Through the use of a laser vibrometer, the resonant frequencies and mass of each of the beams was identified and are presented in Table 15. These results were compared to analytical results that were computed using the lamina properties that were found during the 20 ply tensile testing. With an average value of 144 Hz this is significantly different than the 170 Hz value that was predicted from the analytical solution.

Table 15: Frequency and Mass Experimental Results

	Mode 1	**Mass**
Sample	Freq (Hz)	Grams
1	150.00	22.80
2	140.60	23.50
3	140.20	22.80
4	135.20	22.70
5	148.40	23.40
6	146.10	23.00
7	150.80	23.00
8	151.60	23.70
9	137.50	2.20
10	148.50	24.00
AVG	**144.89**	**21.11**
STD	**5.98**	**6.66**
MAX	**151.60**	**24.00**
MIN	**135.20**	**2.20**

After a considerable period of investigation, it was determined that due to the hand layup of the individual plys and coarse alignment of the laminate to the cutting axis of the laser when the samples were cut, that a significant amount of uncertainty was introduced by the manufacturing process. This is compounded with the fact that as the number of plys decreases the subsequent laminate properties become increasingly sensitive to the smallest of alignment errors. To confirm these findings, a monte carlo solution was conducted, to determine how much variation in ply angle (theta) and laser cut angle (alpha) would account for the differences seen in the experimental and analytical results. Gaussian distributions were used to vary alpha (Mean = 2.5° & 1 Std), theta (Mean = 2.5° & 1 Std), and thickness (Mean =145 um & 1 Std) over a one-hundred-thousand sample set. These populations were based on experimental measurements of the cut angles by the laser manufacturing process, the ply angles, and the thickness of the laminate. Using this probabilistic approach, it is possible to quantify the variation seen in the resonant frequency of the laminate samples. Figure 66, depicts the results of this analysis, where the mean resonant frequency is 144 Hz, as shown in Figure 66, and the laminate axial elastic modulus, E_x, as shown in Figure 67, equals 195 GPa. These results indicate that close attention should be paid during the layup and cutting portions of the manufacturing process for any designs that are to be produced from the subsequent laminate [83].

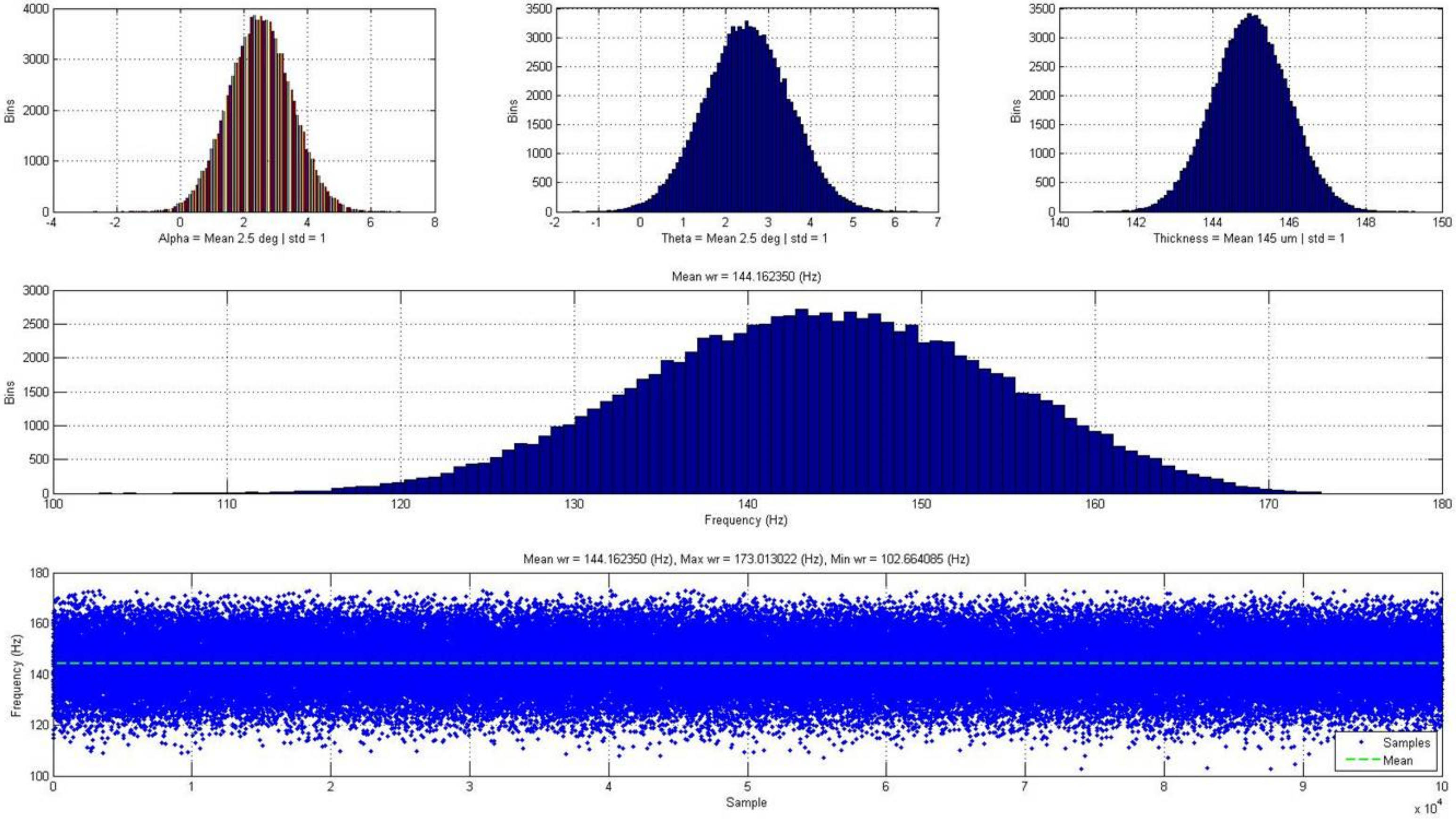

Figure 66: Eigenvalue Sensitivity Analysis on Cut Angle, Ply Angle, and Thickness

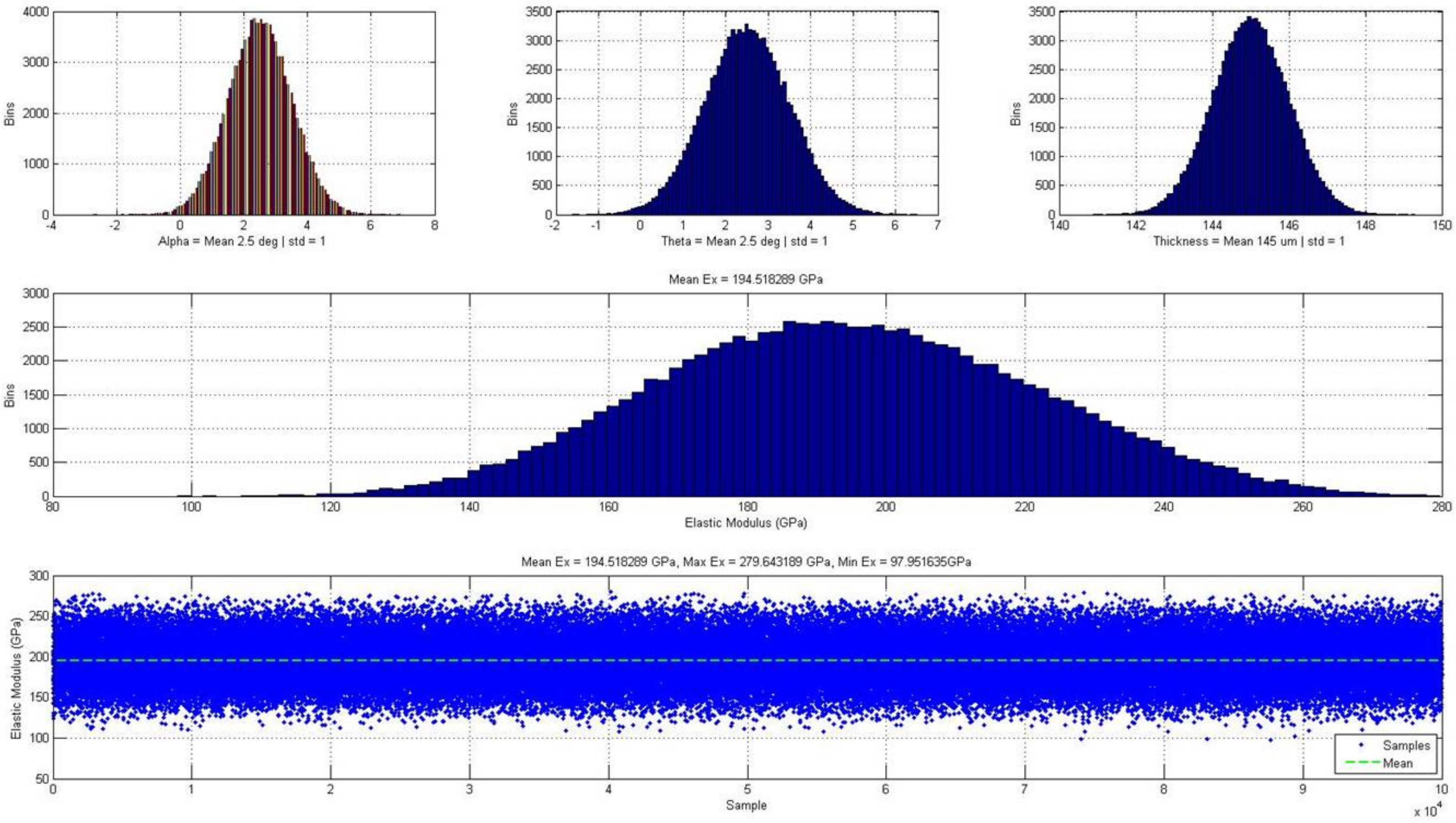

Figure 67: Elastic Modulus Sensitivity Analysis on Cut Angle, Ply Angle, and Thickness

5.2 Engineered Wing Membrane Material Identification

An extensive amount of testing has been conducted to determine the lightest weight polymers avaiable that can properly mimic the structural and aerodynamic response of the biological membrane of the *Manduca Sexta* forewing. Due to previous testing the membrane material properties and thickness are known and can be effectively represented by polymer films. The practical use of a number of films is studied and presented.

5.2.1 Kapton. Polyimide films such as DuPont's Kapton HN general-purpose film has been used successfully in applications at temperatures as low as -269 °C (-452 °F) and as high as 400 °C (752 °F). HN film can be laminated, metallized, punched, formed or adhesive coated. Kapton HN is the recommended choice for applications that require an all-polyimide film with an excellent balance of properties over a wide range of temperatures [21]. Kapton's high temperature capabilities allow for easy fabrication through the use of a laser for micro-machining purposes. Kapton HN is available in thicknesses of 12.5, 25, and 75 μm. To be used as a wing membrane a liquid based (cyanoacrylate) or dry sheet adhesive (Pyrallux) must be used to adhere the vein material to the membrane material. Based on the use of a 50 mm sized engineered wing, the required Kapton film will have a weight of approximately 22.5 milligrams. This mass is quite considerable when compared to the fact that engineered veins weigh approximately 30 milligrams. This large mass is further evidenced when sample test wings were used in a rotary flapper and high inertial loads were found.

5.2.2 Mylar. Mylar is polyester film made from stretched polyethylene terephthalate (PET) and is used for its high tensile strength, chemical and dimensional stability, transparency, reflectivity, gas and aroma barrier properties and electrical insulation [24]. Mylar is available in a variety of thicknesses and can be found as thin as 2.5 μm. It has an elastic modulus of 3.7 GPa and is within the 2.41 ± 1.37 GPa range of the biological membrane venation measurements of Chapter III. Based on the use of a 50 mm sized engineered wing, the required Mylar film will have a weight of approximately 4.5 milligrams. When compared to Kapton equivalent this is a weight savings of 18.5 milligrams. Additionally, Mylar is more sensitive to heat and can therefore be molded in a press and impregnated into a carbon fiber vein structure without any additional adhesives.

5.3 Summary

Based upon the information presented here YSH-70 unidirectional pre-preg laminate tape will be used for the base material to represent the venation of the engineered wing. This laminate will be used in a three layer configuration, where the top and bottom layer will be in parallel and oriented in the zero degree horizonal direction. The inner/mid-plane ply will be allowed to vary in direction from 20-90° from horizontal. Mylar will be used for the venation material based upon its weight savings potential and material property characteristics.

VI. Engineered Wing Design and Fabrication

Using the biological forewing model of Chapter IV as a baseline, the generation of a engineered wing model has been realized. The work presented here focuses on how the engineered finite element material properties and structures that have been updated to reflect the use of the selected engineered material of Chapter V. Several parametric input parameters that are incorporated into this engineering model have been evaluated to determine their effect on the structural response of the model. Using this knowledge a candidate engineered wing design will be identified and manufactured.

6.1 Wing Model Geometry

The basis for the engineered wing model development builds off the previous biological wing FEA model. In this manner an exact replication of the biological venation geometry is used to simplify the process of matching the structural dynamics of the engineered wing as compared to its biological analog. This greatly simplifies the engineered wing model generation as the locations of the nodes, elements, and their associated connectivity do not need to change. Due to the change from Chitin, an isotropic biological material, to YSH-70, an anisotropic composite laminate, it is required to update the engineered finite element section profiles from a tubular structure, to a composite laminate, and finally to an I-beam structure as depicted in Figure 68.

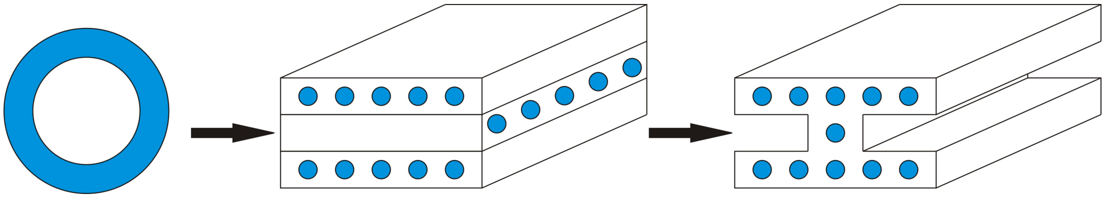

Figure 68: FEA Section Transformation

As shown in Figure 69, the venation of the baseline wing model has significant curvature relatively to the global composite laminate axis. The grid pattern of Figure 69 is used to visualize the orientation of the unidirectional fibers of a 0/90/0 laminate.

If we divide the venation up into small elements, as required by FEA, we can see that the local axis of the elements varies from root to tip.

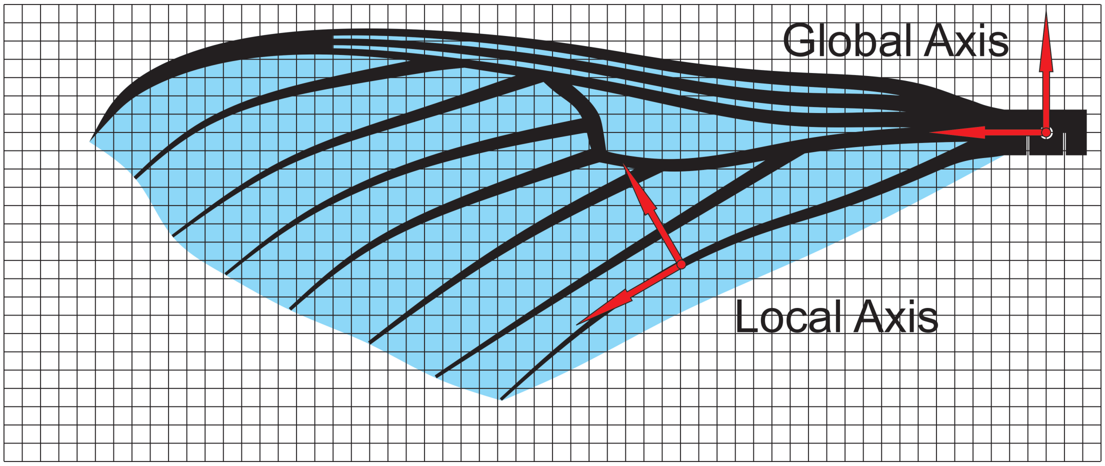

Figure 69: Baseline Engineered Wing Design

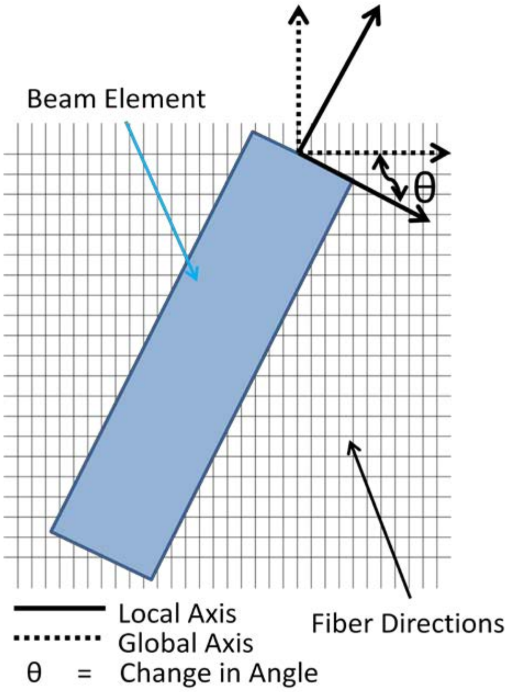

Figure 70: Global Laminate Axis vs. Local Venation Axis [90]

Figure 70 is used to illustrate this variation on an elemental level. Since the material properties of the laminate vary with respect to the ply angles and the local axis of the element a methodology to account for these varying material properties must be implemented. This is done by calculating the angle of the element local axis relative to the global axis. Once the angle for each element has been evaluated, the element material properties can be determined. These calculations are performed in Matlab using Equations 7 - 10. With the local material properties calculated, the material properties from the ply with the highest axial modulus are chosen to represent the entire element. A method to create a cross-section of an equivalent homogeneous beam is then employed to satisfy the requirements of the B32 element definition. It is now required to manipulate the element section properties and density such that an effective moment of inertia can be calculated in order to keep the anisotropic definition of the composite laminate intact. This changes the B32 elements profile from a rectangular shape to a shape similar to an I-beam through a rule of mixtures approach. This process has been previously detailed [90] but is provided here for completeness.

6.1.1 Axial Modulus Ratio. A ratio of the axial moduli of the other two plies to the maximum modulus determines the reduction of area needed by those plies to retain the physical characteristics of the beam. Where $E_{x,ply}$ is the elastic modulus of the lamina in the local x direction. $E_{x,max}$ is the maximum elastic modulus of the lamina in the local x direction for the laminate. N_x is the axial modulus ratio of the x^{th} ply [90].

$$N_x = \frac{E_{x,ply}}{E_{x,max}} \tag{26}$$

6.1.2 Effective Beam Width. The axial modulus ratio is used to change the area of the ply so that when the singular material property is applied, the beam section maintains the same axial modulus. In order to keep the effective moment of inertia the same for the element, the distance of the ply from the neutral axis needs to be kept constant, therefore when changing the area of the height and location of the ply was held constant and only the width was modified. The effective width of each of the two other plies was simply the width of the beam section multiplied by their individual axial modulus ratios as shown in Equation 27. Where $W_{new,ply}$ is the new effective width for the lamina in the models cross section, and W_{orig} is the original cross section width of the lamina in the model [90].

$$W_{new} = N_x * W_{orig} \tag{27}$$

6.1.3 Effective Density. While the stiffness of the element represents the physical characteristics of the carbon fiber, the mass of the element is changed due to the change in area if the density is kept the same. In order to account for this, the density of the material for the element is changed so that the mass of the element is the same as it was prior to the change in area taking place. This is a simple calculation based on the ratios of the cross sectional area of the new beam section compared to the physical cross sectional area of the wing at that point, Equation 28, where ρ_{new} is the new density for the element, ρ_{orig} is the original density of the composite, A_{orig} is the average physical cross section of the manufactured wing at the same location as the element, and A_{new} is the new cross section of the beam element after the effective moment of inertia calculations have been performed [90].

$$\rho_{new} = \rho_{orig} * \frac{A_{orig}}{A_{new}} \tag{28}$$

6.2 Design of Experiments

6.2.1 Design Factors. Inherently critical to the FEA engineered wing model was the requirement to be able to perform a design of experiments (DOE) analysis on the engineered wing design. From Table 16, the critical input parameters that were implemented in the engineered wing FEA model for evaluation are presented. Using the same methodology of the biological FEA model, Matlab is used to make these features variable and thus easily changed through a series of simple variable declarations. This foresight allowed for a new FEA model to be regenerated in a matter of less than 10 seconds. This is a significant improvement when compared to the twenty plus hours required by previous efforts [80]. Using Matlab to invoke the Abaqus command line solver, these models were solved to determine the modal analysis response of the first 10 modes of the wing structure, analyze the effects of 1 milligram point load at the leading edge tip node, and a 1 milligram point load at the trailing edge tip node in a matter of approximately 70 seconds. Matlab routines were also implemented to subsequently post process and store the results of the analysis automatically after each run. This solution time is based upon using a Dell Precision T7500 workstation equipped with 3.6 GHz dual quad core processors and 24 gigabytes of RAM with two 1 terabyte hard drives.

Table 16: Critical Input Parameters

1	Costal Vein Widths
2	Radial Vein Widths
3	Arculus Vein Widths
4	Sub-Radial, Medial, Cubital, and Anal Vein Widths (RMCA) Camber
5	Laminate Orientation
6	Camber
7	Laser Cut Angle (Alpha)

6.2.2 Factor Levels. Based on the ability to quickly change and solve the engineered wing FEA model, a design of experiments approach was implemented to analyze the effects of the first five of the seven critical input parameters listed in Table 16. The remaining critical input parameters will be analyzed in the following sections. A 5 factor, 4 level, full factorial design, consisting of 1024 individual numerical experiments, was implemented to analyze the main interactions and paired interactions of all of the 5 of the critical input parameters. In this manner, each factor is tested at each level in every possible combination with the other factors and their levels. Total solve time for this DOE analysis design was approximately 22 hours. The details of the factors and the respective levels at which they were analyzed are presented in Table 17.

Table 17: DOE Input

	Factor	**Baseline Root Width (um)**	**Baseline Tip Width (um)**	**Level 1**	**Level 2**	**Level 3**	**Level 4**
1	Costal Vein Widths	2500	333	50%	75%	100%	125%
2	Radial Vein Widths	1666	1666	50%	75%	100%	125%
3	Arculus Vein Widths	1666	1666	50%	75%	100%	125%
4	RMCA Vein Widths	1666	333	50%	75%	100%	125%
5	Inner Laminate Orientation	**Degrees**	-	20	30	45	90

Each of the factor levels were chosen in a manner to produce significant result outputs while representing geometry that was also being capable of being manufactured. These outpus are listed in Table 18. The first 4 factor levels were varied as a percentage of the appropriate baseline width of the indicated venation at the root and tip of the wing. This venation is represented as linear taper as shown in Figure 71. The fifth factor only varies the inner laminate of the YSH-70. The two outer plys were kept constant at a zero degree orientation (horizontal) while the inner ply was varied.

Table 18: Full Factorial Outputs

	Output	**Units**
1	Mass	mg
2	Omega 1 - First Bend	Hz
3	Omega 2 - First Torsion	Hz
4	Ratio of Omega 2/Omega1	-
5	Moment of Inertia Ixx	$kg \cdot m^2$
6	Moment of Inertia Iyy	$kg \cdot m^2$
7	Spanwise Bending from LE Point Load	m
8	Chordwise Bending from TE Point Load	m

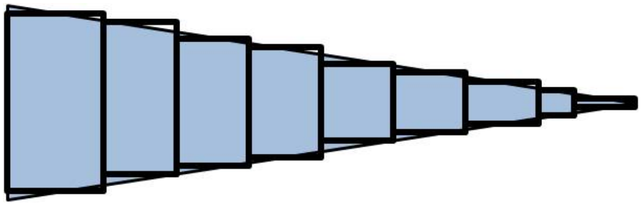

Figure 71: Linearly Taperered Beam Elements [90]

6.2.3 Results. Using JMP, a statistical software package, quantification and visualization of the the results of our full factorial design is made possible. Specifically, JMP makes it much easier to quantify the effects of multiple inputs with multiple outputs (MIMO). Two processes are used to view this MIMO output. Firstly, JMP's prediction profiler will use a graphics based approach to view the outputs. Secondly, JMP's sorted parameter estimate output will also use a graphical approach in conjunction with several common statistical measures for quantification of the MIMO output.

6.2.3.1 Prediction Profiler. The results from this full factorial evaluation can be represented in a number of ways. The first of these is presented in Figure 72. The 5 columns of data represent the input parameters of Table 17. While the 8 rows of data represent the output parameters of Table 18. This 8x5 matrix of data allows for the global assessment of all the parameter inputs and their respective outputs. This makes the visualization of the 1024 different combinations and the representative trends that these inputs provide much easier to comprehend.

6.2.3.2 Sorted Parameter Estimates. The Sorted Parameter Estimates (SPE) of Figure 73 have been included to depict the three primary outputs of the DOE that we are interested in. While the prediction profiler of Figure 72 provides a good visual indication of the DOE results, the SPEs present a statistical quantification of the input parameters significance on the presented output factor. The SPEs provide not only primary input significance, but also present secondary interactions and their subsequent significance.

The t-Ratio is defined in Equation 29 and is used in testing the null hypothesis that the population mean is equal to a specified value μ_0. Where $\bar{x}$ is the sample mean, s is the sample standard deviation of the sample, and n is the sample size [70]. The slope of the output lines in Figure 72 and the pink bar graphs in Figure 29 can be directly related to the magnitude of the t-ratio. Three factors effect the magnitude of the t-ratio. Firstly, the difference of the sample and population means; the larger the difference the greater the magnitude. Secondly, $\hat{s}$, the unbiased estimate of the standard deviation, μ, of the population; power increase as $\hat{s}$ decreases. Finally, n, the number of subjects in the sample; larger sample sizes, if all else is equal, produce t-ratios of greater power [70]. The p-value is the probability of obtaining a test statistic less than the one that was actually observed. We will reject the null hypothesis when the p-value is less than the significance level,α, which is .05 in our DOE study.

$$t = \frac{\bar{x} - \mu_0}{\frac{\hat{s}}{\sqrt{n}}} \tag{29}$$

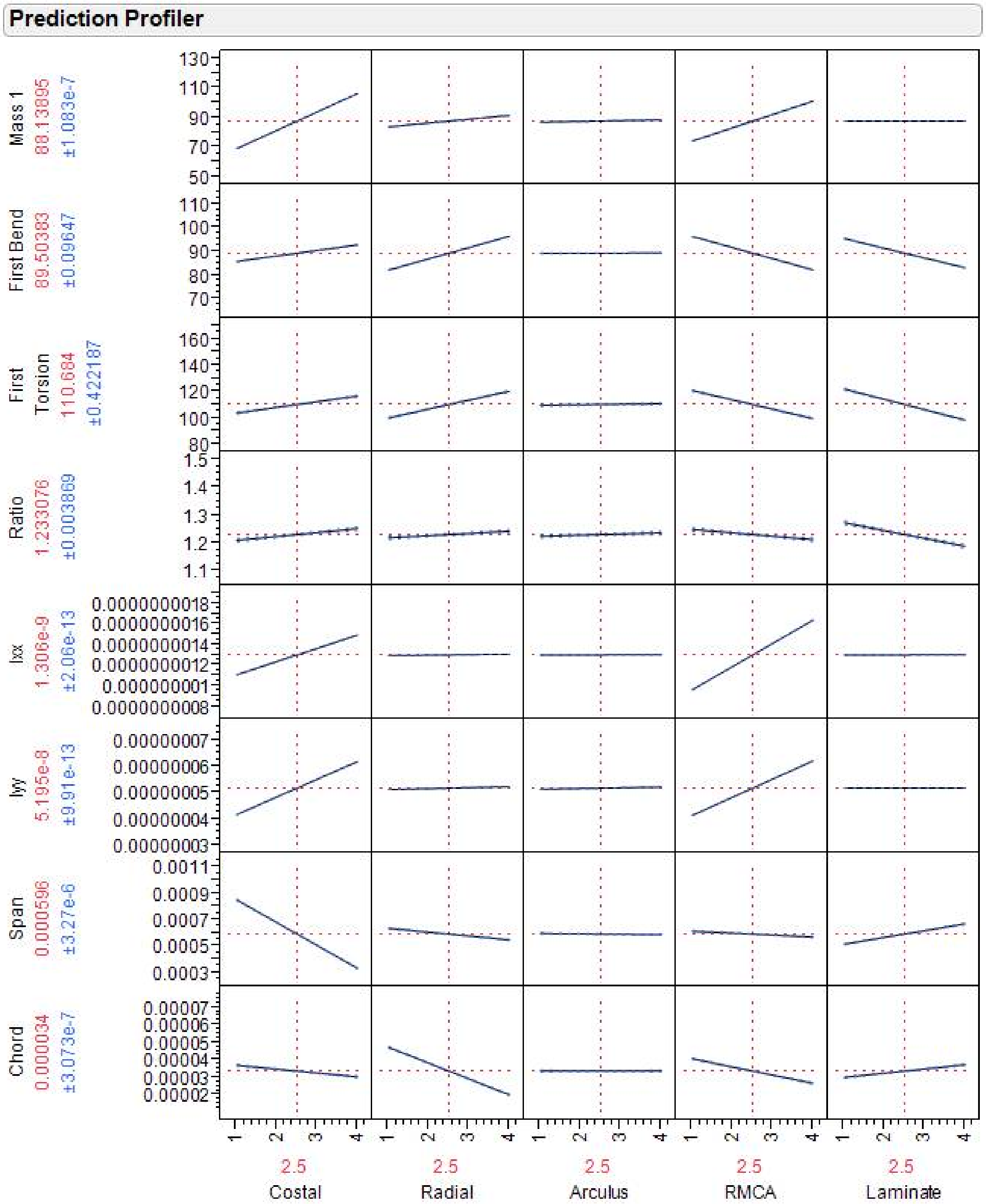

Figure 72: Input Factors vs Output Results

6.2.3.3 Arculus Factor. Prior to this investigation it was believed that the arculus vein was the primary driver that linked the dynamic span wise bending of the wing with the chord wise bending of the wing. Based on the data presented here, the size of the arculus vein width represents a near zero slope for all the ouput parameters. From Figure 72, the arculus factor levels have almost no effect on either frequency of the first bend natural frequency, the first torsion natural frequency, and the ratio of these two modes. The only effect that is seen is a small increase in mass from the Level 1 to the Level 4 factors that were tested. These observations are further confirmed in Figure 73, where the t-Ratio values for the arculus outputs are very small. Due to the neutral response/impact of the arculus venation it would be wise to make the arculus vein widths as small as possible to limit the mass impact of this factor.

6.2.3.4 Mass Output. In terms of of the mass output, from Figure 72, the costal and RMCA factors have large positive slope values. While the radial and arculus values have small positive slopes. The t-Ratios confirm that these four factors are statistically significant, however the costal and RMCA factors are an order of magnitude greater than the radial and arculus values. The laminate factor does not change the mass of the wing and results in a zero slope line of this factor's mass output.

6.2.3.5 First Bend Output. The frequency at which the First Bend eigenvector occurs for the FEA model varies significantly based on the factors and their levels. Both the radial and costal factors increase the resonant frequency of this mode as the element beam width increases. While an increase in RMCA element beam width and increasing the inner ply laminate orientation (effectively producing a less stiff laminate) serve to decrease the first bend natural frequency. Secondary interactions also come into play for this result output as 6 of 8 secondary interactions are shown to reject the null hypothesis.

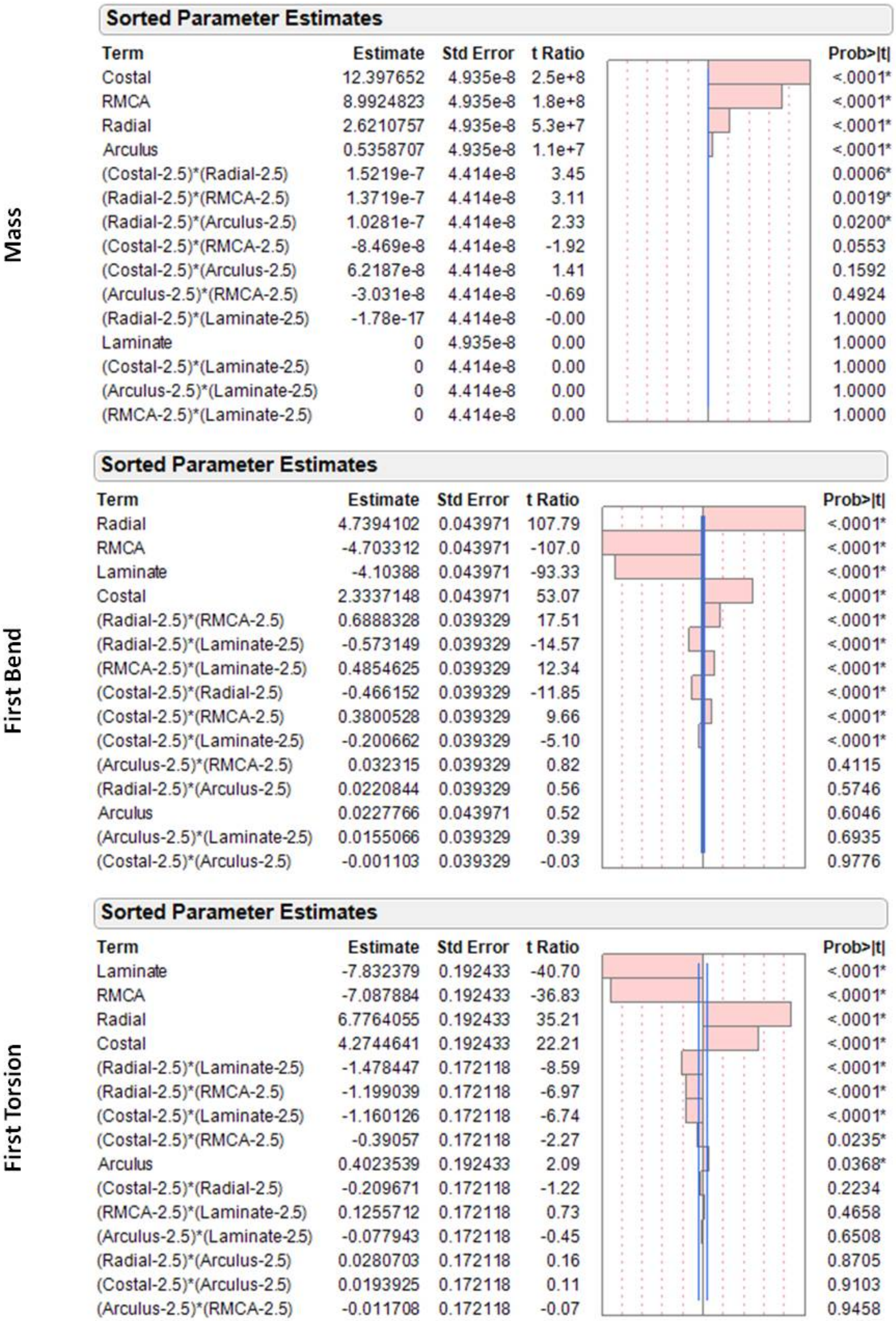

Mass

Sorted Parameter Estimates

Term	Estimate	Std Error	t Ratio	Prob>|t|
Costal	12.397652	4.935e-8	2.5e+8	<.0001*
RMCA	8.9924823	4.935e-8	1.8e+8	<.0001*
Radial	2.6210757	4.935e-8	5.3e+7	<.0001*
Arculus	0.5358707	4.935e-8	1.1e+7	<.0001*
(Costal-2.5)*(Radial-2.5)	1.5219e-7	4.414e-8	3.45	0.0006*
(Radial-2.5)*(RMCA-2.5)	1.3719e-7	4.414e-8	3.11	0.0019*
(Radial-2.5)*(Arculus-2.5)	1.0281e-7	4.414e-8	2.33	0.0200*
(Costal-2.5)*(RMCA-2.5)	-8.469e-8	4.414e-8	-1.92	0.0553
(Costal-2.5)*(Arculus-2.5)	6.2187e-8	4.414e-8	1.41	0.1592
(Arculus-2.5)*(RMCA-2.5)	-3.031e-8	4.414e-8	-0.69	0.4924
(Radial-2.5)*(Laminate-2.5)	-1.78e-17	4.414e-8	-0.00	1.0000
Laminate	0	4.935e-8	0.00	1.0000
(Costal-2.5)*(Laminate-2.5)	0	4.414e-8	0.00	1.0000
(Arculus-2.5)*(Laminate-2.5)	0	4.414e-8	0.00	1.0000
(RMCA-2.5)*(Laminate-2.5)	0	4.414e-8	0.00	1.0000

First Bend

Sorted Parameter Estimates

Term	Estimate	Std Error	t Ratio	Prob>|t|
Radial	4.7394102	0.043971	107.79	<.0001*
RMCA	-4.703312	0.043971	-107.0	<.0001*
Laminate	-4.10388	0.043971	-93.33	<.0001*
Costal	2.3337148	0.043971	53.07	<.0001*
(Radial-2.5)*(RMCA-2.5)	0.6888328	0.039329	17.51	<.0001*
(Radial-2.5)*(Laminate-2.5)	-0.573149	0.039329	-14.57	<.0001*
(RMCA-2.5)*(Laminate-2.5)	0.4854625	0.039329	12.34	<.0001*
(Costal-2.5)*(Radial-2.5)	-0.466152	0.039329	-11.85	<.0001*
(Costal-2.5)*(RMCA-2.5)	0.3800528	0.039329	9.66	<.0001*
(Costal-2.5)*(Laminate-2.5)	-0.200662	0.039329	-5.10	<.0001*
(Arculus-2.5)*(RMCA-2.5)	0.032315	0.039329	0.82	0.4115
(Radial-2.5)*(Arculus-2.5)	0.0220844	0.039329	0.56	0.5746
Arculus	0.0227766	0.043971	0.52	0.6046
(Arculus-2.5)*(Laminate-2.5)	0.0155066	0.039329	0.39	0.6935
(Costal-2.5)*(Arculus-2.5)	-0.001103	0.039329	-0.03	0.9776

First Torsion

Sorted Parameter Estimates

Term	Estimate	Std Error	t Ratio	Prob>|t|
Laminate	-7.832379	0.192433	-40.70	<.0001*
RMCA	-7.087884	0.192433	-36.83	<.0001*
Radial	6.7764055	0.192433	35.21	<.0001*
Costal	4.2744641	0.192433	22.21	<.0001*
(Radial-2.5)*(Laminate-2.5)	-1.478447	0.172118	-8.59	<.0001*
(Radial-2.5)*(RMCA-2.5)	-1.199039	0.172118	-6.97	<.0001*
(Costal-2.5)*(Laminate-2.5)	-1.160126	0.172118	-6.74	<.0001*
(Costal-2.5)*(RMCA-2.5)	-0.39057	0.172118	-2.27	0.0235*
Arculus	0.4023539	0.192433	2.09	0.0368*
(Costal-2.5)*(Radial-2.5)	-0.209671	0.172118	-1.22	0.2234
(RMCA-2.5)*(Laminate-2.5)	0.1255712	0.172118	0.73	0.4658
(Arculus-2.5)*(Laminate-2.5)	-0.077943	0.172118	-0.45	0.6508
(Radial-2.5)*(Arculus-2.5)	0.0280703	0.172118	0.16	0.8705
(Costal-2.5)*(Arculus-2.5)	0.0193925	0.172118	0.11	0.9103
(Arculus-2.5)*(RMCA-2.5)	-0.011708	0.172118	-0.07	0.9458

Figure 73: DOE Results Table

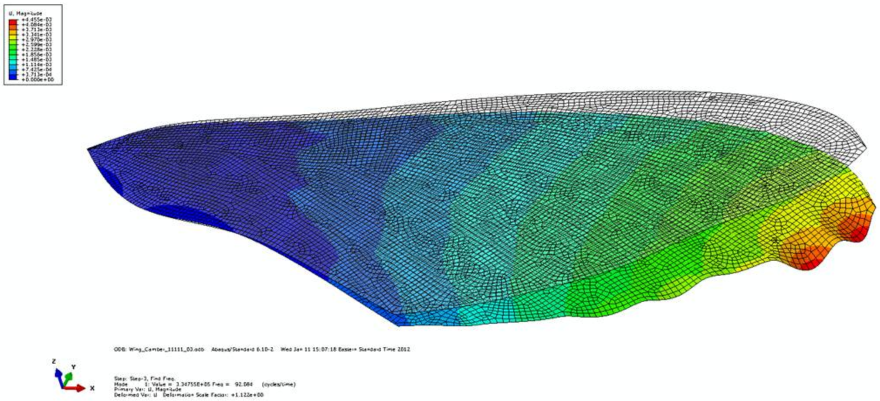

Figure 74: Engineered Wing First Bend Modeshape

6.2.3.6 First Torsion Output. Increasing the inner ply laminate orientation (effectively producing a less stiff laminate) and increasing the RMCA beam element width serve to decrease the first torsion natural frequency. On the other hand, increasing the radial and costal beam widths drives the natural frequency of this mode up. These effects produce similar results, in that the outputs either increase or decrease the resonance of these two modes, however the magnitude of the changes do vary from one output to another.

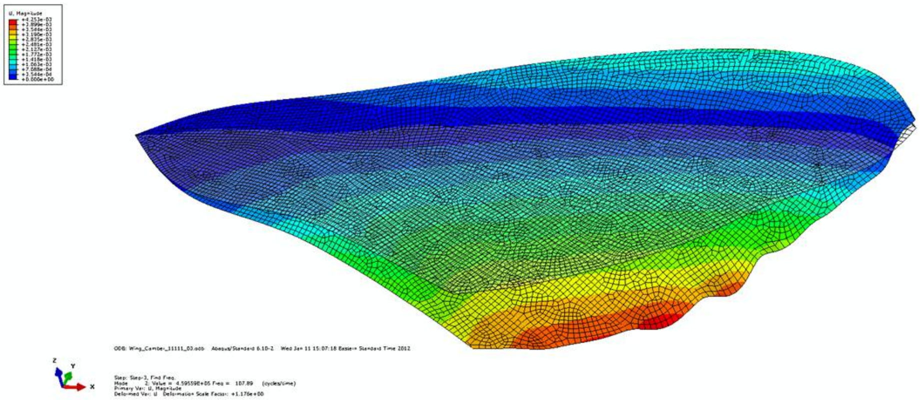

Figure 75: Engineered Wing First Torsion Modeshape

6.2.3.7 Summary. Through the use of DOE the ability to realize the effect of varying factor levels on the output is made possible. The primary concern in this design process is making a wing as light and stiff as possible. Therefore to minimize mass and maximize stiffness the radial vein appears to be the most important venation element of the wing. This factor should be set to a size as large as possible, level 4 in this case. The costal, arculus, and RMCA veins size should be set to as small as possible, to minimize mass and maximize stiffness. Finally, the inner ply laminate angle should be set as small as possible to produce a stiff laminate with as many fibers oriented along the leading edge of the wing.

Through the use of the 1024 cases a simple spreadsheet of the output parameters can be realized. In doing so, this spreadsheet can be used to sort the resultant data in a manner that will automatically define candidate designs that produce the lightest and stiffest wings. This is performed by sorting the candidate designs in ascending order based on mass, first bend natural frequency, and first torsion natural frequency. In doing so, a baseline wing design has been identified as Wing 22334. This design was lightest and stiffest wing that had a venation width structure that could be easily manufactured and based off prior empirical experimental testing, could survive a battery of experimental testing with a high degree of confidence. The numbers of this design refer to the factors (1-5) and levels (1-4) presented in Table 17. For the remainder of this document Wing 22334 will serve as the baseline wing design. From Table 19, the predicted wing mass and moment/product of inertia properties are shown. All of these values are comparable to the biological FEA wing data presented previously in Table 10.

Table 19: Engineered Wing Mass, Moment/Product of Inertia Properties

Mass		**Total**		
		3.82E-05		kg
Center of Area	**X**	**Y**	**Z**	
	22.1E-03	4.0E-03	0	m
Center of Mass	**X**	**Y**	**Z**	
	20.9E-03	4.7E-05	0	m
Moment of Inertia at Origin	**Ixx**	**Iyy**	**Izz**	
	7.69E-10	3.05E-08	3.13E-08	kg· m^2
Product of Inertia at Origin	**Ixy**	**Iyy**	**Izz**	
	-1.13E-10	-2.00E-32	-1.37E-31	kg· m^2
Moment of Inertia at Center of Mass	**Ixx**	**Iyy**	**Izz**	
	7.68E-10	8.1E-09	8.87E-09	kg· m^2
Product of Inertia at Center of Mass	**Ixy**	**Iyy**	**Izz**	
	-6.24E-11	-2.0E-29	-1.37E-31	kg· m^2

6.3 Single Variable Modal Analysis

After performing the design of experiments analysis of the previously defined input factors, it was decided that several other variables should be considered in the design process to access their effects on the structural dynamics of the baseline engineered wing design. The 3 inputs that were considered were the effects due to camber, laser cut angle (alpha), and the inner laminate ply angle of the laminate. With these variables the ability to tailor the structural response without completely redesigning the wing pattern is evaluated for options to change the structural dynamics of wings for experimental study.

6.3.1 Camber. As previously discussed, the ability to add camber to the engineered wing is possible as was the case for the biological FEA model. A concave up to concave down profile was applied to the FEA model where the maximum amount of camber over the wing was varied from 0.2-2.0 mm in a 10 step linear increment. The output for this analysis was only the identification of the first bend natural frequency, first torsion natural frequency, and the ratio of these 2 modes as defined in Equation 1. The results of this analysis are presented in Figure 76. It can be seen that as the amount of camber increases so does the natural frequency of these modes. This is expected since the camber adds stiffness to the structure. The camber appears to slightly increase the chordwise first torsion mode more than the spanwise first bend mode. This results in a slight increase in the ratio of modes calculation from a baseline of 1.17 to 1.26. As it stands, the ability to impart this camber and increase the stiffness of the wing can be done without adding mass and therefore offers the potential for inclusion into a possible manufacturing option.

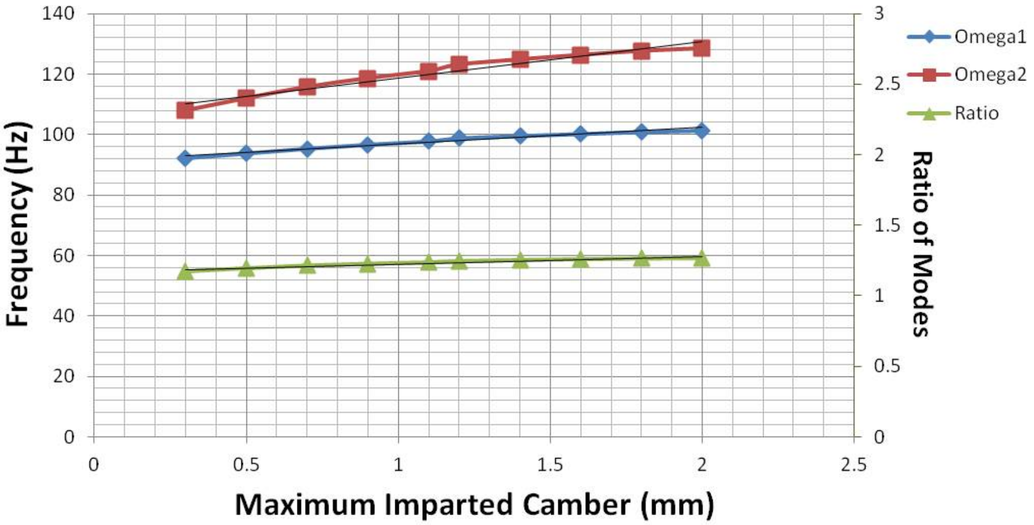

Figure 76: Analytical Camber Modal Analysis

6.3.2 Laser Cut Angle - Alpha. In addition to the ability to change the individual ply layup of the lamina to vary the structural response of the wings it is possible to vary the alignment of wing local axis to the composite lamina local axis. In reality this is achieved by rotating the wing design off the axis of the two outer lamina plies when the wing is manufactured. This angle of rotation is defined as the Alpha cut angle. The results of this analysis are presented in Figure 77. By varying Alpha over a range of 0-45 degrees the effects of this factor become very clear. Specifically, the first bend natural frequency drops quite significantly from 91.23 Hz to 32.56 Hz in a nearly linear fashion. While the first torsion natural frequency remains relatively constant over a range of 108.76 Hz to 101.21 Hz respectively. This results in a nearly linear rise in the ratio of modes from 1.19 to 3.11. Up till now this single factor produces the largest change in the first bend natural frequency and subsequently the ratio of modes. This input factor offers the potential to vary the ratio of modes over a significant range such that the ability to test the aerodynamic performance of wings with a ratio of modes above and below 1.85 is possible.

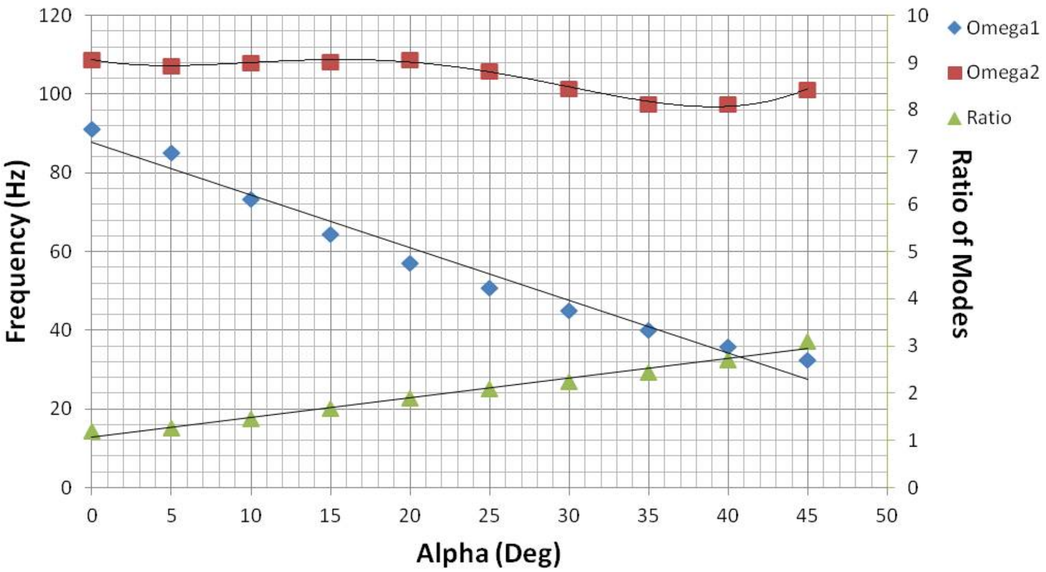

Figure 77: Analytical Alpha Modal Analysis

6.3.3 Inner Laminate Angle. During the design of experiments the inner laminate angle was varied and analyzed to determine the global trend of this factor. Given that a baseline design has been identified, this input factor is reanalyzed to determine the effects of this factor specifically for this design. The inner laminate angle was varied over a range of values at 20, 30, 45, and 90 degrees. As was predicted in the design of experiments analysis, by increasing the inner laminate angle decreases the global laminate bending stiffness, and decreases both the first bend (104.9 Hz to 91.23 Hz)and second bend natural frequency (134.61 Hz to 108.76 Hz). The slope of this change is nearly constant and is reflected in a nearly flat, but decreasing slope in the ratio of modes value from 1.28 to 1.19.

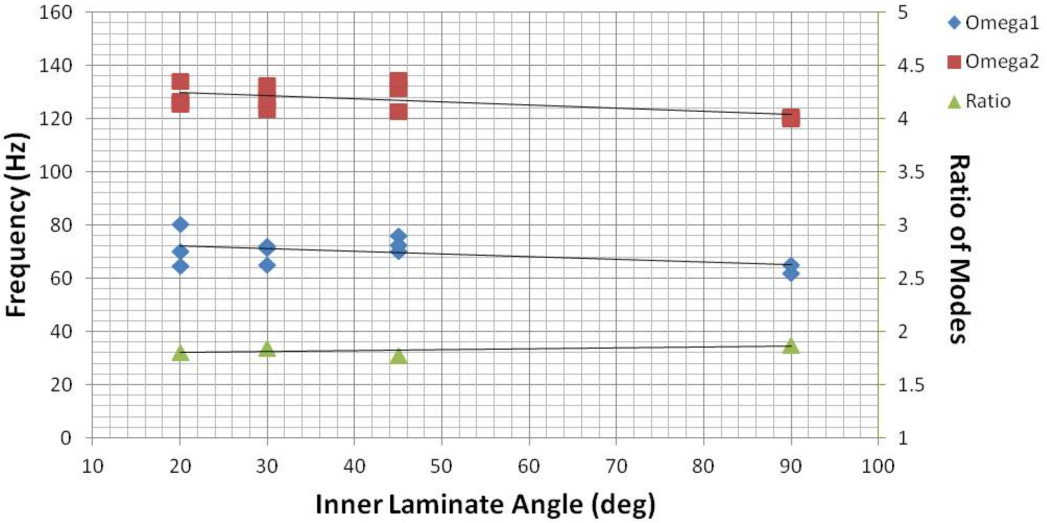

Figure 78: Analytical Laminate Modal Analysis

6.4 Non-Linear Large Deformation Flapping

In addition to performing the modal analysis and simple static point load analysis a non-linear large deformation flapping of the wing was performed. This is done to predict structural response of the wing in a clamped boundary condition while flapping in a vacuum. This model serves as another datapoint for comparison in the ability to characterize the dynamic structural response of the engineered wing.

6.4.1 Model Setup and Definition. Due to the increased computational requirements of an explicit analysis several definitions of the model are required to be updated or changed. Specifically, the shell element types used to define the membrane elements must be changed from S8R, 8 noded reduced integration elements to S4R, 4 noded reduced integration quadratic elements. Additionally, the beam elements that were used to define the venation are changed from B32, 3 noded quadratic elements to B22 3 noded explicit quadratic elements. Without these changes, it would not be possible to solve this model using Abaqus' explicit solver.

To simulate the input of angular displacement at the base of the wing a sinusoidal rotation input of ±45° was applied at the base of the wing in the UR2 direction. This rotation was applied at $\omega = 22$ Hz as shown in Equation 30.

$$\begin{gathered} y(t) = A * sin(\omega t + \phi) + B * cos(\omega t + phi) \\ A = 0 \; and \; B = 1 \end{gathered} \tag{30}$$

Additionally, to help the explicit solution reach a steady-state condition, the use of Rayleigh Mass Damping was included in the venation and membrane material definitions. The Rayleigh Damping factors are expressed in Equation 31. Based on experimental modal analysis of the biological and previously fabricated engineered wings a ζ value of 0.054 was determined to present in these systems. Setting ζ=0.054 we can use Equation 31 to calculate α, mass proportional damping, which in this case equals 15. Due to the relatively low frequency that we are flapping at we will only require mass proportional damping, and therefore β, stiffness proportional damping, is set to zero.

$$\zeta(\omega_\alpha) = \frac{\alpha}{2\omega_\alpha} + \frac{\beta\omega_\alpha}{2} \tag{31}$$

6.4.2 Solution. With these parameters set the solution is solved in parallel on the previously defined dual quad core workstation. Due to the significant computational solution requirements of this problem, Abaqus is set to run in parallel on 16 processors (8 physical, 8 virtual) using the hyperthreading capabilities of this system's processors. Solution time for 0.5 seconds of flapping solved in approximately 22 hours. The solution reaches steady state at approximately 342 ms into the solution as shown in Figure 79. Figure 80 is the resultant output of a single cycle of flapping after reaching the steady state condition.

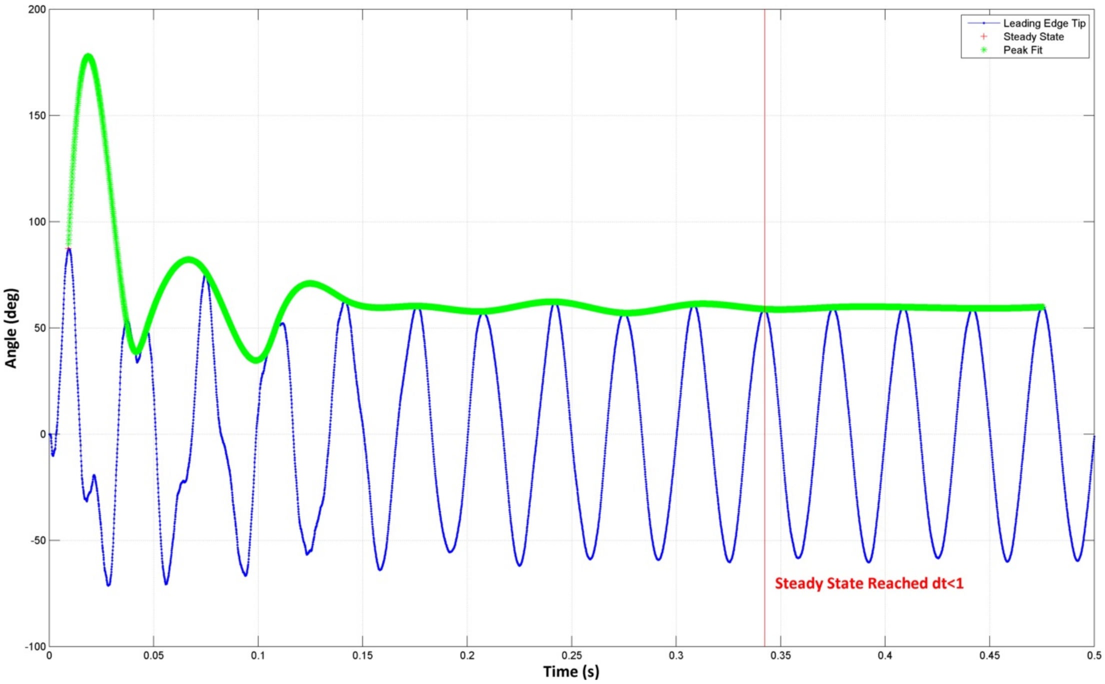

Figure 79: Steady State Flapping Determination

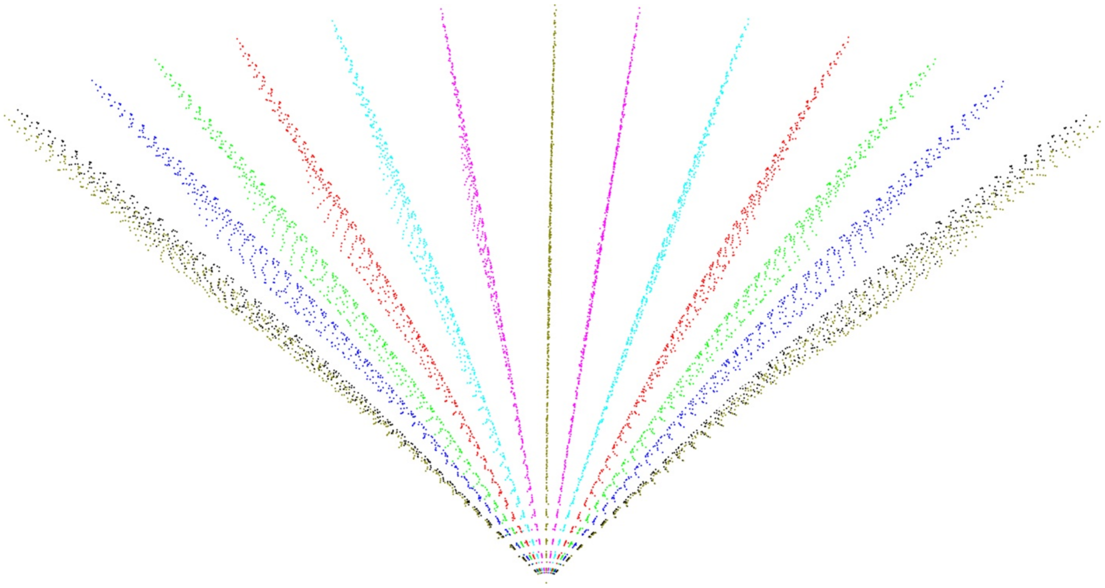

Figure 80: 22 Hertz Flapping Analysis ±45°

It can be seen that the wing is dominated by modal participation of the first bend flapping frequency throughout a majority of the stroke. It is difficult to observe, in Figure 80, but in video analysis of the flapping motion the wing exhibits slight chordwise bending at stroke reversal consistent with the first torsional modeshape. This analysis is consistent with previous efforts to dynamically model the flapping response of a biological *Manduca Sexta* forewing [13]. In doing so, this model provides the basis for a large amount of confidence that the engineered wing will behave much like the biological analog that it was designed to mimic under experimental flapping conditions.

6.5 Wing Fabrication

Through the use of FEA it is possible to realize a candidate design that is of low mass and high stiffness based upon the engineered materials that are currently available. The transition from simple beam element geometry models to three dimensional hardware must be completed. A multi-step process that translates point and line data to two dimensional CAD and computer aided machining (CAM) software is implemented. With geometry files created the composite laminate material must be fabricated and machined. Finally, the mylar membrane must be affixed to the venation and final machining of the wing is completed.

6.5.1 Computer Aided Design. In a manner similar to the development of the FEA geometry, Matlab is used to take the individual lines that represent the venation and secondary and tertiary lines that represent the true width of the venation being represented. Matlab is used to generate the required Visual Basic API required to import splines directly into the Solidworks CAD environment. The results of this effort are seen in Figure 81. Close visual inspection will reveal that this translation is far from perfect. There are many intersecting and overlapping lines that require further refinement. However, the basis of the three dimensional wing model is beginning to take shape. By exporting this framework of curves from Solidworks to the Drawing Exchange Format (DXF) this series of lines can be imported into another software package for further processing. Specifically, CorelDraw is used to import the resulting DXF file. This software package is used for its ability to quickly and easily manipulate complex two dimensional vector illustrations. After, cleaning up the imported geometry, adding fixturing elements, and the membrane profile the engineered wing depicted in Figure 82 is realized. This wing has a length of 50 mm and a chord length of 20 mm.

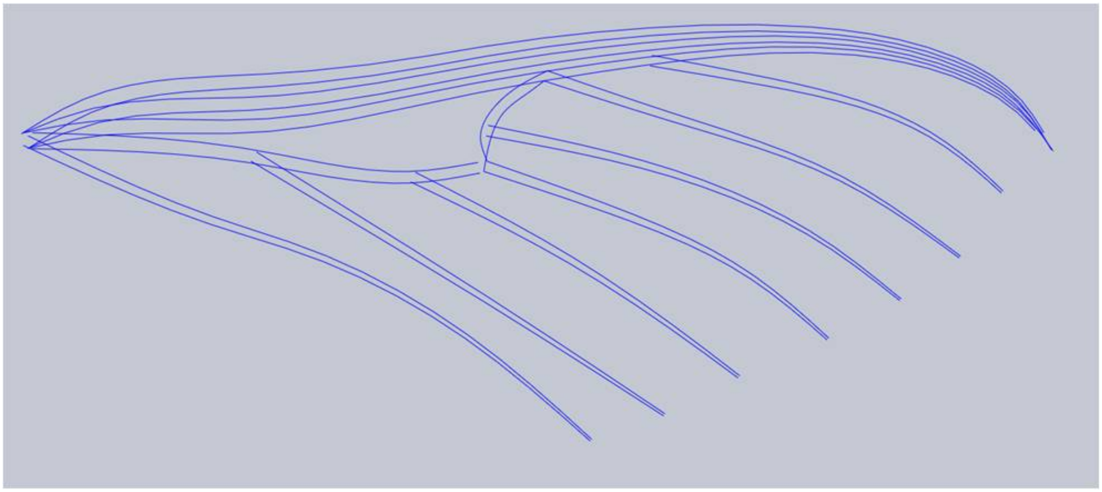

Figure 81: SolidWorks Untrimmed Venation Geometry

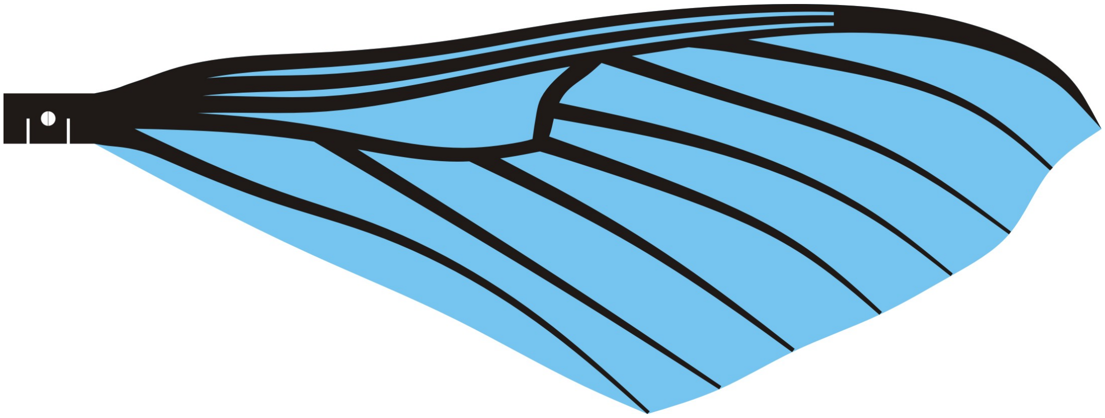

Figure 82: Baseline Engineered Wing Design

6.5.2 Composite Laminate Layup. The composite laminate that is used for the manufacture of the wings is received as a 500 ft x 12 inch wide pre-preg unidrectional laminate tape. The YSH-70A composite fibers are embedded in a RS-3C epoxy resin. This laminate tape has a wax paper layer on one side and a plastic backing on the other, Figure 83. Upon receipt the laminate tape is unrolled and trimmed into 8 in x 11 in sections. The pre-preg sheets are then placed into a large plastic storage bag that is then placed into freezer at approximately 20°F.

Figure 83: Pre-preg Roll and Pre-preg Sheet with Backing Material

When a single composite panel is ready to be processed, three sheets of the pre-preg lamina are removed from cold storage. A single piece of non-porous teflon coated fiberglass sheet is placed on a work table. The paper and plastic backing of the pre-preg sheet are removed and the sheet is placed upon the non-porous teflon. The paper backing is reapplied and using a small plastic squeeqee all air bubbles are removed by working from the center of the composite outward. The paper backing is removed after the completion of the removal of all air bubbles. The second pre-preg sheet backing is now removed and the second pre-preg sheet is placed upon the first. The fiber orientation of this second sheet, relative to the first, will determine the inner ply angle of the composite. Again, the paper backing is reapplied and all air bubbles are removed. Now the third pre-preg sheet is applied and the fiber direction of this third sheet should match that of the first. Again, all air bubbles are removed. A porous teflon coated fiberglass sheet is now placed over the composite laminate. This porous teflon sheet will allow excess resin to flow from the composite laminate into the thin cloth bleeder sheet that will be placed upon the porous teflon sheet. Finally, an additional sheet of non-porous teflon is now placed over the bleeder cloth, preventing the flow of resin onto the hydraulic press plates that will be used to compress the composite laminate.

Figure 84: LPKF Multipress

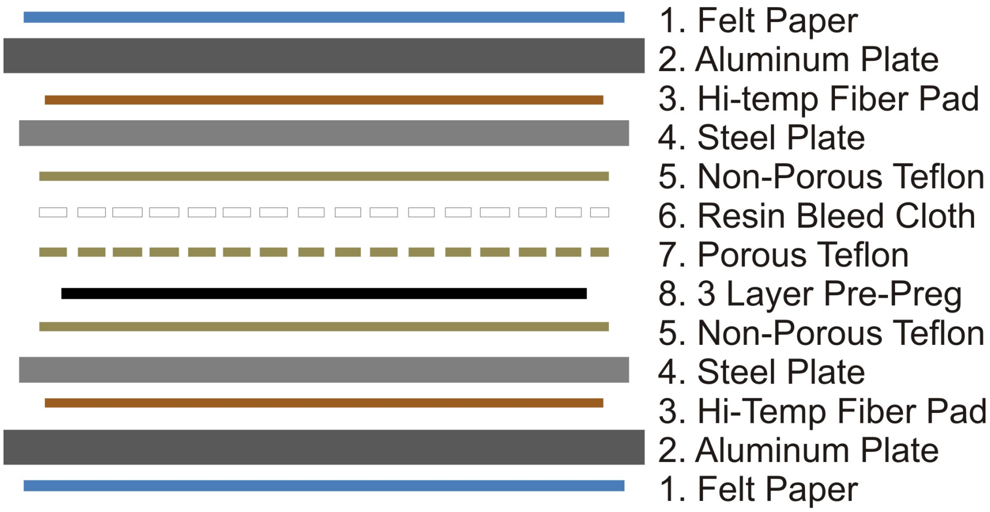

Figure 85: Laminate Composite Curing Stackup

This stackup of pre-preg composite curing materials is now placed into a LPKF Multipress S. This press was designed to cure composite laminates at specific preprogrammed temperature and pressure profiles. This system uses a cartridge system to properly apply this heat and pressure, Figure 85. The press is set to apply 100 n/cm^2 of pressure at 192°C for 120 minutes. When cooled the cured composite laminate is removed from the press and is now ready for further processing.

6.5.3 Laser Machining Center. All the composite laminate pieces and mylar membrane pieces of the wing are fabricated on a ultraviolet laser machining center. Specifically, an LPKF Protolaser U has been employed for a majority of the material cutting associated with the wing and is critical to the machining process. This machine has a 200 mm x 280 mm work table that allows for the laser ablation of a multitude of thin materials. The use of the ultraviolet laser allows for the ablation of material while minimizing heat absorption. An extremely fine spot size of 20 microns coupled with ±2 micron resolution scanning galvometers allows for the rapid machining of extremely fine component pieces. Details on the ultraviolet laser are presented in Table 20.

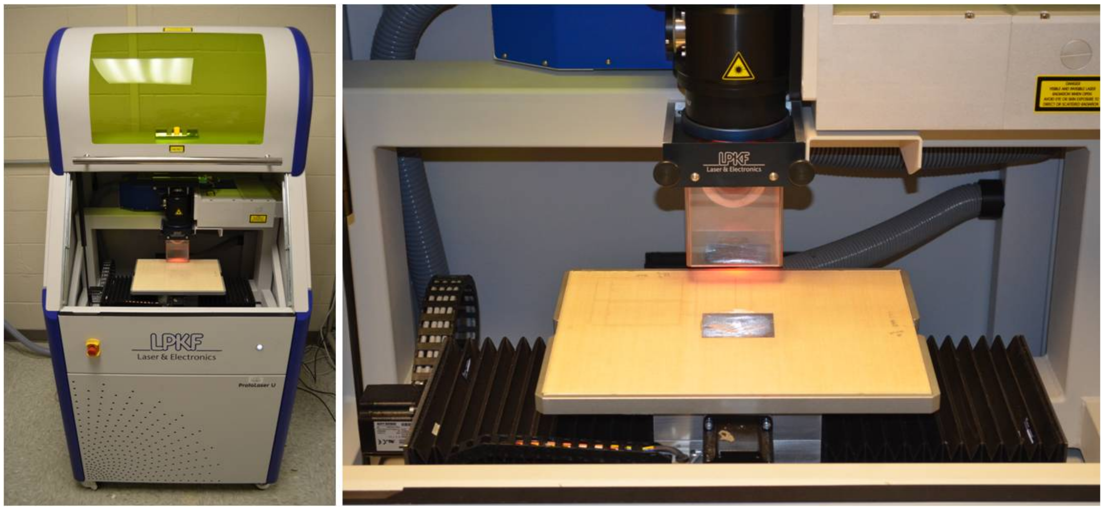

Figure 86: LPKF Protolaser U Machining Center

Table 20: Ultraviolet Laser Source Technical Specs

Wavelength	355	nm
Pulse Duration	900	ns
Avg power	8.95	Watts
PRR	40	kHz
Pulse Engery	0.22375	mJ/pulse
Peak Power	2.49E+02	Watts
Spot Size	20	um
Area	3.14E+02	um2̂
Avg. Power Density	2.85E+06	Watts/cm2̂
Fluence	71.22	J/cm2̂
Peak Power Density	7.91E+07	W/cm2̂
-	4.00E+14	Photons/Pulse
-	0.32	Peak Irradiance

The laser is typically set to ablate 20-30 microns of material per pass over a cutting line. Repeated passes allow for the complete removal of material where a cut line is desired. A vacuum table covered with a porous foam board and lined with a porous teflon sheet ensures that the material being cut is held in place and allows for the easy removal of the parts after being machined. The laser system settings for a particular material are determined through repeated testing of representative sacrificial material samples. Two main variables can be changed to vary the effective power delivered to the material. They are the frequency at which the laser is fired and the speed at which the laser galvometers scan. For this laser, the current to the laser is regulated at a set current and cannot be continuously varied. What can be changed is the frequency at which the laser fires and the scanning speed of the galvometers that direct the laser. This laser is able to operate over a frequency range of 30 - 150 KHz.

Table 21: Protolaser U Power Output

Freq	**Average Power (W)**
30	9.1
40	8.8
50	8.2
60	7.4
70	6.7
80	5.9
90	5.3
100	4.7
110	4.2
120	3.8
130	3.4
140	3.1
150	2.9

The average power that is capable of being delivered over this frequency range varies significantly as shown in Figure 87. The power curve, Table 21, has been normalized by the peak power at 30 KHz. Using the data from Figure 87 allows for a curve fit of the normalized power versus laser frequency to be calculated as shown in Equation 32. Where x represents the desired power level from (0-1) and f, is the resultant frequency. In this manner a user can determine the % power they wish to fire the laser at and the specified frequency can be easily determined.

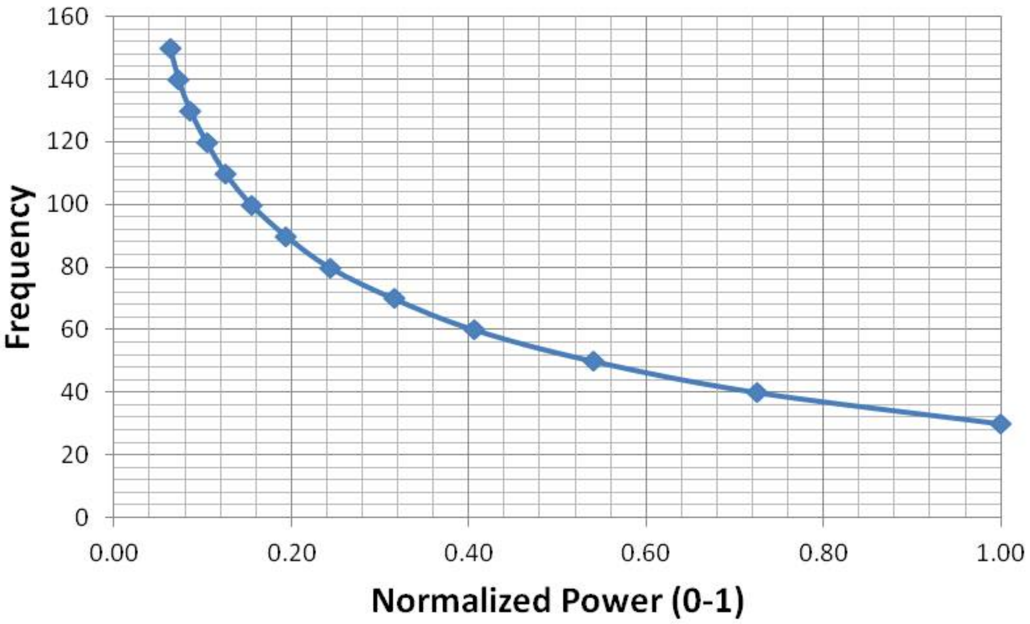

Figure 87: Normalized Power Output vs Frequency

$$\begin{aligned} f(x) &= a^{bx} + c^{dx} \\ a &= 128.3 \\ b &= -13.26 \\ c &= 100.9 \\ d &= -1.261 \end{aligned} \tag{32}$$

Changing the frequency at which the laser fires allows you to effectively change the power being delivered by the laser. However, due to the change in frequency, the mark speed of the galvometers must be changed to maintain a consistent laser pulse spacing (microns) or laser pulse overlap (percentage). It is recommended that a 65% pulse overlap or 7 micron spacing be maintained when defining laser settings. This pulse overlap will ensure that the heat imparted to the material is minimized, yet will also produce a cleanly cut edge surface free from scalloping. Figure 88 represents the effects of varying the pulse spacing. This laser system is capable of reliably scanning at mark speeds of 0-600 mm/sec.

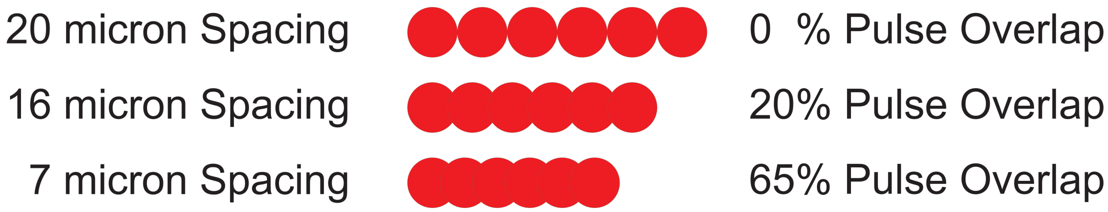

Figure 88: Laser Pulse Overlap

By determining the frequency at which to fire the laser the subsequent scan speed that should be set can easily be determined through the use of Equation 33.

$$Scan\ Speed = (1 - Pulse\ Overlap) * Frequency * Spot\ Size \tag{33}$$

Typical settings for the materials used in the wing fabrication process are presented in Table 22

Table 22: Material Laser Settings

Material	**Thickness**	**Frequency**	**Scan Speed**	**Passes**	**Steps**	**Step Height**
-	um	KHz	mm/sec	-	-	um
YSH-70	150	40	100	5	-	-
YSH-70	300	40	100	5	1	50
Mylar	2.5	100	600	2	-	-
Non-Porous Teflon	50	40	100	3	-	-
Porous Teflon	50	40	100	2	-	-
Pyrallux	5	80	600	5	-	-
Kapton	12	60	400	2	-	-
Kapton	25	60	400	2	-	-
Kapton	125	60	400	7	-	-
PZT (Score)	191	150	545	750	-	-
PZT(Cut)	191	180	545	1000	4	50

6.5.4 Laser Machining. With the engineered wing design complete, it is now required to translate this design into the format required for fabrication. The wing will be constructed in a three step process. First, the wing venation is cut out of the composite laminate using the Protolaser U, Figure 86. Second, the mylar membrane is thermo pressed onto the composite laminate using the Multipress S. Finally, the remaining membrane and venation are laser cut to yield the design shown in Figure 82.

Step 1 involves simpling cutting the venation geometry in a small 60mm x 50mm section of composite laminate. The venation is held in place at the root of the wing while the remainder of the material surrounding the venation is removed. In doing so, a protective framework is provided by the remaining composite. In step 2, the mylar membrane is draped over the venation and thermoset into place by using a heated press that provides 100 psi of pressure at $350°F$ for 15 minutes. In step 3, the resultant venation and membrane framework are then cut, releasing the completed wing. The CAM file geometry associated with steps 1-3 are shown in Figure 89.

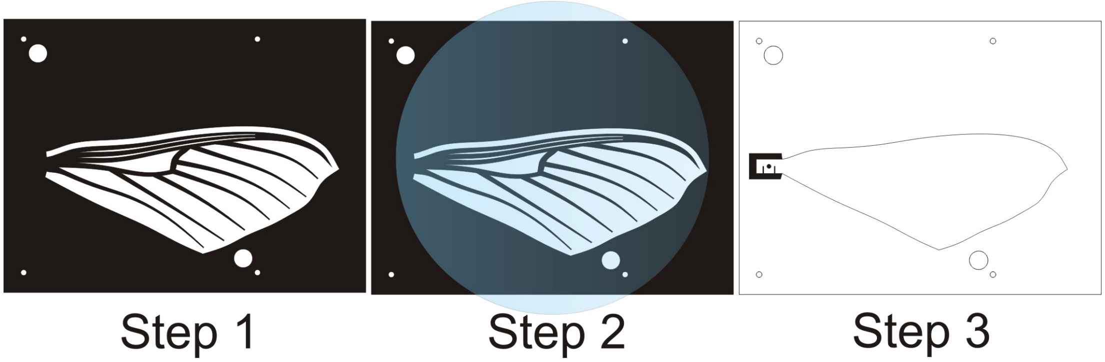

Figure 89: Venation Cutting Pattern and Venation/Membrane Release Pattern

6.6 Summary

The results of the efforts described here can be clearly seen in Figure 90. The analytical design, evaluation, and manufacture of a engineered wing based on the forewing of the *Manduca Sexta* species has been realized. This baseline wing possesses nearly identical geometry, structural dynamics, and weight as compared to its biological analog as shown in Table 23. This represents the culmination of all the developmental research that has been done to properly measure, quantify, and reproduce an engineered version of the *Manduca Sexta* forewing. In this manner, a truly biomimetic wing design has been achieved in an unprecedented manner in the field of FWMAVs.

Table 23: Experimental Biological Wing vs. Experimental Baseline Wing Design

	Mass (mg)	First Bend (Hz)	First Torsion (Hz)	Ratio
Bio	34.66	65.2	110.15	1.689417
FEA	38.2	62.109	120.89	1.946417

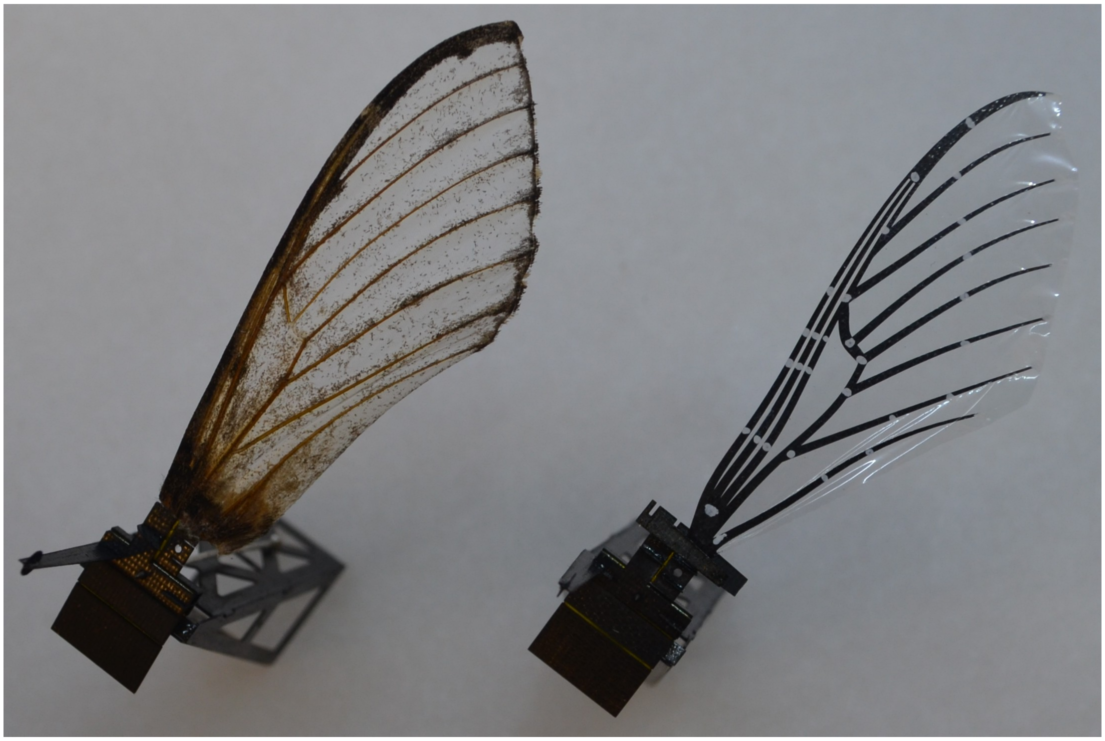

Figure 90: Biological Wing vs. Baseline Engineered Wing

VII. Experimental Testing

Experimental quantification of the aerodynamic performance of both the biological and engineered wing design is presented to show the effectiveness of this methodology to produce a biomimetic wing that is capable of producing lift on the same order of magnitude as it biological analog. This experimental study will cover the design, fabrication, and experimental evaluation of a method to produce and analyze the aerodynamic performance of biological and engineered wings through a wing stroke motion comparable to the *Manduca Sexta* species.

7.1 Flapping Mechanism Design

It is required that biological *Manduca Sexta* forewing and the biomimetic engineered wing be flapped in a manner that is similar to that of the *Manduca Sexta.* The ability to flap both wings under the same prescribed kinematics and under the same boundary conditions has allowed for the aerodynamic evaluation and comparison of each in a manner that has not been achieved in prior research. Such a system has been achieved and is presented in Figure 91.

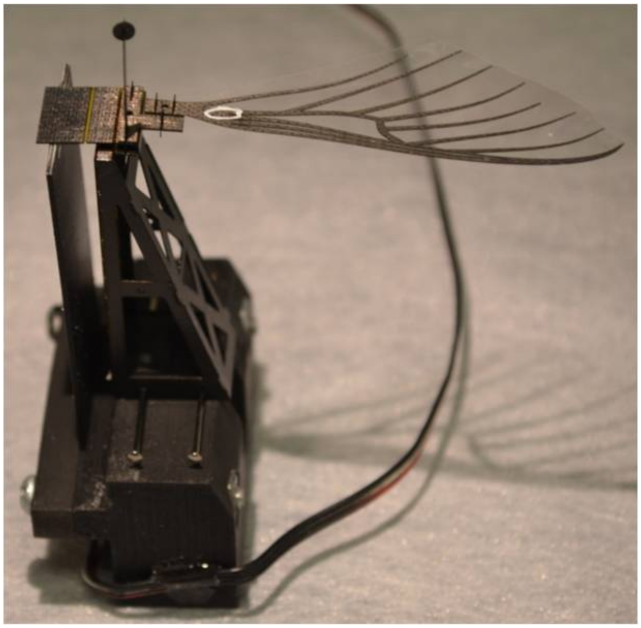

Figure 91: Flapping Mechanism

7.1.1 Linkage Kinematics. The geometry of the flapping mechanism and the resulting rigid body kinematics are chosen based on the expected displacement of the drive actuator and the desired wing motion. The mechanism was designed to have a maximum wing stroke amplitude of ±60° for a total wing stroke amplitude of 120°. The mechanism was designed to provide this travel with a piezo actuator that has an effective length 50 mm and ± 2 mm of travel. To design the linkage geometry, a script was created in Matlab to calculate the linkage kinematics from a given geometry, animate the wing trajectory and report the maximum and minimum wing stroke angle [5].

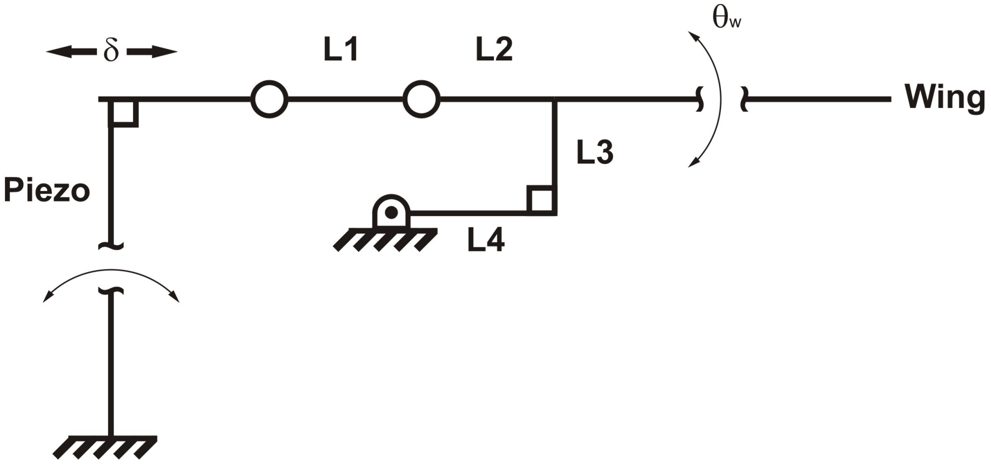

Figure 92: Linkage Kinematics

To define the linkage, the link lengths, L_1-L_4 must be specified. Then, a given actuator deflection, δ, defines the position of the linkage, which defines the wing stroke angle, θ_w, as shown in Equation 34 [25].

$$\begin{aligned}\theta_w = -\frac{\pi}{2} &+ arccos[\big(L_3^2 + (L_1 + L_2 - L_4 - \delta_1)^2 + L_3^2 + (L_2 - L_4)^2 - L_1^2\big) \\ &\left(2\sqrt{L_3^2 + (L_2 - L_4)^2} \times \sqrt{L_3^2 + (L_1 + L_2 - L_4 - \delta)^2}\right)^{-1}] \\ &+ arctan\left(\frac{L_3}{L_1 + L_2 - L_4 - \delta}\right) + \ arctan\left(\frac{L_2 - L_4}{L_3}\right) \\ L_1 = 2.96\ mm\ , L_2 &= 2.36\ mm\ , L_3 = 1.25\ , mm\ , L_4 = 2.50\ mm\end{aligned} \tag{34}$$

Figure 93 depicts the fabricated linkage mechanism and corresponding link identifications.

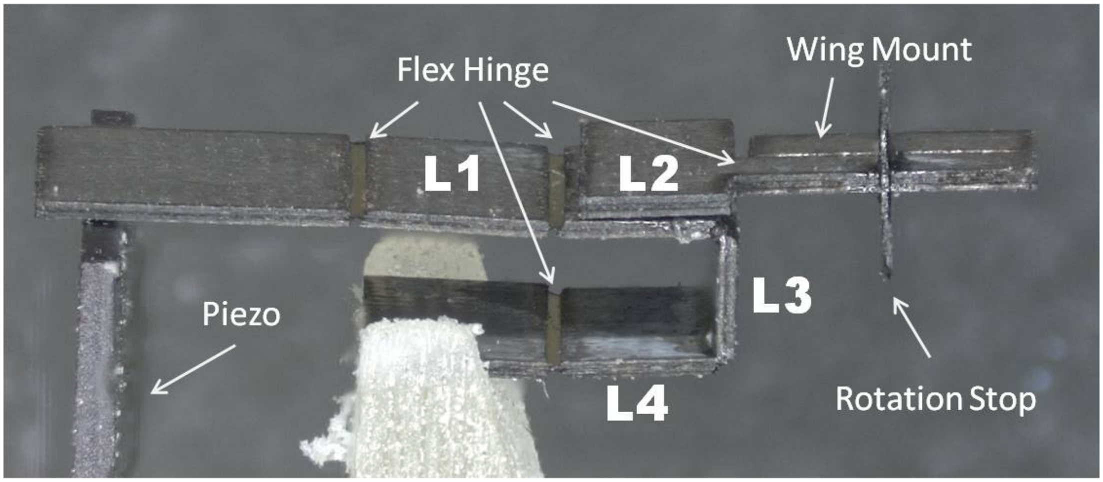

Figure 93: Fabricated Linkage Side View

The ratio of L$_2$ versus L$_4$ will determine whether θ_w will be upstroke or downstroke biased. The transmission ratio of this design is approximated by Equation 35 and represents the ratio of the output angular displacement (wing) to the input linear displacement (actuator) [107].

$$T \equiv \frac{\theta_w}{\delta} \approx \frac{1}{L_3} \tag{35}$$

7.1.2 Piezo Actuator. The flapper mechanism is actuated by the use of a bi-morph piezo actuator. This actuator allows the response of the mechanism to be varied by the input voltage amplitude and frequency. Since these signals are digitally generated they are easily varied through software and a data acquisition system. This is in direct contrast to previous efforts that focused on the use of a rotary motor where the flapping frequency was the only input that could be varied [17]. The piezo actuator is an Omega Piezo, OPT 60/20/0.6 and is driven in a parallel configuration with a DC bias to maximize the drive potential of the actuator and is physically connected as shown in Figure 94 [111].

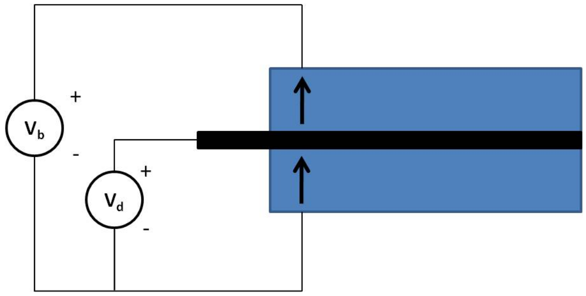

Figure 94: Piezo Actuator in a Parallel Bias Drive Configuration

There are two waveforms that must be generated to drive the Piezo actuator in this configuration and are defined in Equation 36. There are two primary variables that can be used to vary the stroke amplitude of the wing that is generated. A, represents a variable amplitude value from 0-1 and ν, represents a bias of the positive to negative cycles of the sinusoid signal. The drive signals originate from a desktop PC via Matlab, to a National Instruments USB-6229 (±10V) capable of generating voltages from ±10 volts, are amplified 30X, and then fed to the actuator. This configuration allows for the ability to quickly and efficiently change dynamic test parameters over previous efforts [82].

$$\begin{aligned} Sinusoidal\ Drive\ Signal &= A \cdot V_{bias} * (\tfrac{1}{2} + Sin(\omega t) + \eta) \\ DC\ Bias\ Signal &= A \cdot V_{bias} \\ V_{bias} &= 200\ V \end{aligned} \tag{36}$$

7.1.3 Passive Rotation. For the purposes of only evaluating the structural dynamics of the biological wing as compared to a engineered wing there is no need to provide a flexible rotation joint to the flapping mechanism. In this manner, the boundary condition of a clamped condition can be met and makes for easier comparison between the two wing types. Additionally, since the comparison between the two types is to be conducted in a vacuum, the need to model passive rotation is not required. However, if the effects of aerodynamics are to be considered for the engineered wing, it is required for the flapping mechanism be able to allow the wing to rotate. This is especially needed for the evaluation of lift. A passive rotation joint has been designed that allows for the tuning of the torsional stiffness and rotation limits to be set.

$$G = \frac{E_h w_h t_h^3}{12 l_h} \tag{37}$$

The torsional stiffness G (N/radian^{-1}), Equation 37, can be changed with the hinge width, length, and thickness as where E_h is the Youngs modulus of the flexure hinge and w_h, l_h, t_h are the width, length, and thickness of the hinge, respectively as shown in Figure 95 [93]. For our purposes, E_h equals 2.59 GPa, while w_h and l_h are fixed at 5 mm and 125 μm respectively. To date the flexure stiffness has been evaluated with 12.5, 25, and 75 μm thick Kapton as shown in Figure 95. A 12.5 μm thick Kapton provided a rotation joint with a resonance that was below the resonance of that of the wing and resulted in a wildly oscillating wing that quickly failed at the flexure joint. A 25 μm thick Kapton joint produced the highest lift results of all the tests. Both 50-75 μm flexures resulted in a much stiffer system but did not allow the wing to passively rotate in a manner conducive to the production of lift. For the remainder of this document all passive rotation joints are manufactured with a 25 μm flexure and a rotational stiffness of 8.14E-8 N/radian^{-1}.

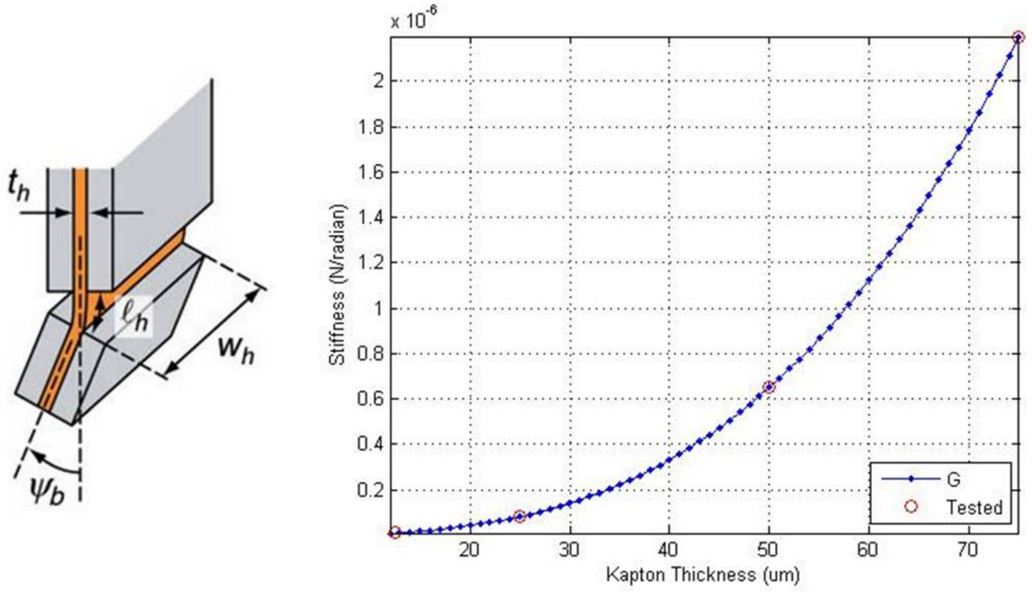

Figure 95: G for Passive Rotation Joint [93]

The location of the passive rotation joint has been located just ahead of the mass and area centroids as shown in Figure 96. The location of this hinge axis directly corresponds to the biological specimen where the wing attaches to the tergal plate of the *Manduca Sexta*.

Incorporated into the passive rotation mechanism is the ability to limit the travel at the root of the wing. This is achieved by using a physical stop to limit the rotation of the wing. This rotation stop limits the angular motion at the root of the wing to ±45°. The manufactured passive rotation joint and stop are depicted in Figure 97.

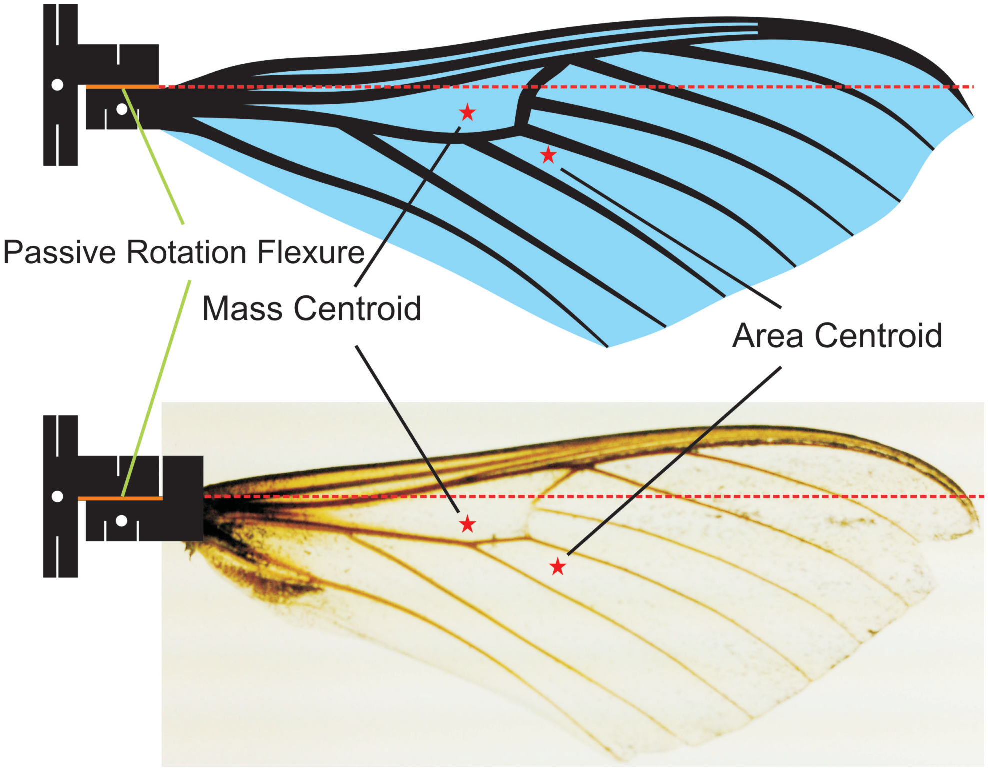

Figure 96: Passive Rotation Joint Location

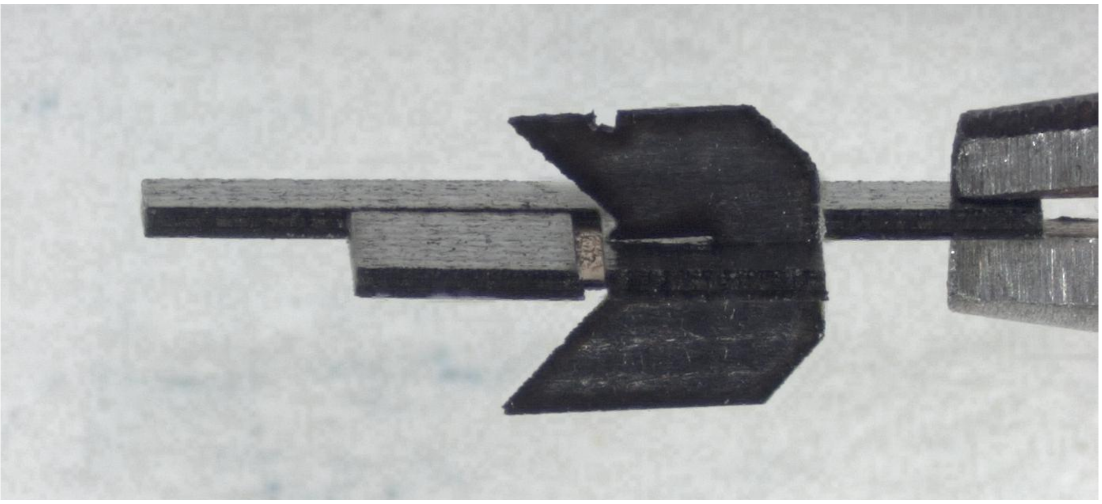

Figure 97: Fabricated Passive Rotation Joint and Stop

7.2 Flapping Mechanism Fabrication

With the completion of the design phase of the flapping mechanism the generation of the CAD and CAM files can be accomplished. From these files the appropriate composite material stack up is fabricated and then laser cut. After the parts are cut the final assembly of the mechanism can be completed. A significant amount of time has been spent to simplify this process such that a simple and repeatable method to assemble these devices has been found.

7.2.1 Composite Carbon and Kapton Stack up. The concept of using Kapton to function as a type of living hinge is unique and novel concept that has been employed extensively for use with piezo based flapping actuators both at Harvard [5, 107–109] and AFIT [5]. The idea is to create a 5 layer composite stack up as shown in Figure 98. Sections of the top and bottom layers of carbon are selectively removed where a flexure is desired.

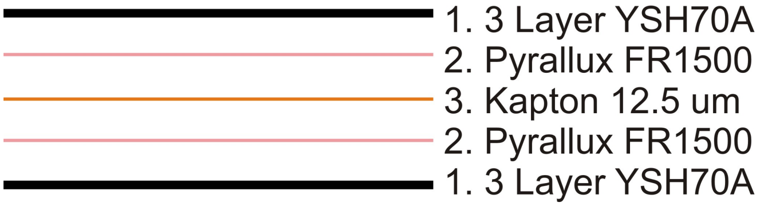

Figure 98: Flapper CAM Patterns

This 5 layer stack up is created through a multi-step curing and pressing process. This process is commonly employed in the generation of thin film circuit boards and is adapted for use here. To begin, 2 sheets of 8.5 in x 11 in three layer YSH-70A laminate, with a lamina orientation of 0/90/0 are cured in the LPKF Multipress at the same temperature and pressure profile as the composite wing. These sheets are then layered, on a single side, with a single sheet of 12.5 μm Pyrallux FR1500. This material is a sheet adhesive commonly used to bond copper coated Kapton with a protective Kapton layer. This material is tack bonded to the carbon fiber by preheating the LPKF Multipress to 350° F and pressing the two materials together at 100 N/cm^2 for 5 minutes. At this point, the top and bottom carbon and Pyrallux sheets are laser cut to size as shown in the left image of Figure 99. When the cutting is performed it is pertinent that the carbon be placed face up with the Pyrallux FR1500 side face down upon a sheet of porous teflon. This minimizes exposure of the Pyrallux to the heat effects of the laser and excess bonding agent being removed. Next, the 12.5 μm Kapton film is cut as shown in the middle image of Figure 99. These two layers are placed on a set of metal plates with precision alignment pins and are pressed together in the LPKF Multipress at 350° F for 60 minutes. After this curing cycle the composite stack up is cut as shown in the right image of Figure 99.

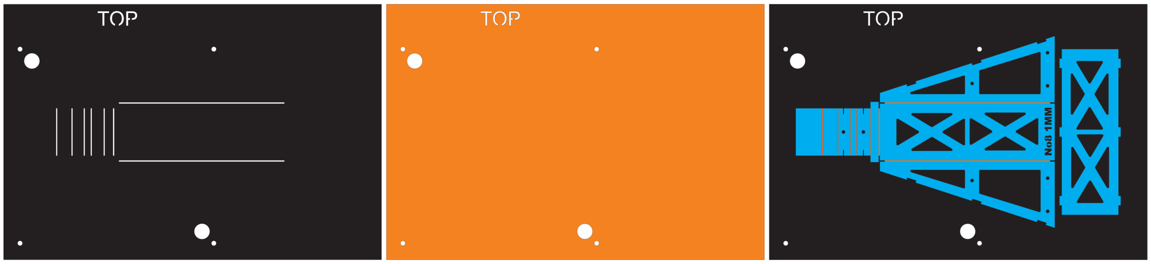

Figure 99: Flapper CAM Patterns

A similar approach is taken for the passive rotation joint shown in Figure 100. This passive rotation joint is a separate piece from the flapping mechanism and serves to attach the wing to the flapping mechanism while providing an additional degree of freedom necessary for lift generation.

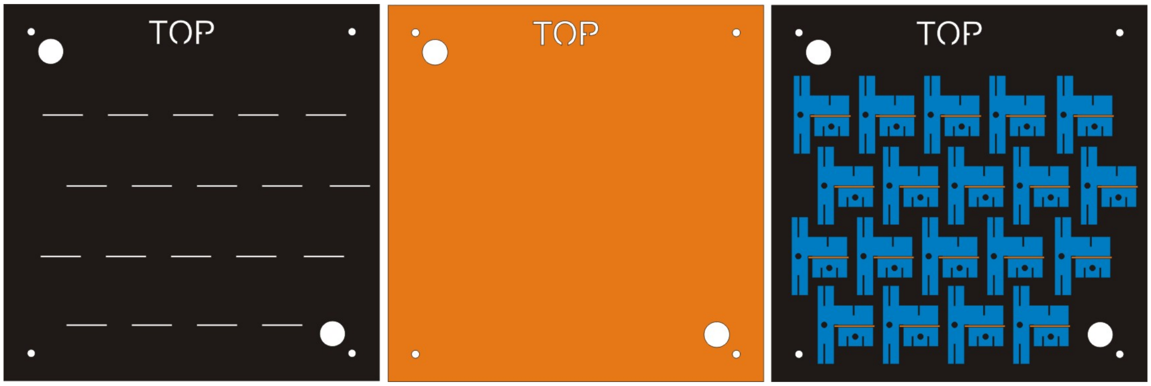

Figure 100: Passive Rotation Joint CAM Patterns

7.2.2 Flapper Assembly Process. At this point the flapping mechanism must be assembled by hand. The implementation of of a number of unique design features separate this mechanism assembly from previous designs. Through the use of clips and pins it is possible to align all the critical components of the mechanism prior to bonding these pieces in place. These methods ensure a highly repeatable and easily assembled mechanism for even the novice technician. A step by step method of assembly is presented in a series of pictorial descriptions as shown in Figures 101-112.

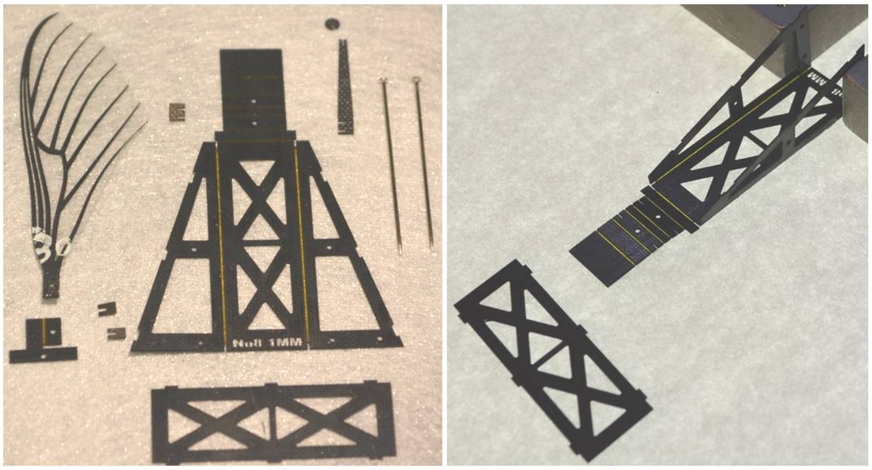

Step 1: Collect Precut Parts **Step 2:** Foldup Base Sides

Figure 101: Flapper Assembly Steps 1-2

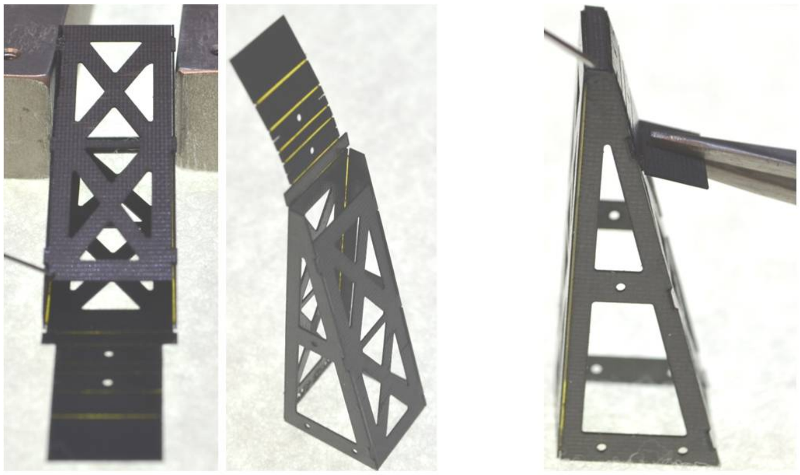

Step 3: Bond Front Plate **Step 4:** Glue Base of Linkage

Figure 102: Flapper Assembly Steps 3-4

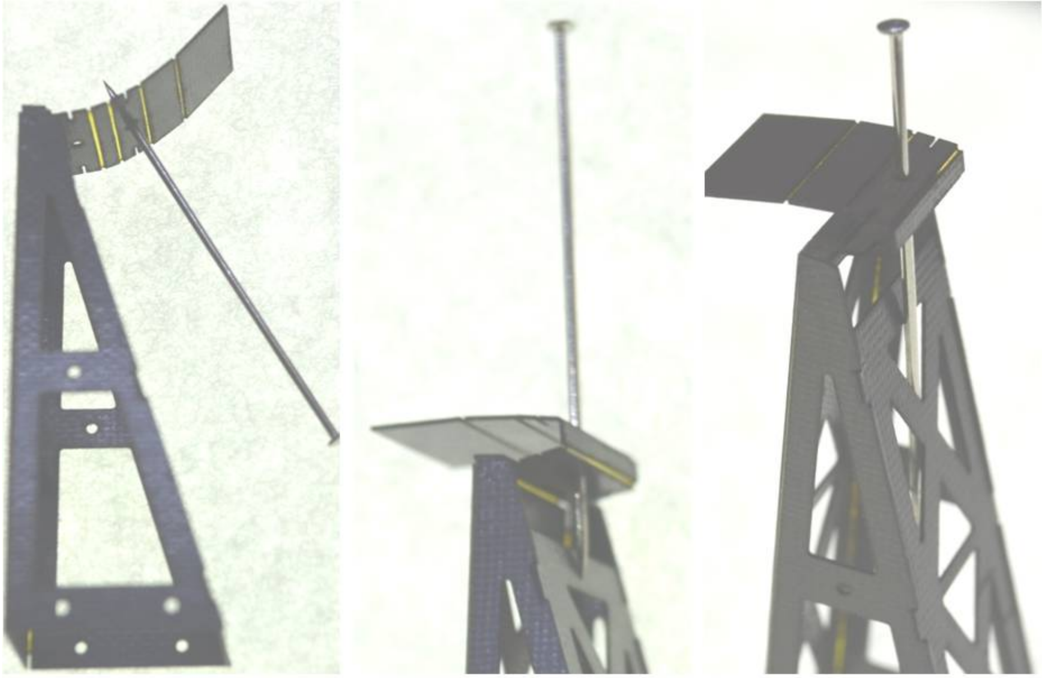

Step 5: Use pin to fold linkage into C-shape

Figure 103: Flapper Assembly Step 5

Step 6: Insert E-clips

Figure 104: Flapper Assembly Step 6

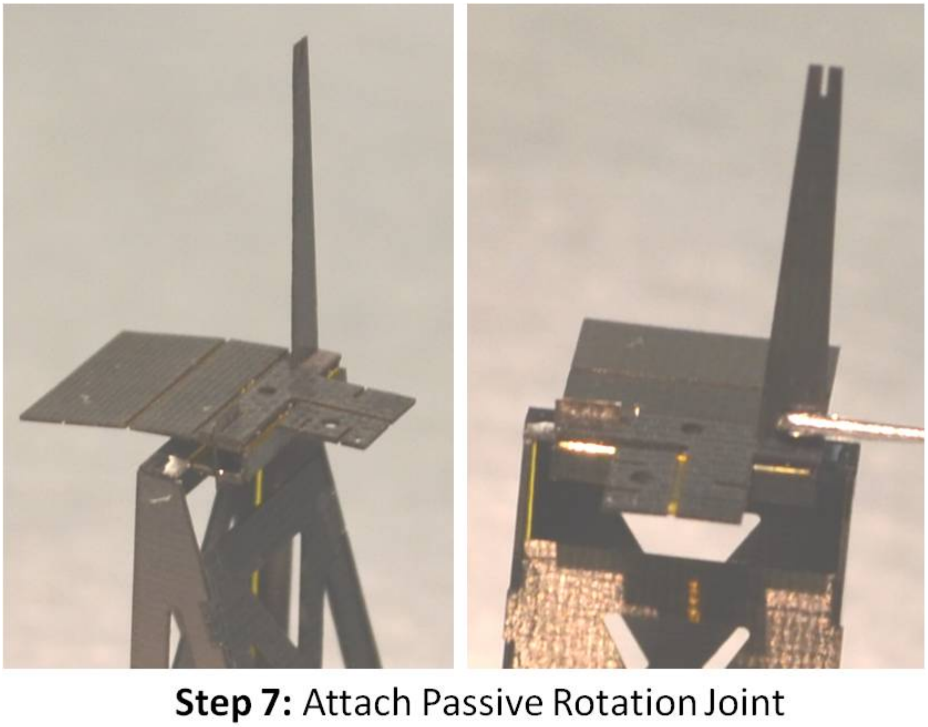

Figure 105: Flapper Assembly Step 7

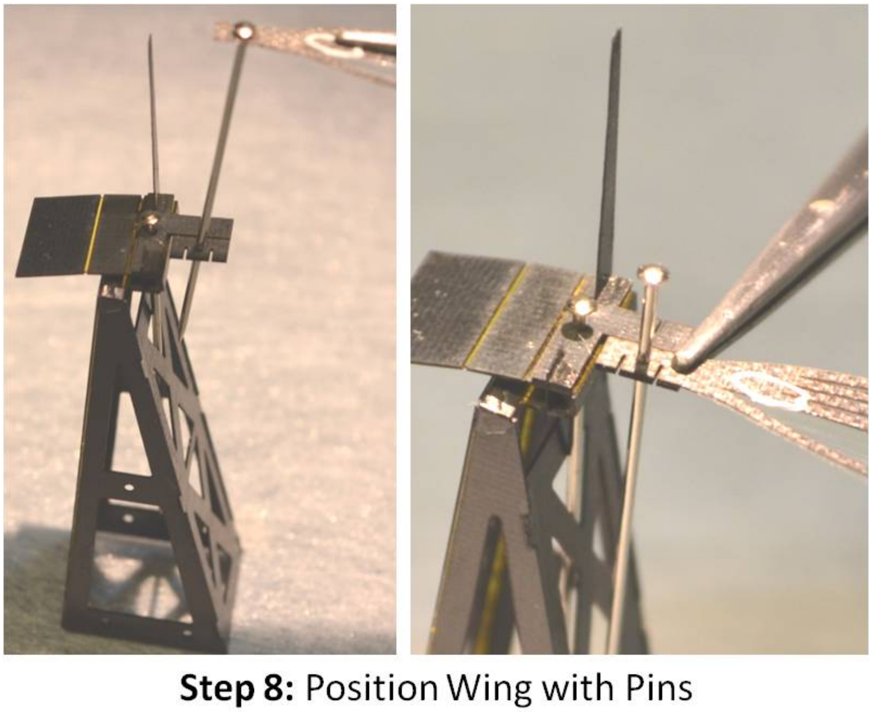

Figure 106: Flapper Assembly Step 8

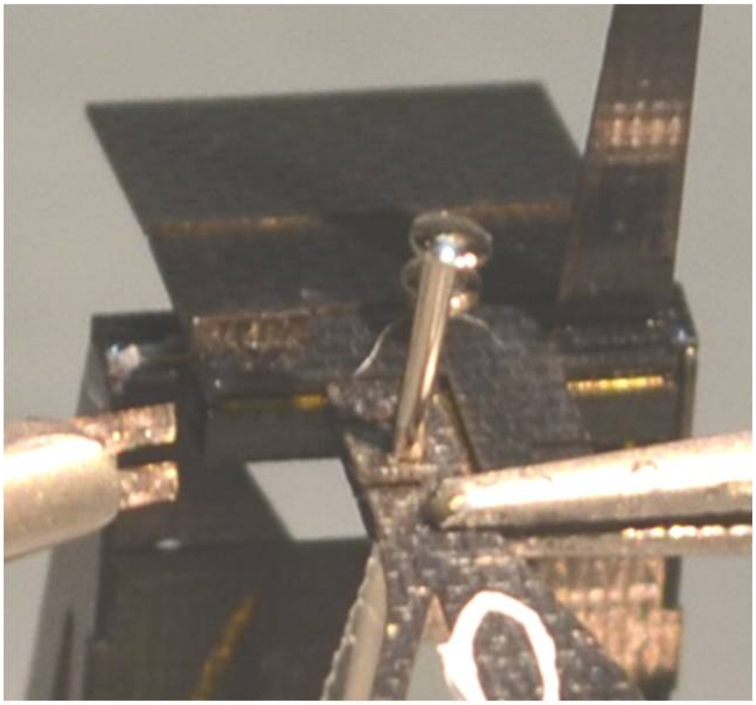

Step 9: Secure Wing with C-clips

Figure 107: Flapper Assembly Step 9

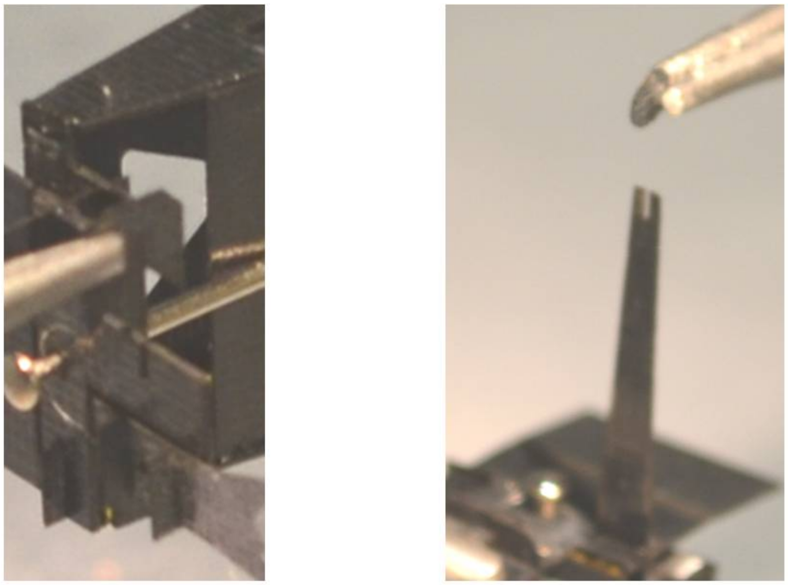

Step 10: Attach Angle Stop

Step 11: Attach Tracking Disc

Figure 108: Flapper Assembly Step 10-11

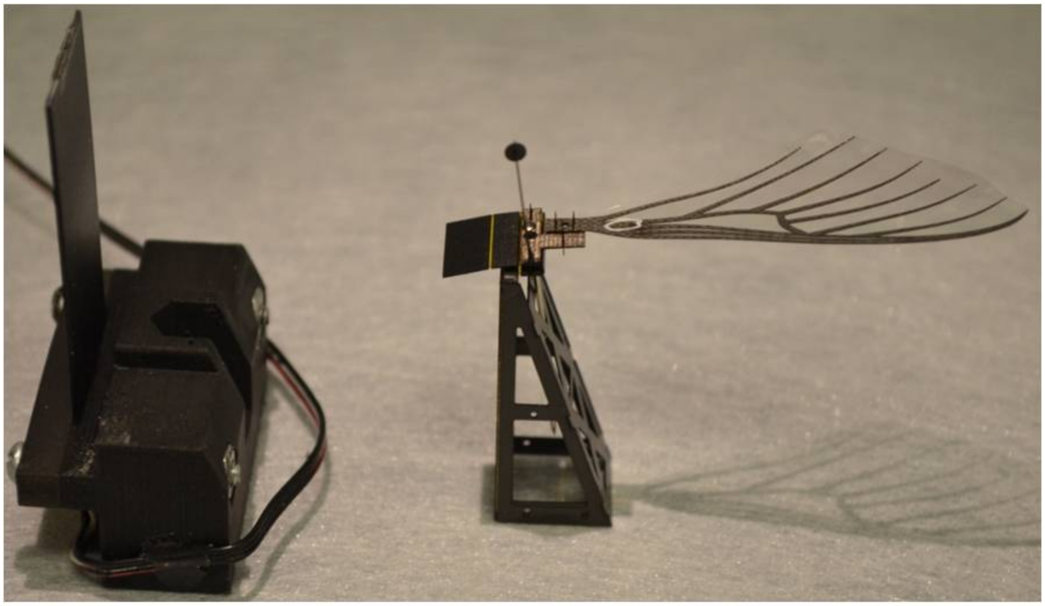

Step 12 : Combine Linkage Assemblies

Figure 109: Flapper Assembly Step 12

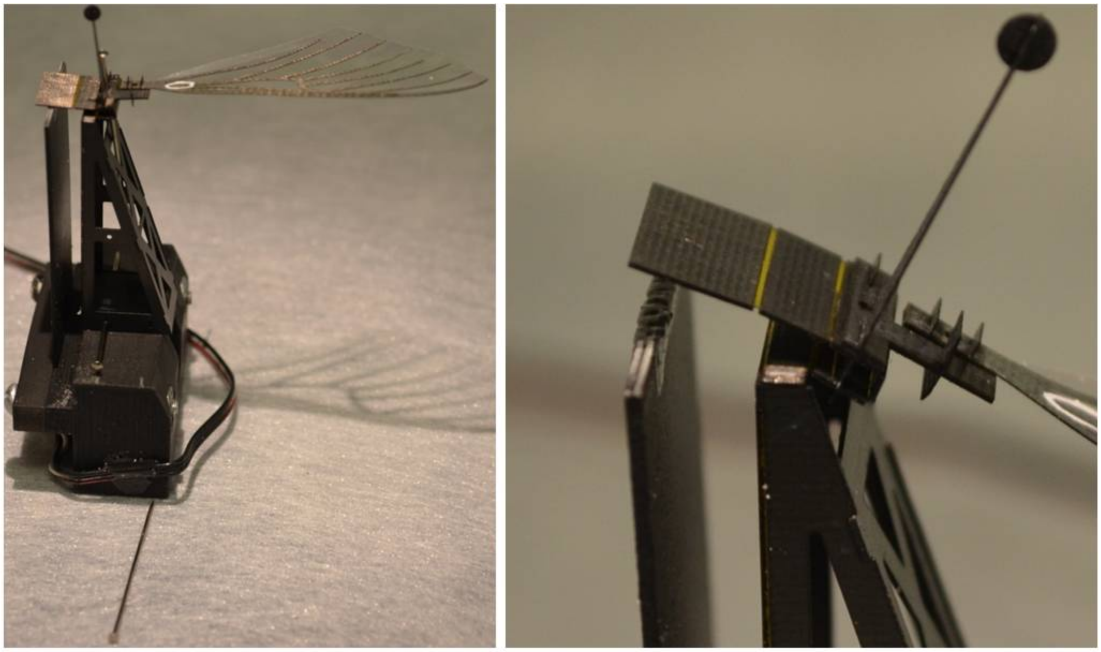

Step 13: Use Pins to Align Base

Step 14: Prep Piezo Tip w/Adhesive

Figure 110: Flapper Assembly Step 13-14

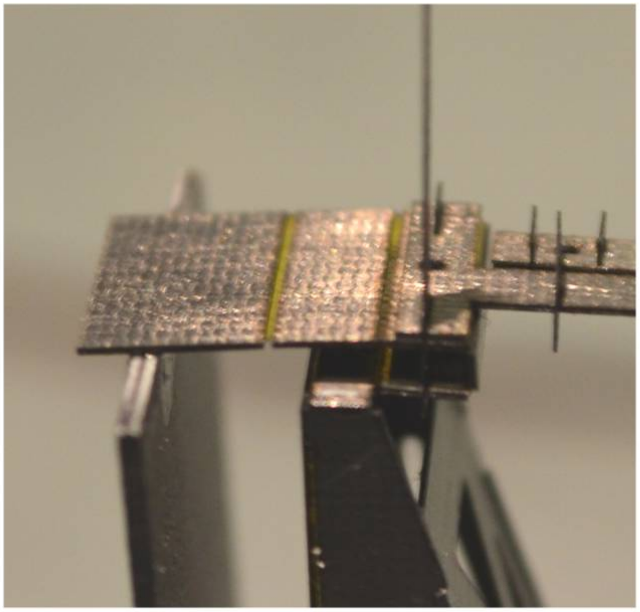

Step 15: Use Heat Gun to Set Crystal Bond

Figure 111: Flapper Assembly Step 15

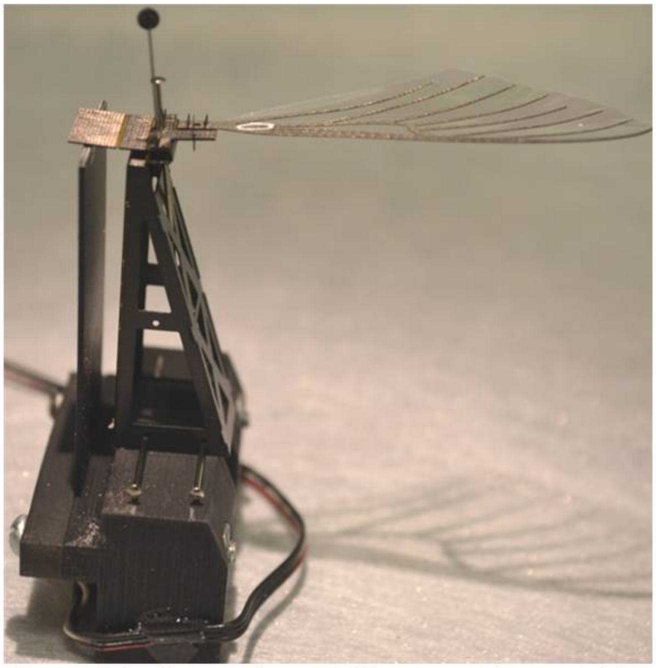

Step 16: Completed Flapper Assembly

Figure 112: Flapper Assembly Step 16

7.3 Experimental Flapping Testbed

With the previously described flapping mechanism designed and assembled, a platform for evaluating the aerodynamic performance of this wing is required. To do this a multitude of rapid prototyped parts and feedback sensors have been used to allow for the evaluation of a single wing or multi wing configuration flapping setup. Critical to this setup are a modular base with a force sensor, tip displacement sensor, and a voltage and current feedback loop. Together, these systems will allow for the experimental quantification of the biological and engineered wings aerodynamic performance.

7.3.1 Modal Analysis.

An experimental modal analysis is performed on all of the engineered wings to determine their first bending and first torsion natural frequencies. The wing is placed into a small clamping device that is lined with a medium density foam on one side of the clamp allowing the wing base held in a clamped condition, but not crushed. The wing and clamping structure are then placed onto a piezo shaker that provided the required base excitation required for modal analysis. A scanning laser vibrometer and a pseudo random excitation allowed for the input and output relationships of the system to be determined. Preliminary tests were performed at 33 locations on the wing as shown in Figure 113. This multi-location scanning allowed for the validation of the first bend and first torsion modeshapes and their eigenvalues. Subsequent tests were performed at a single location at the tip of the wing, as shown in Figure 114, after it was determined that this location was able to correctly identify the correct eigenvalues of the first bend and first torsion modeshapes.

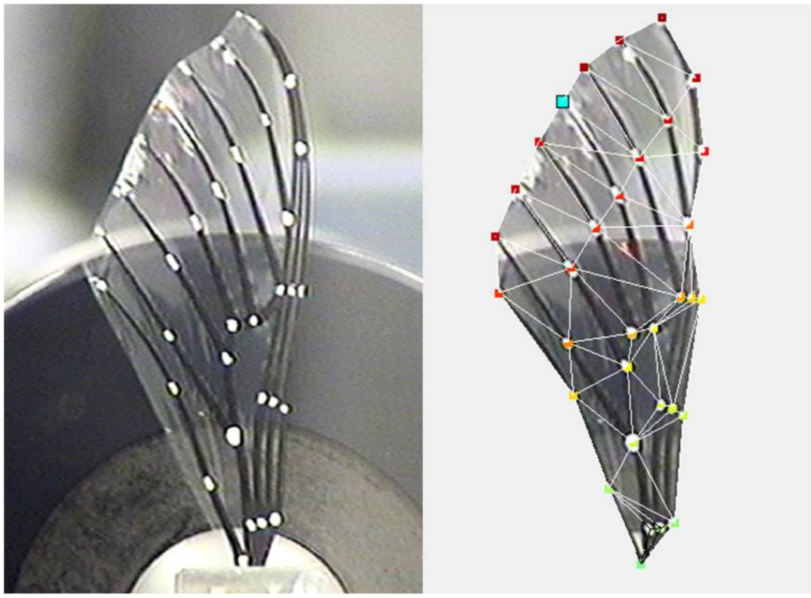

Figure 113: Baseline Engineered Wing and Vibrometry Scan Points

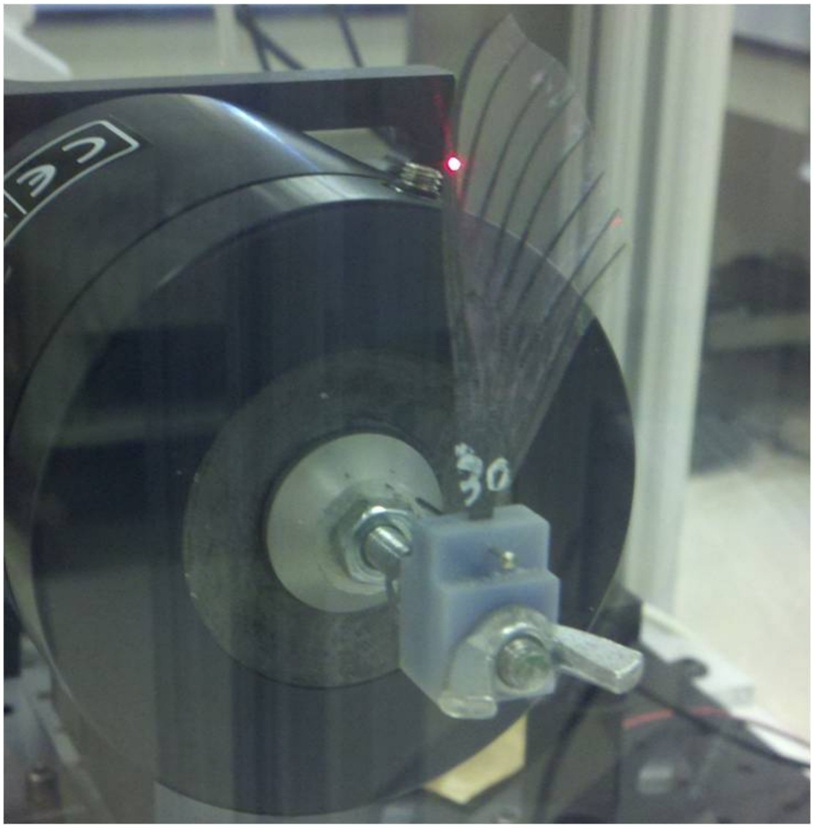

Figure 114: Engineered Wing Single Point Vibrometry Scan Location

7.3.2 Six Axis Force Balance. Due to the modular configuration of an individual flapping mechanism, the ability to mount a second flapping mechanism was designed into a modular base that allowed for the mounting of either one or two flapping wing mechanisms. As such, the performance of a single wing or that of a potential FWMAV configuration could be evaluated. By integrating this modular base onto a six axis dynamic force balance, the real time measurement of aerodynamic forces was accomplished. This small sensor is embedded into the post shown in Figure 115.

In order to reliably measure aerodynamic forces on the order of milligrams, careful selection of the force/torque transducer is essential. To this end a commercially available transducer with the lowest possible resolution was selected to measure flapping forces. This transducer is an ATI Industrial Automation Nano-17 TI with analog signal conditioning. Prior testing at AFIT has shown that this transducer is able to resolve forces in the x, y, and z directions greater than 3.3 mg, 2.8 mg, and 1.91 mg [83].

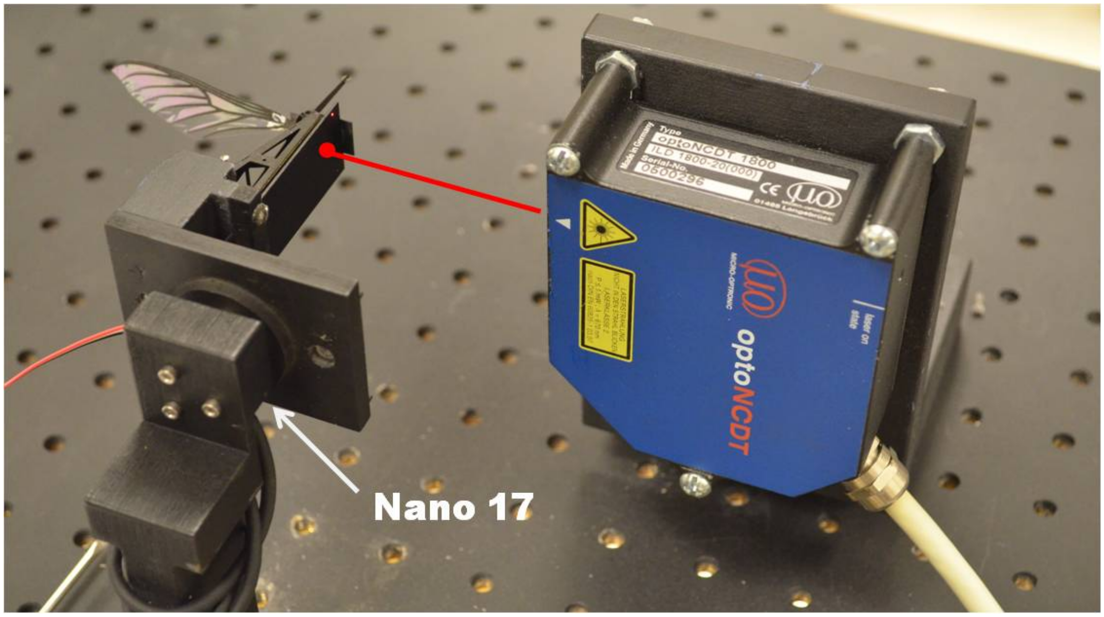

Figure 115: Nano17 Force Transducer and Opto NCDT Displacement Sensor

The Nano-17 measure three primary forces: F_x is the lift force, F_y is the side force, and F_z is the axial force. The aerodynamic lift force is computed as a cycle averaged lift force of F_x over a integer number of cycles. An example of a 3 cycle average of this force is shown in Figure 116 at a sample rate of 5000 Hz.

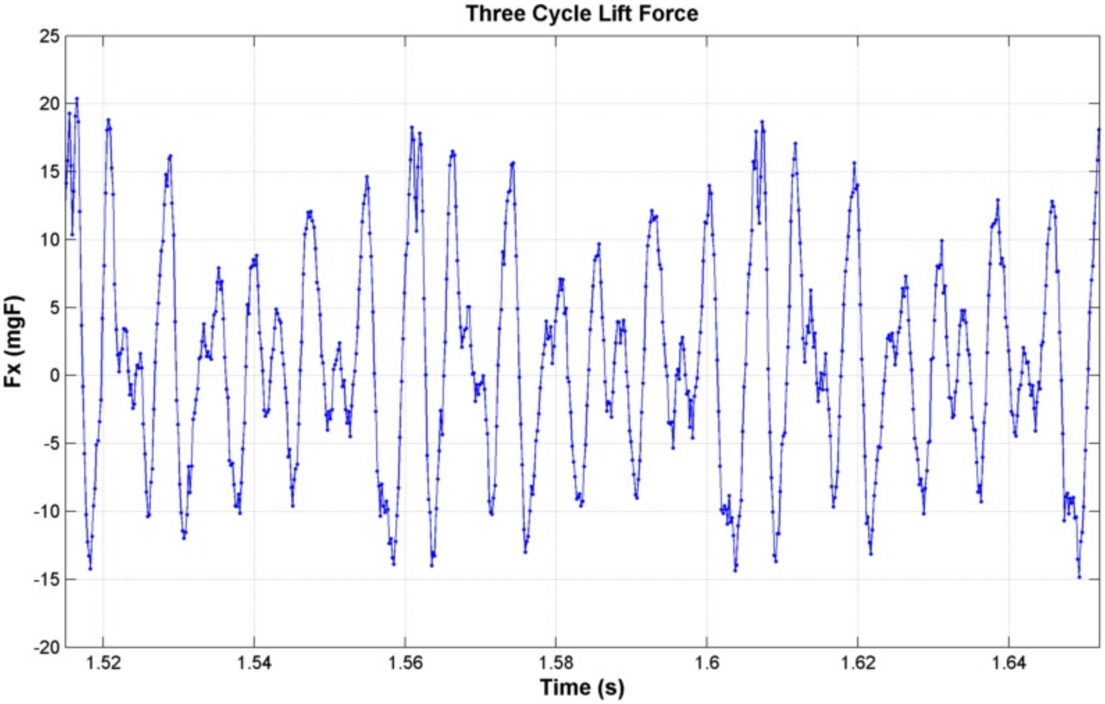

Figure 116: Three Cycle F_x Lift Force

7.3.3 Actuator Tip Displacement. Through the evaluation of the tip displacement, the kinematics of Equation 34 can be evaluated to indirectly determine θ_w of the wing. This is performed with a high resolution intelligent laser-optical displacement measurement sensor. Specifically, the Opto NCDT 1800-20 from Micro-Epsilon has been employed to perform this task as shown in Figure 115. This sensor has a measuring range of 20 mm with a resolution of 2 μm at a measuring rate of 5000 Hz.

7.3.4 Power Measurement. As previously described, the sinusoidal drive signal and DC bias signal are amplified by 30X. This is done by using a Trek Inc. Model PZD700 M/S high voltage piezo amplifier that is capable of generating ±700V at ± 200 mA. This amplifier is also unique in that it provides both a buffered low-voltage replica of both the high voltage output (1V/200V) and the load current (1V/10ma). Together, these two values can be used to determine the power that is consumed through the use of Equation 38 [38].

$$P = I_{rms} \cdot V_{rms} * \cos\theta \begin{cases} V_{rms} = \frac{V_{peak}}{\sqrt{2}} \\ I_{rms} = \frac{I_{peak}}{\sqrt{2}} \\ \theta = Phase\ Shift \end{cases} \tag{38}$$

For our purposes the phase shift of the voltage and current signals is performed by taking the Fast Fourier Transform (FFT) of the two signals over the same time period. The phase angle is the phase difference between the two signals. Through the implementation of this methodology the power required to flap at a particular frequency and amplitude has been determined.

7.3.5 High Speed Imagery. The use of three X-Stream XS-4, black and white, 512x512 pixel resolution cameras capable of capturing 8000 images at 5000 fps from IDT Vision were used to provide insightful visual feedback on the flapping performance of the wings. These cameras were used in a three view configuration. The first view was a top down view that provided visual indication of the flap angle θ_w of the wing. The two remaining cameras were used in a stereo configuration oriented such that they were able to capture the wings passive rotation at up and down stroke reversal. Through the use of a left and right view camera and by performing a precision calibration of the cameras optics and relative orientation to each other the three dimensional location of points along the wing were determined [31, 56].

Figure 117: Synchronized Three View High Speed Camera Images

7.3.6 Point Tracking. For the purposes of evaluating the experimental deformation of either the biological or engineered wing under flapping conditions, it is required that a method be used to measure the actual stroke angle of the wing. Through the use of the top view high speed camera and the addition of a small tracking disk to the wing flapper this can be accomplished using image tracking techniques. Simple black and white thresholding and normalized 2-D cross-correlation [30, 31, 45, 56] techniques were implemented to identify the centroid of the tracking disk, frame by frame, to determine the flap angle of the wing. Presented in Figure 118, is the tracking of this disc and the resulting stroke angles associated with a flapping test.

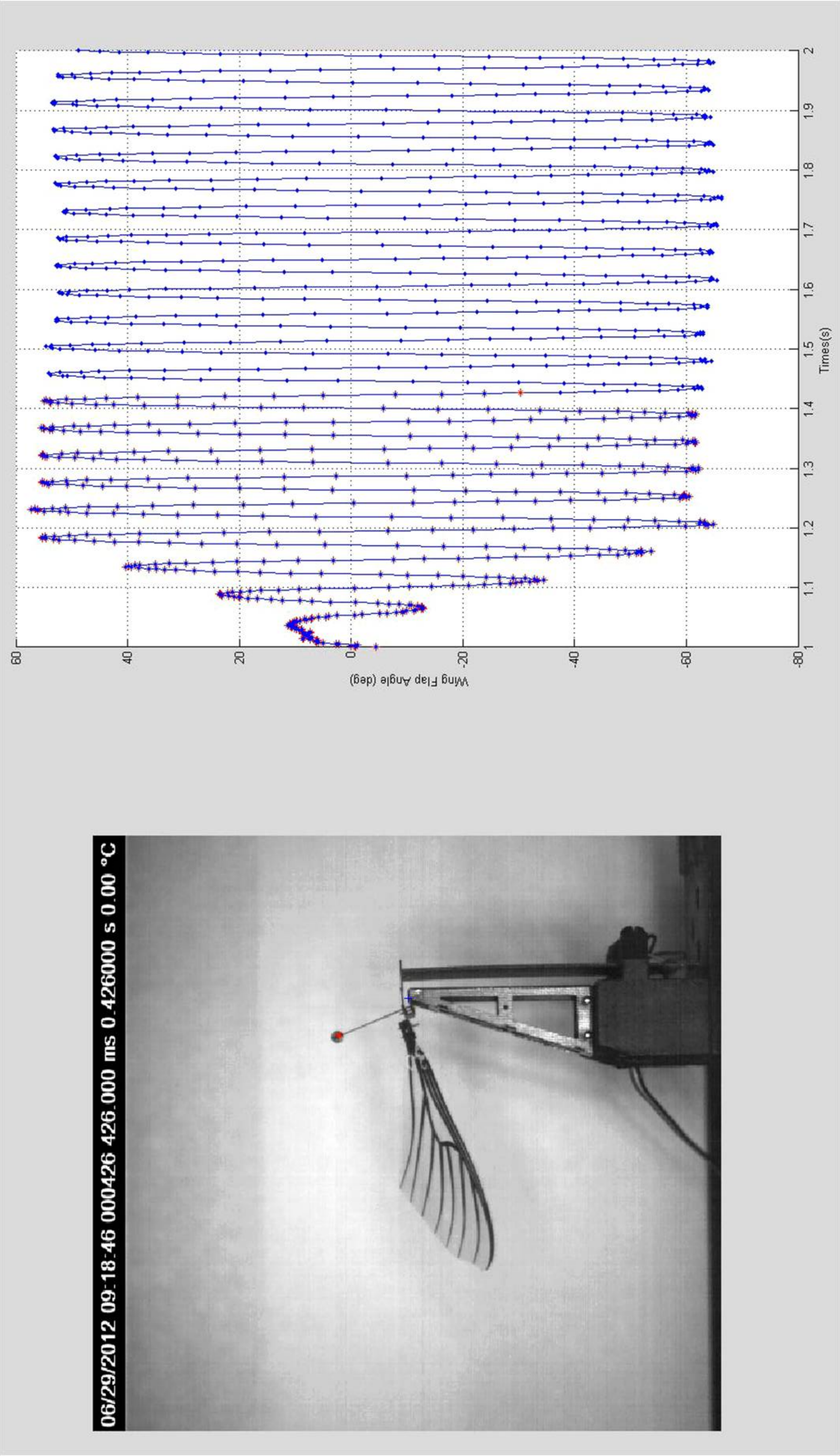

Figure 118: Point Tracking of θ_w Indicator

7.4 Experimental Results

Presented here are the results of the experimental tests that were performed to determine the lift production of a variety of different wings. Specifically, this testing was conducted to experimentally validate that the critical features of the biological wing could be produced in an engineered wing and flapping mechanism such that comparable amounts of lift as the *Manduca Sexta* species could be produced. By experimentally flapping both biological and engineered wings, the thesis statement can be confirmed. Additional testing is provided to draw insightful conclusions about the effects of varying the stiffness of the baseline engineered wing and the effects these have on lift production.

Results of flapping the biological wing with and without scales are presented. Discussion on the impact of the resultant lift and power numbers associated with this comparison will detail the results of this testing and implications for FWMAVs. Testing of the baseline engineered wing is then be presented. This testing includes the determination of maximum lift at the resonant frequency of the flapping mechanism. Presentation of the experimental effects of varying the laser cut angle (Alpha) on the baseline engineered wing and the resultant resonant frequencies, ratio of modes, and maximum lift is completed. Similarly, the experimental effects of varying the inner laminate angle is presented with the same measures. Finally, a summary of the experimental results and the determination of the effects of varying the ratio of modes for a variety of wing are presented.

7.4.1 Biological Wing with Scales.

A single right forewing from an adult female *Manduca Sexta* was liberated from the host and immediately placed upon the flapping mechanism. The duration from harvesting to mounting and the beginning of testing was less than 5 minutes. This wing conveniently had a 55 mm length and 20 mm chord with a mass of 34.6 mg. This is nearly identical to the wing that was chosen to represent the geometry of the base line engineered wing. The resonant frequency of the flapping mechanism and biological wing with scales was determined to be 22.3 Hz. The wing was then put through an automated tuning sequence that incrementally increased the amplitude and η values of Equation 36. This was done in a manner such that a symmetric tip displacement of the piezo actuator was achieved. This auto tuning routine was run until 0.8 mm of tip displacement was achieved. After this, the amplitude and η values were manually tuned to achieve maximal angular displacement of the wing, θ_w, and maximal lift force. The results of this incremental testing are depicted in Figure 119. In the first subplot, the three axes of force are presented, where F_x is the lift force, F_y is the side force, and F_z is the axial force. The x-axis for the force plots represents the amplitude, A, of the sinusoidal drive signal. In the second subplot, the x-axis is the power required to generate a particular force value. From these plots it can be seen that a linearly increase in the amplitude, A, generates a corresponding linear increase in lift force. As voltage increases you would expect to see a linear increase in power consumption as well. However, there is a diminishing return in lift production in terms of power consumed at these higher voltages. A maximum lift force of 1042.3 mgF was produced and required 3.9 mW of power to end with a lift to power ratio of 0.267 mgF/W.

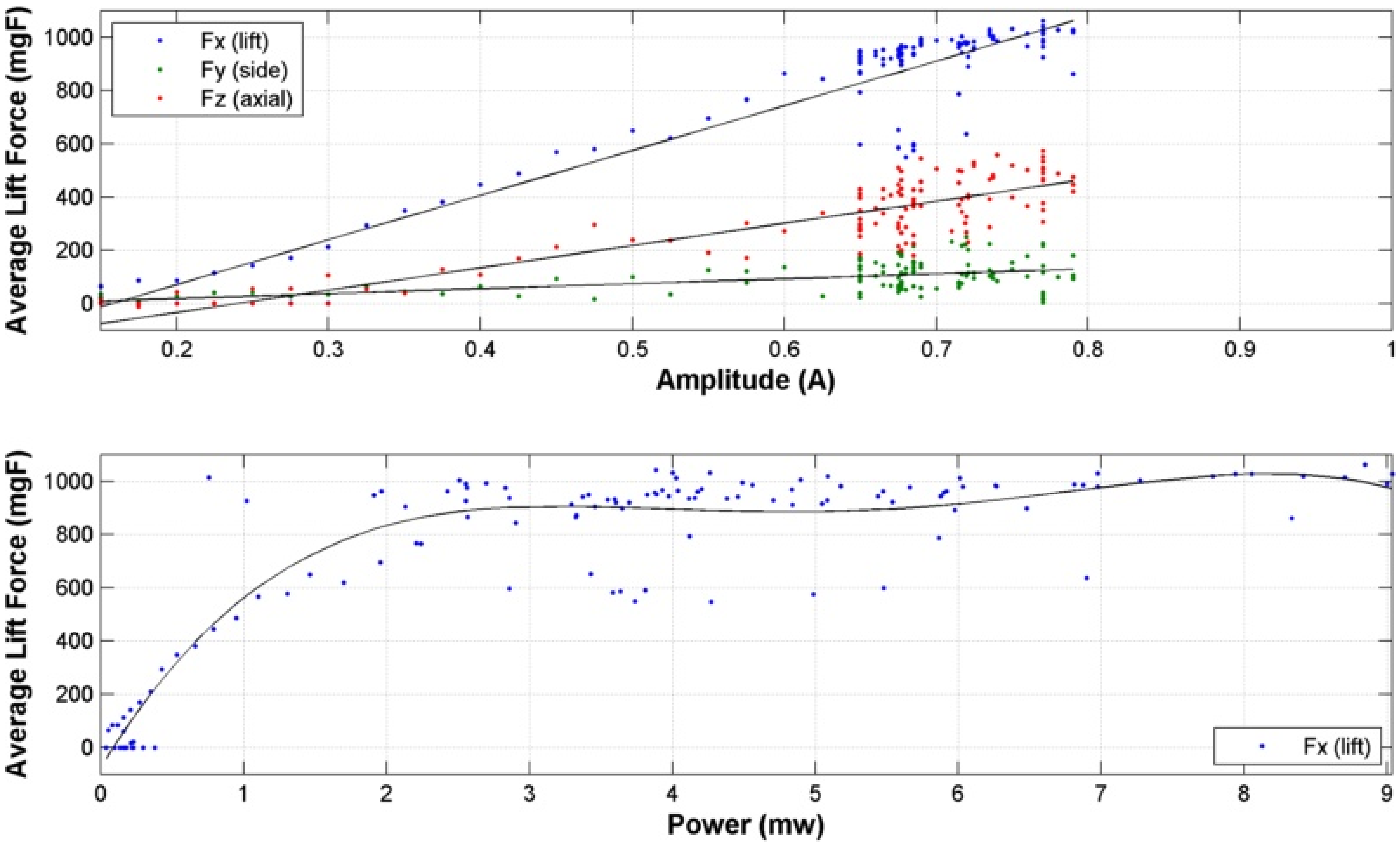

Figure 119: Biological Flapping Analysis with Scales

7.4.2 Biological Wing without Scales. The same wing that was used in the previous section is used here to determine the amount of lift that is possible with the scales removed from the biological wing. Previous testing from Chapter III revealed that the scales of the forewing can represent up to 20% of the wing mass. The determination of the true effects of the wing scales on aerodynamic performance has not been previously completed. Additionally, the engineered wings do not possess the scales present on the biological analog. By removing the scales of the wings their effect on aerodynamic performance can be calculated and a baseline target for lift can be identified for comparision to the engineered wing.

The scales of the forewing were removed in the same manner as the morphological tests that were performed to determine the loss of mass due to the removal of the scales from the forewing. Care was taken to ensure that the underlying wing membrane was not damaged or torn. Because the wing was permanently affixed to the wing flapping mechanism the mass of this wing was not taken with scales removed. Time from the removal of the scales to the completion of this test was less than 10 minutes. Auto tuning and determination of maximal lift was performed identically to the previous test. The results of this testing are presented in a like manner in Figure 120. A maximum lift force of 969.79 mgF was produced and required 3.1 mW of power, thus providing a lift to power ratio of 0.312 mgF/W.

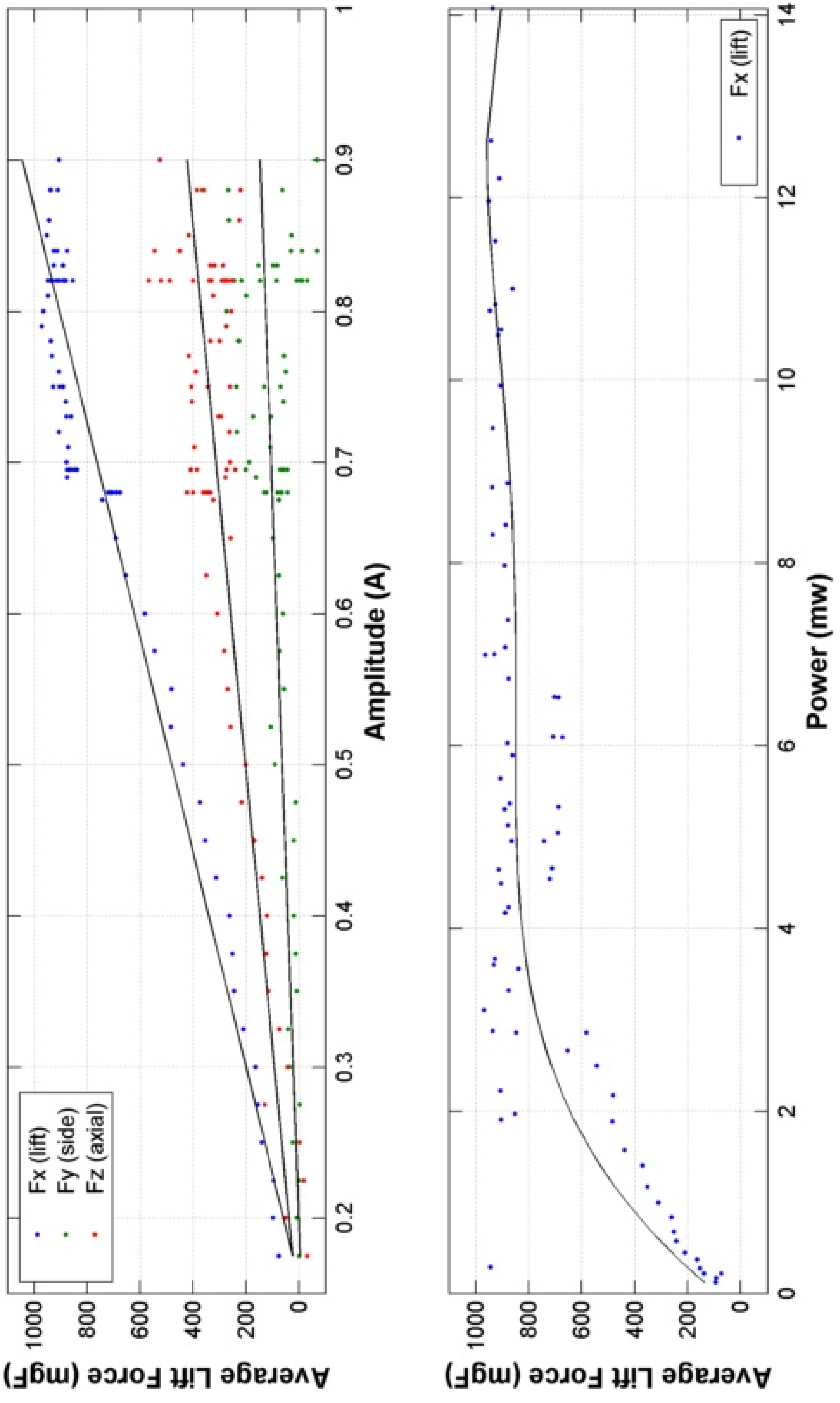

Figure 120: Biological Flapping Analysis without Scales

A comparison of the upstrokes of the two biological wing tests is presented in Figure 121. This side by side comparison allows for the visualization in the similarity in total stroke travel and path. Despite the similarities in stroke travel there is a significant difference in the amount of lift produced. Specifically, a difference of 72.51 mgF or 7% of the maximal lift of the biological wing with scales attached. Although this difference is considerable, higher lift comes at a price. The price in this case is the 0.8 mW of additional power that is required to generate this additional lift. Overall, both of these tests conclude that if another wing was present, it can be assumed that the amount of lift that would be capable of being generated would be 2X what is generated in these tests. Doubling the lift of a single wing would yield 2000 mgF of lift. Considering that the average *Manduca Sexta* specimen weighs 1550 milligrams this would result in a lift to weight ratio of 1.29. A lift to weight of 1.29 is more than enough to allow *Manduca Sexta* to hover and maneuver with extreme agility as can be seen by observing this specimen in flight.

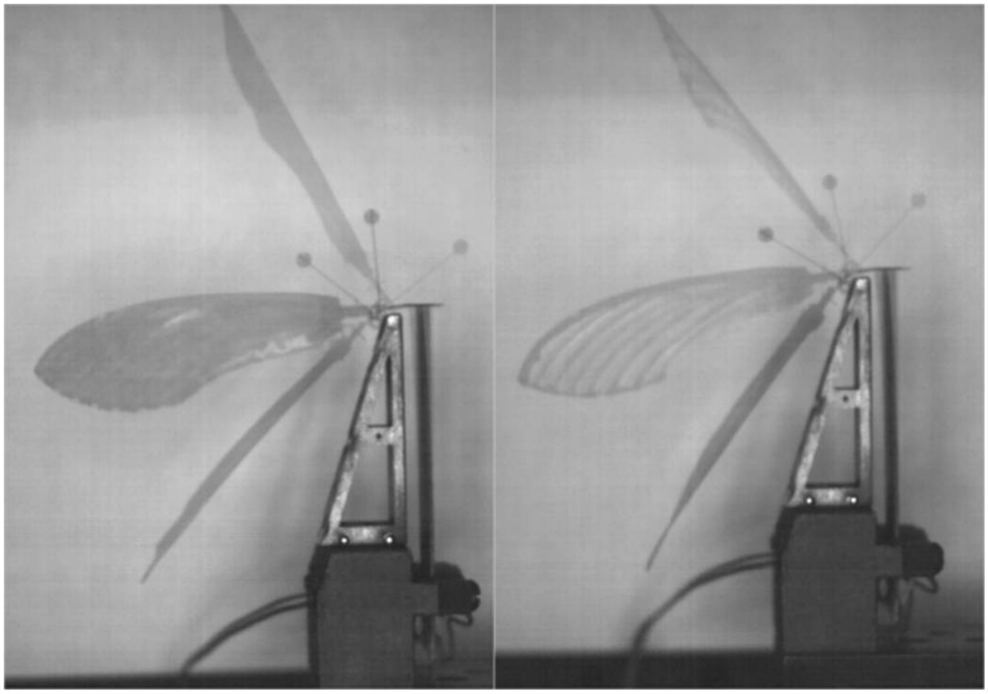

Figure 121: Flapping of Wing with Scales and Without Scales

7.4.3 Baseline Engineered Wing Design. With the completion of testing of the biological wing it is now possible to begin analyzing the baseline engineered wing design. Using the exact same experimental flapping setup and test procedures that have been previously presented the aerodynamic performance of the wing and the relative power that is consumed can be determined. Using a side by side comparison, as shown in Figure 122, the similarity between the biological wing without scales and the baseline engineered wing, on the upstroke, is nearly identical. As presented in Figure 123, the resulting forces and power consumed from the amplitude sweep is presented. A maximum lift value of 893.25 mgF is produced at a power requirement of 2.23 mW. As compared to the biological wing with scales this is a difference of 149 mgF or 14.3% less lift. When compared to the biological wing without scales there is only a difference of 75.8 mgF or 7.8% less lift. Despite this initial difference, the baseline engineered wing design has produced lift comparable to the biological specimen for which the wing was designed to mimic. Additionally, the engineered wing was capable of producing this maximal lift at 2.2 mW. This is a reduction in required power from 1.7 mW to 0.9 mW. As such, the lift to power ratio for the baseline engineered wing is 0.401 mgF/W. Based on this metric the baseline engineered wing exceeds the biological wing in terms of lift generated per unit of power required.

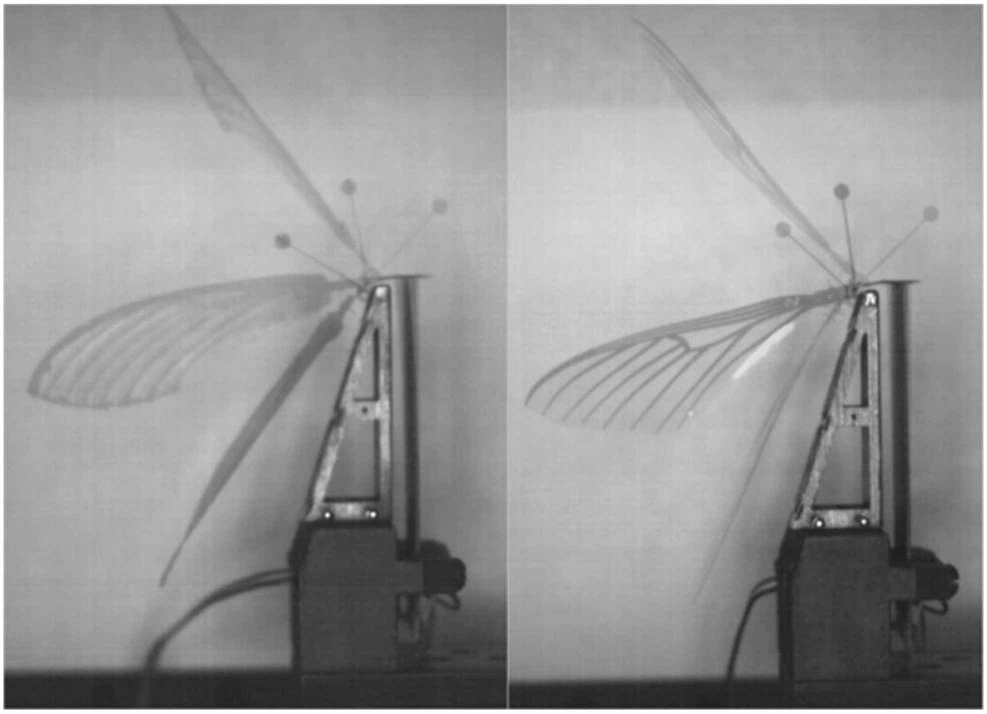

Figure 122: Flapping of Biological Wing Without Scales and Baseline Engineered Wing

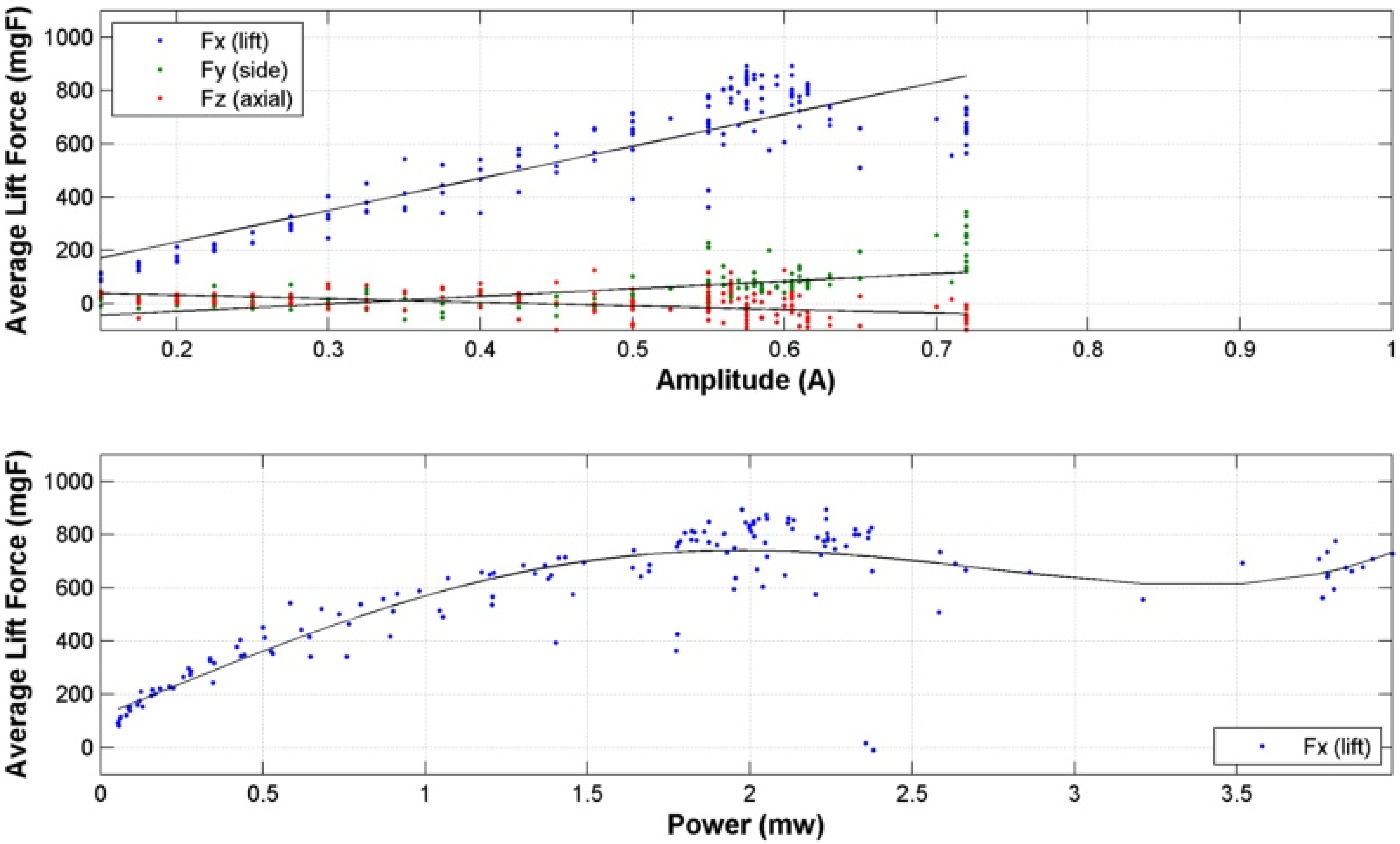

Figure 123: Baseline Engineered wing Flapping Analysis

7.4.4 Experimental Alpha Analysis. Presented in Section 6.3.2 a single variable analysis was conducted to analytically determine the effects of varying the laser cut angle of the wing relative to the global axis of a 0/90/0 laminate. It was determined that this factor would allow for the baseline engineered wing's stiffness to be varied such that the ratio of modes could be varied from 1.19 to 3.11. By changing this factor the determination of relative bending stiffness to chordwise stiffness, expressed through the ratio of modes, and the impact this has on aerodynamic lift could be evaluated. In doing so, the determination of the optimal stiffness of the wing could be explored. Our evaluation of the laser cut angle will focus on determining the experimental ratio of modes and then the maximum aerodynamic lift of multiple wings at varying cut angles.

The experimental first bend and first torsion resonant frequencies were determined as defined in Section 7.3.1. Baseline engineered wings were cut at 0, 7.5, 15, 22.5, 30, 37.5, and 45 degrees respectively. The resulting first bend, first torsion frequencies, and the ratio of these modes are plotted in Figure 124. The linear trendlines in each of the plots show the relative slope of each of the factor outputs. Relative to each other, the analytical and experimental outputs have very similar slopes. However, there is a distinct difference in the slope intercepts of the trendlines of each factor. For the first natural frequency the analytical model over predicts the wings first bend natural frequency. This is unfortunate in that for experimental testing it is desired to have a wing such that the first bend natural frequency is 2X the flapping frequency as is found in the biological system. While for the first torsion natural frequency, the analytical model under predicts the experimental response. As was shown in Section 5.1.4.4, the three layer composite laminate layup is very sensitive to variations in the ply layup. To properly tune the analytical model predictions, these manufacturing variations should be reflected in future analytical test cases. Finally, in terms of the ratio of these modes, the spread of the analytical prediction from 1.19-3.11 was not achieved experimentally, rather a much larger spread of 1.77-4.62 was achieved. In order to determine if a ratio of modes of 1.85 is an ideal stiffness, it would have been preferred that the lowest ratio of modes be less than the experimentally tested value of 1.77.

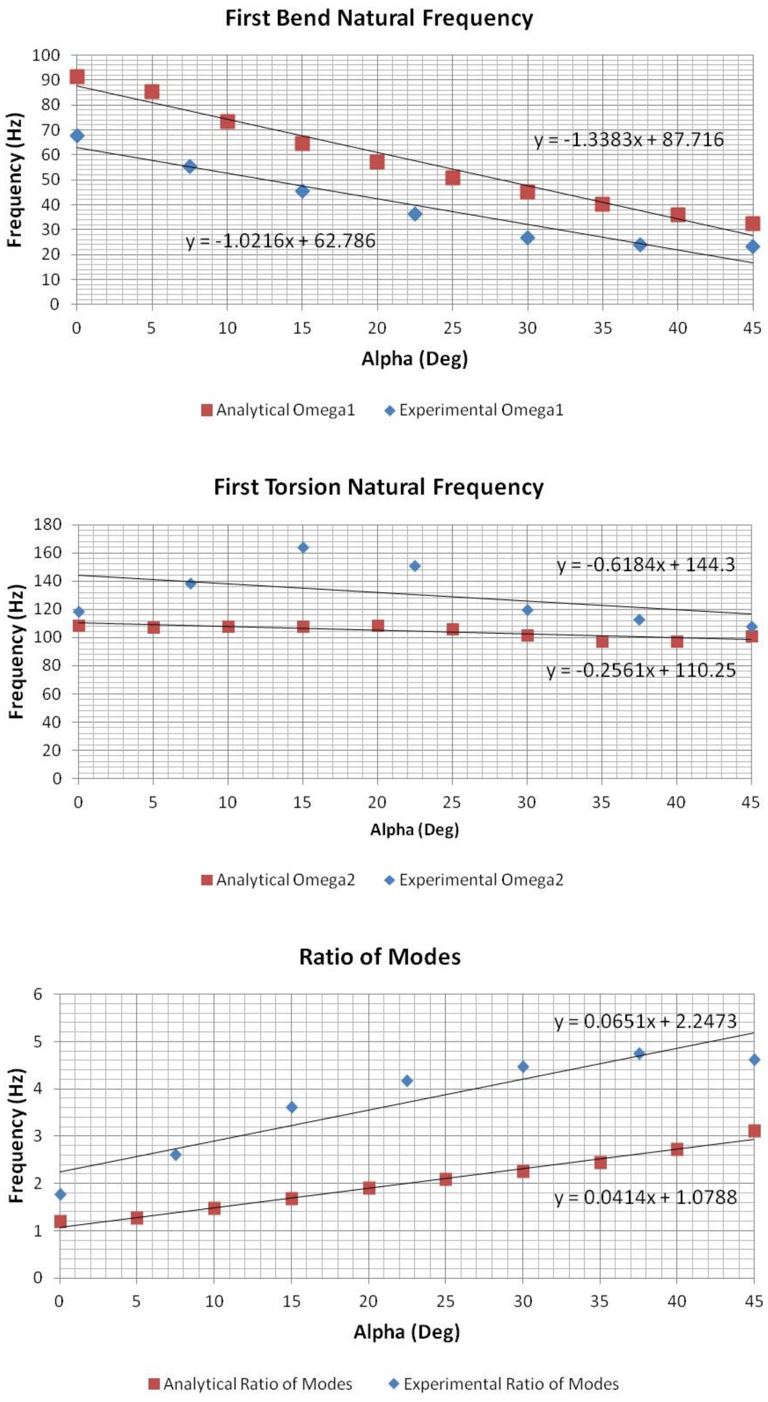

Figure 124: Experimental Alpha Modal Analysis

Upon the completion of the modal analysis of each of the wings they were placed into the experimental flapping testbed and tested as previously described for the biological baseline engineered wings. As such the maximum lift produced was recorded and is plotted in addition to the wings relative ratio of modes in Figure 125. Using this plot the effect between lift production and the ratio of modes is readily apparent in that as the wing ratio of modes increases there is a nearly inverse decrease in lift production.

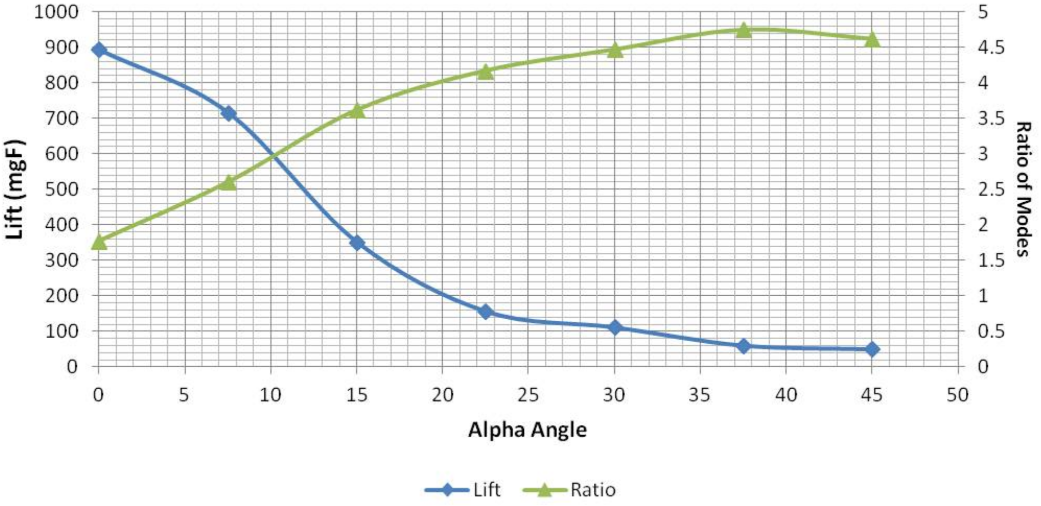

Figure 125: Experimental Alpha Lift Results

Lift production for wings where Alpha > 15° do not produce significant amounts of lift. The fact that the first bending frequency of these wings is less than 2X allows for the modal participation factor of this mode to come into play in the flapping dynamics. As the alpha angle increases so does the flexibility of the wing such that the tip displacement of the wing increases greatly and lags significantly behind the motion at the root of the wing. This causes severe implications in the wings ability to passively rotate at stroke reversal and results in a net decrease in the ability of the system to generate lift.

7.4.5 Experimental Laminate Analysis. By varying the alpha cut angle experimental testing of wings that are less stiff than the baseline engineered wing were tested. As the stiffness of the wing decreased so did the ability of the wing to generate lift. By varying the inner laminate angle from a 0/90/0 configuration to a 0/20/0 configuration we will attempt to produce a stiffer wing, where the inner lamina fiber orientation will follow more closely the local axis of the venation. Experimental modal analysis and aerodynamic performance was characterized for four different inner lamina orientations at 20, 30, 45, and the baseline orientation of 90 degrees respectively.

The results of the inner lamina effects on the resonant frequencies and the ratio of modes from these responses are presented in Figure 126. Once again, the analytical model under predicts the first bend natural frequency of the wing, but does correctly predict a decreasing slope as the inner lamina angle increases. In terms of the first torsional mode, the analytical model is able to closely match both the slope intercept of the experimental test and the overall trend of a small decrease in the resonant frequency of this modes as the inner lamina angle orientation is increased. Finally, due to the analytical models over prediction of wing stiffness the analytical ratio of modes is much smaller at 1.24 versus the experimental value of 1.78. Once again, experimental testing has shown that by only changing fiber orientation the baseline engineered wing design stiffness cannot be changed in a fashion to achieve a wing with a ratio of modes greater than 1.78.

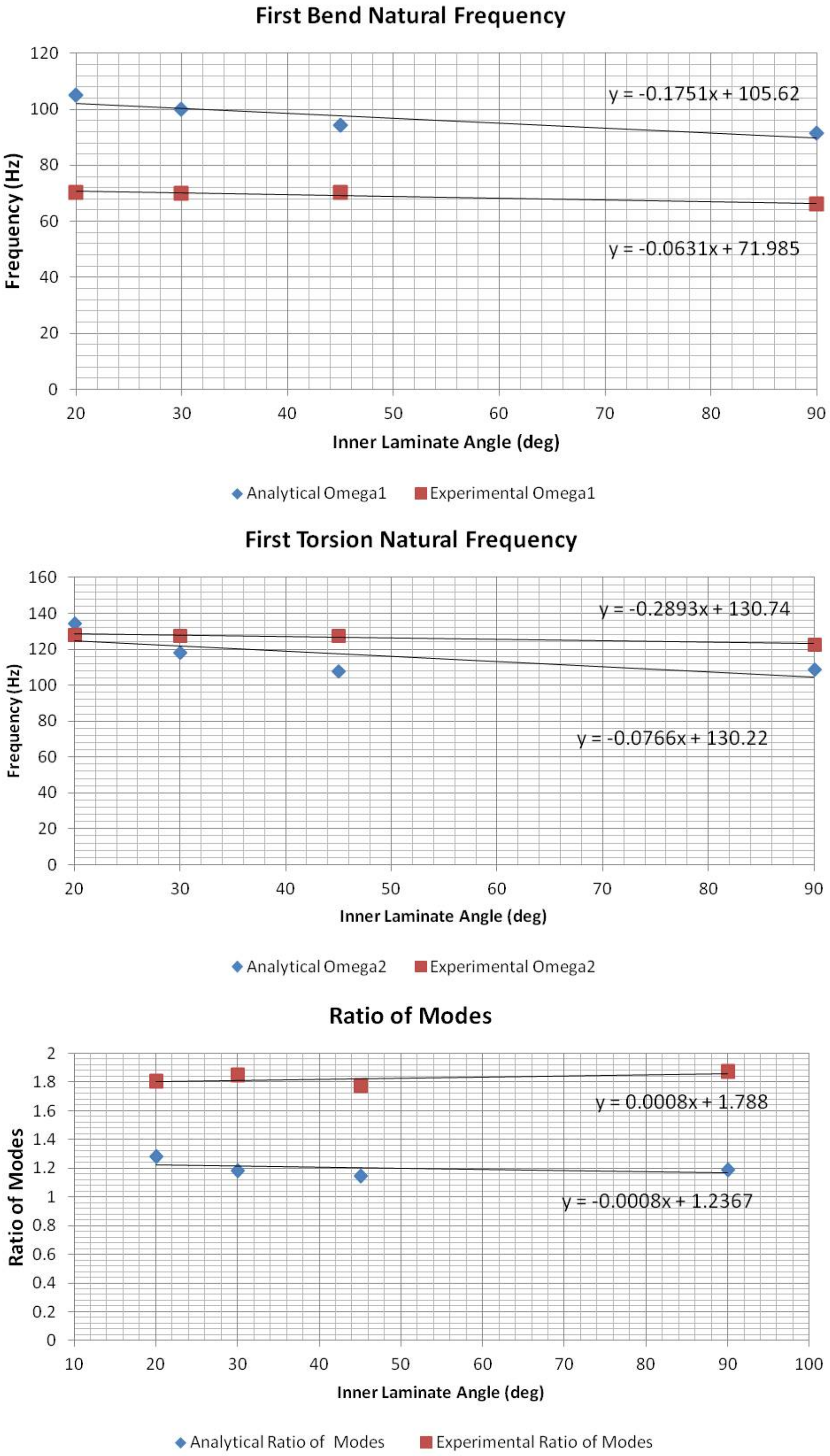

Figure 126: Experimental Laminate Modal Analysis

Despite the experimental modal analysis, that shows only a small difference in the experimental ratio of modes, the wings were flapped to determine which of the lamina orientations produced the highest aerodynamic performance. Once again, the wings were flapped in a manner consistent with the previous tests. The results of this testing are presented in Figure 127. From this chart we can see that an inner laminate orientation of 30° produces the most lift when compared to the other lamina orientations. In fact, this value represents the largest lift of any of the engineered wings presented in this study at 964.8 mgF and consumes 2.55 mW of power with a lift to power ratio of 0.378 mgF/W. This lift value is within 3 mgF of the biological wing without scales and is able to produce this nearly identical amount of lift with 0.55 mW less power. In this sense, the baseline engineered wing venation with an inner lamina orientation of 30° not only produces comparable lift as its biological analog, but does so more efficiently.

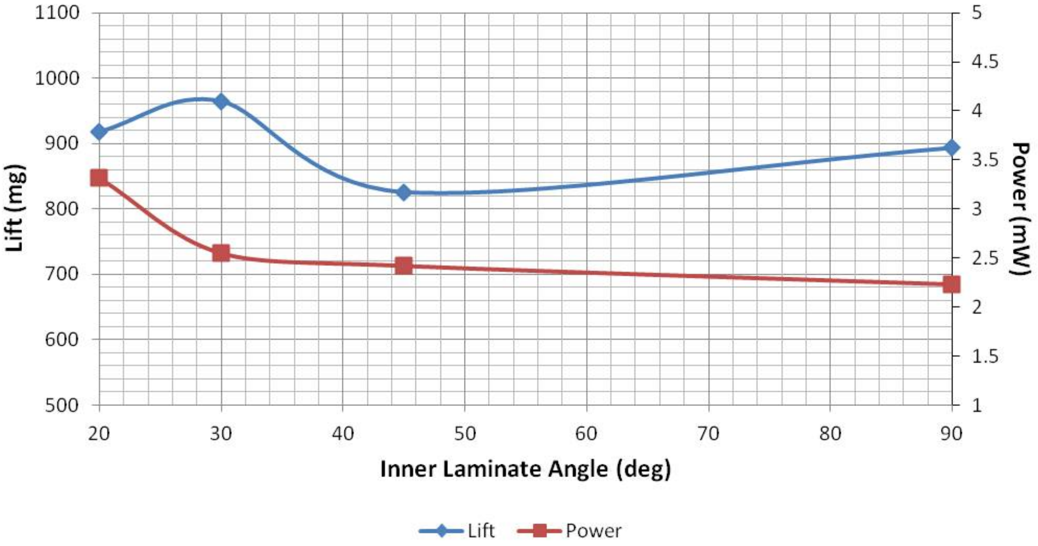

Figure 127: Experimental Laminate Lift Analysis

7.4.6 Ratio of Modes vs. Lift. By investigating the lift generated by numerous engineered wing designs of varying structural stiffness, as represented by their ratio of modes, the determination of the effects of this stiffness can be determined.

By combining the results of the previous factor analysis and plotting them together as shown in Figure 128 the effects of this stiffness upon a wing designs ability to generate lift become clear. The stiffer the wing, a ratio of modes equal to 1.78 for this study, the higher the lift that will be produced. As stiffness decreases, resulting in an increase in the ratio of modes, so does lift. This happens in a linear fashion as shown by the linear trendline in Figure 128. This follows suit with other research that has been conducted and compared the stiffness of comparable wings and their ability to produce lift [93].

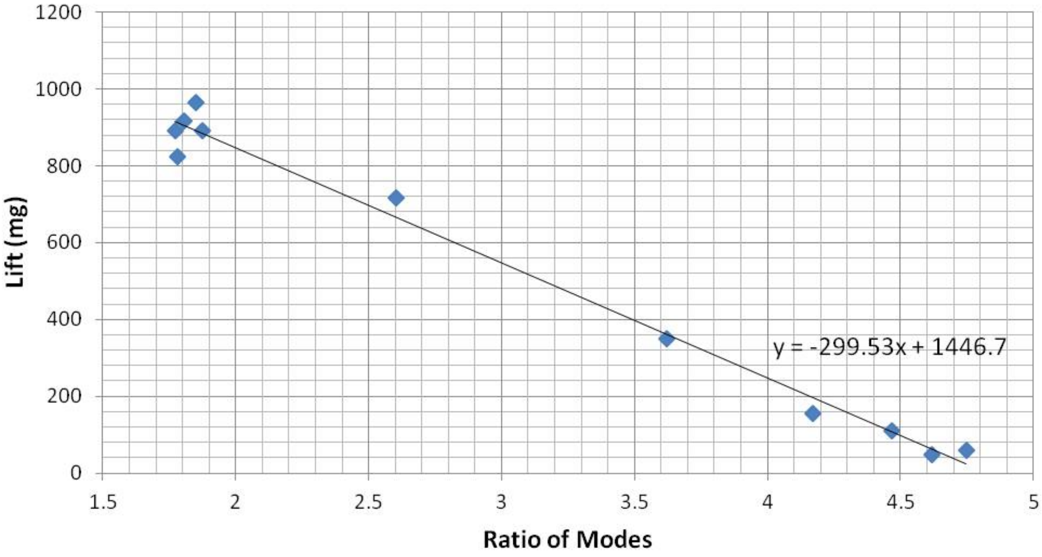

Figure 128: Ratio of Modes Lift Production

7.5 *Summary*

This chapter represents the culmination of an extensive study to determine the aerodynamic performance of both biological wings, with and without scales, and a series of engineered wings under the same boundary conditions. This first ever accomplishment has resulted in the establishment of a method for comparison and qualification of an engineered wing relative to its biological analog. Through the use of force and power measurement, the maximum lift forces and the power required to produce these forces was implemented. As such, an engineered wing was able to match the aerodynamic performance of its biological analog without scales and was able to do so more efficiently. Through this process the thesis statement and primary objective of this research was achieved. Additionally, a general study of the effects of the stiffness of the wings, in terms of the ratio of the first torsion mode relative to the first bending mode, were determined.

VIII. Conclusion

This body of work represents an advance in the state of the art for FWMAVs. Specific focus has been made to apply the art and science of biomimicry to understand the complex forewing structure of the *Manduca Sexta* species. Through the application of critical thought and problem solving associated with multi-disciplinary engineering a biomimetic wing design has been achieved in an unparalleled manner. Throughout this process numerous significant contributions have been made to this ever evolving field in the pursuit of achieving the thesis statement outlined in the beginning of this document:

By carefully characterizing the structural material and geometric properties of the forewing of the Manduca Sexta species it is possible to design, fabricate, and experimentally validate that primary structural features of the biological wing can be produced in an engineered wing and flapping mechanism that produces comparable amounts of lift as the Manduca Sexta species.

The process of confirming this hypotheses began with a thorough review of prior art in the multitude of fields associated with this multidisciplinary problem. A review of the leading technologies associated with the fabrication of biomimetic wings was presented and the considerations associated with the application of each were proposed. A review of candidate flapping mechanisms and the advantages and disadvantages of each design towards application of a FWMAV were conducted. In Chapter II, a review of the *Manduca Sexta* species and the primary structural features of the forewing of this species was presented. A review of the leading technologies associated with the fabrication of biomimetic wings and the considerations associated with the application of each was reported. Additionally, a review of candidate flapping mechanisms was presented and the advantages and disadvantages of each design towards the application of a FWMAV was conducted. Chapter III chronicled a detailed investigation of the morphological features of the *Manduca Sexta* forewing. This investigation led to one of the single most detailed identifications of insect wing morphological properties to include venation and membrane material and structural properties. Based on this study the most detailed parametric three dimensional model of the forewing of the *Manduca Sexta* species was developed and tuned through recursive iteration to match the structural dynamics measured from prior experimental testing in Chapter IV. With a biological FEA model of the wing complete, efforts were made to identify candidate engineered materials that would produce a structure with similar structural dynamics as the biological wing in Chapter V. After the identification of YSH-70, a high stiffness composite laminate, as the venation material and 2.5 μm mylar as the membrane material, an FEA model of a baseline engineered wing was developed in Chapter VI. This model correctly accounted for the unique material properties of YSH-70 under the confines of the model element definitions. The generation and adaptation of the models parametric variable input properties allowed for the analytical investigation and identification and the critical venation structures, the effects of lamina layup, and camber upon the structural dynamics of the engineered wing. With this knowledge in hand, the transition from an engineered baseline wing model into physical reality was made. The identification of implementation of an easy and repeatable manufacturing method was made for both the biomimetic wing, Chapter VI, and also for a biomimetic flapping mechanism, Chapter VII. Experimental testing was conducted to determine the baseline maximal lift production of a biological wing, with and without scales, for comparison to multi-factor variable wing designs. In doing so, the first ever characterization and comparison of biological and engineered wings was conducted under the same boundary conditions and performance feedback equipment. In doing so, an engineered wing was identified that was able to produce lift on the same magnitude and with more efficiency than the biological analog upon which it was based, while confirming the thesis statement upon which this document is based.

8.1 Key Research Goals and Contributions

1. **Detailed Morphological Wing Study of *Manduca Sexta***

   A morphological study was conducted to identify the material and structural properties of a sample of male and female *Manduca Sexta* specimens. The average mass, area, shape, size, and camber of the wing were evaluated using novel measurement techniques. The venation cross section was measured using detailed pathological techniques. The elastic modulus of the leading edge veins and membrance was experimentally determined.

   Contributions

   (a) First database of *Manduca Sexta* species characteristics relative to application to FWMAV.

   (b) First ever measurements of the material properties of the *Manduca Sexta* forewing venation and membrane.

   (c) First documentation of the static camber and development of a mathematical model for the camber of an insect wing.

2. **Parametric Three Dimensional Biological Wing FEA Model**

   Through the application of the previous morphological study, experimental testing, and finite element analysis the structural dynamics of the *Manduca Sexta* forewing were characterized both experimentally and analytically. Laser vibrometry and laser scanning techniques are used to perform modal analysis and static displacement tests for baseline testing of the structure. This testing was coupled with advanced computer vision processing techniques for the automated generation of finite element models (FEA) of the forewing. These models include material properties, venation cross sections, and camber from Chapter III to represent a complete analytical model of the wing. Empirical refinement was used to tune the model to match the results of the experimental testing.

   Contributions

   (a) Generation of the most detailed, biologically based, FEA structural model of an insect wing model to date.

3. **Engineered Wing Material Selection**

   An extensive investigation into the identification of candidates materials that will provide the required mass, stiffness, and manufacturing requirements of an engineered wing is carried out. The identification of such a material is completed and the characterization of this material is validated through extensive material testing.

   Contributions

   (a) Identification and characterization of a thin ply, ultra high stiffness, composite laminate for use with FWMAVs.

4. **Engineered Wing Design**

   Designed and developed a parametric three dimensional engineered wing FEA model that matched the structural dynamics of the *Manduca Sexta* forewing. An extensive design of experiments and two sets of single factor analyses were performed to characterize the critical venation structures and geometry of the wing. Using this methodology a baseline engineered wing was identified and manufactured. The identified manufacturing method is presented and allowed for rapid and repeatable manufacturing of wings.

   Contributions

   (a) Parametric three dimensional engineered wing FEA model.
   (b) Identification of critical input parameters and their effect on the structural dynamics of engineered wings.

5. **Engineered Wing Fabrication**

   Identified, acquired, and implemented the materials, equipment, and process development tools necessary to fabricate bioinspired engineered wings, in house at AFIT, for use with FWMAVs.

Contributions

(a) Delivered in-house capability to fabricate thin ply composite laminate structures for use with FWMAVs.

6. **Designed and Developed a FWMAV Testbed for the Evaluation of Biological and Engineered Wings**

   Through the use of advanced kinematic design and manufacturing techniques a flapping mechanism and associated test hardware was assembled to dynamically flap wings in a manner comparable to the hovering stroke of the *Manduca Sexta*. The ability to characterize the aerodynamic performance and power requirements of a wing were implemented and allowed for the completion of the thesis statement of this document, but also serve as a platform for further development and advancement of FWMAV technology.

   Contributions

   (a) Testbed for the evaluation of wings and flapping mechanism for application to FWMAVs

7. **Conduct a Comparative Experimental Aerodynamic Performance Study Using Biological and Engineered Wings**

   A comparative study was conducted, to determine the aerodyamic performance of a biological wing. The forces associated with lift production and power consumption were measured and identified for biological wings with and without scales. Analysis, of a baseline engineered wing with varying wing stiffness was also conducted. The identification and validation of a baseline engineered wing that produced comparable aerodynamic lift as its biological was completed.

   Contributions

   (a) Measurement of the aerodynamic forces of a biological wing with and without scales

(b) Measurement and identification of a baseline engineered wing with comparable lift production and power consumption as its biological analog.

8.2 Recommendations for Future Work

Presented in this body of work is an extensive and broad study of the use of biomimicry to achieve advancement in the field of FWMAVs. This study has shown that through a thorough and rigorous understanding of a biological system, it is possible to distill the key components that allow this system to function and apply them to derivative engineered designs. This study focused on the forewing of the *Manduca Sexta* species. This is but one small mechanism associated with the requirements necessary to field a complete FWMAV. The methods presented here could easily be applied to other functional areas of the *Manduca Sexta* or similarly related species.

Appendix A

Table 24: Manduca Sexta Mass Properites

SAMPLE	**MOTH**	**FW LT**	**FW RT**	**HW LT**	**HW RT**	**HEAD**	**THO**	**ABD**	**Total**	**Diff**
	(grams)	**(grams)**	**(grams)**	**(grams)**	**(grams)**	**(grams)**	**(grams)**	**(grams)**	**(grams)**	**(grams)**
1	1.3799	0.0324	0.0335	0.0091	0.0091	0.1128	0.5737	0.6017	1.3723	0.0076
2	1.0085	0.0290	0.0300	0.0100	0.0096	0.0671	0.3673	0.4854	0.9984	0.0101
3	0.7687	0.0222	0.0220	0.0078	0.0072	0.0585	0.2683	0.3680	0.7540	0.0147
4	1.6211	0.0327	0.0327	0.0089	0.0113	0.0969	0.6073	0.8101	1.5999	0.0212
5	1.4811	0.0270	0.0296	0.0105	0.0096	0.1056	0.5736	0.6634	1.4193	0.0618
6	1.3464	0.0274	0.0271	0.0102	0.0070	0.1032	0.6517	0.4830	1.3096	0.0368
7	1.9846	0.0412	0.0396	0.0141	0.0176	0.1129	0.7173	0.9687	1.9114	0.0732
8	2.2819	0.0425	0.0437	0.0196	0.0169	0.1313	0.8411	1.1139	2.2090	0.0729
9	2.4539	0.0521	0.0494	0.0176	0.0162	0.1348	0.8288	1.3025	2.4014	0.0525
10	1.5127	0.0396	0.0393	0.0125	0.0120	0.1139	0.6085	0.6478	1.4736	0.0391
11	1.4347	0.0383	0.0380	0.0109	0.0117	0.1084	0.5670	0.6499	1.4242	0.0105
12	1.6253	0.0383	0.0415	0.0130	0.0140	0.1264	0.6688	0.7174	1.6194	0.0059
13	1.0105	0.0273	0.0286	0.0109	0.0097	0.0870	0.3784	0.4667	1.0086	0.0019
14	1.0519	0.0322	0.0334	0.0135	0.0125	0.0894	0.4228	0.4375	1.0413	0.0106
15	0.9206	0.0295	0.0311	0.0100	0.0092	0.0807	0.4014	0.3456	0.9075	0.0131
16	1.0586	0.0339	0.0358	0.0109	0.0117	0.0961	0.4698	0.3938	1.0520	0.0066
17	1.0272	0.0330	0.0321	0.0108	0.0100	0.0958	0.4345	0.4112	1.0274	-0.0002
18	1.3285	0.0369	0.0406	0.0132	0.0136	0.1051	0.5181	0.5959	1.3234	0.0051
19	1.7663	0.0398	0.0469	0.0134	0.0151	0.1070	0.6526	0.7796	1.6544	0.1119
20	1.8652	0.0376	0.0412	0.0130	0.0133	0.1198	0.6599	0.9804	1.8652	0.0000
21	1.8261	0.0456	0.0388	0.0149	0.0152	0.1134	0.6598	0.8105	1.6982	0.1279
22	1.7800	0.0436	0.0473	0.0147	0.0147	0.1377	0.6085	0.8012	1.6677	0.1123
23	1.4826	0.0330	0.0358	0.0116	0.0116	0.1056	0.5233	0.6299	1.3508	0.1318
24	2.0363	0.0468	0.0458	0.0162	0.0163	0.1280	0.6865	0.9553	1.8949	0.1414
25	1.9020	0.0313	0.0326	0.0112	0.0112	0.1156	0.6020	1.0991	1.9030	-0.0010
26	1.3830	0.0277	0.0294	0.0090	0.0103	0.0999	0.5702	0.5606	1.3071	0.0759
27	2.7016	0.0349	0.0414	0.0145	0.0150	0.1324	0.7464	1.5976	2.5822	0.1194
28	0.9116	0.0186	0.0199	0.0096	0.0078	0.0842	0.4236	0.2976	0.8613	0.0503
29	1.1571	0.0245	0.0261	0.0080	0.0091	0.0866	0.5696	0.4153	1.1392	0.0179
30	2.4833	0.0408	0.0395	0.0154	0.0175	0.1162	0.9179	1.2606	2.4079	0.0754
AVG	**1.55304**	**0.03466**	**0.03576**	**0.01217**	**0.01220**	**0.10574**	**0.58396**	**0.72167**	**1.50615**	**0.04689**
STD	**0.50759**	**0.00767**	**0.00747**	**0.00286**	**0.00311**	**0.01939**	**0.14861**	**0.32059**	**0.48336**	**0.04658**
MAX	**2.70160**	**0.05210**	**0.04940**	**0.01960**	**0.01760**	**0.13770**	**0.91790**	**1.59760**	**2.58220**	**0.14141**
MIN	**0.76870**	**0.01860**	**0.01990**	**0.00780**	**0.00700**	**0.05850**	**0.26830**	**0.29760**	**0.75400**	**-0.00100**
% Total		**2.23%**	**2.30%**	**0.78%**	**0.79%**	**6.81%**	**37.60%**	**46.47%**	**96.98%**	**3.02%**

Appendix B

Table 25: Manduca Sexta Scale Mass

Sample	**Wing w/Scales (grams)**	**Wing w/out Scales (grams)**	**Difference (grams)**	**Scale Percentage -**
1	0.0401	0.0291	0.0110	27.4%
2	0.0308	0.0247	0.0061	19.8%
3	0.0277	0.0223	0.0054	19.5%
4	0.0318	0.0275	0.0043	13.5%
5	0.0378	0.0260	0.0118	31.2%
6	0.0197	0.0162	0.0035	17.8%
7	0.0258	0.0209	0.0049	19.0%
8	0.0285	0.0231	0.0054	18.9%
9	0.0244	0.0200	0.0044	18.0%
AVG	**0.0296**	**0.0233**	**0.0063**	**20.6%**
STD	**0.0064**	**0.0040**	**0.0030**	**5.4%**
MAX	**0.0401**	**0.0291**	**0.0118**	**31.2%**
MIN	**0.0197**	**0.0162**	**0.0035**	**13.5%**

Appendix C

Table 26: Manduca Sexta Forewing Area Properties

	AR	**S**	**CentroidX**	**CentroidX**	**CentroidY**	**CentroidY**	**Length**	**Chord**
		(mm$\hat{2}$)	**(mm)**	**% Length**	**(mm)**	**% Chord**	**R (mm)**	**C (mm)**
1	13.88	687.30	24.18	49.5%	8.80	46.9%	48.84	18.76
2	13.82	655.39	22.19	46.6%	10.66	57.6%	47.58	18.52
3	15.21	647.32	23.87	48.1%	8.50	48.5%	49.61	17.53
4	13.98	750.80	25.36	49.5%	8.95	45.5%	51.22	19.67
5	15.24	585.32	22.69	48.1%	8.93	53.7%	47.22	16.64
6	14.11	653.75	23.06	48.0%	9.65	52.9%	48.03	18.24
7	14.05	815.72	9.74	18.2%	20.44	67.9%	53.52	30.10
8	14.47	675.42	10.21	20.7%	18.29	67.8%	49.42	26.97
9	14.22	857.53	14.98	27.1%	20.58	72.0%	55.21	28.60
10	14.12	514.00	11.10	26.1%	16.25	70.5%	42.59	23.03
11	13.91	618.66	12.17	26.2%	18.24	74.6%	46.38	24.46
12	14.61	789.97	10.39	19.4%	19.58	67.7%	53.71	28.93
13	14.45	722.04	28.54	55.9%	9.54	50.3%	51.07	18.94
14	14.44	692.42	28.44	56.9%	8.58	46.0%	50.00	18.65
15	14.29	678.61	27.03	54.9%	9.56	51.8%	49.25	18.46
16	14.26	792.13	29.89	56.2%	9.44	47.3%	53.14	19.97
17	15.46	607.31	26.66	55.0%	7.61	45.1%	48.45	16.85
18	14.18	693.16	27.74	56.0%	9.43	50.4%	49.57	18.71
19	14.40	838.82	12.96	23.6%	20.59	65.0%	54.95	31.66
20	14.43	683.12	11.86	23.9%	18.38	69.7%	49.65	26.38
21	14.94	896.06	12.61	21.8%	20.71	63.1%	57.85	32.83
22	14.88	523.22	8.61	19.5%	16.04	78.4%	44.12	20.47
23	14.37	690.97	11.20	22.5%	18.59	67.4%	49.83	27.56
24	14.30	789.96	11.16	21.0%	19.77	67.6%	53.14	29.25
AVG	**14.42**	**702.46**	**18.61**	**37.3%**	**14.046**	**59.5%**	**50.18**	**22.97**
STD	**0.44**	**99.20**	**7.65**	**15.5%**	**5.164**	**10.8%**	**3.53**	**5.31**
MAX	**15.46**	**896.06**	**29.89**	**56.9%**	**20.708**	**78.4%**	**57.85**	**32.83**
MIN	**13.82**	**514.00**	**8.61**	**18.2%**	**7.607**	**45.1%**	**42.59**	**16.64**

Bibliography

1. Abaqus. *26.3.3 Choosing a beam element.* 6.11 Abaqus User Manual, 2011.
2. Anderson, M. and R. Cobb. “Design and Testing of Flapping Wing Control for a Micro Air Vehicle”. Guidance Navigation and Controls Conference, AIAA, 2011.
3. Anderson, M. and R. Cobb. “Evaluation of BABM for Flapping Wing MAV Control”. Proc of the 49th AIAA ASM, AIAA, 2011.
4. Anderson, M., N. Sladek, and R. Cobb. “Design, Fabrication , and Testing of an Insect-Sized MAV Wing Flapping Mechanism”. Proc of the 49th AIAA ASM, AIAA, 2011.
5. Anderson, M. L. “Design and Control of Flapping Micro Air Vehicles”, March 2011. AFIT/GAE/ENY/11-12.
6. ASTM. “Standard Test Method for In-Plane Shear Response of Polymer Matrix Composite Materials by Tensile Test of a 45 Laminate”, April 2000. Accessed 07 July 2011.
7. ASTM. “Standard Test Method for Tensile Properties of Polymer Matrix Composite Materials”, April 2000. Accessed 07 July 2011.
8. ASTM. “Standard Test Methods for Constituent Content of Composite Materials”, April 2000. Accessed 07 July 2011.
9. Berthelot, J.M. *Composite materials: mechanical behavior and structural analysis.* Springer. ISBN 0-387-98426-7.
10. Bomphrey, R.J., N.J. Lawson, N.J. Harding, G.K. Taylog, and A.L.R. Thomas. “Passive wing pitch reversal in insect flight”. *The Journal of Fluid Mechanics*, 591:321–337, 2007.
11. Combes, S. A. “Materials, Structure, and Dynamics of Insect Wings as Bioinspiration for MAVs”. *Encyclopedia of Aerospace Engineering*, 7, 2010.
12. Combes, S. A. and T. L. Daniel. “Flexural stiffness in insect wings I. Scaling and the influence of wing venation”. *The Journal of Experimental Biology*, 206:1079–1094, 2003.
13. Combes, S. A. and T. L. Daniel. “Flexural stiffness in insect wings II. Spatial distribution and dynamic wing bending”. *The Journal of Experimental Biology*, 206:2989–2997, 2003.
14. Combes, S. A. and T. L. Daniel. “Into thin air contributions of aerodynamic and inertial-elastic forces to wing bending in the hawkmoth Manduca sexta”. *The Journal of Experimental Biology*, 206:2999–3006, 2003.

15. Darvizeh, M., A. Darvizeh, H. Rajabi, and A. Rezaei. "Free vibration analysis of dragonfly wings using finite element method". *Int. Jnl. of Multiphysics*, 3:101–110, 2009.

16. Dawson, D. "Repeatable Manufacture of Wings For Flapping Wing Micro Air Vehicles Using Microelectromechanical System (Mems) Fabrication Techniques", March 2011. AFIT/GAE/ENY/11-M06.

17. Deleon, N. "Manufacturing and Evaluation of a Biologically Inspired Engineered MAV Wing Compared to the Manduca Sexta Wing Under Simulated Flapping Conditions", March 2011. AFIT/GAE/ENY/11-M07.

18. Doman, D.B. and M.W. Oppenheimer. "Dynamics and Control of a Minimally Actuated Biomimetic Vehicle: Part I Aerodynamic Model". Proceedings of the AIAA Guidance, Navigation, and Control Conference, AIAA, 2009.

19. Dudley, R. *The Biomechanics of Insect Flight: form, Function, Evolution*. Princeton University Press, 1999. ISBN 0-691-04430-9.

20. Dudley, R. "Mechanisms and implications of animal flight maneuverability". *Integrative and Comparative Biology*, 42:135–140, 2002.

21. Dupont. "Dupont Kapton HN Technical Data Sheet".

22. Ellington, C.P., C. Berg, A. P. Wilmott, and A.R. Thomas. "Leading-edge vortices in insect flight". *Nature*, 384:626–630, 1996.

23. Ennos, A.R. "The importance of torsion in the design of insect wings". *The Journal of Experimental Biology*, 140:137–160, 1988.

24. Films, Dupont Teijen. "Mylar Material Properties".

25. Finio, B.M., J.K. Shang, and R.J. Wood. "Body torque modulation for a microrobotic fly". International Conference on Robotics and Automation, IEEE, 2009.

26. Finio, B.M., J.P. Whitney, and R.J. Wood. "Stroke plane deviation for a microrobotic fly". Int. Conference on Intelligent Robots and Systems, IEEE, 2010.

27. Finio, B.M. and R.J. Wood. "Distributed power and control actuation in the thoracic mechanics of a robotic insect". *Bioinspiration and Biomimetics*, 5:045006, 2010.

28. Gullan, P.J. and P.S. Cranston. *The Insectons: An Outline of Entomology 3rd Edition*. Blackwell Publishing, 2005. ISBN 1-4051-1113-5.

29. Halpin, J.C. and J.L.Kardos. "The Halpin-Tsai Equations: A Review".

30. Haralick, R.M. and L.G. Shapiro. "Computer and Robot Vision". 2:316–317, 1992.

31. Hedrick, T.L. “Software techniques for two and three dimensional kinematic measurements of biological and biomimetic systems”. *The Journal of Experimental Biology*, 3:1–6, 2008.

32. Herakovich, C.T. *Mechanics of Fibrous Composites*. Wiley, John and Sons, Incorporated, 2000. ISBN 978-0471106364.

33. Ho, S., H. Nassef, N. Pornsinsirirak, Y. C. Tai, H. Nassef, and C. M. Ho. “Unsteady aerodynamics and flow control for flapping wing flyers”. *Progress in Aerospace Sciences*, 39:635–681, 2003.

34. Hollenbeck, A. “Evaluation of the Thorax of Manduca sexta for Flapping Wing Micro Air Vehicle Applications”, March 2012. AFIT/GAE/ENY/12-M22.

35. Hwang, S. and C.S. Chang. “Determination of elastic constants of materials by vibration testing”. *Composite Structures*, 49:183–190, 2000.

36. Jantzen, B. and Thomas Eisner. “Hindwings are unnecessary for flight but essential for execution of normal evasive flight in Lepidoptera”. *PNAS*, 105:16636–16640, 2008.

37. Jongerius, S.R. and D. Lentink. “Structural Analysis of a Dragonfly Wing”. *Experimental Mechanics*, 2010.

38. Jordan, T., Z. Ounaries, J. Tripp, and P. Tcheng. “Electrical Properties and Power Characteristics of a Piezoelectric Actuator”. *NASA ICASE Report*, 8, 2000.

39. Karpelson, M., G.Y. Wei, and R.J. Wood. “A Review of Actuation and Power Electronics Options for Flapping-Wing Robotic Insects”. International Conference on Robotics and Automation, IEEE, 2008.

40. Kempf, M. “Determination of Youngs Moduli of the Insect Cuticle”. *Application Note*.

41. Knospe, C. R. “Insect Flight Mechanisms: Anatomy and Kinematics”. *University of Virginia*, 1998.

42. Knowles, K. “Recent Progress Towards Developing an Insect-Inspired Flapping-Wing Micro Air Vehicle”. *Department of Aerospace, Power and Sensors Cranfield University*, 2007.

43. Laboratory, AF Research. “Micro Air Vehicles”, 2009. Transcript of Promotional Video.

44. Lehmann, F.O. “The mechanisms of lift enhancement in insect flight”. *Naturwissenschaften*, 191:101–122, 2004.

45. Lewis, J.P. “Fast Normalized Cross-Correlation”.

46. Liu, H., C.P. Ellington, K. Kawachi, C. Berg, and A.P. Wilmott. “A computational fluid dynamic study of the hawkmoth hovering”. *The Journal of Experimental Biology*, 201:461–477, 1998.

47. Liu, T., K. Kuykendoll, R. Rhew, and S. Jones. "Avian Wings". 24th AIAA Aerodynamic Measurement Technology and Ground Testing Conference, AIAA, 2004.

48. Lopez-Anido, R., J.F. Davalos, and E.J. Barbero. "Experimental Evaluation of Stiffness of Laminated Composite Beam Elements Under Flexure". *Journal of Reinforced Plastics and Composites*, 14:349–361, 1995.

49. Lopez-Anido, R., J.F. Davalos, and E.J. Barbero. "Aerodynamic and functional consequences of wing compliance". *Experiments in Fluids*, 46:873–882, 2009.

50. Madangopal, R., Z.A. Khan, and S.K. Agrawal. "Biologically Inspired Design Of Small Flapping Wing Air Vehicles Using Four-Bar Mechanisms And Quasi-steady Aerodynamics". *Journal of Mechanical Design*, 127:809–816, 2005.

51. Marrocco, J., L.Demasi, and S. Venkataraman. "Investigating the StructuralDynamics Implication of FlexibleResilin Joints on Dragonfly Wings". 2010 Access Proceedings, CSRC, 2010.

52. Mengesha, T.E., R.R. Vallance, M. Barraha, and R. Mittal. "Parametric structural modeling of insect wings". *Bioinspiration and Biomimetics*, 4, 2009.

53. Mengesha, T.E., R.R. Vallance, M. Barraha, and R. Mittal. "Stiffness of desiccating insect wings". *Bioinspiration and Biomimetics*, 6, 2011.

54. Meyer, J.R. "External Anatomy: Wings".

55. Motavalli, M. "Laminate Theory Fibre Composites FS10", 2010.

56. Murray, J. "Development of Photographic Dynamic Measurements Applicable to Evaluation of Flapping Wing Micro Air Vehicles", March 2012. AFIT/GAE/ENY/11-D02.

57. Myers, P. "Manduca Sexta Classification".

58. N.A., Johnson Matthey Noble Metals. "Setting Shapes in Nitinol".

59. Nettles, A.T. *Basic Mechanics of Laminated Composite Plates*. NASA, 1994. Reference Publication 1351.

60. Nguyen, Q.V., H.C. Park, N.S. Goo, and D. Byun. "Aerodynamic force generation of an insect-inspired flapper actuated by a compressed unimorph actuator". *Chinese Science Bulletin*, 2009.

61. Nguyen, Q.V., Q.T. Truong, H.C. Park, and D. Byun. "A Motor-driven Flapping-wing System Mimicking Beetle Flight". International Conference on Robotics and Biomimetics, IEEE, Gullin, China, 2009.

62. Norris, A., A. Palazotto, and R. Cobb. "Structural Dynamic Characterization of and Insect Wing: Toward the Development of Bug Sized Flapping Wing Micro Air Vehicles". *American Institute of Aeronautics and Astronautics*, 2010. AIAA-2010-2790.

63. Objet. “Eden500V 3D Printer”.

64. Objet. “Objet Digital Materials Data Sheet”.

65. OH́ara, R.P. and J.M. Brown. “Experimental Investigation of Geometric Uncertainty Effects on Blade Forced Response”. 40th AIAA/ASME/SAE/ASEE Joint Propulsion Conference and Exhibit, AIAA, Fort Lauderdale, Florida, 2004.

66. OH́ara, R.P., N. DeLeon, and A. Palazotto. “Structural Identification and Simulation of the Manduca Sexta Forewing”. 2011 SDM Conference, AIAA, Denver, Colorado, 2011.

67. OH́ara, R.P. and A. Palazotto. “The morphological characterization of the forewing of the Manduca Sexta species for the application of biomimetic flapping wing micro air vehicles”. *Journal of Bioinspiration and Biomimicry*, 2012.

68. Oliver, W.C. and G.M. Pharr. “Measurement of hardness and elastic modulus by instrumented indentation: Advances in understanding and refinements to methodology”. *Journal of Materials Research*, 19, 2003.

69. Pellegrino, S. “Ultra-thin Carbon Fiber Composites:Constitutive Modeling and Applications to Deployable Structures”. Accessed 04 August 2011.

70. Pittenger, D.J. “Power Calculator: A Collection of Interactive Programs”. *Educational and Psychological Measurement*, 61, 2001.

71. Pornsin-sirirak, T. Nick, Y. C. Tai, H. Nassef, and C. M. Ho. “Titanium-alloy MEMS Wing Technology for a Micro Aerial Vehicle Application”. *Journal of Sensors and Actuators A: Physical*, 8:95–103, March 2001.

72. Pratt, W.K. *Digital Image Processsing*. John Wiley and Sons, 2001. ISBN 978-0471857662.

73. Ramsaroop, A. and K. Kanny. “Using MATLAB to Design and Analyse Composite Laminates”. *Scientific Research*, 2:904–916, 2010.

74. Richman, D. “Tobacco Hornworm”.

75. Richter, C. and H. Lipson. “Untethered Hovering Flapping Flight of a 3D-Printed Mechanical Insect”. Proc. of the Alife XII Conference, Alife, Odense,Denmark, 2010.

76. Sane, S.P. and M.H. Dickinson. “The aerodynamic effects of wing rotation and a revised quasi-steady model of flapping flight”. *The Journal of Experimental Biology*, 205:1087–1097, 2002.

77. Science, I.O.P. “Scope”. *Bioinspiration and Biomimetics*, 2011.

78. Shang, J.K., S.A. Combes, B.M. Finio, and R.J. Wood. “Artificial insect wings of diverse morphology for flapping-wing micro air vehicles”. *Bioinspiration and Biomimetics*, 4:1–7, 2009.

79. Shyy, W., H. Aono, S.K. Chimakurthi, P. Trizila, C.K. Kang, C.E.S. Cesnik, and H.Liu. "Recent progress in flappingwing aerodynamics and aeroelasticity". *Progress in Aerospace Sciences*, 4, 2010. Doi:10.1016/j.paerosci.2010.01.001.

80. Sims, T. *A Structural Dynamic Anaysis of a Manduca Sexta Forewing*. Master's thesis, Air Force Institute of Technology, Wright-Patterson AFB, OH, March 2010. AFIT/GAE/ENY/10-M22.

81. Singha, B., M. Ramasamy, I. Chopra, and J.G. Leishman. "Experimental Studies on Insect-Based Flapping Wings for Micro Hovering Air Vehicles". *AIAA*, 4:1–7, 2009.

82. Sitti, M., D. Campolo, J. Yan, and R. Fearing. "Development of PZT and PZN-PT Based Unimorph Actuators for Micromechanical Flapping Mechanisms". Robotics and Automation, IEEE, 2001.

83. Sladek, N., M. Anderson, and R. Cobb. "Aero and Structural-dynamic Repeatability of a Novel MAV Wing Manufacturing Process". Atmospheric Flight Mechanics Conference, AIAA, Portland, Oregon, 2011.

84. Song, F., K. L. Lee, A. K. Soh, F. Zhu, and Y. L. Bai. "Experimental studies of the material properties of the forewing of cicada". *The Journal of Experimental Biology*, 207:3035–3042, 2004.

85. Steltz, E. and R.S. Fearing. "Dynamometer Power Output Measurements of Miniature Piezoelectric Actuators". *IEEE/ASME Transaction on Mechatronicx*, 14:1–10, 2009.

86. Steltz, E., M. Seeman, S. Avadhanula, and R.S. Fearing. "Power Electronics Design Choice for Piezoelectric Microrobots". Intelligent Robots and Systems Conference, IEEE, Beijing, China, 2006.

87. Stoffregen, D.E. "Personal Correspondence 24 November 2009".

88. Storage, T. "Composite Fiber Database". Accessed 04 August 2011.

89. Storage, T. "Personal Correspondence November 2009 to August 2011". Air Force Research Laboratory Materials Directorate.

90. Szelag, T. "A Finite Element Analysis of a Carbon Fiber Composite Micro Air Vehicle Wing", March 2012. AFIT/GAE/ENY/12-M44.

91. Tanaka, H., K. Matsumoto, and I. Shimoyama. "Fabrication of a three-dimensional insect-wing model by micromolding of thermosetting resin with a thin elastmeric mold". *Journal of Micromechanics and Microengineering*, 17:2485–2490, 2007.

92. Tanaka, H. and I. Shimoyama. "Forward flight of swallowtail butterly with simple flapping motion". *Bioinspiration and Biomimetics*, 5:026003, 2010.

93. Tanaka, H., J.P. Whitney, and R. Wood. "Effect of Flexural and Torsional Wing Flexibility on Lift Generation in Hoverfly Flight". *Integrative and Comparative Biology*, 10:1–9, 2011.

94. Tandon, G.P. "Personal Correspondence November 2009 to August 2011".

95. Tubbs, T. *Biological Investigation of the Stimulated Flapping Motions of the Moth, Manduca Sexta*. Master's thesis, Air Force Institute of Technology, Wright-Patterson AFB, OH, March 2011. AFIT/GSS/ENY/11-M04.

96. Tucker, C.L. and E. Liang. "Stiffness predictions for unidirectional short fiber composites Review and evaluation". *Composites Science and Technology*, 59:655–671, 1999.

97. Usherwood, J.R. and C.P. Ellington. "The aerodynamics of revolving wings I. Model hawkmoth wings". *The Journal of Experimental Biology*, 205:1547–1564, 2002.

98. Vincent, J.F. and U.G. Wegst. "Design and mechanical properties of insect cuticle". *Arthropod Structure and Development*, 33:187–199, 2004.

99. Vogt, R. "Richard Dominick Moth and Butterfly Collection".

100. Walker, S.M. "Deformable wing kinematics in free-flying hoverflies". *Journal of the Royal Society*, 7:131–142, 2009.

101. Whitney, J.P. "Personal Correspondence 12 November 2009".

102. Whitney, J.P. and R.J. Wood. "Aeromechanics of passive rotation in flapping flight". *Journal Fluid Mechanics*, 660:197–230, 2010.

103. Willis, Mark. "Personal Correspondence 1-5 July 2010".

104. Willmott, A.P. and C.P. Ellington. "Measuring the angle of attack of beating insect wings: robust three-dimensional reconstruction from two-dimensional images". *The Journal of Experimental Biology*, 2000:2693–2704, 1997.

105. Willmott, A.P. and C.P. Ellington. "The mechanics of flight in the hawkmoth Manduca sexta. I. Kinematics of hovering and forward flight". *The Journal of Experimental Biology*, 2000:2705–2722, 1997.

106. Willmott, A.P. and C.P. Ellington. "The mechanics of flight in the hawkmoth Manduca sexta. II. Aerodynamic consequences of kinematic and morphological variation". *The Journal of Experimental Biology*, 2000:2723–2745, 1997.

107. Wood, R.J. "Design Fabrication and Analysis of a 3DOF 3cm Flapping Wing MAV". Conference on Intelligent Robots and Systems, IEEE, San Diego, CA, USA, 2007.

108. Wood, R.J. "The First Takeoff of a Biologically Inspired At-Scale Robotic Insect". volume 24, 341–347. IEEE, April 2008.

109. Wood, R.J., S. Avadhanula, M. Menon, and R.S. Fearing. "Microrobotics Using Composite Materials: The Micromechanical Flying Insect Thorax". Int. Conf. on Robotics and Automation, IEEE, 2003.

110. Wood, R.J., B. Finio, M. Karpelson, K. Ma, N.O.Perez-Arancibia, P.S. Sreetharan, H. Tanaka, and J.P. Whitney. "Progress on "pico" air vehicles". Int. Symp. on Robotics Research, IFRR, 2011.

111. Wood, R.J., E. Steltz, and R.S. Fearing. "Optimal Energy Density Piezoelectric Bending Actuators". volume 119, 476–488. elsevier, 2005.

112. Wooton, R.J. "Functional Morphology of Insect Wings". *Annual Review of Entomology*, 37:113–140, 1992.

113. Wooton, R.J., K.E. Evans, R. Herber, and C.W. Smith. "The Hind Wing of the Desert Locust I. Functional Morophology and Mode of Operation". *The Journal of Experimental Biology*, 203:2921–2931, 2000.

114. Wooton, R.J., K.E. Evans, R. Herber, and C.W. Smith. "The Hind Wing of the Desert Locust II. Mechanical Properties and Functioning of the Membrane". *The Journal of Experimental Biology*, 203:2933–2943, 2000.

115. Wooton, R.J., K.E. Evans, R. Herber, and C.W. Smith. "The Hind Wing of the Desert Locust III. A Finite Element Analysis of a Deployable Structure". *The Journal of Experimental Biology*, 203:2945–2955, 2003.

116. Wooton, R.J., R.C. Herbert, P.G. Young, and K.E. Evans. "Approaches to the structural modelling of insect wings". *Philosophical Transactions of the Royal Society*, 358:1577–1587, 2003.

117. Wooton, R.J. and J. Kukalova. "Flight adaptations in Palaeozoic Palaeoptera". *Cambridge Philosophical Society*, 75:129–167, 2000.

118. Xie, L., P. Wu, and P. Ifju. "Advanced Flapping Wing Structure Fabrication for Biologically-Inspired Hovering Flight". 51st AIAA/ASME/ASCE/AHS/ASC Structures, Structural Dynamics, and Materials Conference, AIAA, 2010.

119. Yin, B. "Effect of wing inertia on hovering performance of flexible flapping wings". *Physics of Fluids*, 22:1–10, 2010.

120. Zhao, L., Q. Huang, X. Deng, and S.P. Sane. "Aerodynamic effects of flexibility in flapping wings". *Journal of the Royal Society*, 7:485–497, 2010.

REPORT DOCUMENTATION PAGE	*Form Approved* *OMB No. 0704–0188*

1. REPORT DATE (DD–MM–YYYY) 13-09-2012	2. REPORT TYPE PhD Dissertation	3. DATES COVERED (*From — To*) 17-08-2009 to 13-09-2012

4. TITLE AND SUBTITLE The Characterization of Material Properties and Structural Dynamics of the Manduca Sexta Forewing for Application to Flapping Wing Micro Air Vehicle Design	5a. CONTRACT NUMBER 5b. GRANT NUMBER 5c. PROGRAM ELEMENT NUMBER
6. AUTHOR(S) Ryan P. O'Hara, Maj, USAF	5d. PROJECT NUMBER 5e. TASK NUMBER 5f. WORK UNIT NUMBER
7. PERFORMING ORGANIZATION NAME(S) AND ADDRESS(ES) Air Force Institute of Technology Graduate School of Engineering and Management (AFIT/ENY) 2950 Hobson Way WPAFB OH 45433-7765	8. PERFORMING ORGANIZATION REPORT NUMBER AFIT/DS/ENY/12-06
9. SPONSORING / MONITORING AGENCY NAME(S) AND ADDRESS(ES) Air Force Office of Scientific Research, AFOSR Air Force Research Lab, AFRL	10. SPONSOR/MONITOR’S ACRONYM(S) AFOSR, AFRL 11. SPONSOR/MONITOR’S REPORT NUMBER(S)

12. DISTRIBUTION / AVAILABILITY STATEMENT

APPROVED FOR PUBLIC RELEASE; DISTRIBUTION UNLIMITED

13. SUPPLEMENTARY NOTES

The views expressed in this dissertation are those of the author and do not reflect the official policy or position of the U.S. Air Force, Department of Defense, or the U.S. Government. This material is declared a work of the U.S. Government and is not subject to copyright protection in the U.S.

14. ABSTRACT

The Manduca Sexta species of moth serves as a source of biological inspiration for the future of micro air vehicle flapping flight. The ability of this species to hover in flapping flight has warranted investigation into the critical material, structural, and geometric properties of the forewing of this biological specimen. A rigorous morphological study of the Manduca Sexta forewing was conducted to characterize the physical and material properties of the biological forewing for the purpose of developing an advanced parametric three dimensional model finite element analysis (FEA) model. This FEA model was tuned to match the experimentally determined structural dynamics of the biological specimen and serves as the basis for an engineered wing design. Manufacturing methods are developed and implemented to fabricate the baseline engineered wing design. Biological wings and engineered wings are experimentally tested to determine the aerodynamic lift production of each of wings under the same boundary conditions. Through this research, a structural dynamics based engineering methodology has been used to design, develop, and identify biomimetic engineered wings that experimentally produce aerodynamic forces equivalent to their biological analog.

15. SUBJECT TERMS

flapping wing micro air vehicle, micro air vehicle, Manduca Sexta, forewing, biomimetic, biomimicry, structural dynamics, piezo, nanoindentation, modal analysis, finite element analysis, FEA, lift, hover

16. SECURITY CLASSIFICATION OF:			17. LIMITATION OF ABSTRACT	18. NUMBER OF PAGES	19a. NAME OF RESPONSIBLE PERSON Anthony N. Palazotto, PhD, AFIT/ENY
a. REPORT U	b. ABSTRACT U	c. THIS PAGE U	UU	206	19b. TELEPHONE NUMBER (Include Area Code) 937-255-3636 x-4599 anthony.palazotto@afit.edu

Standard Form 298 (Rev. 8–98)
Prescribed by ANSI Std. Z39.18